Search for Events with Isolated Leptons and Large Missing Transverse Momentum in ep Collisions at HERA

Dissertation
zur Erlangung des Doktorgrades
des Fachbereichs Physik
der Universität Hamburg

vorgelegt von

Dominik Dannheim

aus Hamburg

Hamburg
2003

Gutachter der Dissertation:	Prof. Dr. R. Klanner Prof. Dr. R.-D. Heuer Prof. Dr. A. Caldwell
Gutachter der Disputation:	Prof. Dr. E. Lohrmann Prof. Dr. P. Schleper
Datum der Disputation:	25. Juli 2003
Vorsitzender des Prüfungsausschusses:	Prof. Dr. F.-W. Büßer
Vorsitzender des Promotionsausschusses:	Prof. Dr. R. Wiesendanger
Dekan des Fachbereichs Physik:	Prof. Dr. G. Huber

Abstract

This thesis presents a search for events with isolated leptons and large missing transverse momentum in $e^{\pm}p$ collisions at HERA, using an integrated luminosity of $130\,\mathrm{pb}^{-1}$, collected with the ZEUS detector. Some extensions of the Standard Model predict quark-flavour changing neutral currents (FCNC), which could at HERA lead to the production of single top quarks with subsequent leptonic decay of a W boson: $ep \to etX$, $t \to W^+b$, $W^+ \to e^+\nu$, $\mu^+\nu$, $\tau^+\nu$. In the final selection of the electron- and muon decay channels, no events were observed, while $1.89^{+0.18}_{-0.14}$ events were exptected from Standard Model processes, mainly from the direct production of W bosons. The results were combined with a search for single-top production in the hadronic decay channel of the W boson to constrain single-top production through photon- or Z^0 exchange. The upper limit obtained on the FCNC coupling constant of $\kappa_{tu\gamma} < 0.174$ excludes a substantial region, which has not been ruled out by other experiments. Tau leptons were identified in their hadronic decay modes as collimated jets. Two events containing isolated tau lepton candidates and large hadronic transverse momentum were observed in the data, while only 0.20 ± 0.05 were expected from Standard Model background processes. The sensitivity of the ZEUS experiment to signals from processes beyond the Standard Model will increase in the future HERA II data taking by using a recently installed silicon microstrip detector. A radiation monitoring and automatic beam-dump system has been developed and successfully used in the ongoing HERA II commissioning phase to prevent the silicon detector and its readout electronics from radiation damage.

Kurzfassung

In dieser Arbeit wird eine Suche nach Ereignissen mit isolierten Leptonen und großem fehlenden Transversalimpuls in $e^{\pm}p$ Kollisionsdaten bei HERA beschrieben. Es wurde eine mit dem ZEUS Detektor gesammelte integrierte Luminosität von $130\,\mathrm{pb}^{-1}$ analysiert. Erweiterungen des Standard Modells sagen quark-flavour verändernde neutrale Ströme (FCNC) voraus. Diese könnten bei HERA zur Produktion von einzelnen top-Quarks mit folgendem leptonischen Zerfall eines W Bosons führen: $ep \to etX$, $t \to W^+b$, $W^+ \to e^+\nu$, $\mu^+\nu$, $\tau^+\nu$. In der Endselektion des Elektron- und Myon-Kanals wurden keine Ereignisse gefunden, bei $1.89^{+0.18}_{-0.14}$ von Standard Modell Prozessen erwarteten Ereignissen, hauptsächlich von direkter W Produktion. Die Ergebnisse wurden mit einer Suche nach Produktion von einzelnen top-Quarks im hadronischen W Zerfallskanal kombiniert, um Ausschlußgrenzen auf die Produktion von einzelnen top-Quarks durch Photon- und Z^0-Austausch zu setzen. Die resultierende Obergrenze für die FCNC Kopplungskonstante von $\kappa_{tu\gamma} < 0.174$ deckt einen wesentlichen Bereich ab, der von anderen Experimenten nicht ausgeschlossenen wurde. Tau Leptonen wurden in ihren hadronischen Zerfallskanälen als kollimierte Jets identifiziert. Zwei Ereignisse mit isolierten Tau-Lepton Kandidaten und hohem hadronischen Transversalimpuls wurden in den Daten gefunden, bei nur 0.20 ± 0.05 erwarteten Untergrundereignissen aus Standard Modell Prozessen. Durch die Verwendung eines kürzlich im ZEUS Experiment installierten Silizium Mikrostreifendetektors kann in der zukünftigen HERA II Datennahmeperiode mit erhöhter Sensitivität nach Signalen von Prozessen jenseits des Standardmodells gesucht werden. Ein Strahlungsmonitor- und automatisches Strahlabschaltungs-System wurde entwickelt und in der andauernden HERA II Inbetriebnahme-Phase erfolgreich eingesetzt, um den Siliziumdetektor und seine Ausleseelektronik vor Strahlenschäden zu schützen.

Contents

1 Introduction **1**

2 The ZEUS experiment at HERA **3**

2.1 HERA 3

2.2 ZEUS 5

2.2.1 The central tracking detector 8

2.2.2 Calorimeter 9

2.2.3 Luminosity monitor 10

2.2.4 Trigger and data acquisition 12

3 Theoretical overview **15**

3.1 The Standard Model 15

3.2 Lepton-nucleon scattering at HERA 17

3.2.1 Kinematic variables 17

3.2.2 The electron-proton cross section 19

3.2.3 QCD factorisation and extraction of the parton density 19

3.2.4 Photoproduction 21

3.2.5 Lepton pair production 22

3.2.6 Production of single W bosons 23

3.3 Supersymmetry 26

3.3.1 The minimal supersymmetric model (MSSM) 26

3.3.2 R-parity violating SUSY 27

3.4 The signal process $ep \to etX$ 30

3.4.1 The top quark 30

3.4.2 Possible production of single top quarks at HERA 31

3.4.3 Leading order cross-section and decay-width calculations 34
3.4.4 Next-to-leading-order cross-section calculations 36

4 Search Strategy **39**
4.1 Generic search for isolated leptons and missing transverse momentum . 39
4.2 Single-top quark production 39
4.2.1 Existing constraints on single-top production 39
4.2.2 Single-top production signatures at HERA 40
4.3 Background processes 42
4.3.1 Standard Model e-p background 42
4.3.2 Non *ep* background 43

5 Monte Carlo Simulation **45**
5.1 QCD radiation 45
5.2 Hadronisation models 46
5.3 Simulation of the signal process 47
5.4 Photoproduction processes (PhP) 49
5.5 Neutral and charged current deep inelastic scattering (NC and CC DIS) 53
5.6 Lepton pair production 53
5.7 Production of single $W^{\pm}$ bosons 55
5.8 Detector simulation 57

6 Dataset and event reconstruction **61**
6.1 Dataset 61
6.2 Definition of the reconstructed variables 61
6.2.1 Calorimeter energy corrections 61
6.2.2 Global calorimeter variables 63
6.2.3 Track and vertex finding 65
6.2.4 Electron identification 65
6.2.5 Muon identification 65
6.2.6 Tau identification 65
6.2.7 Jet finding 66

6.2.8 Jet-energy correction . . . 67
6.2.9 Jet estimators . . . 67
6.2.10 Additional event variables . . . 68

7 Search for isolated electrons and muons 73
7.1 Control selection . . . 73
7.1.1 Electron candidates (control selection) . . . 77
7.1.2 Muon candidates (control selection) . . . 81
7.2 Preselection of isolated lepton events . . . 85
7.2.1 Track selection . . . 85
7.2.2 Electron candidates (preselection) . . . 87
7.2.3 Muon candidates (preselection) . . . 92
7.3 Final selection of top decay candidates . . . 99
7.3.1 Optimisation of the final selection cuts . . . 99
7.3.2 Results of the final single-top selection . . . 103
7.3.3 Cross efficiencies . . . 104
7.3.4 Single-top efficiencies . . . 105
7.4 Statistical and systematic uncertainties . . . 106
7.5 Search for single-top production in the hadronic channel . . . 109

8 Exclusion limits on single-top production 111
8.1 Limit setting procedure . . . 111
8.2 Exclusion limits in the $\kappa_{tu\gamma}$-v_{tuZ} plane . . . 113
8.3 One-dimensional exclusion limits . . . 113
8.4 Exclusion limits based on NLO calculations . . . 113

9 Search for isolated tau leptons 117
9.1 Tau identification . . . 117
9.1.1 Properties of the tau lepton . . . 117
9.1.2 Inclusive CC DIS control selection . . . 118
9.1.3 Jet shape observables . . . 120
9.1.4 Tau discriminant . . . 123

9.2 Preselection of tau candidate events 128
9.3 Selection of events with large hadronic transverse momentum 131
9.4 Systematic uncertainties 136
9.5 Results 137

10 Comparison to other searches for isolated lepton events at HERA 139
10.1 Results from the H1 collaboration 139
10.1.1 Search for isolated electrons and muons in events with missing p_T 140
10.1.2 Search for single-top production in the leptonic channel 141
10.1.3 Search for single-top production in the hadronic channel 143
10.1.4 Exclusion limits on single-top production 143
10.2 Processes beyond the Standard Model 144
10.2.1 Anomalous W production 144
10.2.2 Single-top production 146
10.2.3 Anomalous tau production 147
10.3 H1 and ZEUS isolated lepton events in the future 148

11 A radiation monitor for the ZEUS Micro Vertex Detector 153
11.1 The HERA upgrade and the ZEUS Micro Vertex Detector 153
11.2 Radiation background in the ZEUS interaction region 154
11.2.1 Synchrotron radiation 154
11.2.2 Lepton beam-gas background 155
11.2.3 Proton-beam background 157
11.3 Tolerable radiation dose for the MVD 157
11.4 Requirements for the radiation monitor 158
11.5 Components of the radiation monitor system 159
11.5.1 Layout 159
11.5.2 Silicon PIN diodes 160
11.5.3 Silicon diode and NTC readout 165
11.5.4 Leaky bucket integrated dose measurement 166
11.5.5 Diode current readout parameters 167
11.5.6 Radiation field-effect transistors 169

11.5.7 Thermoluminescent dosimeters 170
11.6 Bulk damage in silicon devices 170
11.6.1 NIEL hypothesis 170
11.6.2 Leakage-current increase and long-term annealing 171
11.6.3 Short-term annealing 172
11.6.4 Dose estimation 173
11.7 Results from the HERA II commissioning phase 174
11.7.1 Temperature correction 174
11.7.2 Dose rate and leaky bucket measurements 174
11.7.3 Offset current measurements 176
11.7.4 Total dose estimates 179
11.7.5 Outlook 181

12 Summary **185**

A Trigger bit definitions **189**
A.1 DST bit 10 189
A.2 DST bit 34 189
A.3 SLT 190
A.4 TLT 190

B Event displays of electron and muon candidate events **191**

C Event displays of tau candidate events **196**

D ZEUS preliminary results for EPS 2001 **199**

List of Figures

2.1 Aerial view of the DESY area in Hamburg, Germany 4
2.2 Schematic view of the HERA accelerator 5
2.3 Integrated luminosity delivered by HERA 6
2.4 Cross section of the ZEUS detector along the beam axis 7
2.5 Cross section of the ZEUS detector perpendicular to the beam axis . . 8
2.6 Cross section view of a CTD octant 9
2.7 View of an FCAL module 11
2.8 The ZEUS luminosity monitoring system 12
2.9 The ZEUS trigger and data acquisition system 14

3.1 Diagram illustrating positron proton scattering 18
3.2 Differential NC and CC cross sections as function of Q^2 20
3.3 PDFs from the ZEUS NLO QCD fit 21
3.4 Diagrams for hard photoproduction processes 22
3.5 Diagrams for lepton-pair-production and QED compton processes . . . 23
3.6 Diagrams for $W^{\pm}$ boson production processes 24
3.7 Diagrams for NLO corrections to the photoproduction of W bosons . . 25
3.8 Diagram for selectron-squark production 27
3.9 Diagram for stop-quark production with subsequent two-body decay . 28
3.10 Diagram for stop-quark production with subsequent bosonic decay . . 29
3.11 Diagram for R-parity violating production of tau leptons 30
3.12 Diagrams for SM top-quark production at HERA 31
3.13 Diagrams for FCNC 33
3.14 Single-top production through FCNC 33
3.15 Diagrams for anomalous top-quark decays 34

3.16 Cross section for single-top quark production 35
3.17 Relative contribution of the interference term to single-top cross section 36
3.18 NLO corrections to the single-top cross section 37

4.1 Diagram for single-top production through FCNC at LEP 40

5.1 Diagrams for 3-jet production 46
5.2 Kinematic variables for the single-top MCs (I) 50
5.3 Kinematic variables for the single-top MCs (II) 51
5.4 Kinematic variables for the single-top MCs (III) 52
5.5 EPVEC and NLO W-production cross sections at $\sqrt{s} = 300\,\mathrm{GeV}$ . . . 58
5.6 EPVEC and NLO W-production cross sections at $\sqrt{s} = 318\,\mathrm{GeV}$ . . . 59

6.1 Jet-energy resolution for the signal MC 68
6.2 Event acoplanarity 69

7.1 Number of dead CAL cells 76
7.2 Position of dead CAL cells 76
7.3 Kinematic variables control selection electron channel (I) 79
7.4 Kinematic variables control selection electron channel (II) 80
7.5 Event yields control selection electron and muon channel 81
7.6 Kinematic variables control selection muon channel (I) 83
7.7 Kinematic variables control selection muon channel (II) 84
7.8 Isolation plot D_{trk}-D_{jet} for preselection 86
7.9 Kinematic variables preselection electron channel (I) 88
7.10 Kinematic variables preselection electron channel (II) 89
7.11 p_T^{hadr}-$M_T^{l\nu}$ distribution preselection electron channel 90
7.12 p_T^{el}-p_T^{miss} distribution preselection electron candidates 91
7.13 Event yields preselection electron and muon channel 92
7.14 Kinematic variables preselection muon channel (I) 94
7.15 Kinematic variables preselection muon channel (II) 95
7.16 p_T^{hadr}-$M_T^{l\nu}$ distribution preselection muon channel 96
7.17 p_T^{mu}-p_T^{miss} distribution preselection muon channel 97

7.18 Expected 95% C.L. upper limits electron channel 101
7.19 Expected 95% C.L. upper limits muon channel 102
7.20 Event yields final selection of electron and muon candidates 104

8.1 95% C.L. limits for single-top production 115

9.1 QCD jet and tau jet in the ZEUS detector 119
9.2 Global event variables for CC DIS control selection 121
9.3 Jet shape observables for CC DIS control selection 124
9.4 Discriminant calculation in arbitrary jet-observable space 125
9.5 Tau discriminant for CC DIS control selection 126
9.6 Signal efficiency and separation for CC DIS control selection 127
9.7 Control plots for not identified isolated tracks 130
9.8 Tau discriminant for tau preselection 132
9.9 Control plots for tau selection ($D > 0.95$) 133
9.10 Event yields tau search 135

10.1 Reconstructed top mass 142
10.2 Negative log-likelihood function for hypothetical BSM signals 151
10.3 Poisson probabilities of future event yields 152

11.1 Horizontal view of the HERA lepton beamline 156
11.2 The radiation monitor system inside the ZEUS detector 161
11.3 Radiation monitor module before and after assembly 162
11.4 Long term test of the diode leakage current 163
11.5 Integrated fluence and resulting diode leakage current 164
11.6 Connection scheme of a radiation monitor module 166
11.7 Time and integrated dose before a beam-dump request 168
11.8 Change in the transfer characteristic of a RadFET after irradiation . . 169
11.9 Schematic of the RadFET readout 170
11.10 NIEL scaling factors for neutrons, protons, pions and electrons 171
11.11 Leakage current after proton irradiation spill 173
11.12 Temperature correction for diode leakage current 175

11.13 Dose rate measurement during positron injection 177
11.14 Dose rate and leaky-bucket level before automatic beam dump 178
11.15 Current increase and annealing after positron beam-loss 180
11.16 Integrated dose estimates from RadFET measurements 182
11.17 Offset leakage current in the radiation monitor diodes 182

B.1 Muon candidate event (run 31224, event 19966) 192
B.2 Electron candidate event (run 32859, event 53874) 192
B.3 Muon candidate event (run 33719, event 5856) 193
B.4 Muon candidate event (run 34348, event 9897) 193
B.5 Muon candidate event (run 35081, event 34896) 194
B.6 Muon candidate event (run 35092, event 49609) 194
B.7 Electron candidate event (run 36544, event 24240) 195

C.1 Tau-candidate 1 197
C.2 Tau-candidate 2 and 3 198

List of Tables

3.1 The fundamental interactions in the Standard Model 16
3.2 The fundamental fermions in the Standard Model 16
3.3 Single-top-production-parametrisation coefficients 35
3.4 Top decay-width coefficients 37

5.1 MC samples for single-top production 48
5.2 MC samples for photoproduction 52
5.3 MC samples for NC DIS 54
5.4 MC samples for CC DIS 54
5.5 MC samples for lepton-pair production 56
5.6 MC samples for single W-boson production 57

6.1 Running conditions and luminosities for 1994-2000 data taking 62
6.2 CAL energy-correction factors 62

7.1 CAL-timing cuts and minimal energy requirements 74
7.2 Observed and expected events control selection electron channel 78
7.3 Observed and expected events control selection muon channel 85
7.4 Observed and expected events preselection electron channel 92
7.5 Observed and expected events preselection muon channel 93
7.6 Kinematic variables for electron and muon preselection candidates . . 98
7.7 Observed and expected events electron/muon channels final selection . 103
7.8 Cross efficiencies for single-top signal MC 105
7.9 Single-top efficiencies for the different signal MC samples 106
7.10 Statistical and systematic uncertainties preselection electron/muon ch. 108
7.11 Statistical and systematic uncertainties final selection electron/muon ch. 108

7.12 Summary observed and expected events electron/muon channels 109

8.1 Parameters for single-top production limit calculation 114
8.2 95% C.L. limits for coupling constants and cross sections 116

9.1 Main decay modes of the tau lepton 118
9.2 Kinematic variables for events from the tau preselection 131
9.3 Event yields tau search 134
9.4 Systematic and statistical uncertainties tau search 137
9.5 Summary isolated lepton searches 138

10.1 Comparison main selection requirements electron/muon channels . . . 140
10.2 Observed and predicted event rates electron/muon channels H1 141
10.3 Most probable cross-section values for BSM W production signal . . . 146
10.4 Most probable cross-section values for single-top production signal . . 147
10.5 Most probable cross-section values for anomalous tau-production signal 148

11.1 Parameters of the silicon diodes used for the radiation monitor 162
11.2 Parameters for the diode current and integrated dose measurement . . 168
11.3 Integrated dose estimates TLDs 183

D.1 Event yields EPS 2001 single-top analysis 200

Chapter 1

Introduction

The Standard $SU(3) \otimes SU(2) \otimes U(1)$ Model (SM) of particle physics describes the electroweak and strong interactions between elementary particles in both the low- and the high-energy regime to an amazing accuracy. It is, however, unsatisfactory in the sense that many fundamental facts such as the quark-lepton symmetry and the structure of the gauge groups remain unexplained. Furthermore, the inclusion of gravitation as the fourth fundamental force in nature remains an open question. The experimental observation of deviations from the SM would provide an important guidance to develop theories providing a deeper understanding of the structure of matter. Rare SM processes with clean experimental signatures are a particularly interesting place to search for such deviations, with possibly spectacular results even for low event rates observed.

At HERA, isolated leptons in events with large missing transverse momentum in the detector are a striking signature with a very low rate expected from SM processes. An observed excess of such events would be a clear signal of new physics. Direct production of single W bosons with subsequent leptonic decay is the only SM process with a measurable cross section (about 1 pb), which leads to events at HERA with an isolated lepton and missing transverse momentum in the final state. However, certain extensions of the SM predict quark-flavour changing neutral currents (FCNC) that could lead to the direct production of single top quarks, with subsequent leptonic decay of a W boson: $ep \to etX$, $t \to W^+b$, $W^+ \to e^+\nu$, $\mu^+\nu$, $\tau^+\nu$. Events from the electron- and muon-decay channel of the W decay are characterized by an isolated lepton of high energy, missing transverse momentum, and a large transverse momentum for the hadronic system. The H1 collaboration has observed an accumulating excess of such events over the HERA I data taking periods [1–5].

The analysis presented here covers all ZEUS HERA I data from the years 1994 to 2000, with an integrated luminosity of 130 pb^{-1}, collected at centre-of-mass energies of 300 GeV and 318 GeV. Starting from a generic search for events with isolated tracks and large missing transverse momentum, the tracks were subsequently identified as electrons, muons or tau leptons.

This thesis is organized as follows: Chapter two describes the HERA collider and the ZEUS detector, which were used to perform the analysis presented. The third chapter

gives an overview of the theoretical concepts relevant for the following analysis. The SM and the processes considered for this search are described. Extensions of the SM are discussed with emphasis on Supersymmetric Models and models predicting the production of single-top quarks through FCNC at HERA that could lead to isolated lepton events. Chapter four introduces the search strategy of the analysis and explains how the single-top production signal process and various background processes can contribute to the signature of interest. The Monte Carlo simulations of the signal and background processes are explained in chapter five. They are key ingredients of this search in an extreme region of the SM phase space, where also an accurate monitoring of the quality of the detector simulation is essential. Chapter six defines the dataset and the reconstructed variables. The search for isolated electrons and muons is presented in chapter seven. This search is carried out via three stages. A control selection was applied to compare kinematic variables for a larger event sample, followed by a preselection of isolated electron and muon events, and a final selection of events with large hadronic transverse momentum that was optimized to isolate events from single-top quark production. Based on these results for the electron and muon channel, exclusion limits on the single-top production process through FCNC were set, which are discussed in chapter eight. Chapter nine describes the search for isolated leptons in the tau channel, which has not been performed before at HERA. It starts from the preselection of isolated tracks that were not identified as electrons or muons. The tau leptons were identified in their hadronic decay modes as collimated jets, exploiting jet shape observables to separate tau jets from quark- or gluon-induced jets. Due to the lower efficiency in the tau channel, any observed excess of events above the SM prediction is unlikely to proceed through the SM decay of a W boson, as it would be accompanied by a much larger excess in the electron and muon channel. Chapter ten compares the search results in all channels with those from similar searches performed by the H1 collaboration. In addition, an outlook to the anticipated high-luminosity HERA II data taking period is given. The search for isolated leptons at HERA II will largely profit from the improved tracking capabilities of a new Silicon Microvertex Detector (MVD) installed in the ZEUS detector. A background radiation monitoring and automatic beam-dump system based on silicon PIN diodes and Radiation Field Effect Transistors has been designed and built to protect the MVD from synchrotron and particle radiation damage. Chapter eleven discusses the radiation background at HERA and introduces the concept and the components of the radiation monitor. Results from the ongoing HERA II commissiong phase are presented. Chapter twelve summarises the results of this thesis.

Chapter 2

The ZEUS experiment at HERA

This chapter introduces the HERA electron-proton collider and the ZEUS detector. The detector components relevant for the following analysis are explained in more detail.

2.1 HERA

HERA (Hadron-Elektron-Ring-Anlage) is the name of the accelerator facilitity at the Deutsche Elektronen-Synchrotron (DESY, see Fig. 2.1) in Hamburg, Germany. Built between 1984 and 1990 in a tunnel 15 m - 25 m underground, it is the only collider in the world, where two different types of particles - electrons/positrons and protons - are accelerated, stored and brought to collision. The accelerator is 6.3 km long and consists of four circular and four straight sections (Fig. 2.2). The ring tunnel has a circular cross section with an inner diameter of 5.2 m. The leptons and protons are stored in two seperate rings. The lepton beam is accelerated by super-conducting cavities to compensate for the energy loss due to synchrotron radiation, whereas the proton beam is accelerated by normal-conducting cavities. For the focussing magnets the situation is reversed: the leptons are focussed using conventional magnets, whereas for the protons super-conducting magnets are used. The two beams are brought into collision at zero crossing angle in the north and south experimental areas, where the collider experiments H1 and ZEUS are located. The HERMES experiment is situated in the east hall. It uses only the lepton beam (which is longitudinally polarised in that area) to study the spin structure of the nucleon with an internal polarised gas target. The HERA-B experiment is located in the west hall. It has been designed to measure $\mathcal{CP}$-violation in the $B^0\bar{B}^0$-system. The B-mesons are produced by collisions of the proton beam halo with a wire target.

HERA can collide electrons[1] as well as positrons with protons. In the data taking period from 1994-2000, which is considered in this thesis, the lepton beam energy

[1] In the following, unless stated explicitly otherwise, the term 'electron' will denote generically both the electron (e^-) and the positron (e^+).

Figure 2.1: View of DESY from an airplane approaching Hamburg airport from the west. The HERA collider and the pre-accelerator PETRA, which encloses the main DESY site, are marked with the dashed lines. The HERA south hall with the ZEUS detector is situated off the DESY main ground, right beside the trotting course.

was 27.5 GeV[2]. The proton beam energy was 820 GeV from 1994-1997 and 920 GeV since 1998. The resulting centre of mass energy, $\sqrt{s}$, was 300 GeV from 1994-1997 and 318 GeV from 1998-2000. The beams in HERA consist of up to 210 bunches of approximately 10^{10} particles. The beam crossing rate is 10.4 MHz. During normal operation, some bunches remain unfilled, resulting in unpaired bunches, which are used for background studies. Figure 2.3a) shows the integrated delivered luminosity of the HERA collider as a function of the operating time in the years from 1993-2000. Figure 2.3b shows the amount of data recorded by the ZEUS detector that can be used for analysis purposes. The ratio of useful to delivered luminosity is about 70%-80% for the periods from 1994-2000, which were considered in this analysis.

[2]Natural units are used throughout this thesis ($c = 1$, $\hbar = 1$). Hence energies and momenta are given in GeV.

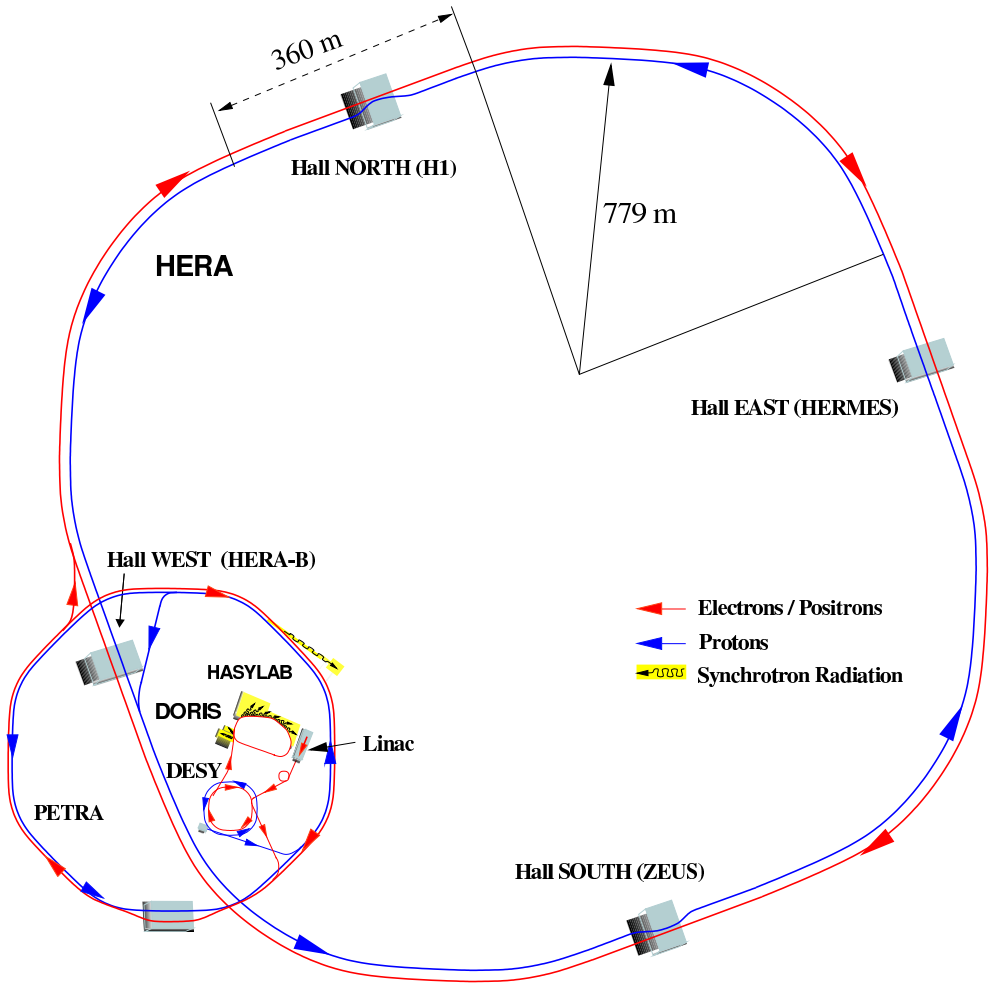

Figure 2.2: Schematic view of the HERA accelerator.

2.2 ZEUS

The ZEUS[3] detector [7] is a general purpose detector designed to study various aspects of lepton proton scattering. The detector has a large forward-backward asymmetry to accomodate the boost of the center-of-mass in the proton beam direction with respect to the lab-frame, which is caused by the large asymmetry in the energies of the lepton and proton beams. The right-handed ZEUS coordinate system is aligned such that its origin is at the nominal interaction point, with the x axis pointing towards the center of the HERA ring, the y axis pointing upwards and the z axis pointing in the direction of the outgoing proton beam, also referred to as the forward direction. The polar angle θ and the azimuth angle ϕ are measured relative to the z and x axes respectively. The detector has been in operation since 1992, however, new detector components have been added continuously. The main part of the ZEUS detector has

[3]The acronym ZEUS is derived from ancient greek: ΖΕΥΣ: Ζήτησις καθ' Εὑρετής Ὑποκειμένης Συμμετρίας = Search to Elucidate Underlying Symmetry [6].

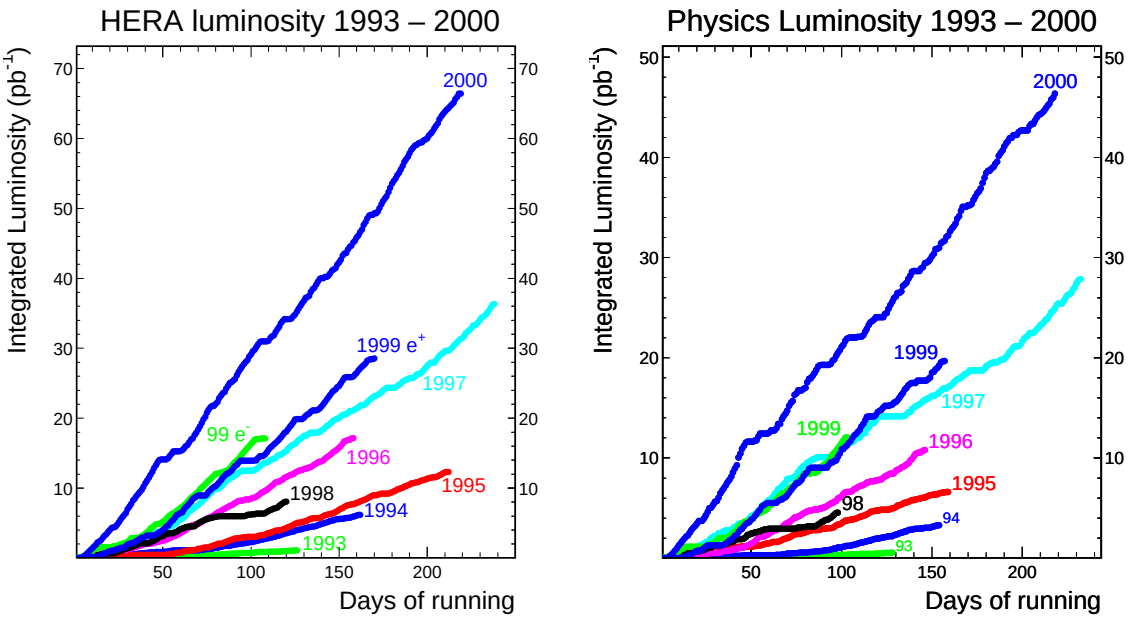

Figure 2.3: Integrated luminosity delivered by HERA (left) and useful luminosity for data analysis recorded with the ZEUS detector (right), for the data taking periods from 1993-2000.

a size of 12 m x 10 m x 19 m and a weight of 3600 tons. An overview of the detector is shown in a cross section along the beam direction in Fig. 2.4 and perpendicular to it in Fig. 2.5.

In the following a short description of the main components of the detector is given. A more detailed description of the components relevant for the analysis presented in this thesis can be found in the next sections. The innermost part of the ZEUS detector was a vertex detector (VXD), which was removed during the shutdown 1995/1996. In 2001 a silicon micro vertex detector (MVD) was installed at the same place. The central tracking detector (CTD), which is a cylindrical drift chamber, surrounds the beam pipe in the region of the interaction vertex. It is enclosed by a super-conducting magnet providing a field of 1.43 T for the determination of charge and momentum in the tracking system. The CTD is supplemented in the forward direction with three sets of planar drift chambers (FTD) with transition radiation detectors (TRD) inbetween (labeled as FDET in Fig. 2.4) and in the rear direction with one planar drift chamber consisting of three layers (RTD).

The tracking system is surrounded by a high-resolution uranium-scintillator calorimeter (CAL), which is used as the main device for energy measurements. It is divided into three parts: the barrel (BCAL), forward (FCAL) and rear calorimeter (RCAL). In front of the calorimeter modules there are presampler detectors mounted. An iron yoke encloses the CAL, providing a return path for the solenoid magnetic field flux. It is instrumented with proportional chambers, which allow a measurement of the

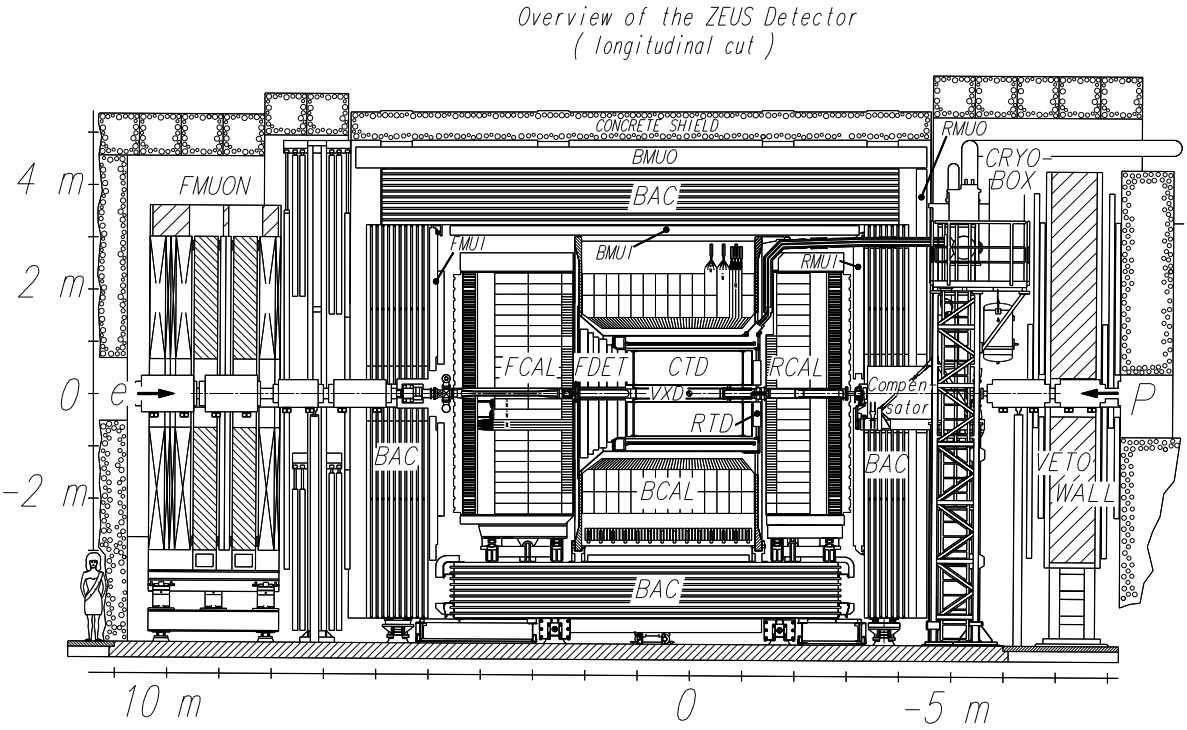

Figure 2.4: Cross section of the ZEUS detector along the beam axis.

energy leakage of the CAL, and therefore called backing calorimeter (BAC). Muon identification chambers are mounted inside and outside the BAC (FMUI, BMUI, RMUI and FMUO, BMUO, RMUO). A detector composed of iron and scintillator, called VETO wall, is located in the rear direction at $z = -7.3\ m$. It is used to reject beam related background.

Several additional components are installed close to the beamline, outside the main detector, allowing a measurement of particles scattered at low polar angles. In the forward direction at $z = 5\ m$ and $z = 24\ m$, the lead-scintillator strip detectors forming the proton-remnant tagger (PRT) are located, covering a pseudorapidity[4] range of $4.3 < \eta < 5.8$. It is followed by the leading proton spectrometer (LPS), a set of silicon strip detectors, mounted in six Roman pots from $z = 24\ m$ to $z = 90\ m$. The LPS allows the momentum of protons scattered with low transverse momentum ($< 1\,\mathrm{GeV}$) to be measured. The forward neutron calorimeter (FNC), located at $z = 105.6\ m$, is used to detect neutrons produced at small forward angles. In the direction of the outgoing beam electron, the beam pipe calorimeter (BPC) and beam pipe tracker (BPT) were used to detect electrons scattered under very low polar angles. Additional electromagnetic calorimeters (LUMIE and LUMIG) are placed at $z = -34\ m$ and $z = -107\ m$ to measure bremsstrahlung events ($ep \to ep\gamma$) for the determination of the luminosity. They are also used for tagging photoproduction events in addition to the taggers at $z = -8\ m$ and $z = -44\ m$. In photoproduction events the scattered

[4]The pseudorapidity η is defined as $\eta = -\ln(\tan\frac{\theta}{2})$.

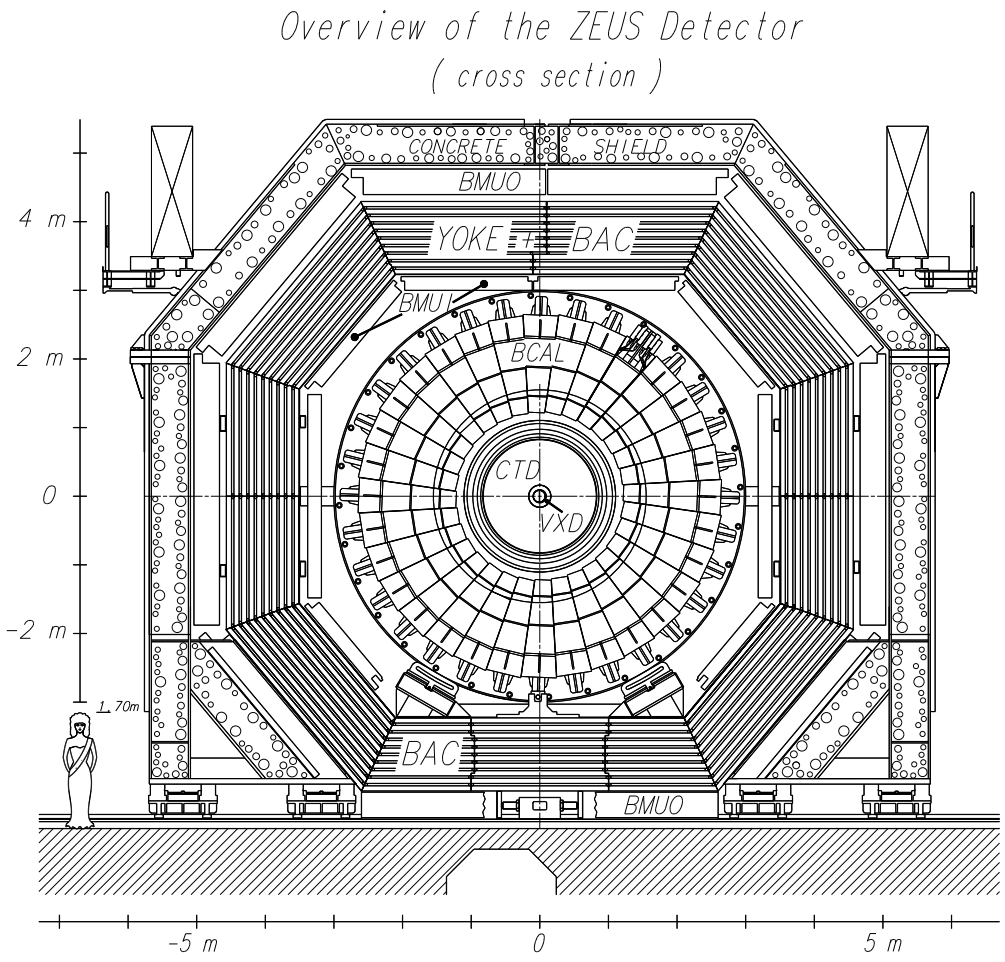

Figure 2.5: Cross section of the ZEUS detector perpendicular to the beam axis.

electron escapes the electron beam through the beam pipe, driven by the magnetic field of the beam magnets, due to its reduced energy.

2.2.1 The central tracking detector

The central tracking detector (CTD) [8] is a cylindrical gas-filled wire chamber. It allows a measurement of the charge and transverse momentum of charged particles. In addition particle information is provided through the measurement of the energy loss dE/dx.

The length of the CTD is 205 cm, its outer and inner diameter is 159 cm and 36 cm respectively. It covers the polar angle range between $11.3^o < \theta < 168.2^o$ and has a complete azimuthal angular coverage. The 4608 signal wires are mounted in 72 radial layers, which are organized in 9 superlayers (SL), each SL consisting of 8 wire layers (see Fig. 2.6). SL 1,3,5,7,9 are parallel to the beam axis, whereas the remaining 4 SLs are inclined by about $\pm 5^o$ to provide a determination of the z position of the hit. This stereo technique yields a resolution of $\sigma_z = 1.0 - 1.4$ mm. In addition the layers

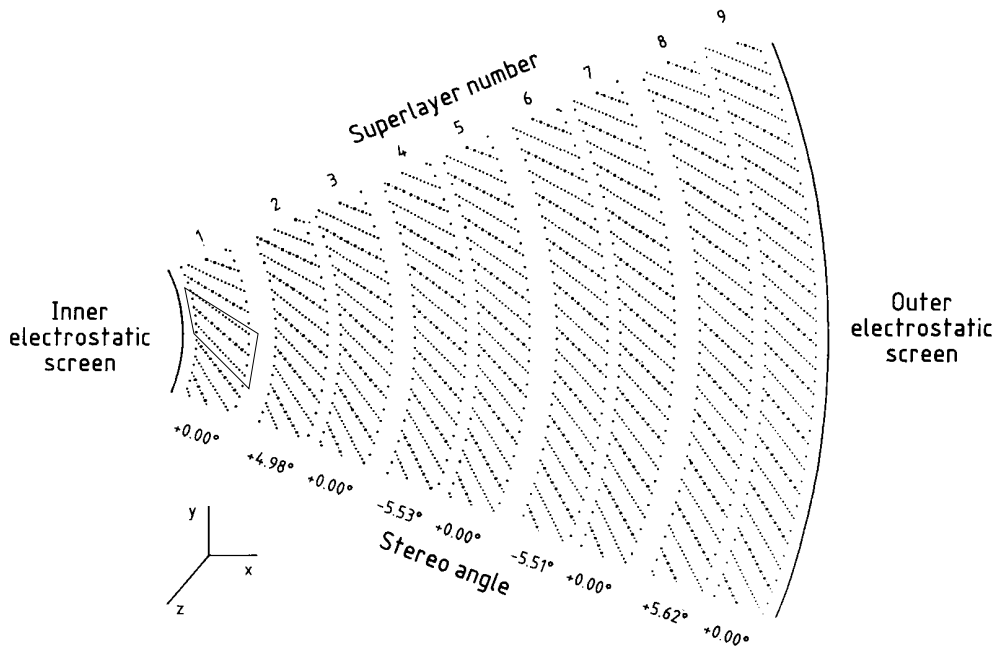

Figure 2.6: Cross section view of a CTD octant. The wires are arranged in 9 superlayers.

1, 3 and 5 are equipped with a z-by-timing system, allowing a determination of the z coordinate with a resolution of approximately 4 cm. The z-by-timing information is mainly used for trigger purposes. The active volume of the CTD is filled with a mixture of argon, CO_2 and ethane. Traversing charged particles ionize the gas molecules along their trajectory (10-20 atoms per cm for minimal ionizing particles). The electrons drift to the positive sense wires with a velocity of approximately 50 μm/ns, whereas positive ions are attracted by the negative field wires. Avalanche-like multiplication occurs in the field of the sense wires with an amplification factor of approximately 10^4. The relative transverse momentum resolution for full-length tracks, originating from the nominal vertex position with transverse momentum $p_T > 150\,\mathrm{MeV}$, can be parametrised as

$$\sigma(p_T)/p_T = 0.0058\; p_T \oplus 0.0065 \oplus 0.0014/p_T, \tag{2.1}$$

with p_T in GeV. The first term gives the contribution from the position resolution of the hits, whereas the other two terms are due to multiple scattering before and inside the CTD, respectively. The typical primary vertex resolution is 4 mm in beam direction and 1 mm in transverse direction. It is, however, possible to constrain the transverse coordinates of the vertex by the beam profile, which has width of 330 µm in $x-$ and of 90 µm in y-direction.

2.2.2 Calorimeter

The ZEUS calorimeter (CAL) [9] is a compensating sampling calorimeter consisting of alternating layers of absorbing and scintillating materials. The sampling layers

are made of 3.3 mm thick depleted uranium (98.1%U^{238}, 1.7% Nb, 0.2% U^{235}) plates wrapped in stainless steal foils. They act as absorbers reducing the energy of traversing particles resulting in a shower development. The energy is measured using the scintillation from the interaction of of the shower particles with the active detector in the scintillator layers, made of 2.6 mm thick plastic scintillator (SCSN38) plates. The thickness of the layers was optimized to provide compensation, i.e. the detector response is the same for both electrons and hadrons of the same energy (e/h=1.00$\pm$0.02). The energy resolution of the CAL was determined in testbeam measurements for electromagnetic and hadronic showers as:

$$\frac{\sigma_e}{E} = \frac{18\%}{\sqrt{E}} \quad \text{and} \quad \frac{\sigma_{\text{hadr}}}{E} = \frac{35\%}{\sqrt{E}} \ , \tag{2.2}$$

with E in GeV.

The CAL consists geometrically of three different parts: The forward calorimeter (FCAL), the barrel calorimeter (BCAL) and the rear calorimeter (RCAL), covering altogether 99.8% of the forward and 99.5% of backward hemisphere. Each part is subdivided into single modules. Figure 2.7 shows an FCAL module. FCAL and RCAL modules are rectangular, whereas the 32 BCAL modules, which surround the cylindrical CTD, are wedge-shaped.

Each module consists of so called towers of 20×20 cm^2, which are subdivided longitudinally into one electromagnetic section (EMC) and two (only one for RCAL) hadronic section (HAC1, HAC2). The EMC sections are further transversely subdivided into four cells (only two in RCAL). The depth of the towers ensures that at least 90% of the jets, with energies corresponding to the kinematically allowed maximum energy, deposit at least 95% of their energy in the CAL. The detection efficiency under normal running conditions is even higher, since most jets are less energetic. The 5918 cells form the smallest readout unit in the CAL. Each cell is read out on two sides via wavelength shifters by photomultiplier tubes (PMT). Whereas the sum of the signals of both photomultipliers are independent of the impact point of the particle, the horizontal position can be determined by comparing the two signals. The excellent time resolution of < 1 ns (for energy depositions larger than 4.5 GeV) is used to reject non-*ep* background with characteristic timing patterns already on trigger level.

The CAL is calibrated on a daily basis using the stable signal from the natural radioactivity of U^{238}. Additional calibrations for both the PMTs and the readout electronics are performed using laser, LED and test pulses.

2.2.3 Luminosity monitor

The time integrated luminosity $\mathcal{L}_{\text{int}}$ is defined as

$$\mathcal{L}_{\text{int}} = \frac{N_{\text{proc}}}{\sigma_{\text{proc}}}, \tag{2.3}$$

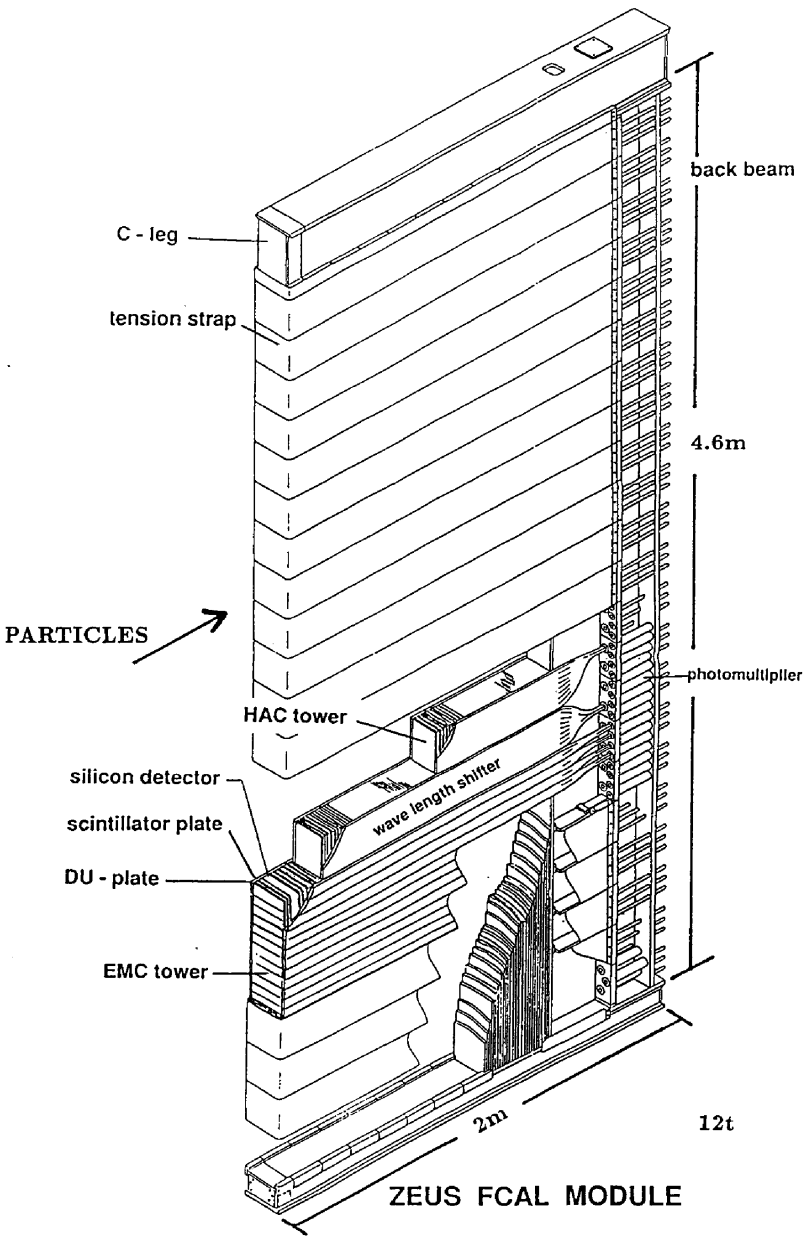

Figure 2.7: View of an FCAL module.

where N_{proc} is the number of produced events for a process with cross section σ_{proc}. The determination of the luminosity at HERA is based on the measurement of the Bethe-Heitler QED Bremsstrahlung process [10]

$$ep \to ep\gamma. \tag{2.4}$$

This process has a large cross section ($\sigma_{BH} \geq 20\,\text{mb}$) and the differential cross section as a function of the photon energy can be calculated to an accuracy of 0.5%. Thus a precise measurement of the rate and energy of the Bremsstrahlung photons allows for an accurate determination of the ep luminosity.

Bremsstrahlung photons emitted at an angle $\theta_\gamma < 0.5\,\text{mrad}$ with respect to the beam axis that leave the beam pipe through a Cu-Be window at $Z = -82$ m can be detected by a lead/scintillator sampling calorimeter (LUMIG) at $Z = -106$ m (Fig. 2.8). The detector is shielded from synchrotron radiation by a carbon/lead filter. With this filter an energy resolution of $23\%/\sqrt{E}$ (E measured in GeV) has been achieved in test-beam measurements. The impact position of the photons can be reconstructed with a resolution of 2 mm, making use of embedded layers of scintillator fingers. Electron Bremsstrahlung on the residual gas leads to a large background with the same experimental signature. This background can be subtracted statistically by measuring the Bremsstrahlung rate of unpaired electron bunches together with a measurement of the current in both paired and unpaired bunches.

The recorded Bethe-Heitler rates are sufficiently large, such that the statistical uncertainties are negligible. The systematic uncertainty of the luminosity measurement originates mainly from the background subtraction, pile-up effects and the energy calibration, linearity and acceptance of the photon calorimeter. The overall systematic uncertainty for the 1994-2000 data taking periods is 1.93%.

2.2.4 Trigger and data acquisition

The HERA beam bunch structure leads to a beam crossing every 96 ns, corresponding to a rate of potentially interesting events of 10.4 MHz. The rate of ep events ranges from less than 0.1 Hz for NC DIS events with $Q^2 > 100\,\text{GeV}^2$ (Q^2 being the negative four-momentum transfer to the exchanged boson) to 250 Hz for soft photoproduction (for an instantaneous luminosity of $2 \cdot 10^{31}\,\text{cm}^{-2}\,\text{s}\,-1$). The rate of background events, on the other hand, exceeds the rate of physics events by several orders of magnitude:

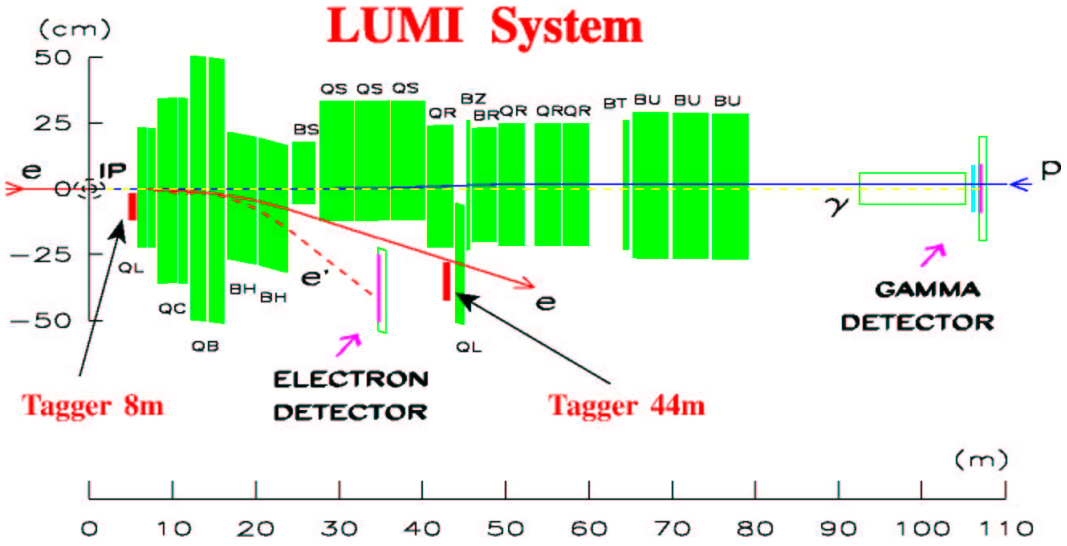

Figure 2.8: The ZEUS luminosity monitoring system with the photon detector (LUMIG) at $z = -106$ m and the electron detector (LUMIE) at $z = -35$ m.

interactions of electrons or protons with the residual gas nuclei or elements from the beamline (beam gas events) occur typically at a rate of 10 kHz and cosmic muons traverse the CTD at a rate of approximately 500 Hz. The total data size per event is 0.5 MB and the writing speed is limited to 0.5 MB/s. Hence a significant reduction of the data rate and size is required.

A three level trigger system [7, 11] with increasing complexity of the decision making algorithm and decreasing throughput rate is used to select events online, as illustrated in Fig. 2.9:

- *First Level Trigger (FLT).* Each detector component is equipped with its own FLT, which is implemented in hard-wired single-component logic circuits. Each FLT provides a fast trigger decision based on such properties as energy sums, thresholds or timing information and passes it on to the global first level trigger (GFLT) while the event data is stored in logical pipelines. By combining different trigger slots a decision is made by the GFLT after $\sim 4.4\,\mu s$ and the accepted events are passed to the next trigger stage. The GFLT output rate has to be below 1 kHz to avoid deadtimes.

- *Second Level Trigger (SLT).* The SLT is implemented in a transputer network. The decision of the GFLT is analyzed further and the event quantities are recalculated to a higher degree of precision. Beam gas background is rejected on the basis of CAL timing information, which is available at this stage. The decisions of several branches of the SLT are collected by the global second level trigger (GSLT), which provides a decision after 7 ms, reducing the event rate to 50-100 Hz.

- *Third level trigger (TLT).* For accepted events the data of all components is combined in a single record of ADAMO [12] database tables by the event builder and passed on to the TLT. The TLT uses a computer farm for the analysis and classification of each event. Based on physical quantities of the fully reconstructed events, such as kinematical variables, output of the electron finding algorithms, topologies of hadronic final states etc., a decision is made and the accepted events are classified. Accepted events (with a size of approximately 100 kB) are written to tape at a rate of 5-10 Hz and offline fully reconstructed by the ZEUS software.

During the offline reconstruction a pseudo fourth-level trigger is introduced by assigning so called DST bits (data summary tapes) to the event according to physics quantities such as missing transverse momentum or the existence of an NC DIS electron candidate. The DST bits allow fast access to a given type of events in the offline data analysis.

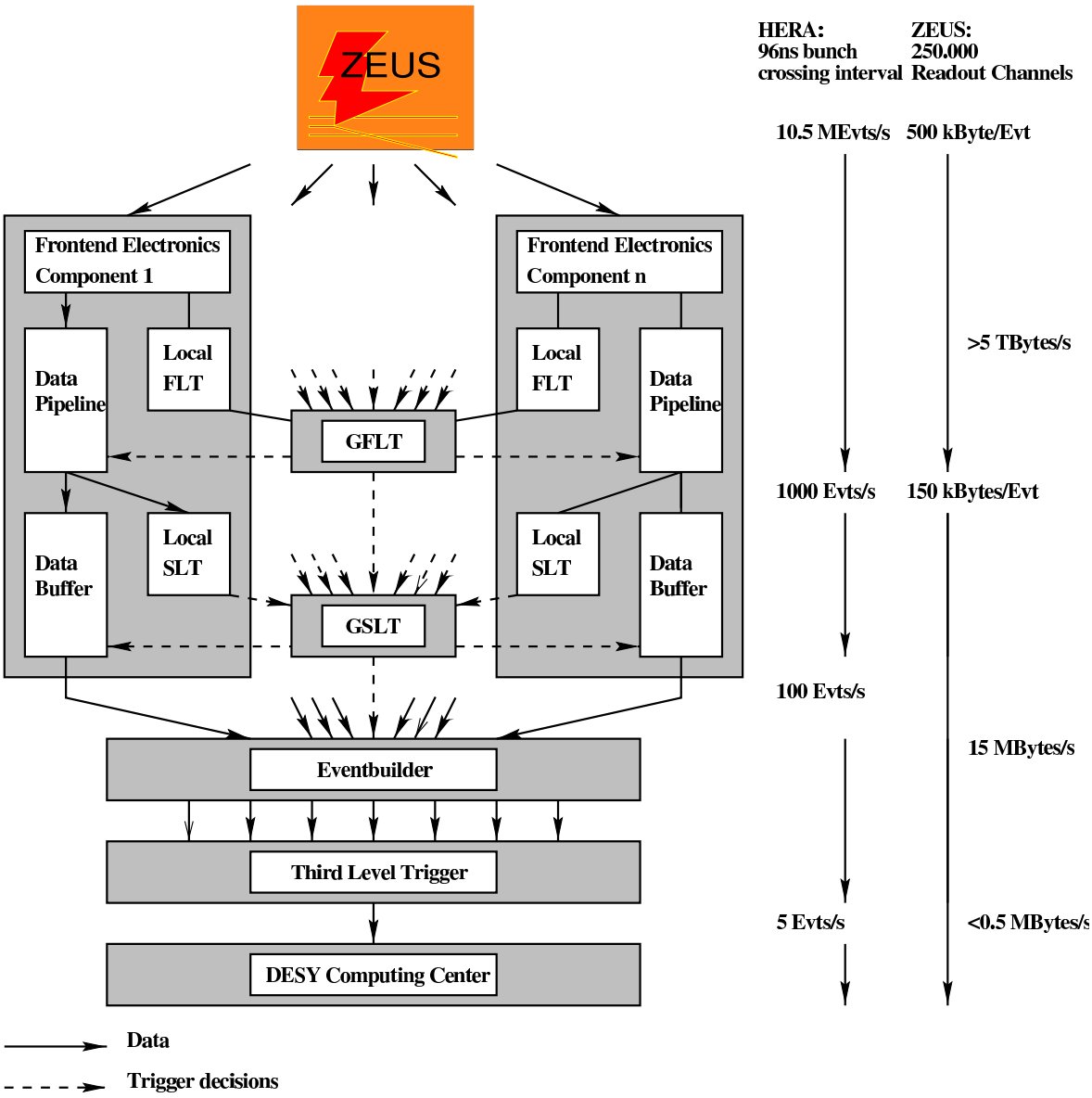

Figure 2.9: The ZEUS trigger and data acquisition system.

Chapter 3

Theoretical overview

In this chapter the theoretical concepts relevant for the following analysis are described. The Standard Model is briefly introduced with emphasis on the remaining open questions, which motivate searches for phenomena beyond the Standard Model. Lepton nucleon scattering at HERA is described, including all physics processes that were considered in the following search for isolated leptons. Theories beyond the Standard Model are introduced that could produce the signature of interest. Emphasis is given to a generic model describing the production of single top quarks through quark-flavour changing neutral currents, which is chosen as the signal process in the search for isolated electrons and muons. For this model also cross-section and decay-width calculations are presented.

3.1 The Standard Model

The Standard Model (SM) of particle physics describes the behaviour of the subatomic world in the framework of renormalizable gauge theories. In the SM the forces between the fundamental particles (fermions) are mediated by the exchange of (virtual) gauge vector bosons, which are related to the gauge symmetries of the field theories. The fundamental gauge bosons and forces described by the SM are listed in Tab. 3.1 and the SM fermions in Tab. 3.2. For each particle there exists a corresponding anti-particle with the same mass but oppositely signed quantum numbers. The gravitational force is not incorporated in the SM.

The group structure of the SM is

$$SU(3)_C \times SU(2)_L \times U(1)_Y, \tag{3.1}$$

where $U(n)$ denotes the group of all unitary $n \times n$ matrices and $SU(n)$ is the group of all unitary $n \times n$ matrices with determinant 1. The weak and electromagnetic interaction (called electroweak interactions) are unified in the gauge group $SU(2)_L \times U(1)_Y$. Through a process called spontaneous symmetry breaking, the bosons of the

Interaction	boson	Q_{EM}	related group
electromagnetic	γ	0	$SU(2)_L \times U(1)_Y$
weak	$\left\{ \begin{array}{l} Z^0 \\ W^{\pm} \end{array} \right.$	$\begin{array}{l} 0 \\ 1 \end{array}$	$SU(2)_L \times U(1)_Y$
strong	8 gluons g	0	$SU(3)_C$

Table 3.1: The fundamental interactions in the Standard Model. The value of the electromagnetic charge, Q_{EM}, is given in multiples of the elementary charge unit.

	Generations			Q_{EM}	Interactions el.magn.	weak	strong
Quarks	$\begin{pmatrix} u \\ d \end{pmatrix}$	$\begin{pmatrix} c \\ s \end{pmatrix}$	$\begin{pmatrix} t \\ b \end{pmatrix}$	$+2/3$ $-1/3$	yes yes	yes yes	yes yes
Leptons	$\begin{pmatrix} \nu_e \\ e \end{pmatrix}$	$\begin{pmatrix} \nu_\mu \\ \mu \end{pmatrix}$	$\begin{pmatrix} \nu_\tau \\ \tau \end{pmatrix}$	0 -1	no yes	yes yes	no no

Table 3.2: The fundamental fermions in the Standard Model, ordered in three generations. The value of the electromagnetic charge, Q_{EM}, is given in multiples of the elementary charge unit.

weak interactions (Z^0, $W^{\pm}$) aquire masses ($M_W = 80.41\,\mathrm{GeV}$, $M_Z = 91.187\,\mathrm{GeV}$), whereas the photon remains massless.

Quantum chromodynamics (QCD) describes strong interactions as an exact $SU(3)_C$ gauge symmetry. The charge is called "colour". The force carriers of the colour interactions are the massless gluons, forming a colour octet. Three colours are assigned to each quark, making it a fundamental triplet representation of $SU(3)_C$. Gluons have not been observed experimentally and quarks seem to be confined in colourless packages of two (mesons) and three (baryons). Therefore any single quark or gluon in the final state of an elementary reaction ends up in a jet of produced particles. Leptons do not carry colour charge and are hence singlet representations of $SU(3)_C$. All quarks and leptons are subject to the weak force. The electrically charged fermions participate in the electromagnetic interactions, described by the theory of quantum electrodynamics (QED).

The SM has been probed down to length scales of 10^{-18} m. No deviations from the predictions have been found so far. There are however many open questions and problems, some of which are listed below:

- *Higgs Boson.* The massive scalar Higgs boson has been introduced in the SM to explain the generation of particle masses. Gauge bosons and fermions are assumed to obtain their masses through interaction with the Higgs field. So far the Higgs boson has not been observed. The LEP II data collected by four

experiments (Aleph, Delphi, L3 and Opal) excluded a SM Higgs up to Higgs masses of $M_H = 114\,\text{GeV}$.

- *Fine-tuning problem.* Radiative corrections to the Higgs boson masses have quadratic divergences. At large scales, the corrections to the Higgs mass are many orders of magnitude larger than the Higgs mass itself.

- *Particle masses.* The masses of quarks and leptons are among the 26 free parameters, which are not predicted by the SM and have to be determined experimentally. In particular the wide spread in the masses of the leptons (from $\approx 10^{-2}\,\text{eV}$ for the neutrinos up to 1.7 GeV for the tau lepton) and quarks (from few MeV for the u-quark up to 175 GeV for the top quark) is puzzling.

- *Generation problem.* The existence of three families of quarks and leptons is not explained by the SM.

- *Gravity.* The SM does not include the gravitational force and it is not understood why the strength of gravity is 36 orders of magnitude weaker than that of the electromagnetic force.

It is widely believed that the SM is only a low energy approximation of an overlying more complete theory. Extensions to the SM have been proposed, such as Grand Unified Theories (GUTs), string theories or Supersymmetry (SUSY). Any search for deviations from the SM is hence also a search for an indication of a more general theory.

3.2 Lepton-nucleon scattering at HERA

Scattering experiments have been a rich source of information for understanding the structure of matter in the past decades. At the HERA electron-proton collider the structure of the proton and the nature of the electroweak and strong force are probed at small distances with higher precision than at any other experiment before, down to lengthscales of 10^{-18} m. The following sections introduce the kinematics of electron-proton scattering at HERA and the processes that might contribute to the signature of interest in the search for isolated lepton events performed in this analysis.

3.2.1 Kinematic variables

Figure 3.1 illustrates the interaction of an electron or positron with the proton. The incoming lepton ($e^{\pm}$) interacts with the proton (p) via the exchange of a virtual vector boson in a charged current (CC) or neutral current (NC) process. The NC process is mediated either by a virtual photon or a Z^0 boson. In the CC process the exchanged boson is a virtual charged W-boson, which changes the flavour of the incoming lepton to a neutrino.

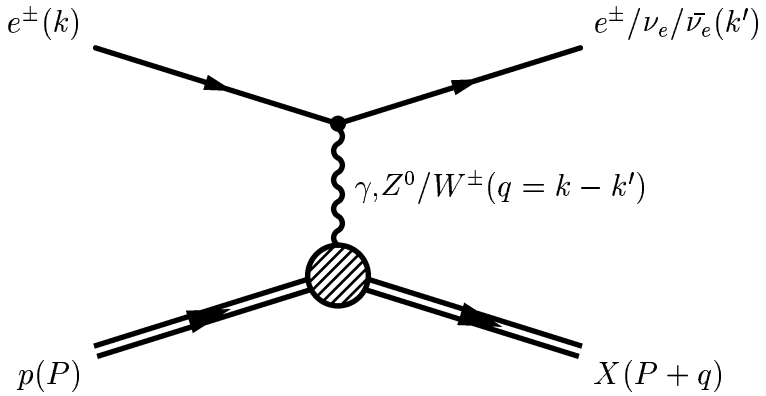

Figure 3.1: Diagram illustrating positron proton scattering. The four vectors of the particles are given in parentheses.

Given the four-vectors of the initial and final states, $k = (E_e, \vec{k})$, $P = (E_p, \vec{P})$ and $k' = (E', \vec{k}')$, $P' = (E_X, \vec{P}')$, where E_e, $\vec{k}$ and E_p, $\vec{P}$ are the energy and momentum of an incoming electron and proton, respectively, and E', $\vec{k}'$ and E_X, $\vec{P}'$ the energy and momentum of an outgoing electron and proton, respectively, the event kinematics can be described in terms of the following Lorentz invariant variables:

$$s = (k + P)^2 \tag{3.2}$$

$$Q^2 = -q^2 = (k - k')^2, \quad 0 \leq Q^2 \leq s \tag{3.3}$$

$$x = \frac{Q^2}{2P \cdot q}, \quad 0 \leq x \leq 1 \tag{3.4}$$

$$y = \frac{q \cdot P}{k \cdot P}, \quad 0 \leq y \leq 1 \tag{3.5}$$

The variables are related by the equation

$$s = \frac{Q^2}{xy}. \tag{3.6}$$

The centre-of-mass energy $\sqrt{s}$ is fixed at HERA to a value of 318 GeV (300 GeV for 1994-1997) by the beam energies of 27.5 GeV and 920 GeV (820 GeV from 1994-2000) for leptons and protons respectively. Hence only two of the four variables are independent. The negative square of the exchange boson mass, Q^2, denotes the virtuality of the exchanged boson and determines the resolution of the interaction. Deep inelastic scattering processes (DIS) are characterized by values of Q^2 much larger than $1\,\mathrm{GeV}^2$. Up to now HERA data cover a Q^2 region up to $40000\,\mathrm{GeV}^2$, corresponding to a resolvable distance scale of $\lambda \approx \hbar c/\sqrt{Q^2} = 10^{-18}\ m$, which is 1/1000 of the proton radius. In the Quark Parton Model, DIS is described as the incoherent sum of elastic scattering processes of the lepton off point like constituents (partons) in the proton. The partons, which in this model do not interact with each other, are identified with the quarks in the proton. The Bjorken scaling variable x denotes in this model the fraction of the proton momentum carried by the massless parton interacting with the lepton. The inelasticity parameter y can be interpreted as the fraction of the lepton energy

transferred to the hadronic system in the rest frame of the proton. In this system HERA collisions are equivalent to fixed target collisions with an incident lepton energy of $\approx 50\,\mathrm{TeV}$.

3.2.2 The electron-proton cross section

The electron's scattering off a proton via the exchange of a virtual gauge boson can be described, at lowest order in QED, in terms of two structure functions, $F_1(x, Q^2)$ and $F_2(x, Q^2)$, which describe the distribution of electric charge within the proton. The double differential cross sections for the neutral- and charged-current DIS ep cross sections with respect to x and Q^2 are determined by these structure functions as:

$$\frac{d^2\sigma_{NC}(e^{\pm}p \to eX)}{dxdQ^2} = \frac{4\pi\alpha^2}{xQ^4}\left[xy^2F_1 + (1-y)F_2\right] \tag{3.7}$$

$$\frac{d^2\sigma_{CC}(e^{\pm}p \to eX)}{dxdQ^2} = \frac{G_F^2}{2\pi}\left(\frac{M_W^2}{M_W^2+Q^2}\right)^2\left[xy^2F_1 + (1-y)F_2\right], \tag{3.8}$$

where α and G_F denote the fine structure constant and the Fermi constant, respectively. In the Quark Parton Model, F_1 and F_2 can be expressed as a sum of the quark- and antiquark-densities in the proton and are related by the Callan-Gross relation [13]:

$$F_2 = 2xF_1. \tag{3.9}$$

Taking QCD corrections into account, also the longitudinal structure function F_L enters.

At low $Q^2 \ll M_Z^2$, the ep cross section is dominated by photon exchange. The exchange of Z and W bosons is suppressed by their large masses ($M_{Z,W^{\pm}}$) and contributes only for large values of Q^2:

$$\frac{\sigma(Z, W^{\pm})}{\sigma(\gamma)} \sim \left(\frac{Q^2}{Q^2 + M_{Z,W^{\pm}}^2}\right)^2. \tag{3.10}$$

Figure 3.2 shows the differential NC and CC cross sections measured by the H1 and ZEUS collaborations as a function of Q^2 for e^-p and e^+p scattering. The CC cross section is suppressed with respect to the NC cross section until Q^2 reaches values close to the vector boson masses ($\mathcal{O}(10^4\,\mathrm{GeV}^2)$). In this region, $\gamma - Z^0$-interference becomes important and leads to sizeable deviations from a pure QED prediction. The CC cross section is larger for e^-p scattering than for e^+p scattering, due to the larger u-quark content of the proton, which is relevant for W^- exchange for e^-p scattering, as opposed to the smaller d-quark content, which is relevant for W^+ exchange in e^+p scattering.

3.2.3 QCD factorisation and extraction of the parton density

Hadron-hadron and lepton-hadron interactions are described in QCD calculations as an incoherent sum of the interactions of the constituent partons (quarks and gluons)

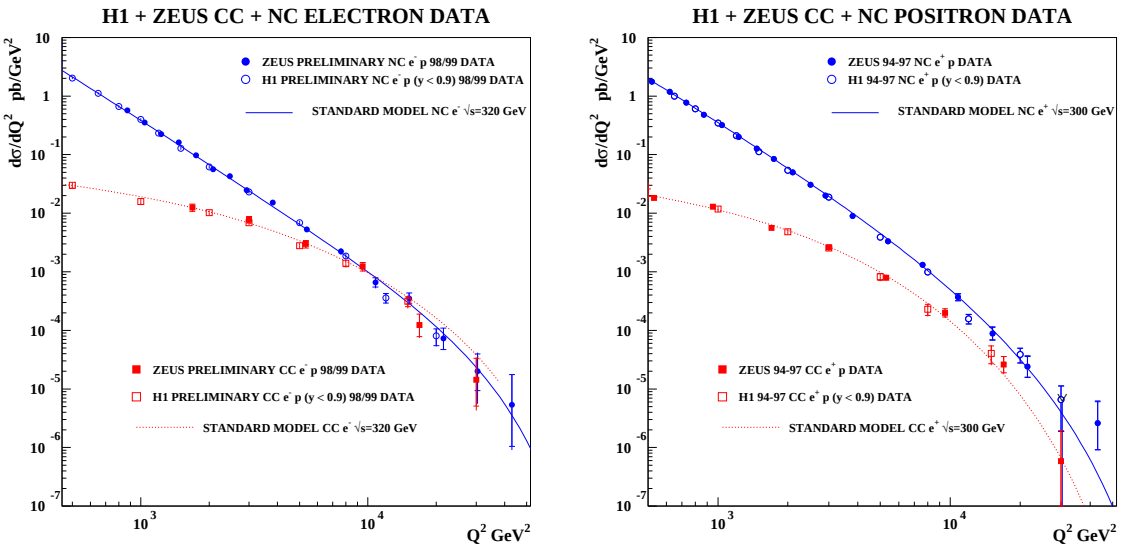

Figure 3.2: The differential NC and CC cross sections as function of Q^2, as obtained by the H1 and ZEUS collaborations [14] for e^-p (left) and e^+p (right) scattering. The solid and dashed lines correspond to NC DIS and CC DIS predicitions from the standard model, respectively.

from one hadron with those from the other hadron or with the lepton. At present the distribution of partons in hadrons cannot be calculated from first principles within perturbation theory. A separation of the short-range part (hard process) of a DIS interaction from the long-range part (soft process) is introduced, called factorisation. In this approach the proton structure function F_2 can be expressed as a convolution of the perturbatively calculable hard scattering subprocess and the parton distribution functions:

$$F_2(x,Q^2) = \int_x^1 \mathrm{d}x' f(x',\mu_F^2)\hat{\sigma}(\frac{x}{x'},Q^2,\mu_F^2), \tag{3.11}$$

where $f(x',\mu_F^2)$ is the probability to find a quark with momentum fraction x' in the proton and $\hat{\sigma}(\frac{x}{x'},Q^2,\mu_F^2)$ is the cross section for that quark scattering elastically off a photon with virtuality Q^2. The quark can radiate a gluon before interacting, thus lowering its effective momentum fraction of the total proton momentum from x' to x. The factorization scale μ_F defines the scale at which this gluon radiation is absorbed into the parton density function f (PDF) rather than into the hard scattering cross section. The structure function F_2 as a physical observable is independent of the arbitrary choice of the factorisation scale μ_F.

It is possible to calculate the evolution of the PDFs as a function of Q^2, using the DGLAP evolution equations [15]. These equations use the measured values of the PDFs at a given scale to predict their evolution to some new scale. The knowledge of the evolution of the PDFs can be exploited to determine them experimentally. If the

perturbative part is calculated and the cross section of a certain process is measured, the PDF can be extracted from the data. The factorisation theorem of QCD states that the PDFs are process independent. Once determined for a given process, they can be used to make a prediction for another process.

Figure 3.3 shows as an example the PDFs extracted from a ZEUS next-to-leading order QCD analysis of data on deep inelastic scattering [16]. As can be seen from the figure, the u and d valence-quark densities dominate at large values of $x \gtrsim 0.3$, while sea-quarks and gluons become important only at low values of x.

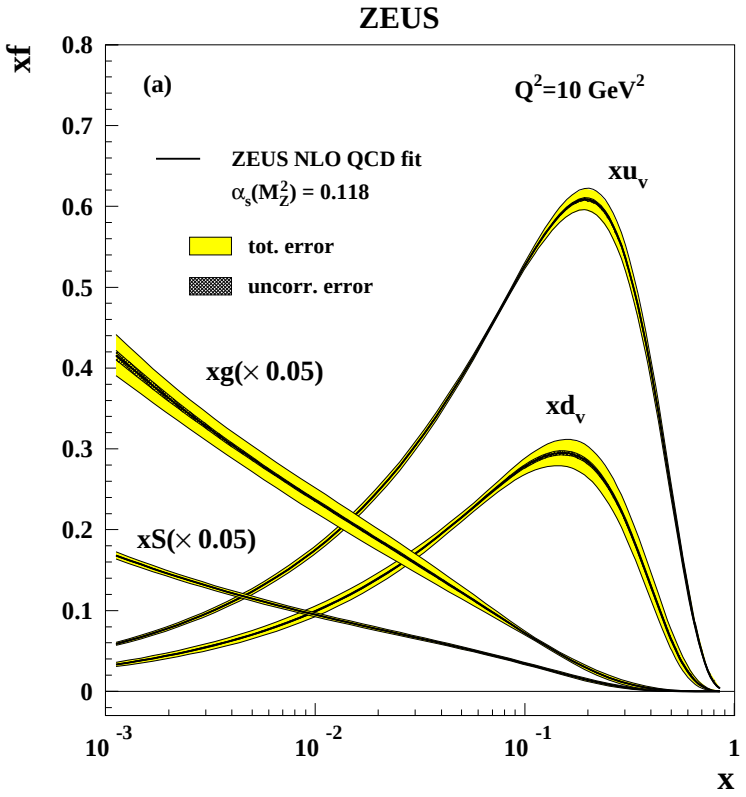

Figure 3.3: The gluon, sea, u and d valence distributions extracted from the ZEUS NLO QCD fit at $Q^2 = 10\,\mathrm{GeV}^2$ (from [16]).

3.2.4 Photoproduction

Photoproduction (γp) is defined as the interaction of a (quasi-)real photon ($Q^2 \ll 1\,\mathrm{GeV}^2$) with the proton. It is the dominant process at HERA with a total cross section of approximately 150 µb. The majority of γp interactions are soft, i.e. the transverse energy of the final state particles is small, and hence they are not observed in the main detector. Hard γp interactions, resulting in jets at high transverse momenta, allow for perturbative QCD calculations to be made. The hard interactions can be subdivided into two types:

- *Direct Process.* In the direct process the photon couples as a point-like particle to a parton from the proton. The two direct processes in leading order (LO) of the strong coupling constant α_S, which are dominant at HERA, are the QCD Compton process (see Fig. 3.4 a) and boson-gluon-fusion (BGF) (see Fig. 3.4 b).

- *Resolved process.* In this process the photon acts through vacuum fluctuation, as a source of partons. One of these partons, carrying a fraction of the total photon momentum, interacts strongly with a parton from the proton. Figure 3.4 c) shows an example diagram for a resolved photon interaction. The resolved photon structure can be subdivided in a part, which can be treated by perturbation theory (anomalous resolved process) and a nonperturbative part, which is usually modelled by the Vector Meson Dominance Model (VDM) and needs to be fixed by data.

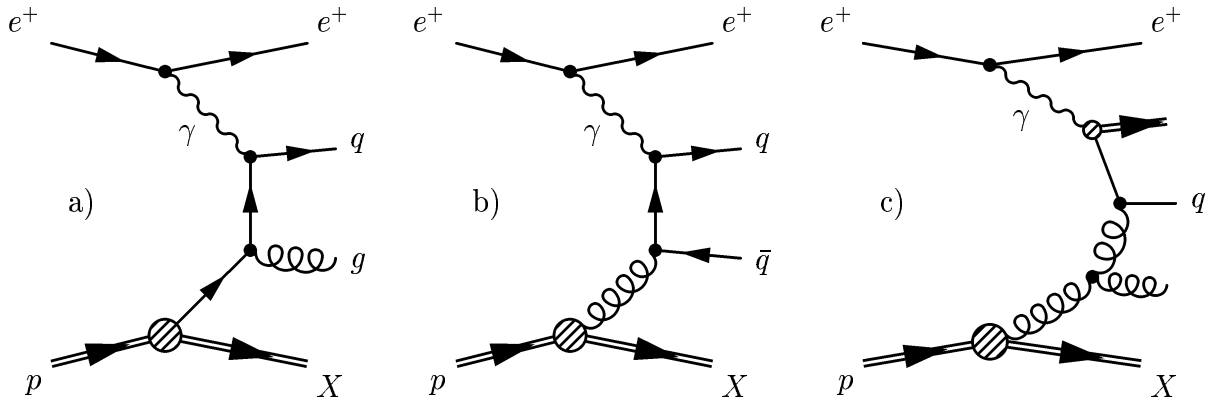

Figure 3.4: Leading order Feynman diagrams for direct and resolved hard photoproduction processes: a) QCD Compton process (direct) b) boson-gluon-fusion (direct) and c) resolved photon process.

3.2.5 Lepton pair production

Lepton pairs are produced at HERA mainly through the following two processes:

- *Bethe-Heitler process.* The dominant production mechanism for lepton pairs is the Bethe-Heitler process $ep \to \gamma\gamma \to l^+l^-$. A quasi-real photon emitted from the electron interacts with a photon radiated from a quark inside the proton. The two photons produce a lepton anti-lepton pair e^+e^-, $\mu^+\mu^-$ or $\tau^+\tau^-$, as shown in Fig. 3.5 a). The total cross section for the photon-photon interactions is relatively large, but falls off steeply with the transverse momenta of the produced leptons ($\sim P_{T,l}^{-3}$). The leptons are produced with opposite charge and have a back-to-back topology. For an elastic reaction, with low momentum transfer on the proton side, the proton stays intact in the scattering process. An additional hadronic jet from

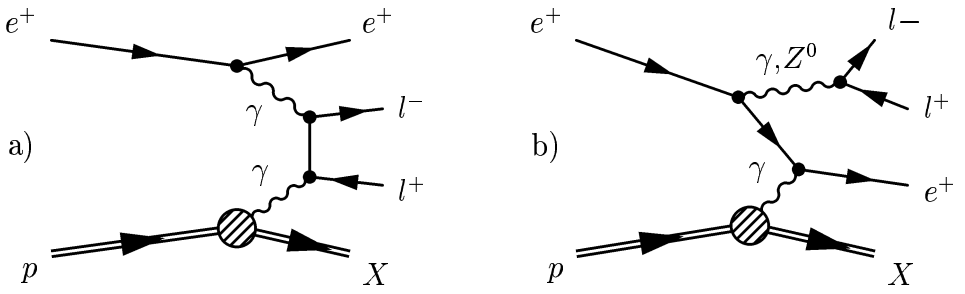

Figure 3.5: Feynman diagrams for the a) $\gamma\gamma$ lepton-pair-production process and b) an example for a QED compton process with a photon or Z^0 boson emitted from the final state electron.

the scattered quark can be produced for large momentum transfers on the proton side. In a quasi-elastic reaction the proton is transformed into an excited nucleon state, which decays into a nucleon and mostly pions. In an inelastic reaction with a large momentum transfer from the incoming proton to the hadronic final state, the proton breaks off and many hadrons are produced. In case of high momentum transfer on the electron side, the scattered electron can be observed in the main detector.

- *Internal photon conversion and Z^0 production.* An example for the production of an on- or off-shell boson with subsequent decay to a lepton pair is shown in Fig. 3.5 b). The lepton pairs are produced with a back-to-back topology in such reactions. The cross section peaks at low values of the invariant mass of the two leptons and at the invariant mass of the Z^0 boson.

Requiring that at least one of the produced leptons is accepted by the main detector and has a sizeable transverse momentum ($p_T > 5\,\mathrm{GeV}$), a total cross section for lepton pair production of approximately 120 pb is expected at HERA energies.

3.2.6 Production of single W bosons

In the SM the direct production of single W bosons at HERA can occur via the processes:

$$ep \to eWX \quad \text{and} \quad ep \to \nu WX, \tag{3.12}$$

where X denotes the hadronic final state [17]. The second process $ep \to \nu WX$ is ignored in the following, since its cross section is only about 5% of the total cross section. Seven diagrams contribute to the process $ep \to eWX$ at leading order, as shown in Fig. 3.6 for the case of positron proton scattering and with subsequent leptonic decay of the produced W bosons. Diagrams a) and b) correspond to the radiation of a W boson from the incoming and scattered quark, respectively. The u-channel exchange of a quasi-real photon and a massless quark in these diagrams has the largest contribution to the W production cross section. Diagram c) contains the $WW\gamma$ triple-gauge-boson coupling. With a W cross-section measurement it is thus

possible to probe possible anomalous $WW\gamma$ couplings. Diagrams d) and e) contain off-shell W bosons. Diagrams f) and g) represent the coupling of the W boson to the scattered neutrino and the incoming positron, respectively.

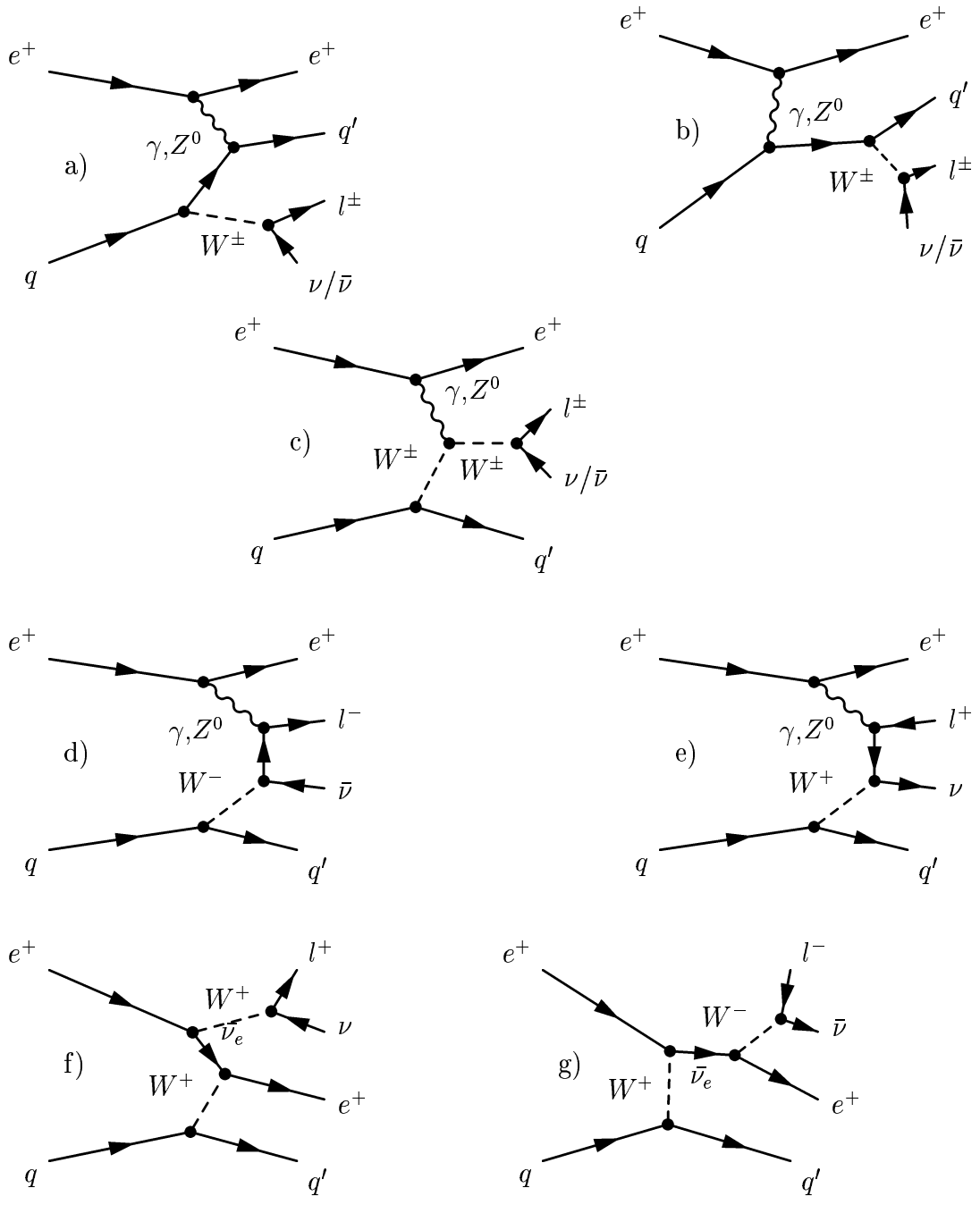

Figure 3.6: Feynman diagrams for the lowest order single $W^\pm$ boson production processes in positron quark scattering at HERA, including the subsequent decay $W \to l\nu$.

Examples of next-to-leading-order (NLO) real and virtual QCD corrections to the W production process are shown in Fig. 3.7. The total calculated cross section for single W-boson production at HERA, including NLO QCD corrections for the photoproduction regime, amounts to 0.96 pb (1.16 pb) for $\sqrt{s} = 300\,\text{GeV}$ (318 GeV) [18–21]. Taking into account the NLO QCD corrections, the remaining theoretical uncertainty on the W production cross section is approximately 15%.

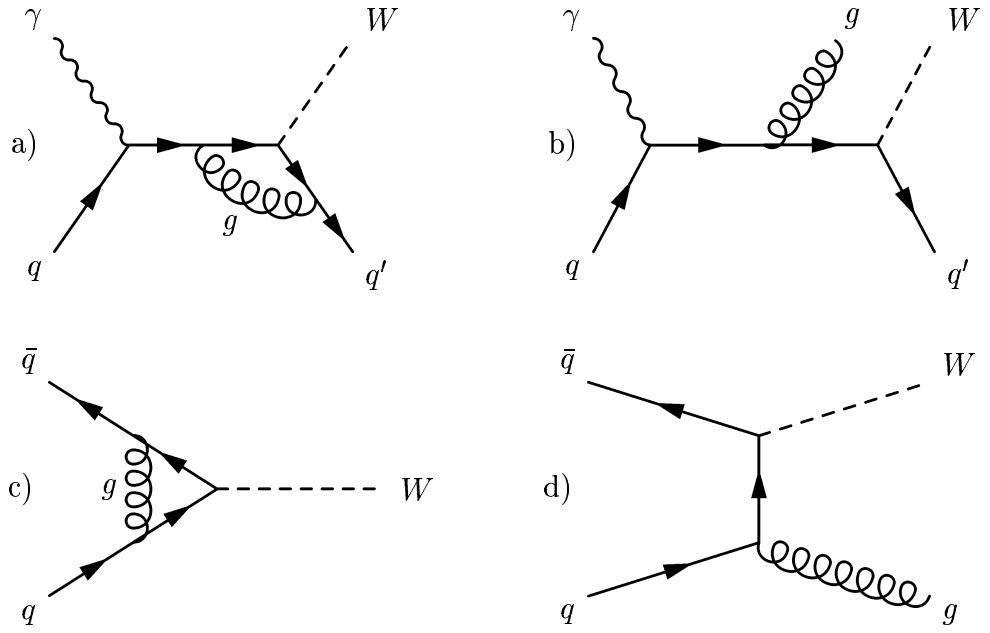

Figure 3.7: Typical NLO diagrams contributing to the photoproduction of W bosons: a) virtual correction and b) real correction to the direct mechanism, c) virtual correction and d) real correction to the resolved mechanism.

The experimental signature for W production depends on the subsequent decay of the W boson. For the leptonic decays $W \to e\bar{\nu}_e,\ \mu\bar{\nu}_\mu$ one expects an electron or a muon at high transverse momentum and missing transverse momentum due to the undetected neutrino. For the leptonic decay $W \to \tau\bar{\nu}_\tau$ the signature depends on the subsequent tau decay mode. For the leptonic tau decays $\tau \to e\nu_e\nu_\tau$ and $\tau \to \mu\nu_\mu\nu_\tau$ the signature is similar to the electron and muon decay channels of the W decay, except for the larger expected missing transverse momentum from the additional neutrinos in the tau decay. For the hadronic tau decay modes, one expects a narrow jet with low particle multiplicity and also additional missing transverse momentum due to the additional neutrino from the tau decay (see also chapter 9). Hadronic decays $W \to q\bar{q}'$ lead to events with two jets. An additional jet can be expected for all decay modes of the W boson in case of a sizable momentum transfer to the scattered quark. Since it originates from a different vertex in the diagrams (Fig. 3.6), it is separated from the W decay products in the detector. The cross section for single W boson production is dominated by photoproduction, leading to a steeply falling transverse momentum spectrum of the scattered quark.

3.3 Supersymmetry

This section introduces the concept of Supersymmetry (SUSY), which is a candidate theory to describe possible physics beyond the SM. The various SUSY models predict a broad spectrum of new particles and interactions. In the following, emphasis is given to the predicted experimental signatures at HERA that are relevant for the search presented in this thesis.

3.3.1 The minimal supersymmetric model (MSSM)

SUSY is a global symmetry which establishes a relation between the bosons and the fermions. Extending SUSY as local symmetry plays a key role in theories incorporating gravity. SUSY would give rise to a supersymmetric partner (sparticle) for each SM particle, which has the same quantum numbers, but differs by one half-unit of spin. Particles and corresponding sparticles would have the same mass, if supersymmetry were exact. Since no sparticles have been found so far, SUSY has to be broken, if it exists. SUSY resolves the hierarchy (or naturalness) problem, i.e. it explains the stability of the electroweak scale, $\mathcal{O}(10^2)$ GeV, relative to GUT scale, $\mathcal{O}(10^{19}\,\text{GeV})$, in the presence of quantum corrections.

The minimal supersymmetric model (MSSM) is a direct generalization of the SM, containing the smallest number of new particles and new interaction compatible with the SM. In the MSSM, electroweak symmetry breaking occurs via vacuum expectation values of two different Higgs superfields, denoted H^1 and H^2. Baryon number and lepton number are conserved separately, which is expressed in a new multiplicative quantum number R-parity. It is defined for each particle as $R_p = (-1)^{3B+L+2S}$, with B, L and S denoting baryon number, lepton number and spin of the particle, respectively. R_p is 1 for particles and -1 for SUSY particles. In R-parity conserving models, sparticles are created in pairs and the lightest supersymmetric particle (LSP) is stable and neutral. In the MSSM it is thus expected that signatures with missing energy would arise, since the LSP would escape undetected. The experimental reach at HERA for discovering MSSM particles is however limited, due to the restriction to pair-production of SUSY particles.

The spectrum of particles in the MSSM includes all SM particles and, in addition, scalar squarks and leptons, spin-1/2 charginos, neutralinos, the gluino and five different Higgs bosons. Charginos and neutralinos are the charged and neutral mass eigenstates of the mixed supersymmetric partners of the $W^{\pm}$, Z^0 and γ (gauginos) and the two Higgs doublets (higgsinos). Cosmological arguments suggest that the LSP is neutral and it is therefore often assumed that the lightest neutralino, χ_1^0, is the LSP. Due to the large number of possible couplings, the MSSM contains many new parameters, which can only be reduced to a managable number if an assumption on the SUSY breaking mechanism is made. Often supergravity models are used.

The dominant MSSM process expected at HERA is the production of a selectron and a squark via neutralino exchange, $ep \to \tilde{e}\tilde{q}X$, as shown in Fig. 3.8. The selectron

and squark are assumed to decay into the lightest neutralino plus SM particles. The experimental signature is an isolated electron of the same charge as the beam lepton, a jet and missing transverse momentum from the undetected neutralinos.

Typical experimental mass limits for supersymmetric particles are set from LEP at $\approx 100\,\mathrm{GeV}$, and, for squarks and gluinos, from Tevatron at a few hundred GeV. At present, HERA is not competitive in this field.

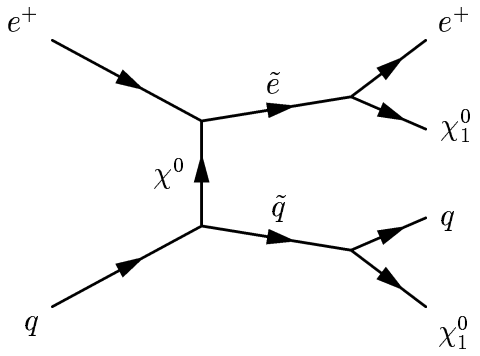

Figure 3.8: Example Feynman diagram for selectron-squark production via neutralino exchange and the subsequent decay into the lightest supersymmetric particle χ_1^0.

3.3.2 R-parity violating SUSY

The general superpotential allows for Yukawa couplings between the SM fermions and squarks or sleptons, which would violate R-parity conservation. The corresponding terms in the superpotential would in some cases lead to proton decay, which has very stringent experimental constraints. Therefore the R-parity violating couplings must be small.

The R-parity violating superpotential terms, where an *ep* collider is most sensitive, are of the form $\lambda'_{ijk} L_L^i Q_L^j \bar{D}_R^k$. Here L_L, Q_L and $\bar{D}_R$ denote left-handed lepton and quark doublets and the right-handed d-quark singlet chiral superfields respectively, and the indices i, j and k denote their respective generations. Expanded into four-component Dirac notation, the corresponding terms of the Lagrangian are:

$$\mathcal{L} = \lambda'_{ijk} \left[\tilde{\nu}_L^i \bar{d}_R^k d_L^j + \tilde{d}_L^j \bar{d}_R^k \nu_L^i + (\tilde{d}_R^k)^* (\bar{\nu}_L^i)^c d_L^j - \tilde{e}_L^i \bar{d}_R^k u_L^j - \tilde{u}_L^j \bar{d}_R^k e_L^i - (\tilde{d}_R^k)^* (\bar{e}_L^i)^c u_L^j \right] + h.c. \tag{3.13}$$

At HERA, where electrons or positrons are the only leptons in the initial state, $i = 1$ is relevant, and the last two terms will result in up and down-type squark production in *ep* collisions. All possible right-handed down-type squarks and left-handed up-type squarks can be produced in *ep* collisions. For both, production and decay via λ'_{1jk}, the final state will be indistinguishable, event-by-event, from Standard Model NC and CC events. However, the angular distribution of the final state lepton will be flat for the

s-channel exchange of the scalar squark in its restframe, as opposed to the NC and CC cross section with a strong angular dependence of the cross section ($\frac{d\sigma}{dy} \sim \frac{1}{y}$ for NC DIS, which is the main background in searches for R-parity violating squark production at HERA). For decay via λ'_{2jk} or λ'_{3jk}, the final state consists of an isolated muon or tau-lepton, respectively, which will be found in a back-to-back configuration with a jet from the decay of the final state quark. Figure 3.9 shows an example Feynman diagram for the R-parity violating production and subsequent R-parity violating two-body decay of the lightest stop quark, as it could occur at HERA, if R-parity violating couplings at the decay vertex are considered that are different from the one at the production vertex. The stop quark decays in this case to SM particles via $\tilde{t}_1 \to b\tau$. It was shown that there exists a parameter region in which this tau-decay mode could be important, which is not yet excluded by experiments [22]. It is of particular interest in the context of the search for events with missing transverse momentum and isolated tau leptons (cf. chapter 9), as it would introduce a process with enhanced tau production that does not occur through W boson decays. Therefore it would allow for an excess of isolated tau events, that is not accompanied by a much larger excess in the electron and muon decay channel of the W boson, as it would be expected due to the lower detection efficiency anticipated in the tau channel. For a subsequent hadronic tau decay, the signature of such an event would be a narrow jet from the tau-decay, missing transverse momentum from the tau neutrino pointing in the direction of the tau jet and a high-energy jet from the decay of the b quark. The tau and the b jet would be expected in a back-to-back configuration, thus making it difficult to separate such events from badly reconstructed NC DIS events, where the electron is not clearly identified.

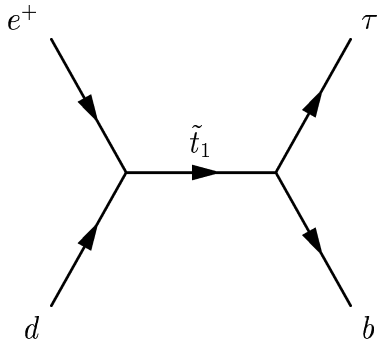

Figure 3.9: Example Feynman diagram for R-parity violating resonant stop-quark production at HERA with subsequent R-parity violating two-body decay to SM particles.

In addition to the Yukawa couplings, there are also gauge couplings, allowing for a squark decay via SM boson, neutralino or chargino radiation, with subsequent decay of the SM boson, neutralino or chargino [23]. Figure 3.10 shows an example for R-parity violating resonant $\tilde{t}$ production with subsequent gauge decay $\tilde{t} \to \tilde{b}W^+$. The produced $\tilde{b}$-quark decays via λ'_{131}: $\tilde{b} \to \bar{\nu}_e d$. For a leptonic decay of the W^+ boson, $W^+ \to e^+\nu_e, \mu^+\nu_\mu, \tau^+\nu_\tau$, the experimental signature would be an isolated lepton at large transverse momentum, missing transverse momentum from the two neutrinos

and a jet from the d-quark. This process could thus contribute as a W-decay signal to the search for isolated leptons presented in this thesis.

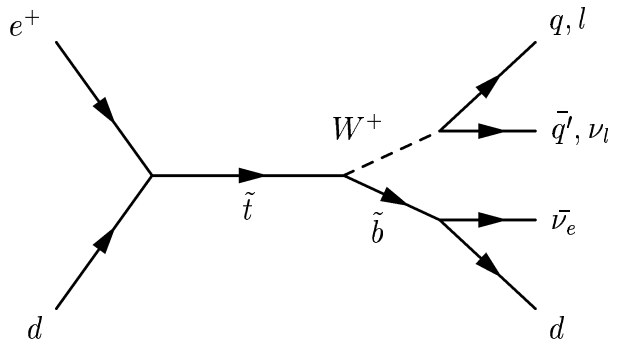

Figure 3.10: Example Feynam diagram for resonant stop-quark production at HERA with subsequent bosonic decay.

An example for an R-parity violating SUSY process leading to a tau lepton, missing transverse momentum and several jets in the final state is shown in Fig. 3.11. A stop quark is resonantly produced through an R-parity violating λ'_{131} interaction, followed by a gauge decay $\tilde{t} \to b\tilde{\chi}^+$, where the b-quark results in a jet. In many SUSY scenarios the electron- and muon-sneutrinos are heavier than the chargino, such that decays of the chargino involving electrons or muons could be kinematically forbidden and only the tau-decay channel remains. In this example a tau lepton is produced in the decay $\tilde{\chi}^+ \to \tau^+\tilde{\nu}_\tau$. The neutralino subsequently decays to a tau neutrino and a $\tilde{\chi}^0$. The $\tilde{\chi}^0$ decays to $\bar{\nu}_e$ and $\tilde{\nu}_e$, with subsequent R-parity violating decay of the $\tilde{\nu}_e$ via $\tilde{\nu}_e \to \bar{b}d$, resulting in two colour-connected jets, which might be collinear and thus be visible as only one jet in the detector. Missing transverse momentum would arise due to the two neutrinos in the final state. Several SUSY couplings involved in the production and decay chain described by this Feynman diagram would have to be large enough to allow for a detectable rate of this process. It is however an interesting example of a process, where tau leptons are produced together with additional missing transverse momentum and where no W decay is involved in the production of the tau leptons.

The examples given above show that the large SUSY parameter space allows for various processes, that could lead to events with missing transverse momentum and isolated leptons. Most of these processes involve the decay of W bosons, thus leading to an equal number of expected electrons, muons and tau leptons from such reactions. Enhanced tau couplings are however possible in certain regions of the SUSY parameter space, given the large number of parameters in SUSY models, which lead to various signatures and kinematical properties. None of the SUSY processes mentioned above was considered quantitatively as a possible signal process in the course of this analysis. A more general effective theory beyond the SM was used instead, which will be introduced in the following section.

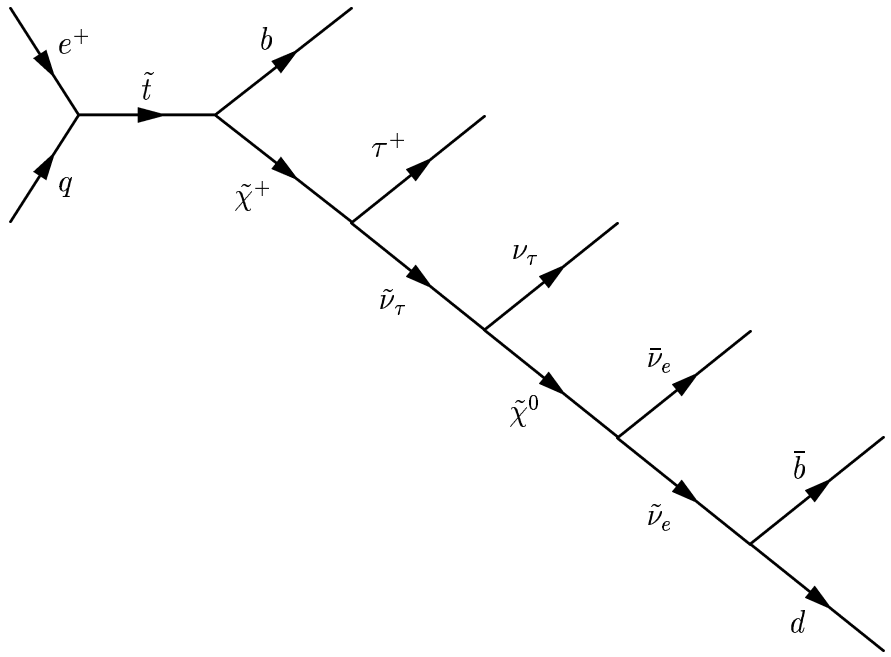

Figure 3.11: Example Feynman diagram for R-parity violating resonant squark production at HERA with a subsequent decay chain leading to a tau lepton, missing transverse momentum and several jets in the final state.

3.4 The signal process $ep \to etX$

This section gives a short summary of the properties of the top quark and describes possible production and decay mechanisms of single top quarks at HERA. Cross section and decay-width calculations are presented for a hypothetical model beyond the SM, which involves enhanced couplings of the top quark to c or u quarks through flavour changing neutral currents (FCNC). This model is considered as the signal process in the following search for events with isolated electrons or muons, missing transverse momentum and large hadronic transverse momentum.

3.4.1 The top quark

The top quark was discovered in 1995 in $p\bar{p}$ collisions at the Tevatron [24, 25]. With a mass of $M_{\text{top}} = 174.3 \pm 5.1\,\text{GeV}$ [26], measured from decays of pair produced top-quarks, it is the heaviest elementary particle known to date. Since its mass is close to the electroweak symmetry breaking (EWSB) scale, the properties of the top quark could give insights into the nature of EWSB and into new physics possibly arising at higher mass scales. The top quark decays rapidly ($\tau \approx 10^{-24}\,\text{sec}$) and almost exclusively through the single mode $t \to bW$, before the formation of top flavoured meson states can take place. Unlike for the lighter quarks with longer lifetime it is thus possible to study properties of the top quark, such as spin correlations, without the difficulty that

light quarks fragment before they can be detected. Possible deviations from the SM could therefore be first observed in the top sector.

The centre-of-mass energy of $\sqrt{s} = 1.96$ TeV at the Tevatron allows for the production of $t\bar{t}$ pairs, while at HERA ($\sqrt{s} = 318\,\text{GeV}$) and LEP ($\sqrt{s} \leq 209\,\text{GeV}$) only single-top production is kinematically allowed.

3.4.2 Possible production of single top quarks at HERA

In the SM, transitions between quarks from different generations occur only via charged currents and are suppressed by the small values of the off-diagonal elements in the Cabibbo-Kobayashi-Maskawa matrix [27, 28]. Figures 3.12 a) and b) show examples of flavour changing charged current interactions leading to the production of single top quarks, as they may occur at HERA. The SM cross section for single top-quark production through charged currents at HERA is about 1 fb [29].

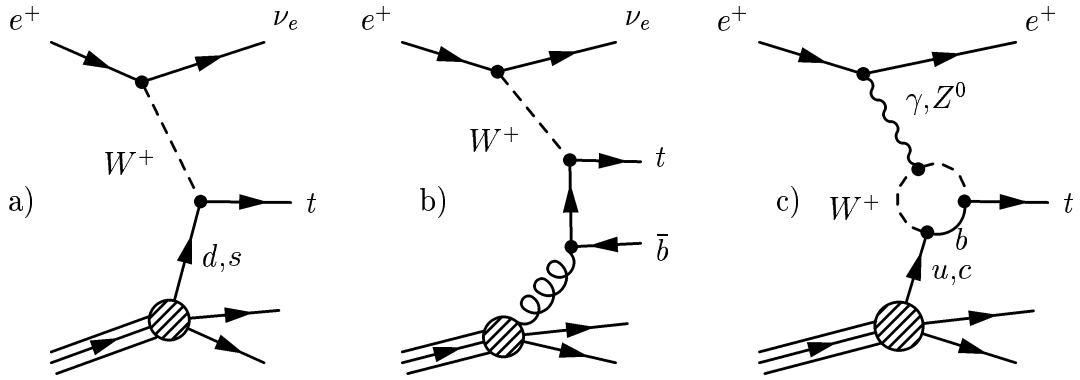

Figure 3.12: Example diagrams for SM top-quark production at HERA: a) charged current process involving a d- or s-quark from the proton, b) resolved process with a b-quark and c) SM flavour changing neutral current process at one-loop level.

Neutral current interactions in the SM preserve the quark flavours in leading order perturbation theory. Quark flavour changing neutral current (FCNC) processes are present only via higher order radiative corrections. Figure 3.12 c) shows an example for a one-loop FCNC process, as it might occur at HERA. The suppression due to the Glashow-Iliopoulos-Maiani (GIM) mechanism [30] leads to the disappearence of such contributions in case of degenerate quark masses. Therefore a sizeable cross section is expected only in cases where the top quark is involved in the loop. The decay $b \to s\gamma$ is an example for such a FCNC process. It was first observed by the CLEO experiment [31, 32]. FCNC decays connecting quarks with charge $+2/3$ are strongly GIM suppressed due to the smaller masses of the charge $-1/3$ quarks, which are involved in the loops. Thus no sizeable cross sections are predicted in the SM for

FCNC processes between the top and the c or u quark. The predicted SM branching ratios for the flavour changing decays $t \to c\gamma$ and $t \to u\gamma$ are [33]:

$$BR(t \to c\gamma) = 4.6 \times 10^{-14} \quad (3.14)$$
$$BR(t \to u\gamma) = 3.7 \times 10^{-16}. \quad (3.15)$$

These small branching fractions make an experimental observation of such processes very difficult. An enhancement of the coupling of top quarks to c or u quarks through FCNC is however predicted by many extensions of the SM [34–38]. Therefore the top-quark sector could be sensitive to physics beyond the SM with FCNC processes being involved. The top quark couplings can not be directly probed in low energy experiments. Hence the constraints from such experiments are less tight in this case, compared to cases where lighter quarks are involved. Examples for theories predicting enhanced FCNC top quark couplings are:

- *Supersymmetry.* Effective FCNC couplings could be produced by new couplings of sparticles to SM particles. In the MSSM however, the enhancements of FCNC couplings are expected to be small, not leading to a sizeable cross section for single top production at HERA energies [37]. Larger FCNC contributions could arise in R-parity violating supersymmetric models [39, 40]. Figure 3.13 a) shows an example for an R-parity violating quark-flavour changing process. The FCNC process arises through the product of R-parity violating couplings $\lambda'_{i1k} \times \lambda'_{i3k}$ of a slepton from the ith generation to SM down-type quarks from the kth generation and to a u and a t quark.

- *Multi-Higgs-Doublet models.* FCNC couplings can occur at tree level in models with two or more Higgs doublets [41, 42]. The diagram in Fig. 3.13 b) shows a one-loop contribution to an effective FCNC process where a charged Higgs boson couples to a d-quark, a u-quark and a t-quark.

- *Exotic quarks.* Exotic quark singlets appear in grand unified theories and in models inspired by string theories [43]. Single top-quark production could be enhanced by mixing with these singlet quarks.

The production of single top quarks through FCNC can be searched for in high-energy e^+e^- and ep collisions. In $p\bar{p}$ collisions, rare decays of the top quark ($t \to q\gamma$ and $t \to qZ$) can be used to probe anomalous FCNC couplings[1].

The dominant production mechanism for single top quarks at the HERA ep collider is expected to come from an anomalous magnetic coupling $\kappa_{tu\gamma}$ at the $t-u-\gamma$ vertex (see Fig. 3.14). The corresponding process with the Z^0 as exchange boson is suppressed due to the large mass in the t-channel propagator. The majority of interactions at HERA involve the exchange of a photon at low virtuality (low Q^2). The mixing with the Z^0

[1]The sensitivity of rare decay experiments is restricted to those scenarios, where the involved particles are lighter than the top quark.

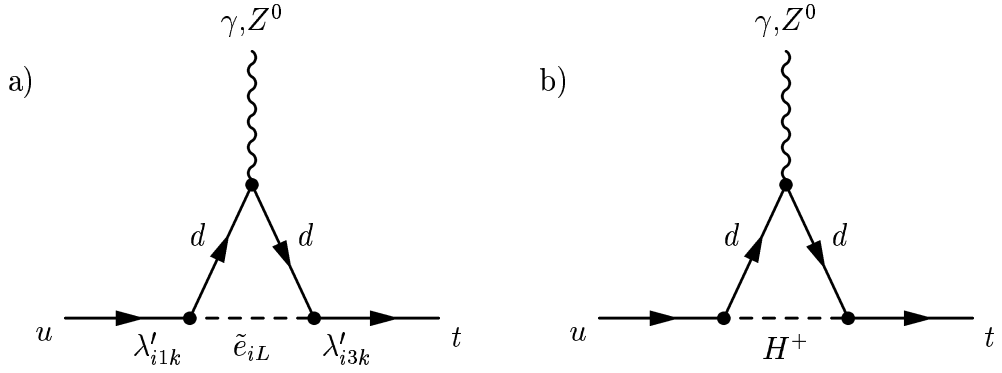

Figure 3.13: Example diagrams for processes leading to effective FCNC couplings through a) exchange of a slepton and b) exchange of a charged Higgs boson.

boson becomes significant at large values of Q^2, close to the square of the Z^0 mass. The cross section falls with $\frac{1}{Q^4}$, such that the sensitivity at high Q^2 is suppressed. An anomalous coupling to the charm quark would not lead to a large cross section due to the small charm-quark density at large values of x in the proton. With an incident lepton energy of 27.5 GeV, the struck quark must carry a minimum momentum of 278 GeV to produce a single top quark with a mass of 175 GeV. This corresponds to $x \approx 0.3$. For $x > 0.3$ the parton density of $u-$valence-quarks is much higher than of $c-$quarks, which appear only in the quark sea (see Fig. 3.3).

In the following, only $\kappa_{tu\gamma}$ and the vector coupling v_{tuZ} at the $t-u-Z^0$ vertex is taken into account, the latter one contributing mainly in case of the possible anomalous decay $t \to uZ$. The possible anomalous top-quark decays $t \to q\gamma$ and $t \to qZ$ $(q = u, c)$ are shown in Fig. 3.15.

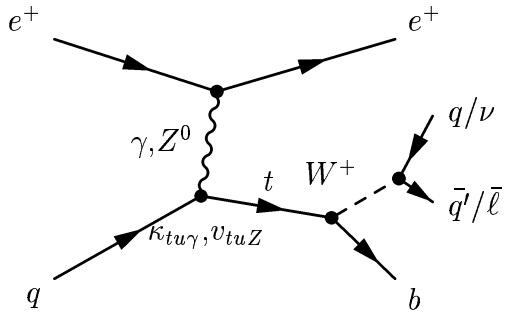

Figure 3.14: Single top-quark production via FCNC transitions at HERA and subsequent SM decay $t \to bW^+$.

Possible anomalous couplings at the $t-u-\gamma$ and $t-u-Z^0$ vertex can be described by an effective Lagrangian of the form [37]:

$$\Delta\mathcal{L}_{\text{eff}} = e\ e_t\ \bar{t}\ \frac{i\sigma_{\mu\nu}q^\nu}{\Lambda}\ \kappa_{tu\gamma}\ u\ A^\mu + \frac{g}{2\cos\theta_W}\ \bar{t}\ \gamma_\mu\ v_{tuZ}\ u\ Z^\mu\ + \text{h.c.}, \tag{3.16}$$

where e (e_t) denotes the electron (top-quark) electric charge, g is the weak coupling constant, θ_W is the weak mixing angle and $\sigma_{\mu\nu} = \frac{1}{2}(\gamma^\mu\gamma^\nu - \gamma^\nu\gamma^\mu)$ (with γ^μ, γ^ν denoting

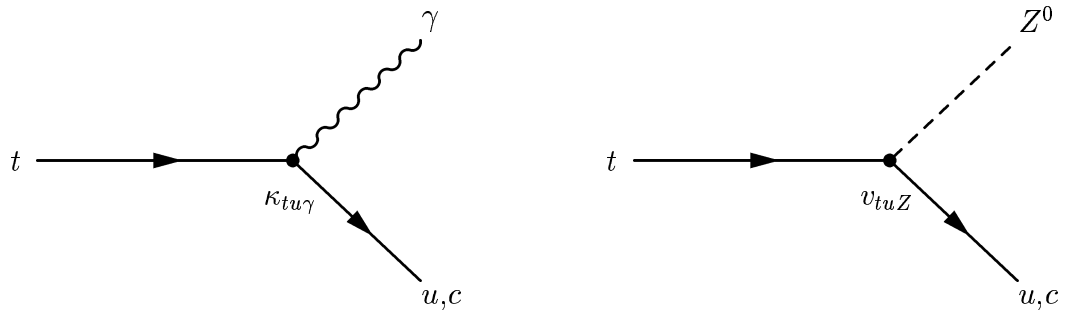

Figure 3.15: Possible anomalous decay modes of the top quark through FCNC.

the Dirac γ-matrices). Λ is the scale, up to which the effective theory is assumed to hold, which by convention is set to the mass of the top quark, M_{top}, t and u are the interacting fermion fields of the top- and u-quark respectively, q is the momentum of the exchanged gauge boson and A^{μ} and Z^{μ} denote the fields of the photon and Z^0 boson, respectively. The values of the coupling constants $\kappa_{tu\gamma}$ and v_{tuZ} in the SM are zero at tree level and extremely small at one loop. In the following it is assumed that $\kappa_{tu\gamma}$ and v_{tuZ} are real and positive.

3.4.3 Leading order cross-section and decay-width calculations

The program CompHEP [44] was used to perform leading order cross section and decay width calculations for anomalous top-quark production and decay through FCNC. All calculations were based on the Lagrangian from eq. (3.16). For the proton structure function MRST [45, 46] was used. Initial state radiation (ISR) of the beam electron was taken into account using the Weizsäcker-Williams approximation [47]. The proton structure function and the ISR were evaluated at the scale M^2_{top}. The ISR was found to decrease the cross section by approximately 10%. The cross section can be parametrised as:

$$\sigma_{\text{single top}} \quad = \quad c_{\gamma} \cdot \kappa^2_{tu\gamma} + c_Z \cdot v^2_{tuZ} + c_{\gamma Z} \cdot \kappa_{tu\gamma} \cdot v_{tuZ}. \tag{3.17}$$

The values for the coefficients c_{γ}, c_Z and $c_{\gamma Z}$, obtained from CompHEP, are summarised in Tab. 3.3 for the CMS energies and masses of the top quark that are considered in the following. The cross section for photon exchange increases by approximately 40% for an increase in the CMS energy from $\sqrt{s} = 300\,\text{GeV}$ to $\sqrt{s} = 318\,\text{GeV}$. The corresponding increase for the Z^0-exchange process is approximately 60%. For a variation of the top mass by $\pm 5\,\text{GeV}$, the resulting change in the cross section is approximately $\mp 25\%$.

Figure 3.16 shows the calculated cross section for single top-quark production $ep \to etX$ via FCNC at the $t - u-$boson vertex as a function of the coupling constants $\kappa_{tu\gamma}$ and v_{tuZ} for $\sqrt{s} = 318\,\text{GeV}$ and $M_{\text{top}} = 175\,\text{GeV}$. The steeper rise with $\kappa_{tu\gamma}$ as opposed to v_{tuZ} corresponds to the suppression of the Z^0 exchange for low values of Q^2. The interference between γ and Z^0 exchange, parametrised with $c_{\gamma Z}$, lowers the cross section for single-top production. The effect, however, is small, as shown in Fig. 3.17, where the

$\sqrt{s}$ (GeV)	M_{top} (GeV)	c_γ (pb)	c_Z (pb)	$c_{\gamma Z}$ (pb)
300	170	5.451	0.1808	−0.01339
	175	4.300	0.1433	−0.01096
	180	3.370	0.1123	−0.00939
318	170	7.520	0.2861	−0.01940
	175	6.076	0.2340	−0.01842
	180	4.886	0.1899	−0.01308

Table 3.3: Values of the coefficients in the parametrisation of the single-top production cross section according to equation (3.17), for different CMS energies and masses of the top quark.

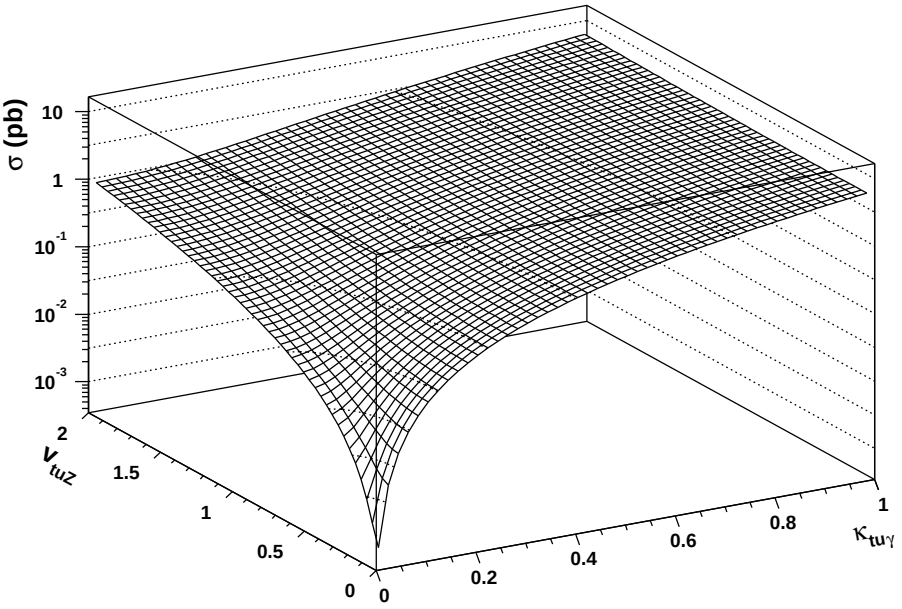

Figure 3.16: Cross section for single top-quark production $ep \to etX$ via FCNC at the $t-u-$boson vertex as a function of the coupling constants $\kappa_{tu\gamma}$ and v_{tuZ} for $\sqrt{s} = 318\,\text{GeV}$ and $M_{\text{top}} = 175\,\text{GeV}$.

relative contribution of the interference term is displayed as a function of the coupling constants $\kappa_{tu\gamma}$ and v_{tuZ} for $\sqrt{s} = 318\,\text{GeV}$ and $M_{\text{top}} = 175\,\text{GeV}$. The contribution is always below 1% and will thus be neglected for the calculation of the exclusion limits (cf. section 8).

The branching ratios $\text{BR}(t \to bW^+)$, $\text{BR}(t \to u\gamma)$ and $\text{BR}(t \to uZ)$ depend as well on the anomalous couplings $\kappa_{tu\gamma}$ and v_{tuZ} and were calculated from the decay widths in

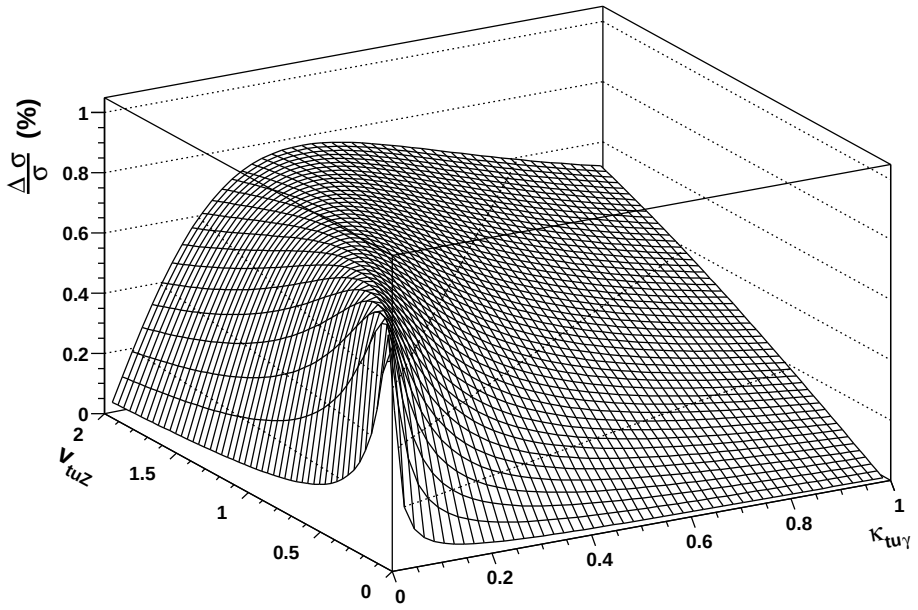

Figure 3.17: Relative contribution $\frac{\Delta\sigma}{\sigma}$ of the interference term to the total cross section for single top-quark production as a function of the coupling constants $\kappa_{tu\gamma}$ and v_{tuZ} for $\sqrt{s} = 318\,\text{GeV}$ and $M_{\text{top}} = 175\,\text{GeV}$.

the corresponding channels as

$$\begin{aligned} \text{BR}(t \to bW^+) &= \frac{\Gamma_{t\to bW^+}}{\Gamma_{t\to bW^+} + \Gamma_{t\to u\gamma} + \Gamma_{t\to uZ}} \\ \text{BR}(t \to u\gamma) &= \frac{\Gamma_{t\to u\gamma}}{\Gamma_{t\to bW^+} + \Gamma_{t\to u\gamma} + \Gamma_{t\to uZ}} \\ \text{BR}(t \to uZ) &= \frac{\Gamma_{t\to uZ}}{\Gamma_{t\to bW^+} + \Gamma_{t\to u\gamma} + \Gamma_{t\to uZ}} \end{aligned} \tag{3.18}$$

The decay widths can be parametrised as:

$$\begin{aligned} \Gamma_{t\to bW^+} &= w_{SM} \\ \Gamma_{t\to u\gamma} &= w_\gamma \cdot \kappa^2_{tu\gamma} \\ \Gamma_{t\to uZ} &= w_Z \cdot v^2_{tuZ}, \end{aligned} \tag{3.19}$$

where the coefficients w_{SM} and w_γ were obtained from CompHEP and w_Z was obtained from an analytical calculation [37] for different top masses as shown in Tab. 3.4.

3.4.4 Next-to-leading-order cross-section calculations

Next-to-leading-order (NLO) QCD calculations were available for single-top production through photon exchange [48]. They were used to obtain the cross section for the

M_{top} (GeV)	w_{SM} (MeV)	w_γ (MeV)	w_Z (MeV)
170	1404	293	1297
175	1554	302	1449
180	1713	310	1610

Table 3.4: Values of the top decay width coefficients in (3.19) for different masses of the top quark. w_{SM} and w_γ were obtained with CompHEP, while w_Z was calculated analytically [37].

process $ep \to etX$ as a function of $\kappa_{tu\gamma}$, neglecting the contribution of the Z^0 exchange process. The renormalisation (μ_R) and factorisation (μ_F) scales were chosen to be $\mu_R = \mu_F = M_{\text{top}}$. The strong coupling constant, α_S, was calculated at two loops with $\Lambda^{(5)}_{\overline{\text{MS}}} = 220\,\text{MeV}$, corresponding to $\alpha_S(M_Z) = 0.1175$. The calculations were performed using the MRST99 parametrisation of the proton PDFs. The uncertainty on the calculation due to terms beyond NLO, estimated by varying μ_R and μ_F between $M_{\text{top}}/2$ and $2 \cdot M_{\text{top}}$, was found to be $^{+1.6}_{-3.8}\%$ ($^{+1.3}_{-3.6}\%$) at a centre-of-mass energy of 318 (300) GeV. The uncertainties on the calculation due to the uncertainty on $\alpha_S(M_Z)$ and on the proton PDFs were $\pm 2\%$ and $\pm 4\%$, respectively. The variation of the cross section on M_{top} was approximately $\pm 25\%$ ($\pm 20\%$) for $\Delta M_{\text{top}} = \pm 5\,\text{GeV}$ at a centre-of-mass energy of 318 (300) GeV.

Figure 3.18 shows the effect of the NLO QCD corrections on the FCNC single-top-production cross section for $M_{\text{top}} = 175\,\text{GeV}$ and the two different CMS energies at HERA. The cross sections were obtained from a program [49], which is based on the NLO calculations [48]. The Born level cross sections are in very good agreement with the CompHEP results. For a coupling of $\kappa_{tu\gamma} = 0.2$, the NLO corrections lead to an increase in the calculated cross section by approximately 20%.

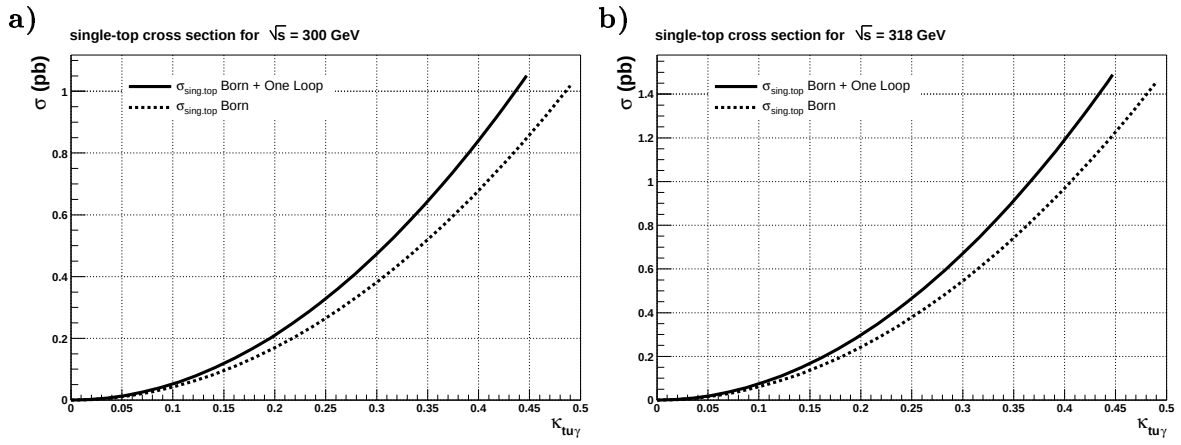

Figure 3.18: Born level cross section and Born+one-loop cross section for FCNC single-top production at HERA as function of the coupling $\kappa_{tu\gamma}$ for a CMS energy of a) 300 GeV and b) 318 GeV.

Chapter 4

Search Strategy

4.1 Generic search for isolated leptons and missing transverse momentum

In this analysis events with an isolated lepton, large missing transverse momentum and, in a final selection, large transverse momentum of the reconstructed hadronic system were searched for. The search was motivated by an accumulating excess of such events over the HERA I data taking periods, observed by the H1 collaboration [1–5].

The analysis started with a generic search for events with isolated tracks and large missing transverse momentum in the calorimeter. The isolated tracks were then matched with electrons, muons or tau leptons, that were found by the corresponding lepton finders.

4.2 Single-top quark production

The production of single top quarks through FCNC with subsequent leptonic decay of the produced W boson was considered as a prototype for a signal process beyond the Standard Model, which could lead to such signatures. In the following the existing constraints on single-top production and the experimental signature of this process at HERA are reviewed.

4.2.1 Existing constraints on single-top production

The FCNC-induced couplings of the type tuV or tcV (with $V = \gamma, Z^0$) have been explored in $p\bar{p}$ collisions at the Tevatron by searching for the top-quark decays $t \to uV$ and $t \to cV$ [50] (see Fig. 3.15). The same couplings involving the top quark were investigated in e^+e^- interactions at LEP2 by searching for single-top production through the reactions $e^+e^- \to t\bar{u}$ (+c.c.) and $e^+e^- \to t\bar{c}$ (+c.c.) [51–54] (see Fig.

4.1). No evidence for such interactions was found at either accelerator and limits were set on the branching ratios $BR(b \to q\gamma)$ and $BR(t \to qZ)$. Assuming that no anomalous couplings to the charm quark exist, the LEP and Tevatron limits were translated into limits on the anomalous coupling constants $\kappa_{tu\gamma}$ and v_{tuZ}, which appear in the Lagrangian (3.16). The published results in the LEP analyses, which have similar sensitivities to the $tu\gamma$ and tuZ couplings, are based on the assumption that the couplings to the c and u quark are of equal strength. A factor $\sqrt{2}$ was therefore applied to rescale their limits. This factor canceled with another factor $1/\sqrt{2}$, which arises from the fact that the Lagrangian used in the LEP analyses differs from (3.16) by a constant multiplicative factor, such that $\kappa_{tu\gamma}^{\mathrm{LEP}} = \sqrt{2}\kappa_{tu\gamma}^{\mathrm{ZEUS}}$ and $v_{tuZ}^{\mathrm{LEP}} = \sqrt{2}v_{tuZ}^{\mathrm{ZEUS}}$. The cancellation of these two factors is purely incidental.

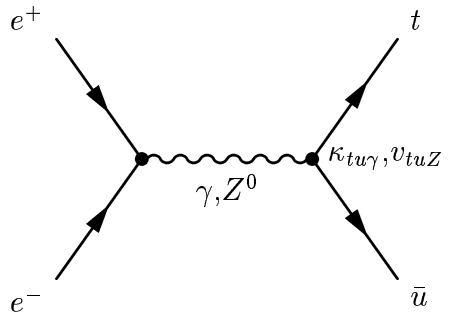

Figure 4.1: Possible production of single-top quarks through FCNC at LEP.

The most stringent constraint on $\kappa_{tu\gamma}$ was obtained by the CDF collaboration [50]. For the anomalous decay $t \to q\gamma$ it was found:

$$BR(t \to q\gamma) < 3.2\% \quad \text{at } 95\% \text{ C.L.}$$

The coupling is constrained from this limit according to eq. (3.19) and for $M_{\mathrm{top}} = 175\,\mathrm{GeV}$ to be:

$$\kappa_{tu\gamma} < 0.41.$$

From this value and (3.17) the expected upper limit on the cross section for single-top production at HERA was obtained to be approximately 0.8 pb (1.1 pb) at $\sqrt{s} = 300\,\mathrm{GeV}$ (318 GeV), assuming $v_{tuZ} = 0$. For the complete HERA I dataset of $130\,\mathrm{pb}^{-1}$ it is therefore not excluded that roughly 120 single-top events would have been produced, which via the branching ratios of the W boson corresponds to 40 leptonic decays.

The most stringent limit on the vector coupling v_{tuZ} was set by the L3 collaboration [54]. For $\kappa_{tu\gamma} = 0$ and $M_{\mathrm{top}} = 175\,\mathrm{GeV}$ it was found:

$$v_{tuZ} < 0.37.$$

4.2.2 Single-top production signatures at HERA

In the following it is assumed that the dominant production mechanism for single top quarks at HERA would be due to the anomalous magnetic coupling $\kappa_{tu\gamma}$ at the $t-u-\gamma$

vertex, for which at HERA the highest sensitivity is expected. Taking into account the existing constraints on the anomalous decay modes of the top quark, it is also assumed that the subsequent decay would be dominated by the SM decay $t \to bW$ (see Fig. 3.14). The event selection was optimized for this scenario. However also the other possible production and decay modes mentioned above were considered in the derivation of the cross-section limits.

The experimental signature of the process $ep \to etX$, $t \to W^+b$ depends on the decay channel of the W^+ boson:

- $W^+ \to e^+\nu, \mu^+\nu$. For the electron and muon decays ($BR = 10.7\%$ per channel), which were searched for in this analysis, it consists of an isolated positively charged lepton, missing transverse momentum and a hadronic system with large transverse momentum, $p_T^{\rm hadr}$. The main background for this process at HERA is the production of real W bosons.

- $W^+ \to \tau^+\nu$. For the decay to a tau lepton ($BR = 10.7\%$), the signature depends on the subsequent tau decay:

  - $\tau^+ \to e^+\nu_e\bar{\nu}_\tau,\ \mu^+\nu_\mu\bar{\nu}_\tau$. For the leptonic tau-decay modes ($BR \approx 18\%$ per channel) the experimental signature is similar to the one for the direct decay of the W boson to electron and muon.

  - $\tau^+ \to$ hadron(s) $\bar{\nu}_\tau$. Due to the large top mass, the hadrons produced from the subsequent tau decay would be expected at high momentum and strongly boosted in the direction of the tau lepton. The tau lepton is colour neutral, such that quark or gluon radiation is inhibited and the emerging energy depositions in the CAL are thus expected to have a narrow, pencil-like shape. This decay channel of the top quark is covered by the search for isolated tau leptons (cf. section 9). The huge background from events with quark or gluon induced jets however makes a stringent selection necessary and leads to a very small expected efficiency. Therefore a significant excess of tau events from W decay would have to be accompanied by a larger excess in the electron and muon decay channel.

- $W^+ \to q\bar{q}'$. The hadronic decay of the W^+ boson ($BR = 68.0\%$) leads to events where one jet emerges from the b quark and two jets from the secondary W^+ decay, all of them at large transverse energies. The dijet invariant-mass distribution for the correct pair of jets would peak at the mass of the W boson and the three-jet invariant mass distribution would peak at the top mass. The main background for this process at HERA is multi-jet QCD production at low Q^2. A search for single-top production in the hadronic decay channel, which was performed by the ZEUS collaboration [55, 56] is shortly reviewed in section 7.5. The results from both the electron/muon and the hadronic decay channel were combined, as described in section 8.

4.3 Background processes

The main contribution from the SM to the signature of interest is expected to come from single W boson production, while other SM sources might contribute through mismeasurements, producing fake leptons and/or large apparent missing transverse momentum.

4.3.1 Standard Model e-p background

The contribution of Standard Model background processes to the expected number of observed events is estimated by including different sets of simulated events in the analysis chain. The following e-p related background processes were taken into account for this analysis.

- *Photoproduction processes (PhP)*

  In photoproduction processes the scattered electron carries only a small p_T ($\sin\theta \to 0$) and is thus not detected within the main detector. Only a mismeasurement of the hadronic final state can lead to a significant missing transverse momentum, which in conjunction with a fake lepton might mimic a signal event.

- *Neutral current deep inelastic scattering (NC DIS)*

  NC DIS events are characterized by large values of Q^2, with the scattered electron usually detected within the main detector. NC DIS events can lead to significant missing transverse momentum in the detector, if one or more of the following conditions apply:

  - The hadronic system contains muons or neutrinos.
  - The hadronic energy is mismeasured.
  - The electron is mismeasured.

  Due to the large cross section for the NC DIS process, it was one of the main sources of background for electron-type events.

- *Charged current deep inelastic scattering (CC DIS)*

  CC DIS events always contain a neutrino in the final state, leading to missing transverse momentum. They can mimic a signal event in case of isolated fake leptons.

- *Lepton pair production*

  The Bethe-Heitler two-photon processes, where photons emitted from the beam electron and the proton interact, lead to the production of a lepton pair, ee, $\mu\mu$, $\tau\tau$ in the final state. Muon pairs with only one of the muons detected are characterized by missing transverse momentum in the CAL and thus contribute as background for muon-type signal events.

- *Production of single $W^{\pm}$ bosons*

  The experimental signature of single W-boson production, followed by leptonic W decay, is similar to the single top signal in the leptonic channel. The scattered electron emerges at small angles with respect to the lepton beam direction and is in most cases not found in the central detector. The observed event topology consists of the hadronic final state X and the W boson decay products. The value of the transverse momentum of the hadronic system, however, is expected to be lower compared to the single top signal, where a b-quark at high transverse momentum is produced in the decay of the heavy top quark.

4.3.2 Non *ep* background

The following sources of background, which are not related to the primary interaction of electrons and protons, were taken into account for this analysis:

- *Beam gas interactions*

  Beam gas reactions are caused by upstream interactions of electrons or protons with the residual gas nuclei or elements from the beamline. The VETO wall suppresses such events only for sufficiently high transverse momenta.

- *Halo Muons*

  Muonic decays of particles produced in beam gas interactions (e.g. $\pi^{\pm}$, $K^{\pm}$) cause a background of muons, which are passing the ZEUS detector mainly parallel to the beamline.

- *Cosmics*

  High-energy muons from interactions of cosmic rays in the atmosphere are traversing the CTD with a rate of about 500 Hz. Most of them pass on straight lines from top to bottom. Shallow angle cosmics can also occur. The cosmic muons can radiate photons or react inelastically ($\mu N \to \nu X$) inside the detector, which leads to large energy deposition and missing transverse momentum in the calorimeter. Cosmic muons may also overlay events from electron-proton interactions.

- *Sparks*

  "Sparks" are spontaneous high voltage discharges at the photomultipliers (PMT) of the CAL. Sparks appear as CAL cells with high energy. They are identified by a large imbalance between the two independent PMTs for a cell. Sparks in cells with only one active PMT are suppressed by requiring a minimum energy in the adjacent cells.

Chapter 5

Monte Carlo Simulation

Monte Carlo (MC) generators are tools used to simulate complex high-energy physics processes on the basis of statistical models. This chapter describes the simulation of all physics processes, that were considered in this analysis, followed by a brief description of the detector simulation.

For all considered processes three different sets of MC samples where used, corresponding to the three different running periods:

- 1994-1997
  Positrons ($E_{e^+} = 27.5\,\text{GeV}$) colliding on protons ($E_p = 820\,\text{GeV}$), $\sqrt{s} = 300\,\text{GeV}$;
- 1998-1999
  Electrons ($E_{e^-} = 27.5\,\text{GeV}$) colliding on protons ($E_p = 920\,\text{GeV}$), $\sqrt{s} = 318\,\text{GeV}$;
- 1999-2000
  Positrons ($E_{e^+} = 27.5\,\text{GeV}$) colliding on protons ($E_p = 920\,\text{GeV}$), $\sqrt{s} = 318\,\text{GeV}$.

The simulation of processes involving strongly interacting particles is usually divided in two parts, one modelling the hard subprocess and parton showering, which can be described perturbatively, and another one simulating the non-perturbative hadronisation phase. The output of the second part contains the four-momenta of the produced particles, which are used as input for the following simulation of the detector response.

5.1 QCD radiation

Higher order QCD processes in photoproduction and DIS can lead to one or more additional jets produced through radiation of additional hard gluons. Example diagrams for 3-jet production through initial and final state gluon radiation are shown in Fig. 5.1.

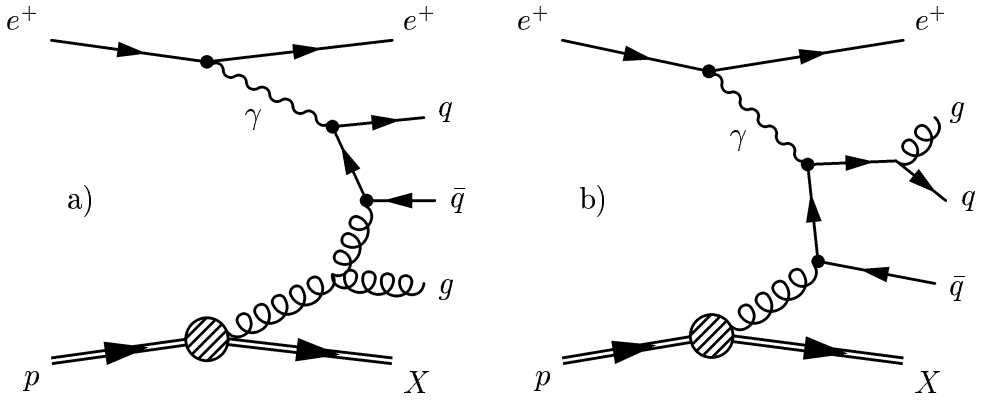

Figure 5.1: Example Feynman diagrams for 3-jet production through a) initial state and b) final state gluon radiation.

Two- and three-jet production in DIS are known in next to leading order (NLO) of QCD. Simulations however are available only in leading order (LO). Two different approaches are commonly used to describe multi-jet production from QCD radiation:

- *Colour Dipole Model (CDM).* In the Colour Dipole Model QCD radiation is described as parton showers evolving from independently radiating colour dipoles [57]. The first dipole is spanned by the quark struck by the photon and the remaining constituents of the proton (called proton remnant). The spatial extension of the proton remnant is taken into account as restriction of the phase space for hard gluon radiation near the proton remnant.
- *Matrix Element and Parton Shower Model (MEPS).* In this model higher orders of perturbation theory are summed up to all orders using the DGLAP leading log approximation (LLA). A planar parton shower is generated, in which the energy fractions in each branching process are determined by the Altarelli-Parisi-splitting functions [15] and angular-ordering is imposed for final radiation. Perturbation theory is applicable down to parton energies of approximately 1 GeV.

5.2 Hadronisation models

For the simulation of the final part of the hadronisation two different approaches are commonly used:

- *Lund model.* The Lund string fragmentation model [58] treats the colour field between diverging $q\bar{q}$ pairs as a string of constant energy density of approximately 1 GeV/fm, thus taking into account the self-interactions of the gluons. The constant energy density along the string leads to an increasing string energy with increasing $q\bar{q}$ distance, until enough energy is reached to create a $q\bar{q}$ pair from the vacuum. The string thus splits consecutively into smaller parts until the process stops when the energy of the initial $q\bar{q}$ pair is exhausted.

- *Cluster hadronisation.* A cluster hadronisation model [59] based on the idea of preconfinement of colour is often used for the final part of the event simulation. Gluons are nonperturbatively split into $q\bar{q}$ pairs. Neighbouring quarks and antiquarks are then combined to low mass colour singlet clusters, which decay isotropically into pairs of hadrons or turn into hadrons themselves by momentum exchange with a neighbouring cluster to adjust the mass.

5.3 Simulation of the signal process

Single top production in ep collisions was simulated using a modified version of the excited fermion generator HEXF [60]. HEXF is based on the phenomenological model of Hagiwara et al. [61–63]. An excited u^* quark with a mass of 175 GeV was produced and forced to decay to bW. The efficiency for detecting the decay products in case of anomalous top decay $t \to uZ$ was estimated from a smaller sample of generated events, in which the excited u^* quark was forced to decay to uZ. HEXF includes initial-state radiation from the beam electron using the Weizsäcker-Williams approximation [47]. The matrix-element and parton-shower model of Lepto 6.1 [64] is implememented for the simulation of the QCD cascade. The hadronisation and decay of unstable particles is simulated using the Lund [58] string model as implemented in JETSET 7.4 [65]. The parton density functions of the proton are evaluated from the MRS (A) parametrisation.

Additional samples of MC events were generated with CompHEP to confirm the results obtained with HEXF and to estimate the efficiency for the production through an anomalous vector coupling v_{tuZ} at the $t - u - Z^0$ vertex. Here the parton density function of the proton were evaluated from the MRST parametrisation [45, 46]. Initial state radiation was not included. CompHEP was interfaced to PYTHIA [66] for the simulation of the QCD cascade and the hadronisation and decay of unstable particles. The QCD radiation is simulated within PYTHIA using a combination of the matrix-element and parton-shower approaches. For the fragmentation the Lund string model of JETSET is used.

In all MC samples the Q^2 scale for the structure functions of the proton was set to ${M_{\text{top}}}^2$.

Table 5.1 lists the different MC samples used for the simulation of the single-top production processes.

Figures 5.2 to 5.4 show distributions of kinematic variables of the generated single top events for the scattered electron, the top quark, the W boson and the b quark from the top decay and for the lepton from leptonically decaying W bosons. All quantities are displayed for the laboratory frame. The following samples are compared, all of them generated at $\sqrt{s} = 318\,\text{GeV}$ and for $M_{\text{top}} = 175\,\text{GeV}$:

- the HEXF sample with top production through γ-exchange and decay $t \to bW$;
- the CompHEP sample with top production through γ-exchange and decay $t \to bW$;

- the CompHEP sample with top production through Z^0-exchange and decay $t \to bW$.

In general, good agreement between the two samples with γ-exchange at the production vertex can be observed.

For single-top production through γ-exchange, the massless propagator has a pole at $Q^2 = 0$. The simulation thus shows the characteristics of a photoproduction process: the momentum transfer to the beam-lepton, as observed from its transverse momentum after the scattering process, is small (Fig. 5.2a). The scattered electron escapes outside the acceptance of the calorimeter (polar angle $\theta^{el}_{scat} > 176^o$) in 65% of the events (Fig. 5.2b). For the production through the massive Z^0 boson, the propagator has no pole at $Q^2 = 0$. The distribution of the transverse momentum of the beam lepton is shifted towards larger values, corresponding to higher values of Q^2. The scattered lepton is thus observed inside the acceptance of the detector most of the time.

The HEXF events are generated for a fixed top-mass. Therefore the distribution of the momentum of the top quark, p_{top}, (Fig. 5.2c) shows a sharp cutoff at the kinematical limit $p_{\text{top}} = 250\,\text{GeV}$, where the top quark is produced at rest in the CMS. For the ComHEP samples, in which the mass of the top has a finite width, this cutoff becomes smeared. Due to its large mass, the top quark is boosted in the proton direction, as can be seen in Fig. 5.2d) from the distribution of the polar angle. The transverse momentum of the top quark has to balance the one of the scattered electron. Thus the polar angle distribution for the top quark becomes shifted towards larger values for the case where a heavy gauge boson is involved in the production.

The transverse momentum of both the W boson and the b quark from the top decay, which balance each other, show a Jacobian peak at $\frac{M^2_{\text{top}} - M^2_W}{2M_{\text{top}}}$ (Fig. 5.3a and c). For the production through Z^0-exchange, this peak is shifted towards larger values, reflecting the difference in the kinematics of the parent particle.

data taking period	generator	production	decay	top mass	# events
$\sqrt{s} = 300\,\text{GeV}$; e^+p	HEXF	$\kappa_{tu\gamma}$	$t \to bW$	$M_{\text{top}} = 170\,\text{GeV}$	46361
	HEXF	$\kappa_{tu\gamma}$		$M_{\text{top}} = 175\,\text{GeV}$	46581
	HEXF	$\kappa_{tu\gamma}$		$M_{\text{top}} = 180\,\text{GeV}$	46764
$\sqrt{s} = 318\,\text{GeV}$; e^-p	HEXF	$\kappa_{tu\gamma}$	$t \to bW$	$M_{\text{top}} = 170\,\text{GeV}$	46074
	HEXF	$\kappa_{tu\gamma}$		$M_{\text{top}} = 175\,\text{GeV}$	46322
	HEXF	$\kappa_{tu\gamma}$		$M_{\text{top}} = 180\,\text{GeV}$	46481
$\sqrt{s} = 318\,\text{GeV}$; e^+p	HEXF	$\kappa_{tu\gamma}$	$t \to bW$	$M_{\text{top}} = 170\,\text{GeV}$	45146
	HEXF	$\kappa_{tu\gamma}$		$M_{\text{top}} = 175\,\text{GeV}$	46309
	HEXF	$\kappa_{tu\gamma}$		$M_{\text{top}} = 180\,\text{GeV}$	46294
$\sqrt{s} = 318\,\text{GeV}$; e^+p	HEXF	$\kappa_{tu\gamma}$	$t \to uZ$	$M_{\text{top}} = 175\,\text{GeV}$	18567
$\sqrt{s} = 318\,\text{GeV}$; e^+p	CompHEP	$\kappa_{tu\gamma}$	$t \to bW$	$M_{\text{top}} = 175\,\text{GeV}$	15074
$\sqrt{s} = 318\,\text{GeV}$; e^+p	CompHEP	v_{tuZ}	$t \to bW$	$M_{\text{top}} = 175\,\text{GeV}$	10000
$\sqrt{s} = 318\,\text{GeV}$; e^+p	CompHEP	v_{tuZ}	$t \to uZ$	$M_{\text{top}} = 175\,\text{GeV}$	9995

Table 5.1: MC samples for the simulation of the single-top production processes.

The polar-angle distribution of the W boson (Fig. 5.3b) is boosted in the proton direction. For the HEXF samples the distribution is peaked at lower polar angles than for the CompHEP events. This difference is caused by the different treatment of the couplings in HEXF and CompHEP: the Hagiwara model, as implemented in HEXF, includes couplings only between left-handed ordinary fermions and right-handed excited fermions. The produced top is thus always right-handed polarized, while for the Lagrangian (3.16), which was implemented in CompHEP, both polarizations are possible. The polar-angle distribution of the W boson in the CMS is thus asymmetric for the HEXF simulation, while it is uniformly distributed for CompHEP, leading to the observed difference of the polar angle distribution in the laboratory frame.

Also the polar-angle distribution of the b quark (Fig. 5.3d) , which corresponds to the direction of a detectable jet, shows the boost in the proton direction. The peak of this distribution is observed at about $\theta = 15^o$ ($\theta = 25^o$ for the HEXF sample), which corresponds to $\eta = 2.0$ ($\eta = 1.5$ for the HEXF sample). The jet from the b-quark can therefore be expected inside the acceptance of the detector most of the time. The observed difference between the HEXF samples and the events generated with CompHEP for γ exchange is caused by the different treatment of the polarization, as already discussed for the polar-angle distribution of the W boson. In cases where the W decays leptonically, also this lepton can be expected to have a sizeable transverse momentum and to be pointing inside the angular acceptance of the detector most of the time (Fig. 5.4a and b).

Despite the observed difference in the polar angle distribution of the W boson and the b quark, the selection efficiency for the CompHEP and HEXF samples were found to agree within 10%. The HEXF samples were used as the default signal MC in this analysis for the $t \to bW^+$ decay mode.

5.4 Photoproduction processes (PhP)

The generator HERWIG [67] was used in its version 5.9 to simulate both direct and resolved photoproduction. The proton structure function was CTEQ4D [68], the photon structure function GRV-G LO [69]. Partonic processes are simulated using LO matrix elements, including initial- and final-state parton showers. Fragmentation into hadrons is performed using a cluster model [59]. The produced samples were restricted at generator level to exceed a threshold in the transverse energy of the produced hadronic system, E_T, or in the individual transverse momentum of the produced hadrons p_T^{hard}.

Table 5.2 lists the PhP MC samples, that were used in this analysis.

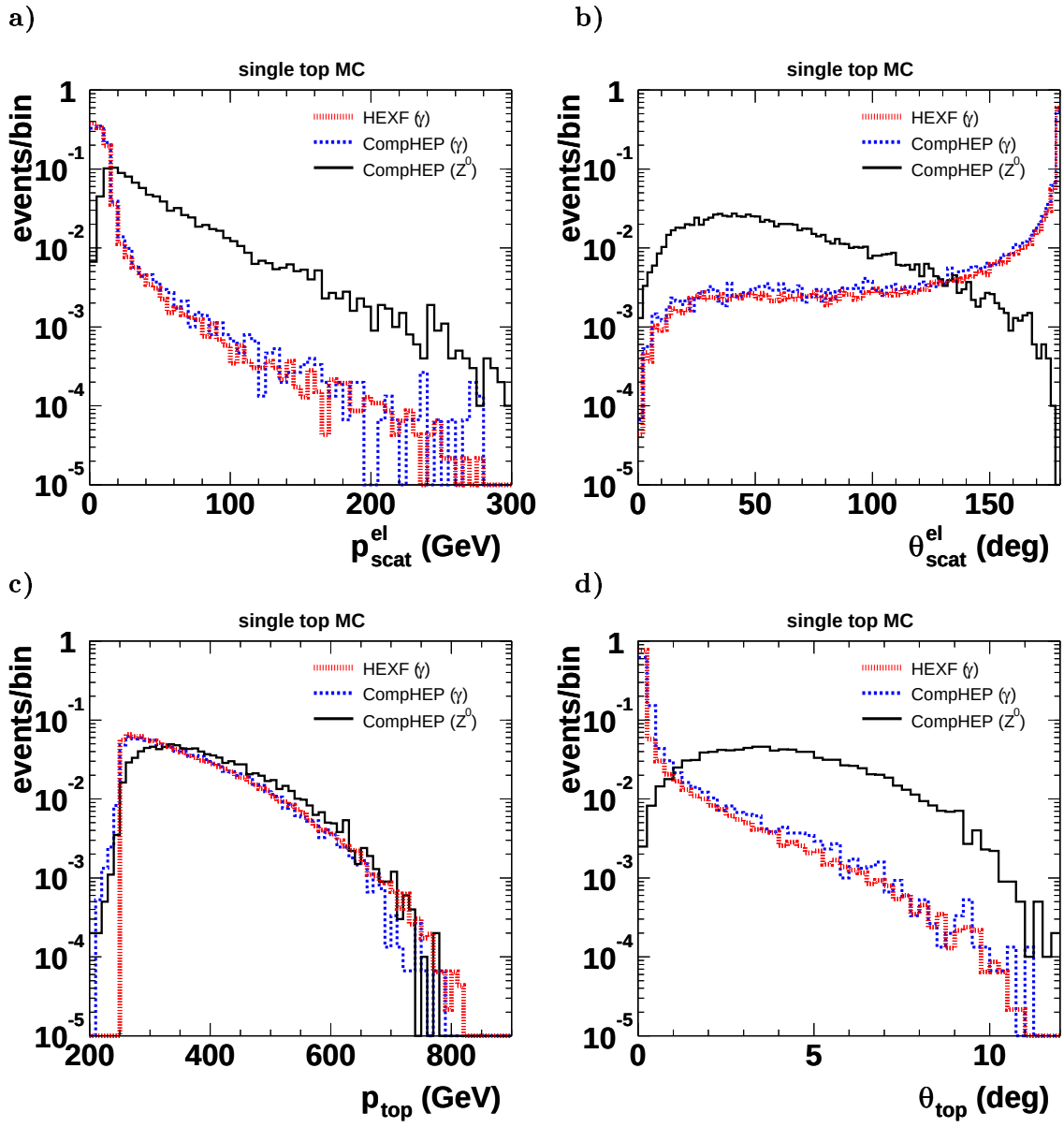

Figure 5.2: a) Momentum, p^{el}_{scat}, and b) polar angle, $\theta^{el}_{\mathrm{scat}}$, of the scattered beam electron, c) Momentum, p_{top}, and d) polar angle, θ_{top}, of the top quark, for events from the single-top signal MCs, in the laboratory frame. The dotted and dashed lines show the signal MC for γ-exchange at the production vertex and decay to bW, generated with HEXF and with CompHEP, respectively. The solid line represents the signal MC for Z^0-exchange at the production vertex and decay to bW. All histograms were normalised to one.

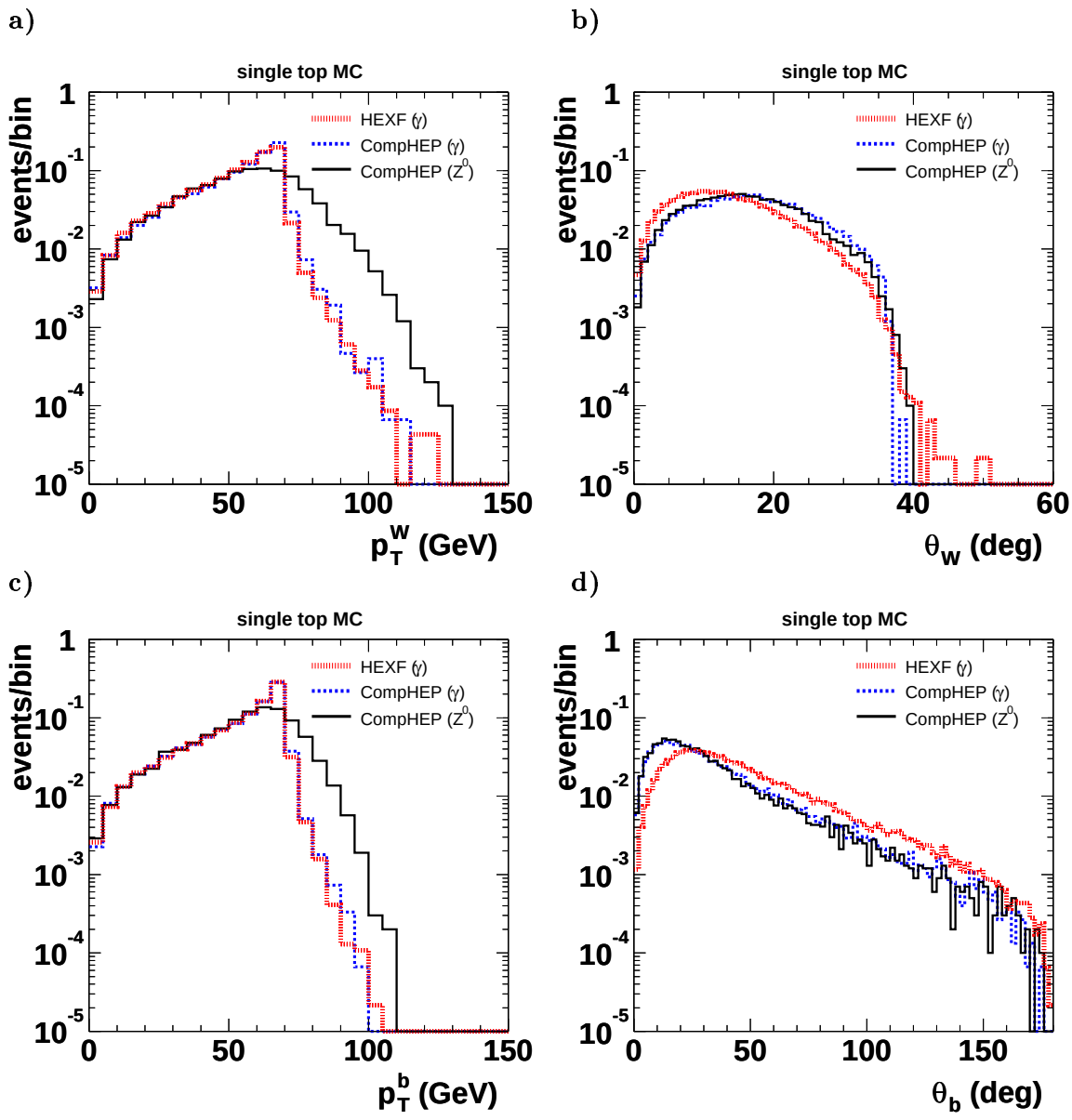

Figure 5.3: a) Transverse momentum, p_T^W, and b) polar angle, θ_W, of the W boson, c) transverse momentum, p_T^b, and d) polar angle, θ_b, of the b quark for events from the single-top signal MCs, in the laboratory frame. The dotted and dashed lines show the signal MC for γ-exchange at the production vertex and decay to bW, generated with HEXF and with CompHEP, respectively. The solid line represents the signal MC for Z^0-exchange at the production vertex and decay to bW. All histograms were normalised to one.

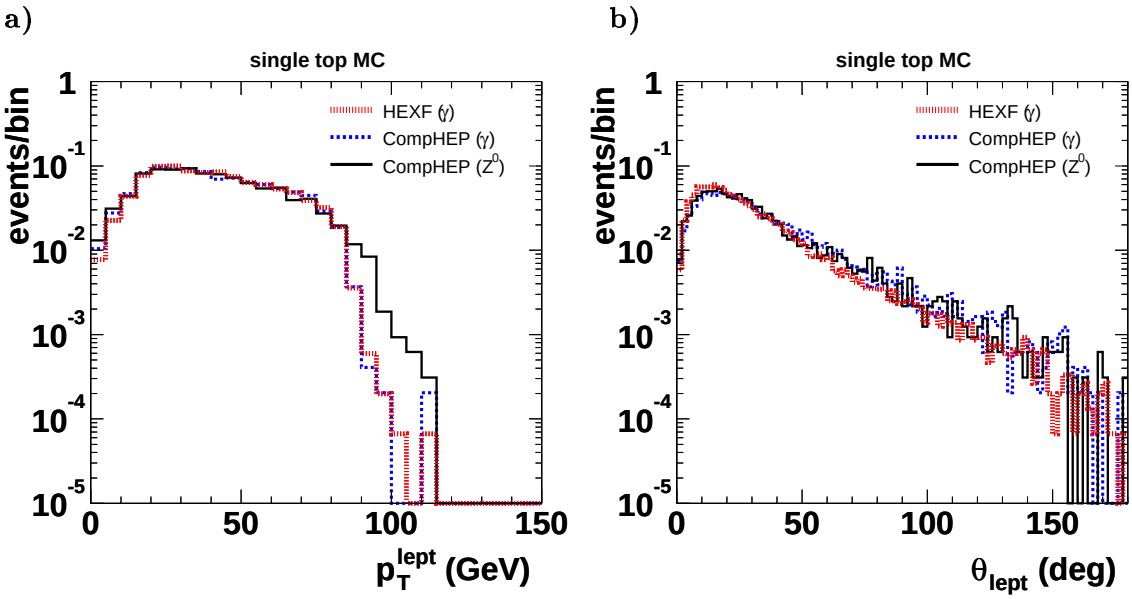

Figure 5.4: a) Transverse momentum, p_T^{lept}, and b) polar angle, θ_{lept}, of the lepton from the W boson decay for events from the single-top signal MC, in the laboratory frame. The dotted and dashed lines show the signal MC for γ-exchange at the production vertex and decay to bW, generated with HEXF and with CompHEP, respectively. The solid line represents the signal MC for Z^0-exchange at the production vertex and decay to bW. All histograms were normalised to one.

period	PhP process	generator cuts	σ (pb)	# events	$\mathcal{L}_{\text{int}}(\text{pb}^{-1})$
$\sqrt{s} = 300\,\text{GeV}$;	direct	(a)	19910	2400k	120.5
e^+p	resolved	(a)	73760	3280k	44.5
	dir.+res.	(c)	1130	208k	184.0
$\sqrt{s} = 318\,\text{GeV}$;	direct	(b)	2780	1200k	431.7
e^-p	resolved	(b)	11900	3600k	302.5
	dir.+res.	(c)	1274	110k	86.2
$\sqrt{s} = 318\,\text{GeV}$;	direct	(b)	2800	520k	185.7
e^+p	resolved	(b)	13100	630k	48.1
	dir.+res.	(c)	1263	417k	330.1

Table 5.2: MC samples for the simulation of Photoproduction processes. The generator cuts applied were: (a) The transverse energy of the produced hadronic system, E_T, had to exceed 20 GeV or the individual transverse momentum of the produced hadrons, p_T^{hard}, had to exceed 6 GeV; (b) $E_T > 30\,\text{GeV}$ or $p_T^{\text{hard}} > 6\,\text{GeV}$; (c) At least two jets with a transverse energy $E_T^{\text{jet}} > 15\,\text{GeV}$ for each of the jets and $p_T^{\text{hard}} > 6\,\text{GeV}$.

5.5 Neutral and charged current deep inelastic scattering (NC and CC DIS)

NC DIS events were simulated for this analysis with the generator LEPTO 6.5 [64] interfaced to HERACLES 4.6.1 [70] via DJANGOH 1.1 [71]. The CTEQ5D [72] parametrisations of the proton PDFs were used. The simulation of the QCD cascades with ARIADNE [73] was based on the colour dipole model (CDM). Hadronic final states were generated with string fragmentation. The CDM model is known to give the best description of most final state data [74,75]. To investigate the influence of the QCD-radiation model on the background expectation, another set of NC DIS MC events was generated using the Matrix Element and Parton Shower Model (MEPS), as implemented in LEPTO MEPS.

The NC DIS MC samples used for this analysis are listed in Tab. 5.3

CC DIS events were simulated in the same framework as the NC DIS events, with the CTEQ4D [68] parametrisations used for the proton PDFs. The corresponding MC samples are listed in Tab. 5.4.

5.6 Lepton pair production

The lepton-pair-production processes were simulated with the generator GRAPE-Dilepton [76].

The phase-space is divided in kinematic regions defined according to the square of the four-momentum transfer at the proton vertex Q_p^2 and the square of the invariant mass of the hadronic final state M_{hadr}^2:

$$Q_p^2 = (p_{e,in} - (p_e + p_{l^+} + p_{l^-}))^2$$

$$M_{hadr}^2 = ((p_{e,in} + p_{p,in}) - (p_e + p_{l^+} + p_{l^-}))^2,$$

where $p_{e,in}$ and $p_{p,in}$ are the four-momenta of the incoming electron and proton, respectively, and p_e, p_{l^+}, p_{l^-} are the four-momenta of the outgoing electron and leptons, respectively. Three kinematic regions were considered:

- elastic: $M_{hadr} = M_p$
- quasi-elastic (I): $Q_p^2 < 1\,\mathrm{GeV}^2$, quasi-elastic (II): $M_p + M_{\pi^0} < M_{\mathrm{hadr}} < 5\,\mathrm{GeV}$
- DIS (I) to (IV): $Q_p^2 > 1\,\mathrm{GeV}^2$ and $M_{\mathrm{hadr}} > 5\,\mathrm{GeV}$, with the subprocesses (I) to (IV) corresponding to the generation of the initial state quark (u; $\overline{u}$; d and s; $\overline{d}$ and $\overline{s}$).

NC DIS			ARIADNE CDM		LEPTO MEPS	
period	$Q^2 >$	σ (pb)	# events	$\mathcal{L}_{\text{int}}(\text{pb}^{-1})$	# events	$\mathcal{L}_{\text{int}}(\text{pb}^{-1})$
300 GeV;	$100\,\text{GeV}^2$	7585.5830	197506	26.0	-	-
e^+p	$400\,\text{GeV}^2$	1097.0656	710607	649.4	599759	546.9
	$1250\,\text{GeV}^2$	182.0800	121932	670.7	259678	1426.8
	$2500\,\text{GeV}^2$	53.1201	41576	782.6	119975	2256.6
	$5000\,\text{GeV}^2$	12.9242	19879	1530.7	119907	9284.3
	$10000\,\text{GeV}^2$	2.2858	16971	7352.1	119943	52454.7
	$20000\,\text{GeV}^2$	0.2244	16886	74389.9	119892	533469.8
	$30000\,\text{GeV}^2$	0.0342	10995	318466.4	59971	1751540.5
	$40000\,\text{GeV}^2$	0.0057	10916	1915087.8	59974	10629165.0
	$50000\,\text{GeV}^2$	0.0008	7990	9987500.0	59969	71107240.0
318 GeV;	$100\,\text{GeV}^2$	8157.8999	374415	45.9	-	-
e^-p	$400\,\text{GeV}^2$	1196.8341	259866	217.2	479757	401.0
	$1250\,\text{GeV}^2$	216.8898	58995	272.0	211475	973.6
	$2500\,\text{GeV}^2$	71.7032	21995	306.6	119986	1671.8
	$5000\,\text{GeV}^2$	21.6327	14490	669.3	119877	5531.7
	$10000\,\text{GeV}^2$	5.3639	16955	3161.4	110519	20598.1
	$20000\,\text{GeV}^2$	0.8470	16973	20034.3	108524	128136.6
	$30000\,\text{GeV}^2$	0.1851	10995	59361.9	59990	324077.6
	$40000\,\text{GeV}^2$	0.0427	10993	257615.3	59987	1406329.9
	$50000\,\text{GeV}^2$	0.0092	11000	1196383.1	59964	6523640.5
318 GeV;	$100\,\text{GeV}^2$	8122.0000	939419	115.7	-	-
e^+p	$400\,\text{GeV}^2$	1167.5764	849236	727.3	564328	483.3
	$1250\,\text{GeV}^2$	197.4970	189696	960.4	239608	1212.0
	$2500\,\text{GeV}^2$	58.9304	63952	1085.3	119931	2036.4
	$5000\,\text{GeV}^2$	14.8413	33975	2288.7	119861	8093.8
	$10000\,\text{GeV}^2$	2.7965	28921	10350.7	125670	45007.5
	$20000\,\text{GeV}^2$	0.3098	28932	93341.9	119925	386530.7
	$30000\,\text{GeV}^2$	0.0544	16990	312142.1	51779	950823.6
	$40000\,\text{GeV}^2$	0.0109	17000	1562265.4	59934	5516752.5
	$50000\,\text{GeV}^2$	0.0021	16985	8038236.5	59923	28241586.0

Table 5.3: MC samples for the simulation of NC DIS events.

data taking period	Model	$Q^2 >$	σ (pb)	# events	$\mathcal{L}_{\text{int}}(\text{pb}^{-1})$
$\sqrt{s} = 300\,\text{GeV};\ e^+p$	CDM	$100\,\text{GeV}^2$	34.70	293406	8456.7
$\sqrt{s} = 318\,\text{GeV};\ e^-p$	CDM	$100\,\text{GeV}^2$	71.51	99938	1397.5
$\sqrt{s} = 318\,\text{GeV};\ e^+p$	CDM	$10\,\text{GeV}^2$	45.20	24990	552.9
	CDM	$100\,\text{GeV}^2$	38.10	449674	11802.5
	MEPS	$100\,\text{GeV}^2$	38.10	449590	11800.3

Table 5.4: MC samples for the simulation of CC DIS events.

At least one of the two leptons was required to be in the polar angle range $5^o < \theta < 175^o$ and at least one of the leptons was required to have a transverse momentum $p_T^{\text{lept}} > 5\,\text{GeV}$.

The proton structure function used was CTEQ5L [72].

Table 5.5 lists the lepton-pair-production MC samples that were used in this analysis.

5.7 Production of single $W^{\pm}$ bosons

Both direct and resolved W boson production were simulated using the event generator EPVEC [77], which is a leading order (LO) program and does not include QCD radiation. The phase space is split into two regions:

$$\sigma = \sigma(|u| > u_{cut}) + \int^{u_{cut}} \frac{\mathrm{d}\sigma}{\mathrm{d}|u|}\mathrm{d}|u|$$

where $u = (p_q - p_W)^2$ is the square of the four-momentum transfer from the incoming quark to the final state W boson. The first term (DIS W boson production) is calculated using helicity amplitudes for the process $e^{\pm}q \to e^{\pm}Wq'$, $W \to l\overline{\nu}$. The cross section for $|u| < u_{cut}$ (resolved photon W boson production) is calculated by folding the cross section for $q\overline{q'} \to W \to l\overline{\nu}$ with the parton densities in the proton and the effective parton densities for the resolved photon emitted by the incoming lepton. The sum of the DIS and resolved cross sections varies little with u_{cut}, chosen here to be $25\,\text{GeV}^2$.

The hadronisation and decay of unstable particles is simulated using the LUND [58] string model as implemented in JETSET 7.3 [65].

Next-to-leading-order (NLO) real and virtual QCD corrections for the photoproduction regime were taken into account by reweighting the EPVEC MC samples to the cross sections obtained from recent LO and NLO calculations [18–21]. In these calculations, two phase space regions were distinguished: the deep inelastic (DIS) regime at large values of Q^2 and the photoproduction regime at small Q^2. The QCD corrections were calculated for the dominant direct photon mechanism at finite transverse momentum of the W boson [20] and for the total cross section of the resolved part [18, 19]. In the NLO calculations CTEQ4M [68] and ACFGP [78] were chosen as parton density distributions for the proton and the resolved photon, respectively. At LO CTEQ4L [68] was used. The reweighting factors for scaling the EPVEC samples to the cross section calculations from [20] were obtained as the ratio of the two cross sections in bins of the transverse momentum of the produced W boson p_T^W:

$$\text{weight}(p_T^W) = \frac{(d\sigma/dp_T^W)_{\text{NLO}}}{(d\sigma/dp_T^W)_{\text{EPVEC}}}$$

		ee			$\mu\mu$			$\tau\tau$		
period	process	σ (pb)	# ev.	$\mathcal{L}_{\text{int}}(\text{pb}^{-1})$	σ (pb)	# ev.	$\mathcal{L}_{\text{int}}(\text{pb}^{-1})$	σ (pb)	# ev.	$\mathcal{L}_{\text{int}}(\text{pb}^{-1})$
$\sqrt{s} = 300\,\text{GeV}$;	elastic	12.6490	30000	2371.7	9.6538	29990	3106.6	5.9924	10000	1668.8
e^+p	quasi-el. I	0.1945	3000	15423.9	0.1460	3000	20535.3	0.0908	5000	55059.3
	quasi-el. II	5.5466	10000	1802.9	4.7605	9995	2099.6	3.4065	2995	879.2
	DIS I	31.9600	40000	1251.6	12.1717	19990	1642.3	4.6780	9995	2136.6
	DIS II	7.9148	12000	1516.1	2.3806	4995	2098.2	0.8563	3000	3503.4
	DIS III	6.1853	10000	1616.7	2.1608	5000	2314.0	0.8185	3000	3665.3
	DIS IV	3.5628	4990	1400.6	1.1227	2637	2348.9	0.4122	2995	7265.6
$\sqrt{s} = 318\,\text{GeV}$;	elastic	13.3651	14000	1047.5	10.1979	10874	1066.3	6.3460	6500	1024.3
e^-p	quasi-el. I	0.2195	2996	13652.3	0.1666	2996	17981.6	0.1046	3000	28686.2
	quasi-el. II	5.7675	5993	1039.1	4.9679	4989	1004.3	3.5612	4000	1123.2
	DIS I	33.2958	33871	1017.3	13.0326	13893	1066.0	5.2411	5487	1046.9
	DIS II	8.0249	8500	1059.2	2.6570	3000	1129.1	1.0414	2995	2876.0
	DIS III	6.4299	6465	1005.5	2.3637	3000	1269.2	0.9497	2979	3136.8
	DIS IV	3.7010	3972	1073.2	1.2187	2984	2448.6	0.4789	3000	6263.9
$\sqrt{s} = 318\,\text{GeV}$;	elastic	13.3651	27000	2020.2	10.1979	20982	2057.5	6.3460	12993	2047.4
e^+p	quasi-el. I	0.2195	2988	13615.8	0.1666	2979	17879.6	0.1046	2993	28619.3
	quasi-el. II	5.7675	11988	2078.6	4.9679	9960	2004.9	3.5612	7500	2106.0
	DIS I	32.7419	66000	2015.8	12.9775	25988	2002.5	5.2280	10993	2102.7
	DIS II	8.2690	16986	2054.2	2.6815	5491	2047.8	1.0462	2995	2862.7
	DIS III	6.4757	13000	2007.5	2.3725	4993	2104.5	0.9514	2993	3146.0
	DIS IV	3.6361	7488	2059.3	1.2127	2995	2469.7	0.4777	2985	6248.2

Table 5.5: MC samples for the simulation of lepton pair production.

Figure 5.5 and 5.6 show the cross sections and correction factors for e^+p configuration at $\sqrt{s} = 300\,\text{GeV}$ and $\sqrt{s} = 318\,\text{GeV}$, respectively. The error bars shown in the plots were obtained from the statistical uncertainty on the number of generated EPVEC events in the corresponding bin. The W-production cross section falls steeply with p_T^W, leading to large statistical fluctuations of the EPVEC cross section at high values of p_T^W. Therefore also the resulting correction factors show larger fluctuations for high values of p_T^W.

No cross section calculations were available for the e^-p, $\sqrt{s} = 318\,\text{GeV}$ configuration. The corresponding EPVEC samples for this configuration were reweighted with the factors obtained from the e^+p, $\sqrt{s} = 318\,\text{GeV}$ configuration, thus neglecting the influence of the different γ-Z/W interference for the e^+p and the e^-p configuration on the correction factors.

The single W production MC samples used for this analysis are listed in Tab. 5.6. The cross section and luminosity numbers in the table refer to the EPVEC samples before reweighting and thus do not inlcude the NLO contributions. The total cross section for single W production, including the recent NLO and LO calculations, amounts to 0.96 pb (1.16) for $\sqrt{s} = 300\,\text{GeV}$ ($\sqrt{s} = 318\,\text{GeV}$). These numbers are identical to the total cross sections obtained from EPVEC, which is considered to be a coincidence: the net effect of the reweighting for the different phase space regions and W charges amounts to zero.

data taking period	W prod. process	σ (pb)	# events	$\mathcal{L}_{\text{int}}(\text{pb}^{-1})$
$\sqrt{s} = 300\,\text{GeV}$; e^+p	W^+ DIS	0.4023	49666	123452
	W^- DIS	0.3305	49948	151126
	W^+ resolved	0.1262	9897	78423
	W^- resolved	0.1000	9997	99970
$\sqrt{s} = 318\,\text{GeV}$; e^-p	W^+ DIS	0.4782	9932	20772
	W^- DIS	0.4058	9995	24632
	W^+ resolved	0.1522	10000	65721
	W^- resolved	0.1207	9995	82785
$\sqrt{s} = 318\,\text{GeV}$; e^+p	W^+ DIS	0.4886	49978	102296
	W^- DIS	0.4015	49925	124335
	W^+ resolved	0.1522	9991	65662
	W^- resolved	0.1207	9989	82735

Table 5.6: MC samples for the production of single W bosons.

5.8 Detector simulation

To compare the MC simulation with the measured data, the generated MC events are passed to a simulation of the ZEUS detector. The program MOZART simulates the

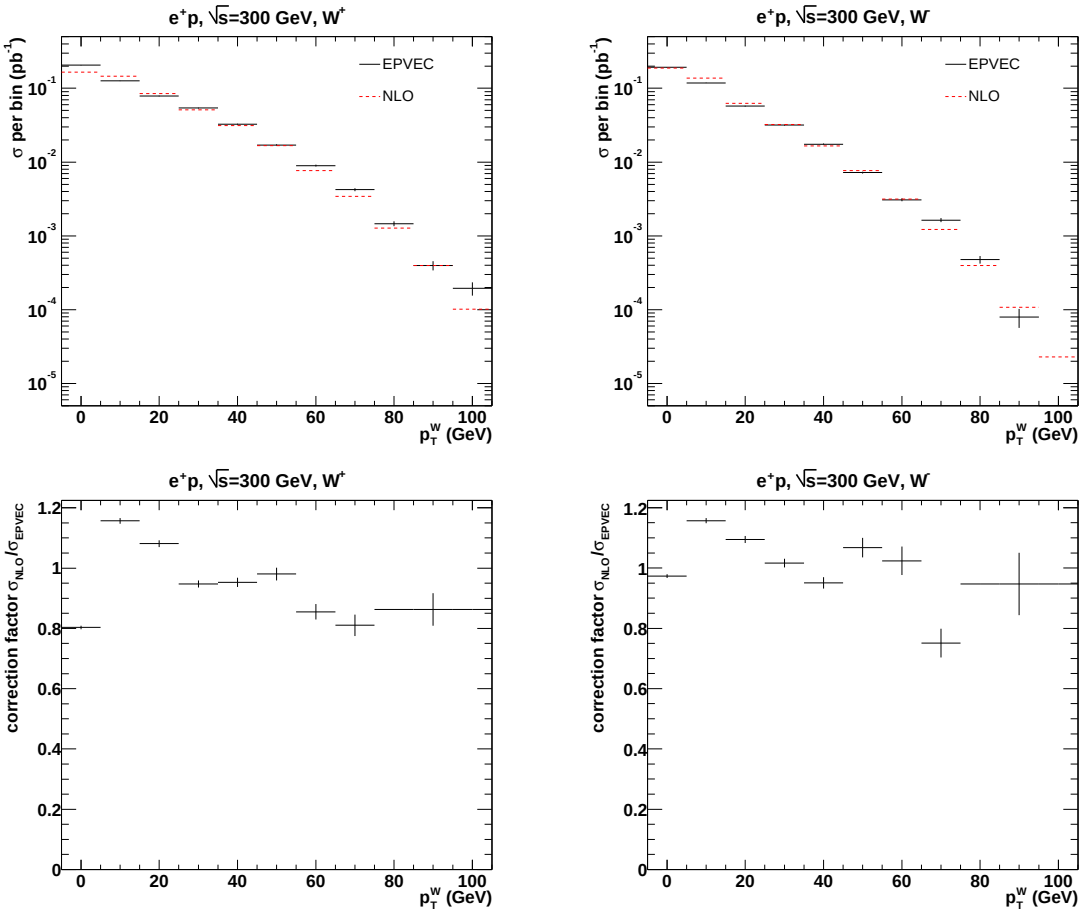

Figure 5.5: Cross section for W^+ (left) and W^- (right) production at $\sqrt{s} = 300\,\text{GeV}$. The upper plots show the cross section in bins of the transverse momentum of the W boson p_T^W for EPVEC and for recent calculations including NLO contributions for the photoproduction part, as described in the text. The bottom plots show the correction factors EPVEC/NLO. The correction factors for $75\,\text{GeV} < p_T^W < 105\,\text{GeV}$ were obtained from the integral of the cross sections in this p_T^W range.

response of the different detector components and the interaction with inactive material. MOZART is based on the GEANT-3.13 package [79]. It was initially optimized with testbeam data and is continuously being improved with performance studies of the running ZEUS experiment. The ouput of MOZART is processed by the trigger simulation program ZGANA and, in case of a positive trigger decision, passed on to the event reconstruction package ZEPHYR. ZEPHYR contains the reconstruction codes of the different components and is used both for data and simulated MC events. It builds physics objects like tracks from single hits and applies calibrations.

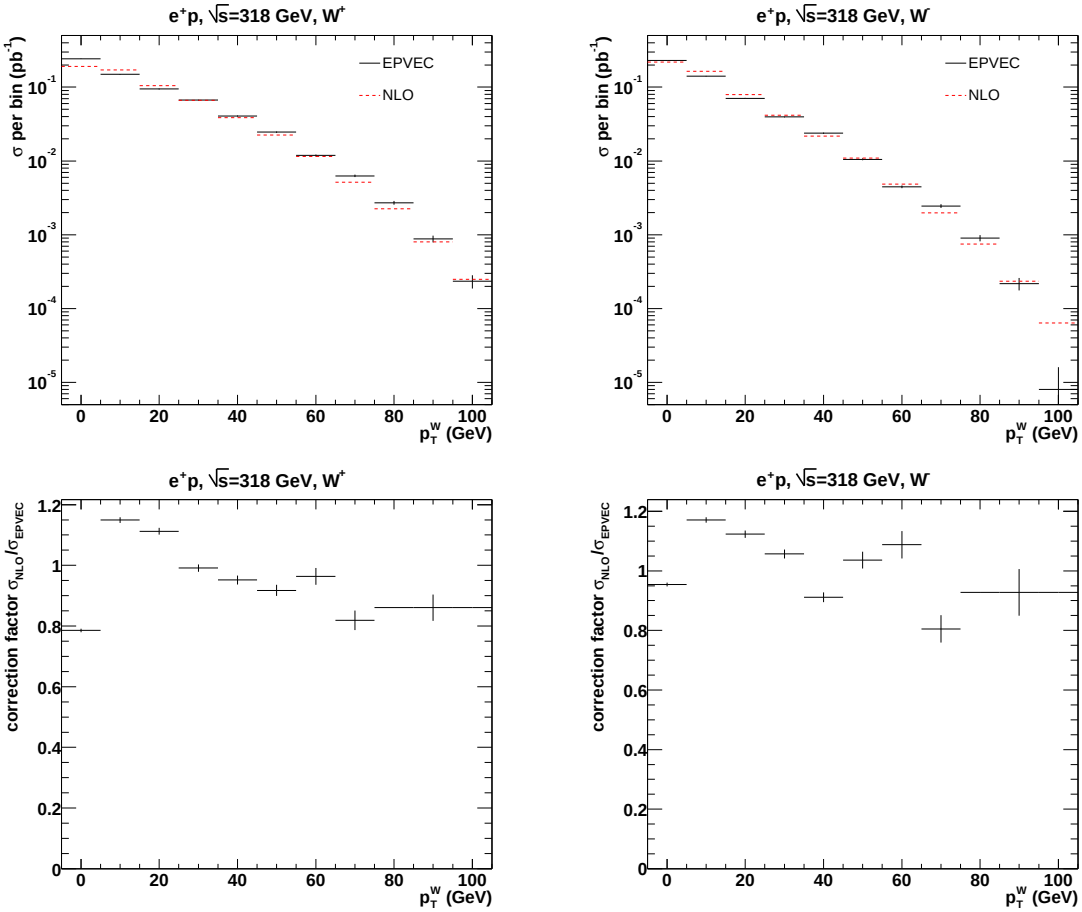

Figure 5.6: Cross section for W^+ (left) and W^- (right) production at $\sqrt{s} = 318\,\text{GeV}$. The upper plots show the cross section in bins of the transverse momentum of the W boson p_T^W for EPVEC and for recent calculations including NLO contributions for the photoproduction part, as described in the text. The bottom plots show the correction factors EPVEC/NLO. The correction factors for $75 < p_T^W < 105$ were obtained from the integral of the cross sections in this p_T^W range.

Chapter 6

Dataset and event reconstruction

This chapter describes the HERA-I dataset from 1994-2000, which was exploited for this analysis, and defines the event variables used in the following chapters.

6.1 Dataset

The analysed data consists of events from e^+p and e^-p collisions at centre of mass energies of $\sqrt{s} = 300\,\text{GeV}$ and $\sqrt{s} = 318\,\text{GeV}$, taken in the years from 1994 to 2000. The total integrated luminosity was $\mathcal{L}_{\text{int}} = 130.13\,\text{pb}^{-1} \pm 1.93\%$. Table 6.1 summarises the running conditions and integrated luminosities for the different periods. The quoted systematic uncertainties for the combined data taking periods were obtained by averaging the luminosity-weighted uncertainties for the single years, i.e. assuming uncorrelated uncertainties. The same values were obtained when assuming a maximal correlation of the individual uncertainties.

6.2 Definition of the reconstructed variables

6.2.1 Calorimeter energy corrections

Isolated CAL cells with an energy below a noise threshold of 80 MeV for electromagnetic cells and 140 MeV for hadronic cells were not taken into account for the reconstruction. For the data from the 1994 running period, the thresholds were 100 MeV and 150 MeV for electromagnetic and hadronic cells respectively. Cells with an energy $E_{\text{cell}} > 1.0\,\text{GeV}$ were also excluded, if there was a large imbalance between the energy values E_{left} and E_{right} from their two independent photomultipliers: $\frac{|E_{\text{left}} - E_{\text{right}}|}{E_{\text{cell}}} > 0.7$. For the data from the 1994 runnning period, the imbalance cut was $\frac{|E_{\text{left}} - E_{\text{right}}|}{E_{\text{cell}}} > 0.8$.

The absolute energy scales of both the electromagnetic and hadronic parts of the three CAL sections were calibrated by applying correction factors to the energy contents

Year	collision type	cms energy	$\mathcal{L}_{\text{int}}$ (pb^{-1})	σ_{syst}
1994	e^+p	300 GeV	2.99 pb^{-1}	1.5%
1995	e^+p	300 GeV	6.32 pb^{-1}	1.1%
1996	e^+p	300 GeV	10.77 pb^{-1}	1.1%
1997	e^+p	300 GeV	27.85 pb^{-1}	1.8%
1994-1997	e^+p	300 GeV	47.93 pb^{-1}	1.5%
1998	e^-p	318 GeV	4.61 pb^{-1}	1.8%
1999	e^-p	318 GeV	12.10 pb^{-1}	1.8%
1998-1999	e^-p	318 GeV	16.71 pb^{-1}	1.8%
1999	e^+p	318 GeV	19.71 pb^{-1}	2.25%
2000	e^+p	318 GeV	45.78 pb^{-1}	2.25%
1999-2000	e^+p	318 GeV	65.49 pb^{-1}	2.25%
1994-2000			130.13 pb^{-1}	1.93%

Table 6.1: Running conditions and integrated luminosities for the different data taking periods considered in this analysis. The systematic uncertainty on the integrated luminosity is also shown.

of all CAL cells of the corresponding section and type. The values of the correction factors are given in Tab. 6.2.

CAL section	cell type	energy correction
FCAL	electromagnetic	+4%
	hadronic	-5%
BCAL	electromagnetic	+4%
	hadronic	+8%
RCAL	electromagnetic	+2.5%
	hadronic	+2.5%

Table 6.2: Energy correction factors for the electromagnetic and hadronic parts of the FCAL, BCAL and RCAL.

The remaining uncertainty in the CAL energy determination is $\pm 1\%$ in the FCAL and BCAL and $\pm 2\%$ in the RCAL [80].

Further energy corrections, which are specific for the reconstructed event variables, are described in the following sections.

6.2.2 Global calorimeter variables

The total energy deposition in the CAL $E_{\rm tot}$ and its projections p_x, p_y, p_z along the space coordinates are defined as:

$$E_{\rm tot} = \sum_{i\neq\mu-{\rm cells}} E_i, \tag{6.1}$$

$$p_x = \sum_{i\neq\mu-cells} E_i \sin\theta_i \cos\phi_i, \tag{6.2}$$

$$p_y = \sum_{i\neq\mu-cells} E_i \sin\theta_i \sin\phi_i, \tag{6.3}$$

$$p_z = \sum_{i\neq\mu-cells} E_i \cos\theta_i. \tag{6.4}$$

The summation index i runs over all CAL cells that do not belong to identified muons. E_i, θ_i and ϕ_i are the energy, polar and azimuthal angles of the i-th CAL cell, respectively. The angles were calculated using the z position of the reconstructed event vertex and the center of each cell. The calorimeter four-vector was corrected for energy loss in inactive material between the interaction point and the CAL, for back-splash from the CAL and for non-uniformity in the energy response of the CAL cells. The correction took into account the difference in the CAL response between data and MC events. The hadronic system and identified electrons were treated separately for this correction and added after the correction to form the total corrected CAL four-vector. The correction for the hadronic system was based on clusters of CAL cells (cone islands), for which a correction factor was applied depending on the energy and position of the islands [81, 82]. Only CAL cells that did not belong to identified muons or electrons were taken into account for this procedure. The energy of identified electrons was obtained and corrected for detector effects as described in section 6.2.4.

The variable

$$E - p_z = E_{\rm tot} - p_z = \sum_i E_i(1-\cos\theta_i) \tag{6.5}$$

has characteristic distributions for different final states. From energy-momentum conservation it follows that for events, where only longitudinal momentum along the proton direction is undetected, $E - p_z$ has a value of 55 GeV, which is twice the energy of the incident $e^{\pm}$ beam.

The imbalance of the of the detected transverse momentum, $\overrightarrow{p_T^{\rm CAL}}$, its magnitude, $p_T^{\rm CAL}$, and the azimuth angle, $\phi_{\rm CAL}$, are given as:

$$\overrightarrow{p_T^{\rm CAL}} = \begin{pmatrix} -p_x \\ -p_y \\ 0 \end{pmatrix}, \quad p_T^{\rm CAL} = \sqrt{p_x^2 + p_y^2}, \quad \phi_{\rm CAL} = \arctan\frac{p_y}{p_x}. \tag{6.6}$$

$p_T^{\rm miss}$ is the imbalance of the detected transverse momentum, taking into account also the momenta of all muons in the event, which are measured by the CTD (cf. section

6.2.5):

$$\overrightarrow{p_T^{\text{miss}}} = \begin{pmatrix} -p_x - \sum_i p_{x,i}^{\mu} \\ -p_y - \sum_i p_{y,i}^{\mu} \\ 0 \end{pmatrix}, \quad p_T^{\text{miss}} = \sqrt{(p_x + \sum_i p_{x,i}^{\mu})^2 + (p_y + \sum_i p_{y,i}^{\mu})^2}, \tag{6.7}$$

where the summation index i runs over all identified muons in the event and $p_{x,i}^{\mu}$, $p_{y,i}^{\mu}$ are the x- and y- components of the muon momenta. ϕ_{miss} is the azimuth angle of $\overrightarrow{p_T^{\text{miss}}}$.

p_T^{ex1IR} is the imbalance of the detected transverse momentum in the CAL, not taking into account the cells from the first inner ring of the FCAL. It is defined similar to p_T^{CAL}:

$$p_T^{\text{ex1IR}} = \sqrt{(\sum_{i \neq 1IR} E_i \sin\theta_i \cos\phi_i)^2 + (\sum_{i \neq 1IR} E_i \sin\theta_i \sin\phi_i)^2}. \tag{6.8}$$

The summation index i runs over all CAL cells except for the cells from the first inner ring of the FCAL. p_T^{ex1IR} was not corrected for inactive material, backsplash and non-uniformity.

The four-vector of the hadronic system is defined in the same way as the total CAL four-vector, except that also cells, which belong to identified electrons, are excluded from the energy summation:

$$E_{\text{hadr}} = \sum_{i \neq \mu+el.-cells} E_i, \tag{6.9}$$

$$p_{x,\text{hadr}} = \sum_{i \neq \mu+el.-cells} E_i \sin\theta_i \cos\phi_i, \tag{6.10}$$

$$p_{y,\text{hadr}} = \sum_{i \neq \mu+el.-cells} E_i \sin\theta_i \sin\phi_i, \tag{6.11}$$

$$p_{z,\text{hadr}} = \sum_{i \neq \mu+el.-cells} E_i \cos\theta_i. \tag{6.12}$$

E_T is the total transverse energy, calculated as the scalar sum of the transverse energies of the individual cells:

$$E_T = \sum_i E_i \sin\theta_i. \tag{6.13}$$

The summation index i runs over all CAL cells. E_T was not corrected for inactive material, backsplash and non-uniformity.

$\overrightarrow{p_T^{\text{hadr}}}$ and p_T^{hadr} are the transverse vector of the hadronic system and its magnitude, respectively:

$$\overrightarrow{p_T^{\text{hadr}}} = \begin{pmatrix} p_{x,\text{hadr}} \\ p_{y,\text{hadr}} \end{pmatrix}, \quad p_T^{\text{hadr}} = \sqrt{p_{x,\text{hadr}}^2 + p_{y,\text{hadr}}^2}. \tag{6.14}$$

ϕ_{hadr} is the azimuth angle of $\overrightarrow{p_T^{\text{hadr}}}$.

6.2.3 Track and vertex finding

Tracks were reconstructed from hits in the CTD [83, 84]. The event vertex was reconstructed from the tracks in the CTD. Only tracks that were originating from the primary event vertex and that had a transverse momentum $p_T^{\mathrm{trk}} > 100\,\mathrm{MeV}$ were considered for this analysis. The charges of the tracks were determined from the sign of the curvature of the tracks. The track-charge determination is reliable only for well reconstructed tracks which have passed a sufficiently large number of CTD superlayers. For this analysis no selection on the track charge was made.

6.2.4 Electron identification

The identification of electrons was based on the electron finder EM [85, 86]. It uses both CAL and tracking information. EM calculates the likelihood for different variables to be originating from an electron, based on a sample of electrons, which were selected by other algorithms. For candidate electrons in this analysis, the product of the likelihoods was required to exceed a value of 10^{-3}. The energy of the electrons was calculated from their energy depositions in the CAL and corrected for energy loss in inactive material according to test-beam measurements. The direction of the electrons was calculated from the CTD track pointing into the direction of the electron candidate. The minimum CAL energy for electrons was 4.0 GeV. Only isolated electrons were taken into account: the energy not belonging to the electron candidate within a cone radius of 0.8 in the η-ϕ plane around the electron candidate was required not to exceed 20% of the energy belonging to the electron candidate.

6.2.5 Muon identification

The identification of muons was based on an algorithm, which matches vertex-fitted tracks in the CTD ($p_T^{\mathrm{trk}} > 2\,\mathrm{GeV}$) with energy depositions in the CAL. The pattern of the energy deposition along the track is required to be compatible with the energy deposition of a minimum ionizing particle (MIP). Tracks that have a distance of closest approach (DCA) to the MIP of less than 30 cm are classified as muons, if there is no other track with a DCA to the muon of less than 100 cm. The momentum and direction of the muon candidates were obtained from the corresponding CTD track.

6.2.6 Tau identification

The tau finder used in this analysis was based on the hadronic tau decay modes into collimated jets. It is explained in detail in section 9.1.

6.2.7 Jet finding

The energy depositions in the CAL were combined to jets with a cell-based inclusive $k_\perp$ algorithm [87,88]. The general noise threshold for CAL cells (see section 6.2.1) was tightened for the jet finding: electromagnetic and hadronic CAL cells were excluded, if their energy was below 100 MeV for electromagnetic and 150 MeV for hadronic cells.

The jet transverse energy, E_T, and the position variables η_{jet} and ϕ_{jet} are defined as:

$$E_T^{\text{jet}} = \sum_i E_{T,i} = \sum_i E_i \sin\theta_i, \tag{6.15}$$

$$\eta_{\text{jet}} = \frac{\sum_i E_{T,i}\eta_i}{\sum_i E_{T,i}}, \tag{6.16}$$

$$\phi_{\text{jet}} = \frac{\sum_i E_{T,i}\phi_i}{\sum_i E_{T,i}}, \tag{6.17}$$

where the sum runs over all cells associated to the jet. E_i, E_T, i, θ_i, η_i and ϕ_i are the energy, transverse energy, polar angle, pseudorapidity and azimuthal angle of cell i, respectively.

The following steps are performed by the $k_\perp$ algorithm during the jet finding:

1. The algorithm starts with a list of CAL cells (called "particles") and an empty list of jets.

2. For each particle i as well as for each pair of particles (i, j) distances d_i and d_{ij} are calculated, where

$$d_i = E_{T,i}^2 R_0^2 \text{ and } d_{ij} = \min(E_{T,i}^2, E_{T,j}^2), \text{ with } R_{ij}^2 = \Delta\eta_{ij}^2 + \Delta\phi_{ij}^2. \tag{6.18}$$

   The free parameter R_0 is set to $R_0 = 1.0$.

3. The smallest value of d_i and d_{ij} for all i and j is labelled d_{min}.

4. If d_{min} belongs to the set of d_{ij}, the particles i and j are merged into a new particle using the recombination prescription in Eq. (6.17) and removed from the list of particles.

5. If d_{min} belongs to the set of d_i, the particle i is removed from the list of particles and added to the list of jets.

6. When no particles are left (i.e. all particles are included in jets) the procedure is finished.

Jets taken into account in this analysis were restricted to the pseudorapidity range $-1 < \eta_{\text{jet}} < 2.5$ and were required to have a transverse energy $E_T^{\text{jet}} > 5\,\text{GeV}$.

6.2.8 Jet-energy correction

The jet energies were corrected for detector effects, based on a sample of generated charged current DIS MC events. For this sample the jet finding was performed both on the reconstructed CAL cells and on the hadronic final state as obtained from the MC. A correction factor was obtained for each jet of this test sample from the difference between the resulting jet transverse energy from the MC and the matching reconstructed jet. A parametrisation of these correction factors as a function of the pseudorapidity η_{jet} and transverse energy E_T^{jet} of the jet was used to correct the jet energies for all data and MC samples. The remaining deviation of the reconstructed jet energies from the MC jet energies was below 2% [89,90]. The effect of the jet-energy correction can be seen in Fig. 6.1, where the jet-energy resolution, $(E_b - E_{\text{jet}})/E_b$, is shown for the single-top signal MC before and after the jet-energy correction. E_b is the true energy of the b-quark from the top decay, as obtained from the MC, and E_{jet} is the energy of the reconstructed jet, that points into the direction of the b-quark. Before applying the jet-energy correction, a systematic shift of the reconstructed jet-energies is observed, corresponding to an underestimation of the b-quark energy by 10% on average due to the energy loss in inactive material. After the correction, the mean value of the reconstructed jet energy matches with the generated b-quark energy within 2%. The tails on the left hand side of the distributions are caused by final-state gluon radiation, leading to additional energy in the jet, that is not included in the true b-quark energy. The tails on the right hand side of the distributions are caused by leptonic b-decays, where the neutrino and/or muon leads to missing energy in the reconstructed jet.

6.2.9 Jet estimators

Additional jet-estimators were calculated, in order to distinguish quark- or gluon-induced jets from electrons that are misidentified as jets or from hadronically decaying tau leptons:

- *Jet radius.* $R_{90\%}$ is the radius of the (η, ϕ)-cone centered around the jet axis, that contains 90% of the jet energy ($R = \sqrt{\Delta\eta^2 + \Delta\phi^2}$). The jet radius is used to distinguish hadronic showers, which usually have a broad energy distribution in the CAL, from lepton-induced fake jets with a narrow energy cluster produced from an electromagnetic shower. For this analysis, jets were required to have $R_{90\%} > 0.1$.

- *Electromagnetic fraction.* $emfrac = E_{EMC}^{\text{jet}}/E_{\text{tot}}^{\text{jet}}$ is the fraction of energy in the jet, which is contained in EMC cells. Electrons usually loose most of their energy in EMC cells. For this analysis, jets were required to have $emfrac < 0.90$.

- *Leading track fraction.* $ltf = \frac{E_{lt}}{E_{\text{jet}}}$ is the leading track fraction, i.e. the energy of the most energetic track belonging to the jet divided by the jet energy. Tracks within a cone around the jet axis of radius one in the η-ϕ plane are considered.

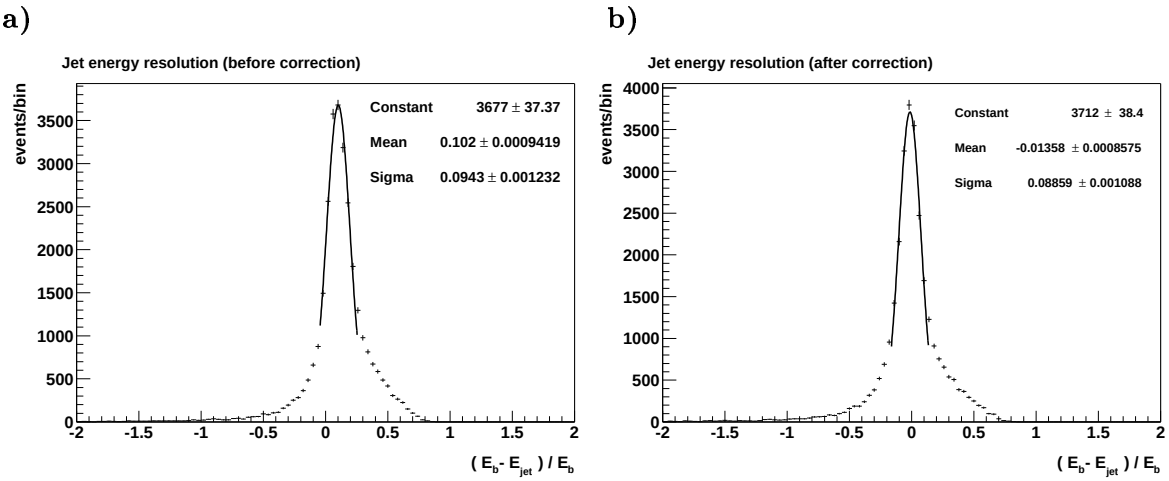

Figure 6.1: Jet-energy resolution for events from the signal MC, a) before and b) after applying the jet-energy correction described in the text. The distribution of the quantity $(E_b - E_{\rm jet})/E_b$ is shown, where E_b and $E_{\rm jet}$ are the true b-quark energy and the reconstructed jet energy, respectively. A match between the direction of the reconstructed jet and the true b-quark direction from the MC was required. A gaussian fit in a small range around the maximum of the distributions and the corresponding fit parameters are also shown.

For fake jets from electrons with well reconstructed tracks, ltf is expected to be close to one. For jets originating from hadronic tau lepton decays on the other hand, a significant fraction of the jet energy can be due to neutral particles and therefore the expected value of ltf is smaller than one. A cut on the sum of ltf and $emfrac$ was used to reject those electrons from the preselection of isolated tau leptons, that were not recognized by the electron finder.

- *Tau finding observables.* In the search for isolated tau leptons a tau finder was used that is based on further jet-shape observables, which are introduced in section 9.1.3.

6.2.10 Additional event variables

- *Acoplanarity.* The event acoplanarity was defined as the azimuthal separation of the electron with the highest value of the transverse momentum from the hadronic system (see Fig. 6.2):

$$\phi_{\rm acopl}^{\rm event} = \pi - |\phi_{\rm elmax} - \phi_{\rm hadr}|, \tag{6.19}$$

where $\phi_{\rm elmax}$ is the azimuth of the electron with the highest value of the transverse momentum and $\phi_{\rm hadr}$ is the azimuth of the hadronic momentum. For electrons without associated CTD track, the azimuthal angle was obtained from the energy depositions in the cluster of CAL cells belonging to the electron. The acoplanarity

in NC DIS events is usually small, i.e. electron and hadronic system are back-to-back in the azimuthal plane. For electron-type events, the acoplanarity between the isolated electron and the hadronic system is defined accordingly:

$$\phi^{\rm el}_{\rm acopl} = \pi - |\phi_{\rm el} - \phi_{\rm hadr}|, \tag{6.20}$$

where $\phi_{\rm el}$ is the azimuth of the isolated electron. For most events $\phi^{\rm event}_{\rm acopl}$ and $\phi^{\rm el}_{\rm acopl}$ are identical. For events with more than one electron however,$\phi^{\rm el}_{\rm acopl}$ can be different from $\phi^{\rm event}_{\rm acopl}$, as it was observed for events from the signal MC in some cases where the scattered electron was detected in addition to the electron from the W decay.

For muon-type events, the acoplanarity between the isolated muon and the hadronic system is defined accordingly:

$$\phi^{\mu}_{\rm acopl} = \pi - |\phi_m u - \phi_{\rm hadr}|, \tag{6.21}$$

where ϕ_μ is the azimuth of the isolated muon. The acoplanarity for isolated tracks that are neither identified as electron nor muon, is defined in an analogous way:

$$\phi^{\rm trk}_{\rm acopl} = \pi - |\phi_{\rm trk} - \phi_{\rm hadr}|, \tag{6.22}$$

where $\phi_{\rm trk}$ is the azimuth angle of the isolated track.

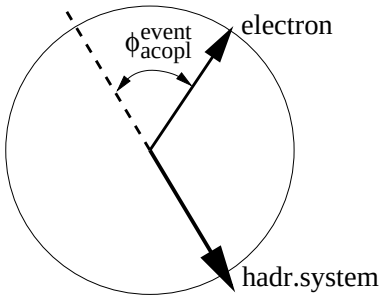

Figure 6.2: Illustration of the event acoplanarity, $\phi^{\rm event}_{\rm acopl}$, which is obtained as the angular separation in the x-y plane between the electron and the vector balancing the hadronic system.

- *Track-track and track-jet distance.* The distance of a track from other tracks in the detector was evaluated with the relativistic invariant track variable $D_{\rm trk}$, which is defined as:

$$D_{\rm trk} = \sqrt{(\Delta\eta_{\rm trk})^2 + (\Delta\phi_{\rm trk})^2}, \tag{6.23}$$

where $\Delta\eta_{\rm trk}$ and $\Delta\phi_{\rm trk}$ are the distance to the closest remaining track in the event. Only tracks, which were fitted to the primary vertex and had $p_T^{\rm trk} > 100\,{\rm MeV}$, were taken into account. Events can have only one well-reconstructed track. In such cases the track isolation was guaranteed by setting $D_{\rm trk}$ to 5.0.

The distance of a track from the closest jet in the detector was defined similarly as:

$$D_{\text{jet}} = \sqrt{(\Delta\eta_{\text{jet}})^2 + (\Delta\phi_{\text{jet}})^2}, \tag{6.24}$$

where $\Delta\eta_{\text{jet}}$ and $\Delta\phi_{\text{jet}}$ are the distance to the closest jet in the event. Single charged hadrons might induce a jet, as is the case for hadronic tau lepton decays. Isolated tracks from such hadrons were included in the search: a jet consisting of not more than one track was not taken into account for the calculation of D_{jet}, if its distance in the η-ϕ plane to the track was below 0.1.

- *Transverse mass.* The transverse mass was defined as

$$M_T^{l\nu} = \sqrt{2p_T^l p_T^{\text{miss}}(1 - \cos(\delta\phi_l^{\text{miss}}))}, \tag{6.25}$$

where p_T^l is the transverse momentum of the lepton and $\delta\phi_l^{\text{miss}}$ is the opening angle in the azimuthal plane between the missing momentum and the lepton. For events from leptonic W decays, where the missing transverse momentum is caused by the neutrino, the distribution of the transverse mass is expected to peak at the mass of the W boson.

- *Reconstructed mass of the lepton-neutrino-b-quark system.* For signal events from a top-quark decay it is expected that the invariant mass reconstructed from the decay products, $M_{l-\nu-hadr}$, has a value close to the top mass. In the following it is assumed that the top quark was produced without sizeable transverse momentum and that the missing transverse momentum originates from a single neutrino. For the lepton and b-quark four vector, the 4-vector of the candidate lepton and of the hadronic system were used, respectively. Two further constraints can be exploited to obtain the complete 4-vector of the neutrino:

  - $E - p_z$ *constraint.* In events, where the scattered beam electron is detected, one can obtain the energy and the longitudinal momentum of the neutrino from the kinematical constraint that the total value of $E - p_z$ corresponds to two times the electron beam energy:

$$(E - p_z)_\nu = 55\,\text{GeV} - (E - p_z)_{\text{visible}}. \tag{6.26}$$

  - $W-$*mass constraint.* In events, where the scattered electron is not reliably detected, one can obtain the lepton-neutrino-b-quark mass from the additional constraint, that the invariant mass of the lepton-neutrino-system, $m_{l\nu}$, corresponds to the mass of the W boson, M_W:

$$M_{l\nu} = \sqrt{(E_l + E_\nu)^2 - (\vec{p}_l + \vec{p}\nu)^2} = M_W. \tag{6.27}$$

    This equation yields two possible solution for $(E - p_z)_\nu$ and thus also for $M_{l-\nu-hadr}$. All solutions that did not meet all of the following conditions

were rejected for this analysis as unphysical:

$$M_{l-\nu-\mathrm{hadr}} < \sqrt{s}, \tag{6.28}$$
$$0 < (E - p_z)_\nu < 55\,\mathrm{GeV}, \tag{6.29}$$
$$(E - p_z)_\nu + (E - p_z)_{\mathrm{visible}} < 75\,\mathrm{GeV}, \tag{6.30}$$
$$E_\nu + E_{\mathrm{hadr}} + E_l < 1000\,\mathrm{GeV}, \tag{6.31}$$

where E_ν, E_{hadr} and E_l correspond to the energy of the reconstructed neutrino, the hadronic system and the lepton candidate, respectively.

In this analysis only the $W-$mass constraint method was used.

Chapter 7

Search for isolated electrons and muons

This chapter describes the search for events with isolated leptons and large missing transverse momentum in the electron and muon channel and the following selection of single-top production candidate events.

The event selection was split into three stages. Electron and muon candidate events were treated separately at each of the three selection stages.

- *Control selection.* Events with large missing transverse momentum and isolated electrons or muons were selected in order to compare data and SM background expectation for a larger event sample.
- *Preselection.* In the preselection the cut on the missing transverse momentum was tightened and an additional cut on the event topology was applied to further reject badly reconstructed NC DIS events. Also at this stage kinematical distributions of the selected data events were compared to the expectations from SM processes.
- *Final top selection.* A final selection for top quark decay candidates was applied, which required large hadronic activity in the CAL.

The selection cuts described in the following sections were appplied to both data and simulated Monte Carlo events, unless otherwise noted.

7.1 Control selection

- *DST bit selection*
  Only those events entered the analysis, which had the charged current trigger bit DST B34 set. DST B34 selects events with large missing transverse momentum, as measured in the CAL cells that are not part of the first inner ring of the FCAL:

$$p_T^{\mathrm{ex1IR}} > 7\,\mathrm{GeV}.$$

The efficiency of this trigger bit for the electron and muon decay channels as measured for the signal MC was 98.5%. The preselection of data events from the 1994 running period required in addition the trigger bit DST B10. DST B10 selects events with a reconstructed vertex. The exact definition of the trigger bits B10 and B45 is given in appendix A.2.

- *Event vertex*
  In order to reduce background from non-ep interactions, the event vertex along the beam direction was required to be close to the nominal interaction vertex:

$$|z_{vtx}| < 50\,\text{cm}.$$

- *Calorimeter timing*
  The timing information from the CAL was used to reject events from proton-beam-gas interactions, which take place upstream the detector. t_f, t_b, t_r, t_u, t_d denote the averaged time in ns for CAL cells in the FCAL, BCAL, RCAL, upper CAL half, lower CAL half, respectively. All cells are calibrated such that the timing for relativistic particles originating from the nominal interaction point is close to 0 ns. Table 7.1 gives the cut values for the timing, together with the minimum energy requirements in the different parts of the CAL. For energies below the threshold, the corresponding timing cuts were not applied. The timing cuts were applied only to data events.

Timing Cut	Minimal energy
$\lvert t_f \rvert < 5\,\text{ns}$	$E_{\text{FCAL}} > 4\,\text{GeV}$
$\lvert t_b \rvert < 5\,\text{ns}$	$E_{\text{BCAL}} > 4\,\text{GeV}$
$\lvert t_r \rvert < 5\,\text{ns}$	$E_{\text{RCAL}} > 4\,\text{GeV}$
$\lvert t_f - t_r \rvert < 6\,\text{ns}$	$E_{\text{tot}} > 5\,\text{GeV}$
$\lvert t_u - t_d \rvert < 6\,\text{ns}$	$E_{\text{tot}} > 5\,\text{GeV}$

Table 7.1: Timing cuts and minimal energy requirements for the different parts of the CAL.

- *Missing transverse momentum*
  Signal events would contain at least one neutrino in the final state, leading to a significant missing transverse momentum in the detector. Therefore a cut on the detected missing transverse momentum in the CAL was applied:

$$p_T^{\text{CAL}} > 15\,\text{GeV}.$$

- *Jets*
  Signal events would contain at least one high-energy jet from the b-quark decay. Events are therefore required to contain at least one well-reconstructed jet:

$$-1 < \eta_{\text{jet}} < 2.5.$$

- *Beam gas rejection*
  Background from proton-beam-gas interactions is reduced with the following cuts:
  - $p_t^{\mathrm{ex1IR}} > 9\,\mathrm{GeV}$
    Proton-beam-gas interactions typically lead to a significant energy deposition only in the inner rings of the FCAL.
  - Track quality
    Events are required to have
    $n_{\mathrm{trk}}^{\mathrm{good}} > 0.2 \cdot n_{\mathrm{trk}} - 20$,
    where n_{trk} is the total number of tracks and $n_{\mathrm{trk}}^{\mathrm{good}}$ is the number of good tracks, i.e. tracks which are fitted to the primary vertex and have $p_T^{\mathrm{trk}} > 200\,\mathrm{MeV}$. This cut reduces background events from proton-beam-gas interactions, since they typically have a large number of low-energy tracks, not originating from a single vertex inside the detector [91].

- *Cosmic rejection*
  High-energy muons from interactions of cosmic rays in the atmosphere usually traverse the detector on a straight line. Events were therefore discarded, if they had only two tracks fitted to the primary interaction vertex with $p_T^{\mathrm{trk}} > 200\,\mathrm{MeV}$, and if those tracks had a 3-dimensional opening angle of more than 178^o. There were three remaining cosmic muon events, that survived also all of the following selection cuts. They were removed from the data sample by a visual scan.

- *CAL holes rejection*
  CAL cells are read out via two independent photomultipliers. The energy deposited in a CAL cell can only be measured, if at least one of the photomultipliers is read out. Otherwise the cell is considered a "dead" cell. Energy deposition in such a cell leads to apparent missing transverse momentum, also in case of events, which are balanced in the transverse plane. Events were discarded, in which a track with $p_T > 3\,\mathrm{GeV}$ pointed into a dead CAL cell ($\delta_{\mathrm{trk,cell}} < 0.1\,\mathrm{rad}$, where $\delta_{\mathrm{trk,cell}}$ is the 3-dimensional opening angle between the track and the cell vector of any dead cell). This cut was applied to data events only. The mean number of dead cells per run varied over the data taking periods (Fig. 7.1). The number of dead cells never exceeded 20 cells and was 1.8 on average. Figure 7.2 shows the distribution of dead cells in both the x-y plane and the z-r plane. The effect of this cut on the data selection efficiency was neglected.

- *Track isolation*
  Signal events contain electrons or muons which have a large transverse momentum and are isolated in the detector. In order to select such events, a search for isolated tracks was performed. The tracks were required to have a transverse momentum of $p_T^{\mathrm{trk}} > 5\,\mathrm{GeV}$, to traverse at least 3 radial superlayers of the CTD (corresponding to $\theta_{\mathrm{trk}} \gtrsim 17^o$ in the forward direction) and to have $\theta_{\mathrm{trk}} < 115^o$. The latter requirement reduces background from NC DIS events with the scattered electron pointing in the backward direction.

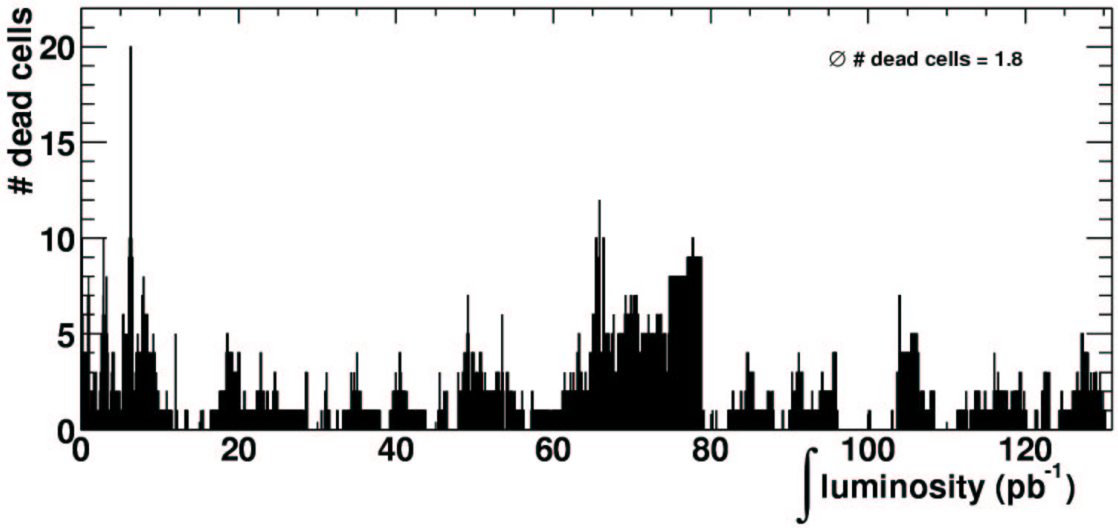

Figure 7.1: Number of CAL cells, for which the readout was not functioning. Events that had high-energy tracks pointing into such cells were rejected.

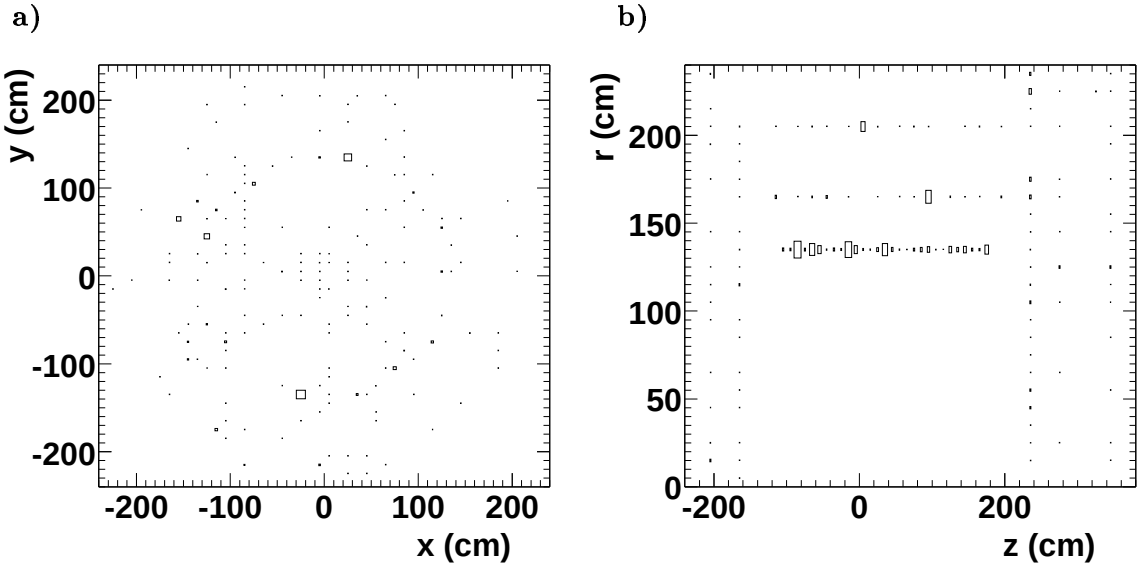

Figure 7.2: a) Position of the CAL cells in the x-y-plane and b) in the z-r-plane, for which the readout was not functioning. The size of the boxes is proportional to the number of such cells, integrated over the data taking periods from 1994-2000.

The isolation of the high-p_T track with respect to other tracks and jets in the event was evaluated with the relativistic invariant isolation variables $D_{\rm trk}$ and $D_{\rm jet}$:

$D_{\rm trk} > 0.5$ and $D_{\rm jet} > 1.0$.

- *Lepton Identification*
  The isolated high-p_T track was finally required to be identified as either electron or muon by the corresponding lepton finder.

7.1.1 Electron candidates (control selection)

Figures 7.3 and 7.4 show the distributions of kinematic variables for the control selection of electron events. The background estimation consists of the simulated events described in section 4.3.1. For the background from NC DIS events, the two different QCD-radiation models CDM and MEPS were used and compared side by side in the figures. At this stage of the selection, the background expectation is dominated by badly reconstructed NC DIS events. 155 events were observed in the data from 1994-2000 and 173$\pm$3.9 events are expected from SM processes, including the NC DIS events from ARIADNE CDM. 132$\pm$2.9 events are expected from SM processes, including the NC DIS events from LEPTO MEPS. The expectation from single W-boson production is 4.1$\pm$0.05 events. Good agreement between data and SM background can be observed in the figures. For both, data and MC simulation, the distribution of the reconstructed z-position of the event vertex (Fig. 7.3a) is peaked at the nominal interaction point ($z = 0$) and shows a similar exponential fall towards the outside of the interaction region. Also the distribution of the transverse momentum of the electron, as measured in the CAL, is well reproduced by the MC simulations (Fig. 7.3b). The distribution of $E-p_Z$ (Fig. 7.3c) shows a peak at around 55 GeV, as expected for NC DIS events. The data events at very large values of $E - p_Z > 60\,\text{GeV}$ are characterized by fluctuations towards large values of the energy measurement in the BCAL or RCAL, leading to unphysical values of $E - p_Z$. These fluctuations are not well reproduced by the MC simulation of the detector. The distribution of the missing transverse momentum in the CAL, $p_T^{\rm CAL}$, falls off steeply, starting from the cut value at 15 GeV, as expected for NC DIS events, where the apparent missing transverse momentum is caused mainly by mismeasurements (Fig. 7.3d). The MC simulation reproduces well the shape of the data distribution in this extreme region of the phase space. The acoplanarity (Fig. 7.4a) is peaked at low values, which is expected for NC DIS events, where the electron and the hadronic system are observed in a back-to-back topology. Good agreement in the shape of both data and MC distribution can be observed. For the transverse mass, $M_T^{l\nu}$, as reconstructed from the electron and the missing transverse momentum (Fig. 7.4b), a peak around the W mass is expected for the production of single W bosons (hatched histogram) and for the signal from single-top production (dashed line). For the data and the simulation of all SM processes, on the other hand, a peak at lower values is observed. The data events at very low transverse mass correspond to NC DIS events where a fluctuation in the energy measurement of either the electron or

the hadronic system leads to missing transverse momentum pointing in the direction of the electron candidate, such that the reconstructed transverse mass becomes small. The rate for such mismeasurements is not well reproduced by the detector simulation, as can be observed from the underestimation of the corresponding range in the histogram. The transverse momentum of the hadronic system, p_T^{hadr}, is shown in Fig.7.4c). For the signal from single-top production the distribution is peaked at large values, as expected from the decay of the heavy top quark, while for the background from NC DIS events low hadronic transverse momentum is expected most of the time, as also observed in the data. The slight excess of data events at large values of $p_T^{\mathrm{hadr}} > 40\,\mathrm{GeV}$ is caused again by fluctuations of the CAL energy measurement, which are not entirely reproduced by the MC simulation.

Table 7.2 summarises the event yields, background expectation and signal efficiencies for the control selection of electron events. Here and in the following, the quoted efficiencies for the single-top signal include the branching ratio of the W boson to the corresponding channel ($BR(W \to e\nu) = BR(W \to \mu\nu) = BR(W \to \tau\nu) = 10.7\%$). The signal efficiency, ϵ, is defined in the canonical way as:

$$\epsilon \equiv \frac{\text{number of events after selection cuts}}{\text{total number of events}}. \tag{7.1}$$

All quoted efficiencies include the branching ratio of the top decay in the corresponding channel. The SM expectation includes simulated events from all background sources discussed in 4.3.1. The quoted uncertainties for the background estimation and the signal efficiency include only the statistical uncertainties. A discussion of the statistical and systematic uncertainties is given in section 7.4. The event yields and the background expectations for the individual sources of simulated SM background processes are shown in Fig. 7.5a) for the control selection of electron events.

Control selection electron candidates							
coll.	$\sqrt{s}$	$\mathcal{L}_{\mathrm{int}}$	Obs.	Exp. (CDM)	Exp. (MEPS)	W only	sig. eff. (%)
e^+p	300 GeV	$47.9\,\mathrm{pb}^{-1}$	41	60.2 ± 2.45	48.6 ± 2.09	1.3 ± 0.02	6.74 ± 0.12
e^-p	318 GeV	$16.7\,\mathrm{pb}^{-1}$	36	25.2 ± 1.35	17.9 ± 0.54	0.6 ± 0.02	6.85 ± 0.12
e^+p	318 GeV	$65.5\,\mathrm{pb}^{-1}$	73	87.4 ± 2.74	65.2 ± 1.92	2.2 ± 0.04	6.76 ± 0.12
Total		$130.1\,\mathrm{pb}^{-1}$	155	172.8 ± 3.92	131.7 ± 2.89	4.1 ± 0.05	6.76 ± 0.12

Table 7.2: Number of observed events and expectation from SM background for the control selection of electron candidate events in different data taking periods. The SM expectation is given including MC simulations for NC DIS both with CDM and MEPS. The expectation only from single W production and the efficiency for the single top signal MC is also shown. The quoted uncertainties are the statisticial uncertainties due to the limited number of generated MC events.

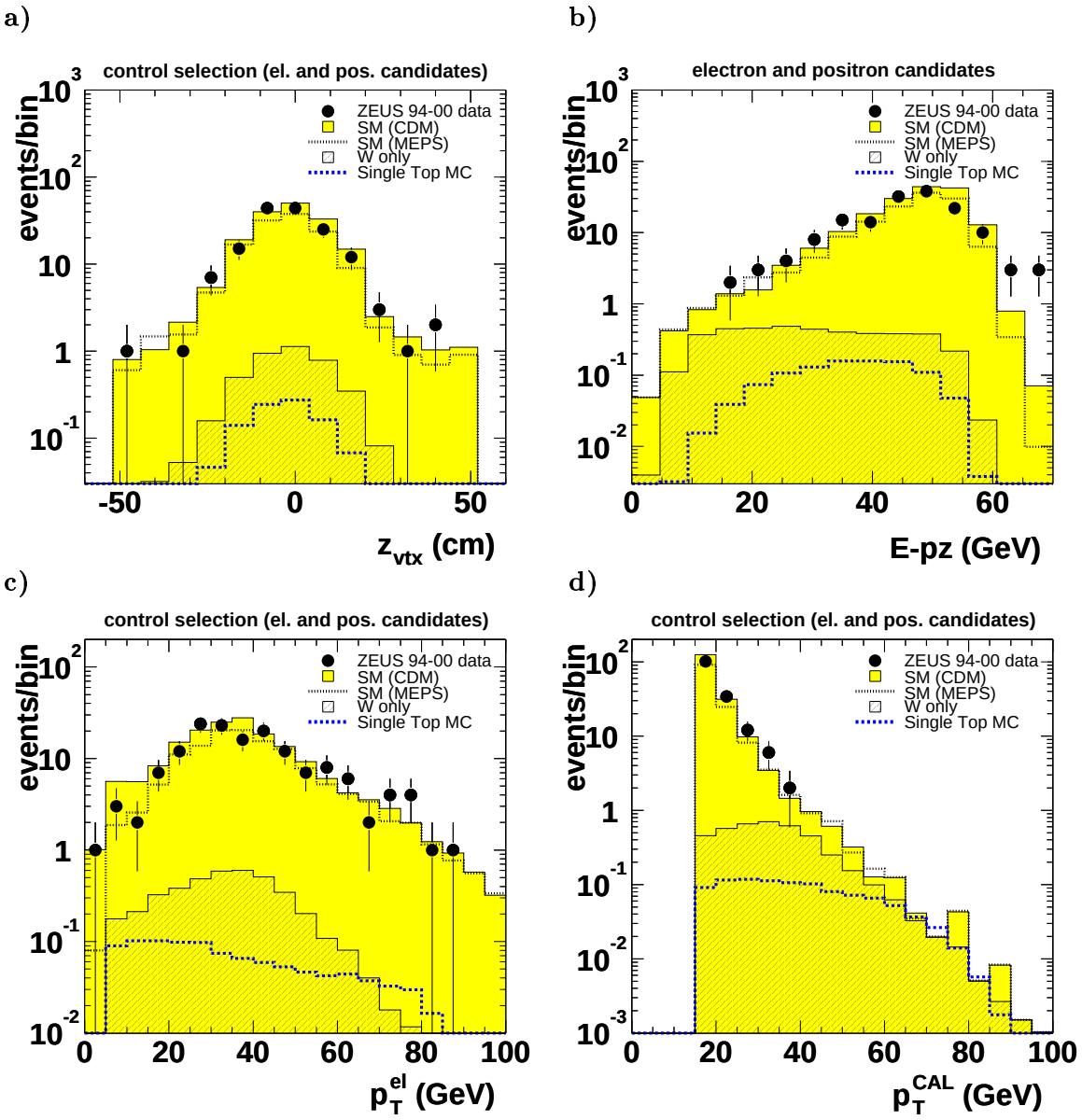

Figure 7.3: a) z-position of the event vertex, z_{vtx}, b) $E-p_z$, c) transverse momentum of the electron as measured in the CAL, p_T^{el}, d) missing transverse momentum in the CAL, p_T^{CAL}, for events with isolated electrons or positrons, after the control selection cuts described in the text. The data points are compared to the expectation from simulated SM processes (solid histograms: all SM processes, simulation of NC DIS with ARIADNE CDM; dotted lines: all SM processes, simulation of NC DIS with LEPTO MEPS; hatched histograms: expectation from single W-boson production) and to a hypothetical single top signal (dashed lines). The single top signal was normalised to an integral of one event.

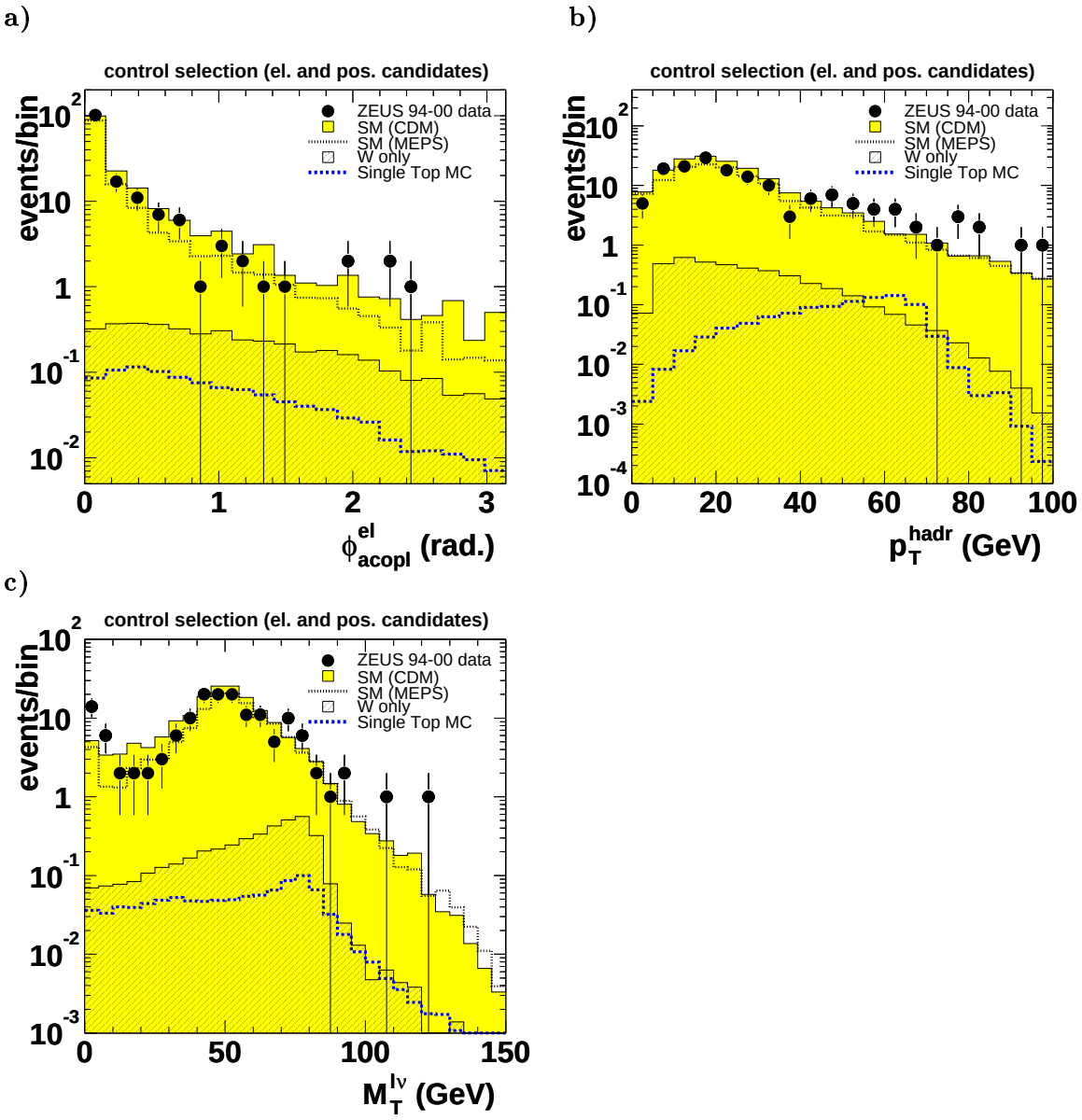

Figure 7.4: a) acoplanarity angle, $\phi^{\rm el}_{\rm acopl}$, b) hadronic transverse momentum, $p_T^{\rm hadr}$, c) transverse mass of the lepton-neutrino system $M_T^{l\nu}$ for events with isolated electrons or positrons, after the control selection cuts described in the text. The data points are compared to the expectation from simulated SM processes (solid histograms: all SM processes, simulation of NC DIS with ARIADNE CDM; dotted lines: all SM processes, simulation of NC DIS with LEPTO MEPS; hatched histograms: expectation from single W-boson production) and to a hypothetical single top signal (dashed lines). The single top signal was normalised to an integral of one event.

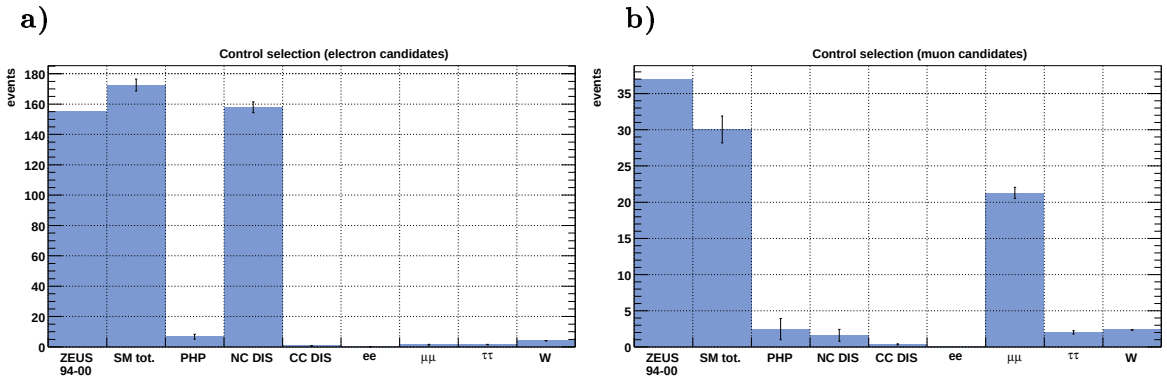

Figure 7.5: Event yields for the control selection of a) electron candidate events and b) muon candidate events in the data from 1994-2000 and for the different sources of simulated SM background. Only ARIADNE CDM is shown for NC DIS. The event yields for the SM background are scaled to the data luminosity. The error bars indicate the statistical uncertainties on the SM background expectations.

7.1.2 Muon candidates (control selection)

Figures 7.6 and 7.7 show the distributions of kinematic variables for the control selection of muon events. Also here good agreement between data and SM background is observed in most cases. The background estimation consists of the simulated events described in section 4.3.1. The background contribution from NC DIS events is very small and is shown in the plots for ARIADNE CDM. At this stage of the selection, the background expectation is dominated by Bethe-Heitler di-muon production. 37 events were observed in the data and 30.0 ± 1.9 events are expected from SM processes. The expectation from single W-boson production is 2.4 ± 0.04 events.

The distribution of the reconstructed z-position of the event vertex (Fig. 7.6a) is in reasonable agreement with the expectation, taking into account the small number of observed and expected events in the muon channel already at this selection stage. Also the distribution of the transverse momentum of the muon candidate, p_T^μ, as measured in the CTD (Fig. 7.6b), is reasonably well reproduced by the MC simulations. Most of the data and of the simulated di-muon events are found at low values, whereas the distributions for muons from single W production and from single-top decays are shifted towards larger values. The overflow bin contains a muon at very high measured transverse momentum, $p_T^\mu > 700\,\text{GeV}$, which was traversing five radial superlayers of the CTD. The error on the transverse momentum measurement for such tracks is above 100%. Also the MC simulation contains events with tracks at very large measured transverse momentum. The distribution of $E - p_Z$ (Fig. 7.6c) peaks at low values for both, data and SM MC simulation. This is expected for di-muon events, where the muons release only a small fraction of their energy in the CAL. For the signal MC on the other hand, the $E - p_Z$ distribution contains more events at larger values, as

expected from the decay products of the b-quark. A visual scan of the data events at low values of $E - p_Z$ revealed a contamination of beam-gas overlay events, which were not included in the MC simulation and thus are responsible for the observed excess both in the total rate and at low $E - p_Z$. Figure 7.6d) shows the missing transverse momentum, as obtained from the sum of the CAL transverse momentum and the transverse momentum of all identified muons in each event. As expected for di-muon events, the missing transverse momentum is small, while for single W production and the single-top signal real missing transverse momentum is produced by the neutrino in the final state. The distribution of the acoplanarity (Fig. 7.7a) is peaked at low values for both, data and SM background expectation. For the signal MC the b-quark and the decay products of the W boson are expected back-to-back in the transverse plane. Due to the low mass of the W-boson as opposed to the top-quark, the neutrino and the lepton from the W decay are expected to be collimated. Hence a low value of the acoplanarity is observed also for the signal MC in most of the generated events. Figure 7.7b) shows the distribution of the transverse mass, $M_T^{l\nu}$, of the lepton-neutrino system, as obtained from the muon track and the missing transverse momentum in the CAL. As opposed to the corresponding distribution in the electron channel (Fig. 7.4b), the distribution for the single W-production MC and the single-top signal MC show no sharp peak at the W mass anymore. This is caused by the additional missing transverse momentum in the CAL caused by the muon track, which adds to the missing momentum of the neutrino. For the data and the di-muon MC, the apparent missing transverse momentum in the CAL is mostly caused by the detected muon und hence the reconstructed transverse mass is small most of the time. For muon-candidates the hadronic transverse momentum, p_T^{hadr}, (Fig. 7.7c) is identical to the transverse momentum in the CAL, p_T^{CAL}, except for events with additional identified electrons, which were subtracted from p_T^{hadr}. The distribution of p_T^{hadr} thus shows a lower cutoff at the cut value of $p_T^{\mathrm{CAL}} > 15\,\mathrm{GeV}$. As expected for di-muon events, where the missing transverse momentum in the CAL is caused by mismeasurements, most of the data and SM MC events are found at low values of p_T^{hadr}. For the signal from single-top production on the other hand, p_T^{hadr} is produced by the b-decay, which follows the decay of the heavy top quark, leading to large values for p_T^{hadr} on average.

Table 7.3 summarises the event yields, background expectation and signal efficiencies for the control selection of muon events. The corresponding event yields and background expectations for the individual sources of simulated SM background processes are shown in Fig. 7.5b).

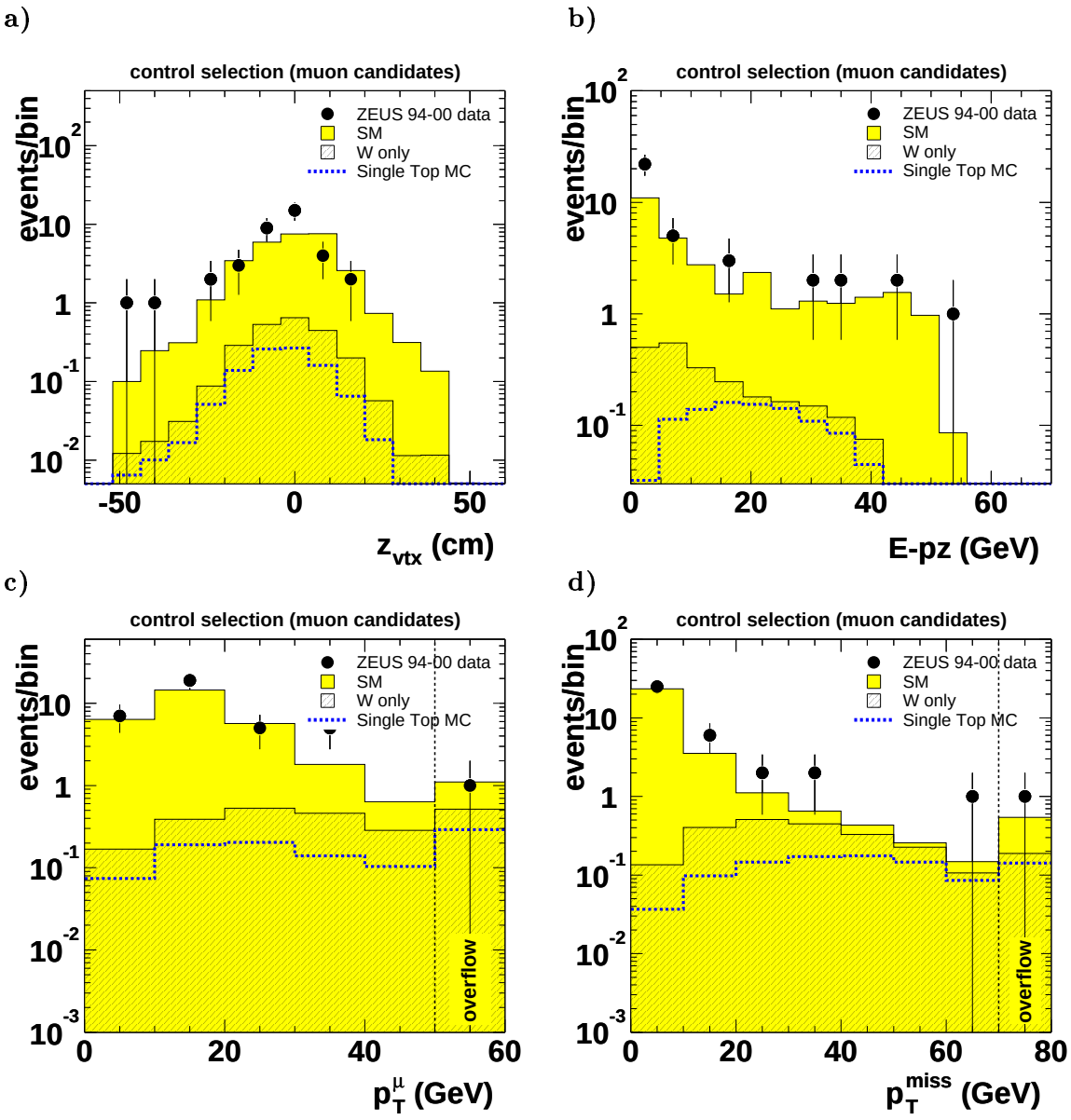

Figure 7.6: a) z-position of the event vertex, z_{vtx}, b) $E-p_z$, c) transverse momentum of the muon as measured in the CTD, p_T^{μ}, d) missing transverse momentum, p_T^{miss}, for events with muons, after the control selection cuts described in the text. The data points are compared to the expectation from simulated SM processes (solid histograms) and to a hypothetical single top signal (dashed lines). The single top signal was normalised to an integral of one event.

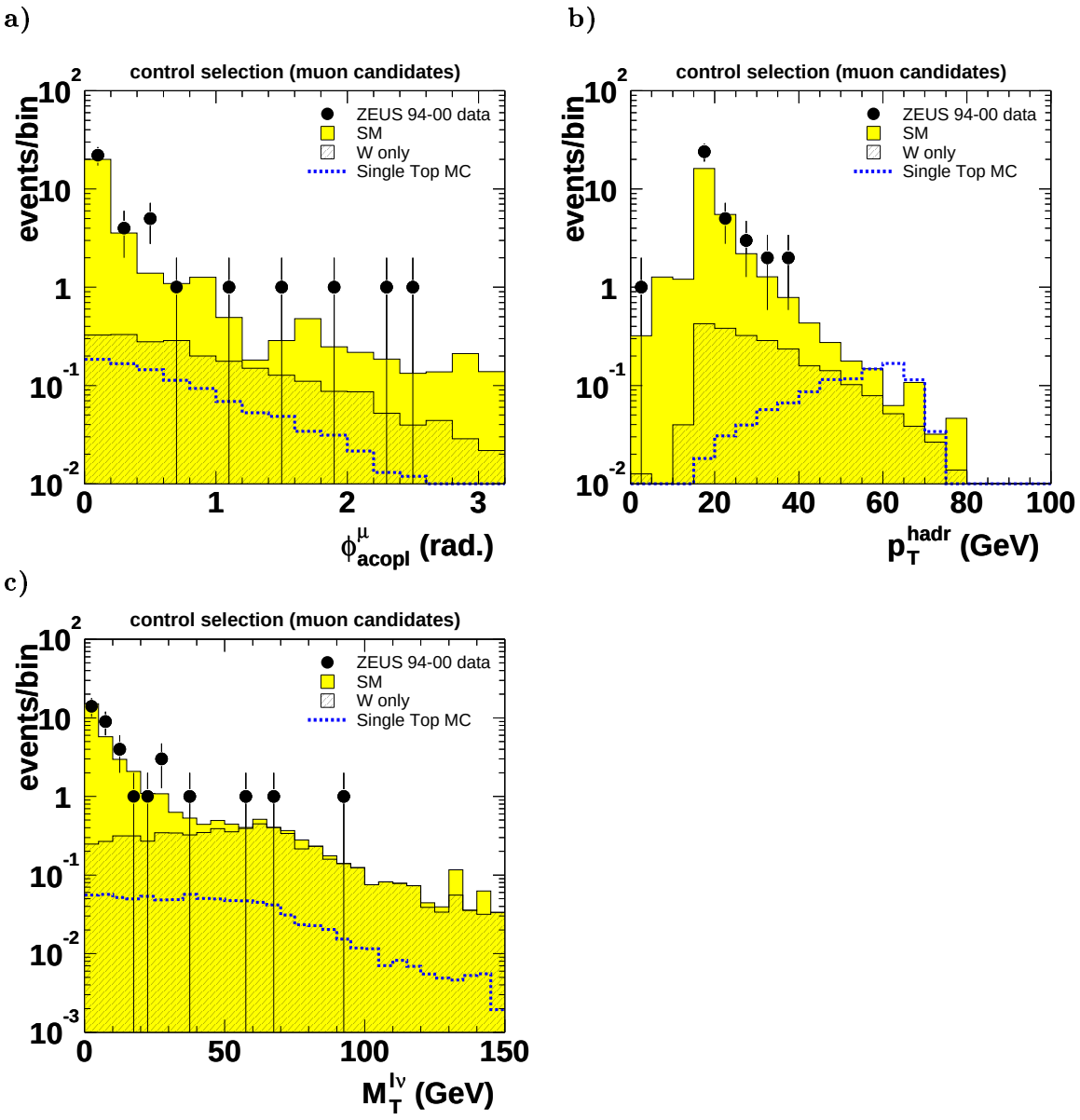

Figure 7.7: a) acoplanarity angle, $\phi^{\rm mu}_{\rm acopl}$, b) hadronic transverse momentum, $p_T^{\rm hadr}$, c) transverse mass of the lepton-neutrino system $M_T^{l\nu}$ for events with isolated muons, after the control selection cuts described in the text. The data points are compared to the expectation from simulated SM processes (solid histograms) and to a hypothetical single top signal (dashed lines). The single top signal was normalised to an integral of one event.

Control selection muon candidates						
coll.	$\sqrt{s}$	$\mathcal{L}_{\text{int}}$	Obs.	SM exp.	W only	signal eff. (%)
e^+p	300 GeV	$47.9\,\text{pb}^{-1}$	11	9.6 ± 0.50	0.8 ± 0.02	4.54 ± 0.10
e^-p	318 GeV	$16.7\,\text{pb}^{-1}$	5	4.0 ± 0.26	0.3 ± 0.02	4.66 ± 0.10
e^+p	318 GeV	$65.5\,\text{pb}^{-1}$	21	16.5 ± 1.77	1.3 ± 0.03	4.51 ± 0.10
Total		$130.1\,\text{pb}^{-1}$	37	30.0 ± 1.86	2.4 ± 0.04	4.54 ± 0.10

Table 7.3: Number of observed events and expectation from SM background for the control selection of muon candidate events in different data taking periods. The expectation only from single W production and the efficiency for the single top signal MC is also shown. The quoted uncertainties are the statisticial uncertainties due to the limited number of generated MC events.

7.2 Preselection of isolated lepton events

In addition to the control selection cuts described above, the following restrictions were applied:

- $p_T^{\text{CAL}} > 20\,\text{GeV}$

  In order to further reduce background from badly reconstructed NC DIS events in the electron channel and from Bethe-Heitler di-muon events, the cut on p_T^{CAL} was tightened from 15 GeV in the control selection to 20 GeV in the preselection of isolated lepton events.

- $\phi_{\text{acopl}}^{\text{event}} > 0.14\,\text{rad}$

  NC DIS events can have significant missing momentum in cases, where the hadronic system is not well measured. Most of these events still have an NC DIS topology, i.e. the hadronic system and the electron are back to back in the azimuthal plane. Therefore a cut is applied on the acoplanarity between the electron with the largest transverse momentum in the event and the hadronic system. This cut was also applied for muon-type events, in case of an additional electron in the event.

7.2.1 Track selection

Figure 7.8 shows the distribution of the selected events in the D_{jet}-D_{trk} plane, with all cuts from the control- and preselection applied, except for the track-isolation and the lepton identification. 53 of those events passed also the isolation cut on $D_{\text{trk}} > 0.5$ and $D_{\text{jet}} > 1.0$. 17 of the isolated tracks were not identified as electron/positron or muon. Instead they were considered as candidates for isolated tau leptons, decaying hadronically with one charged particle associated (cf. chapter 9). The distribution of events expected from all SM processes (Fig. 7.8b) is in good agreement with the

distribution observed in the data, while for events from single W-boson production only (Fig. 7.8c) and from single-top production (Fig. 7.8d), more of the tracks are expected at larger values of $D_{\rm trk}$ and $D_{\rm jet}$.

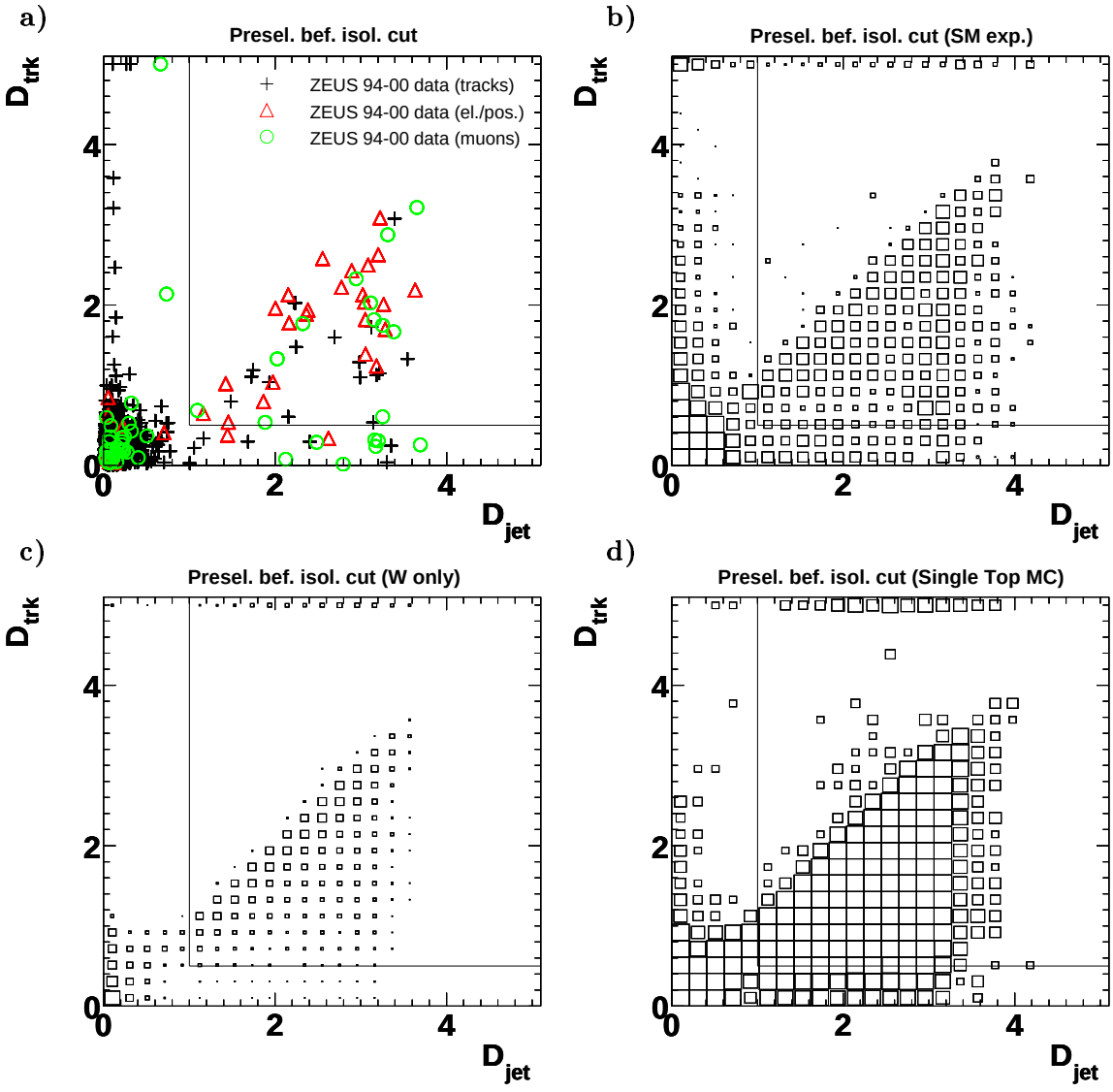

Figure 7.8: Distribution of the selected events in $D_{\rm trk}$ and $D_{\rm jet}$, after applying the preselection cuts described in the text except for the isolation cut on $D_{\rm trk} > 0.5$ and $D_{\rm jet} > 1.0$. For each event the track with the largest value of $\sqrt{D_{\rm trk}^2 + D_{\rm jet}^2}$ is shown. In a) the data is shown, where the crosses represent tracks, that were not identified as electrons or muons. The triangles and circles represent electron and muon tracks, respectively. Further plots show: b) the total SM background expectation, c) the expectation from only single W-boson production and d) the expectation from the arbitrarily normalized signal MC, respectively, for all tracks. The size of the boxes is proportional to the logarithm of the number of expected events.

7.2.2 Electron candidates (preselection)

Figures 7.9 and 7.10 show the distributions of selected event variables for the preselection of isolated electron events. For the background from NC DIS events, the two different QCD-radiation models CDM and MEPS were used and compared side by side in the figures. The agreement between data and SM expectation is still good for this very restrictive event selection. The distributions are similar to the ones from the control selection discussed above. The background expectation is still dominated by badly reconstructed NC DIS events. 24 events were observed in the data from 1994-2000 and 20.6 ± 1.1 events are expected from SM processes, including the NC DIS events from ARIADNE CDM. 16.2 ± 0.9 events are expected from SM processes, including the NC DIS events from LEPTO MEPS. The ARIADNE CDM MC samples show a better agreement with the data for this selection and were therefore chosen as the nominal MC samples in the following. The change in the background expectation by including the MEPS NC DIS samples was treated as a systematic effect (see section 7.4). The expectation from single W-boson production is 3.43 ± 0.04 events.

Figure 7.11 shows the distribution of electron events from the preselection in the $M_T^{l\nu}$-p_T^{hadr} plane. Also in this two-dimensional representation no obvious deviation from the SM prediction was observed at this stage of the event selection. Both data events (Fig. 7.11a) and total SM prediction (Fig. 7.11b) are observed at low values of the transverse mass, $M_T^{l\nu}$, and of the transverse momentum of the hadronic system, p_T^{hadr}. The expectation from single W production alone (7.11c) however is shifted towards higher values of $M_T^{l\nu} \approx M_W$ and the expectation from the single-top signal (7.11d), is shifted towards higher values of p_T^{hadr}, as expected from the top decay. Figure 7.12 shows the events in the p_T^{miss}-p_T^{el}-plane. Both data (Fig. 7.12a) and total SM expectation (Fig. 7.12b) are clustered at low values of the missing transverse momentum, p_T^{miss}, and at low transverse momentum of the electron candidate, p_T^{el}. The distribution for single W-boson production on the other hand (Fig. 7.12c) shows a wider spread in p_T^{miss} and the expectation from the single-top signal MC (Fig. 7.12d) extends even further to very large values of p_T^{miss} and of p_T^{el}.

Table 7.4 summarises the event yields, background expectation and signal efficiencies for the preselection of electron events. The SM expectation includes simulated events from all background sources discussed in section 4.3.1. The quoted uncertainties for the background estimation and the signal efficiency include only the statistical uncertainties. A discussion of the statistical and systematic uncertainties is given in section 7.4. The event yields and the background expectations for the individual sources of simulated SM background processes are shown in Fig. 7.13a) for the preselection of electron events.

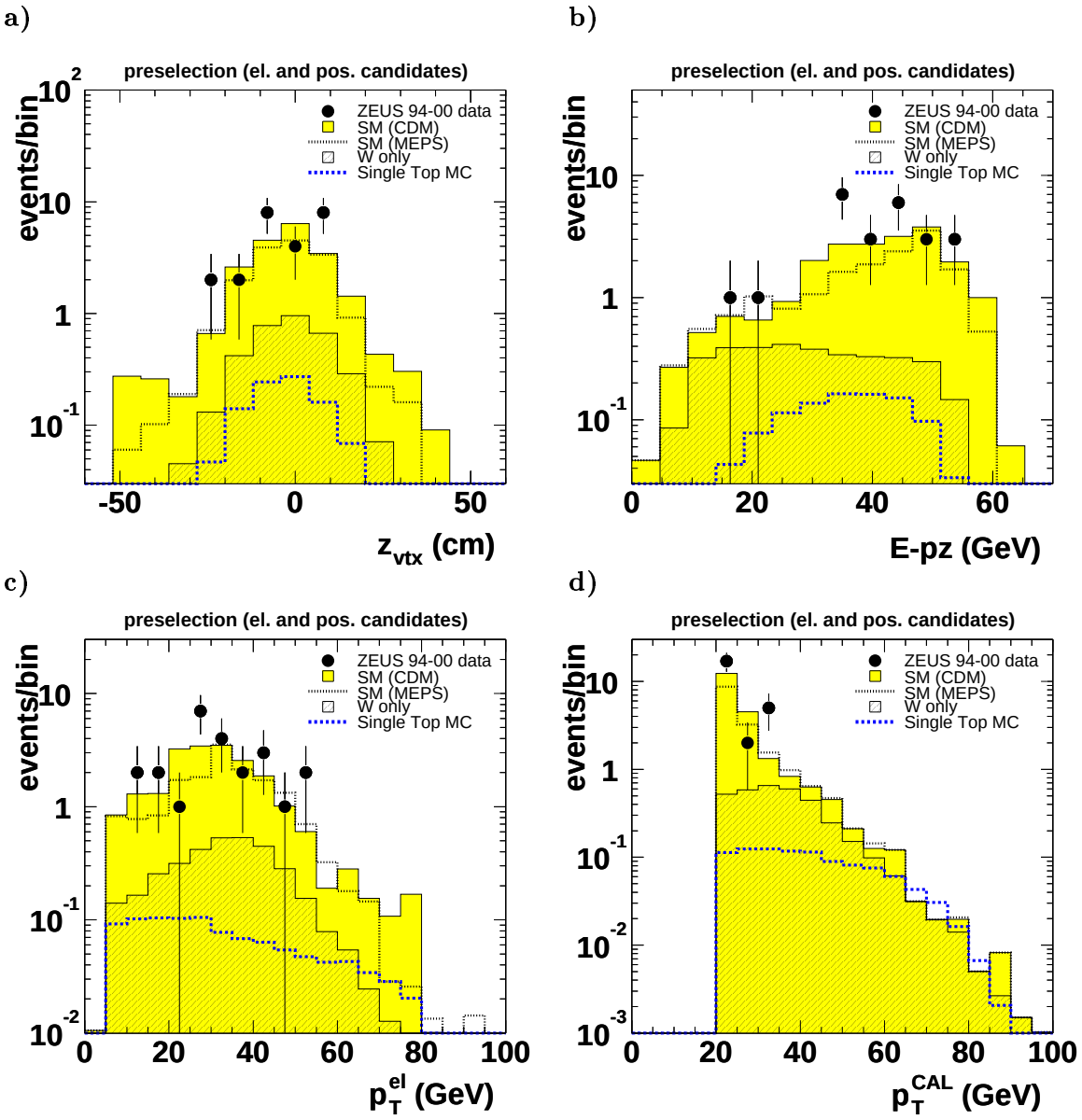

Figure 7.9: a) z-position of the event vertex, z_{vtx}, b) $E-p_z$, c) transverse momentum of the electron as measured in the CAL, p_T^{el}, d) missing transverse momentum in the CAL, p_T^{CAL}, for events with isolated electrons or positrons, after the preselection cuts described in the text. The data points are compared to the expectation from simulated SM processes (solid histograms: all SM processes, simulation of NC DIS with ARIADNE CDM; dotted lines: all SM processes, simulation of NC DIS with LEPTO MEPS; hatched histograms: expectation from single W-boson production) and to a hypothetical single top signal (dashed lines). The single top signal was normalised to an integral of one event.

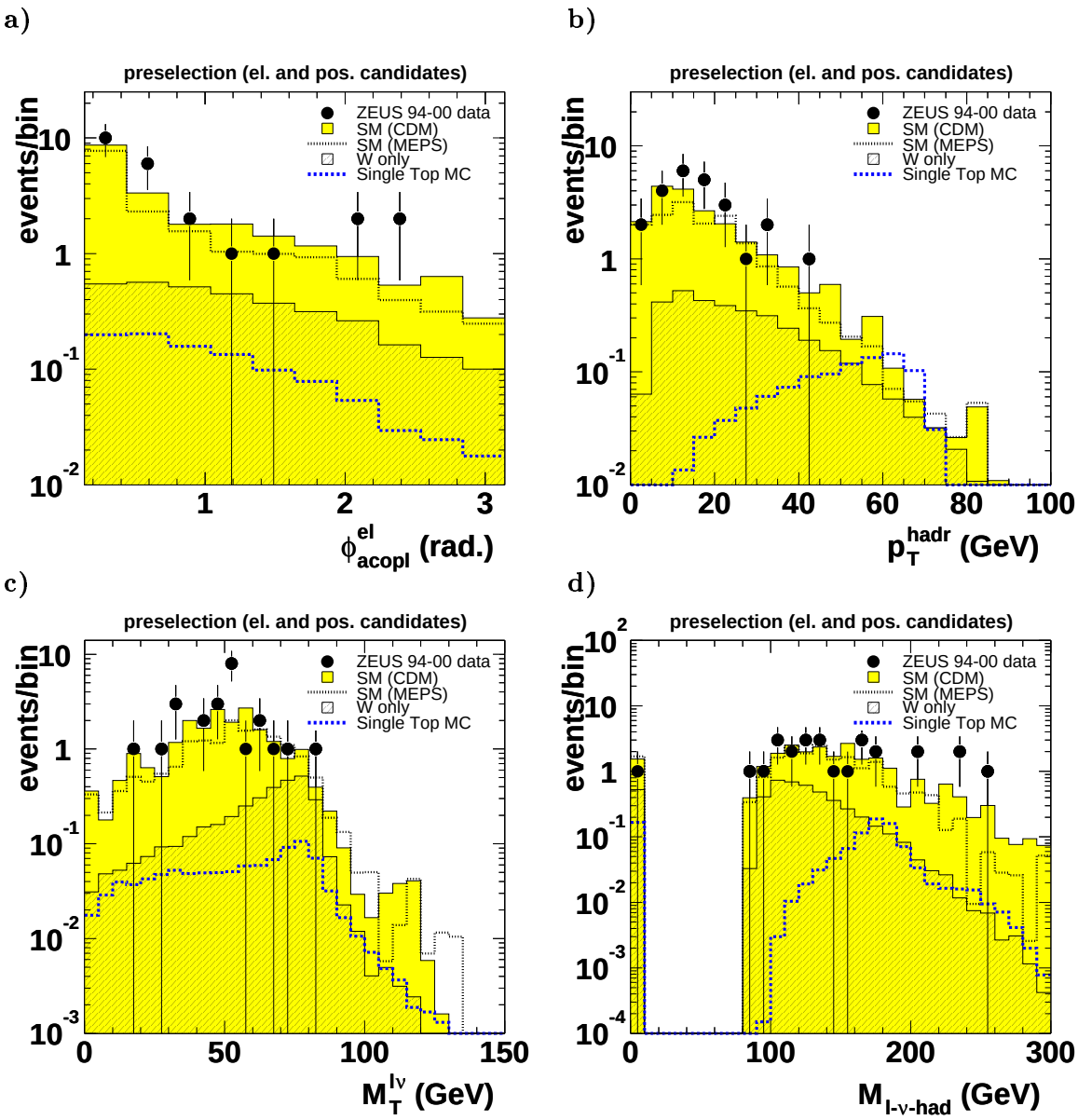

Figure 7.10: a) acoplanarity angle, $\phi^{\rm el}_{\rm acopl}$, b) hadronic transverse momentum, $p_T^{\rm hadr}$, c) transverse mass of the lepton-neutrino system, $M_T^{l\nu}$, d) reconstructed mass of the lepton-neutrino-hadron system, $M_{l-\nu-{\rm had}}$, for events with isolated electrons or positrons, after the preselection cuts described in the text. The data points are compared to the expectation from simulated SM processes (solid histograms: all SM processes, simulation of NC DIS with ARIADNE CDM; dotted lines: all SM processes, simulation of NC DIS with LEPTO MEPS; hatched histograms: expectation from single W-boson production) and to a hypothetical single top signal (dashed lines). The single top signal was normalised to an integral of one event. In d) up to two mass solutions per event might appear.

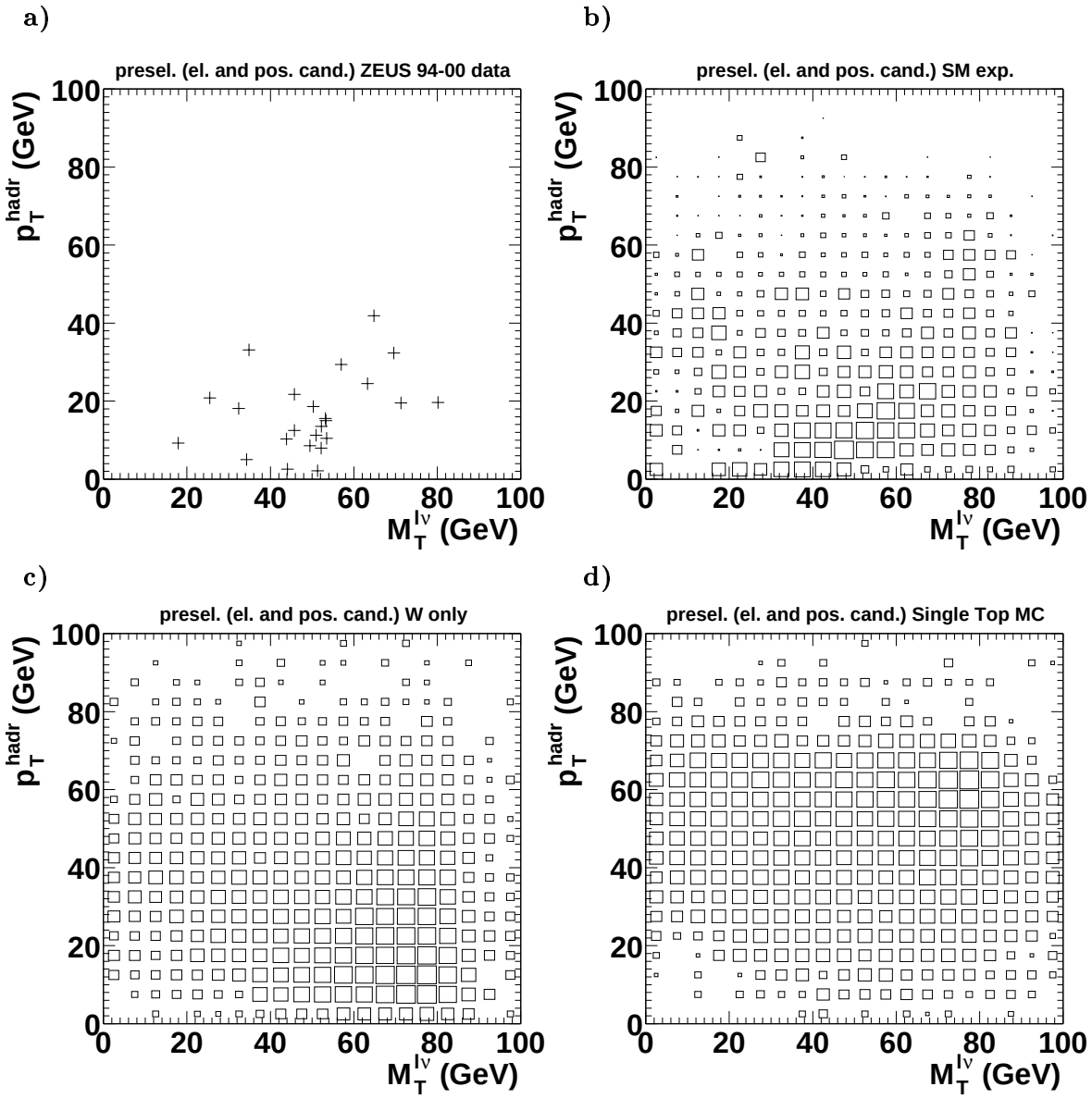

Figure 7.11: Distribution of the selected electron candidate events in the hadronic transverse momentum, $p_T^{\rm hadr}$, and the transverse mass of the lepton-neutrino system, $M_T^{l\nu}$, after applying the preselection cuts described in the text. The plots a), b), c) and d) show the data, the total SM background expectation, the expectation from only single W-boson production and the expectation from the arbitrarily normalized signal MC, respectively. The size of the boxes is proportional to the logarithm of the number of expected events.

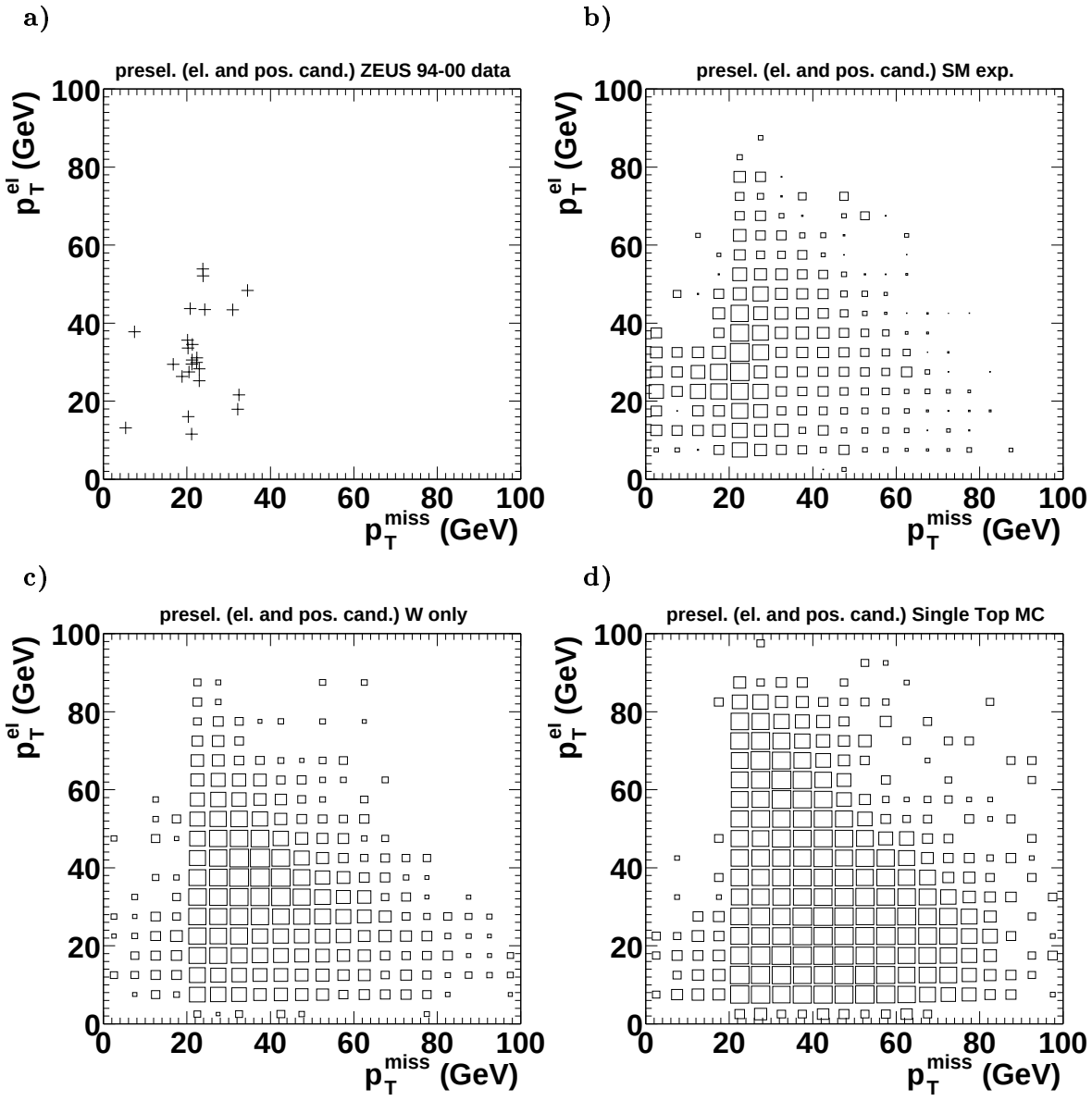

Figure 7.12: Distribution of the selected electron candidate events in the transverse momentum of the electron, p_T^{el}, and the missing transverse momentum, p_T^{miss}, after applying the preselection cuts described in the text. The plots a), b), c) and d) show the data, the total SM background expectation, the expectation from only single W-boson production and the expectation from the arbitrarily normalized signal MC, respectively. The size of the boxes is proportional to the logarithm of the number of expected events.

Preselection electron candidates							
coll.	$\sqrt{s}$	$\mathcal{L}_{\text{int}}$	Obs.	Exp. (CDM)	Exp. (MEPS)	W only	sig. eff. (%)
e^+p	300 GeV	$47.9\,\text{pb}^{-1}$	4	7.3 ± 0.73	5.4 ± 0.57	1.1 ± 0.02	5.73 ± 0.11
e^-p	318 GeV	$16.7\,\text{pb}^{-1}$	7	3.2 ± 0.40	2.4 ± 0.20	0.5 ± 0.02	5.79 ± 0.11
e^+p	318 GeV	$65.5\,\text{pb}^{-1}$	13	10.1 ± 0.75	8.4 ± 0.66	1.9 ± 0.03	5.77 ± 0.11
Total		$130.1\,\text{pb}^{-1}$	24	20.6 ± 1.12	16.2 ± 0.893	3.4 ± 0.04	5.76 ± 0.11

Table 7.4: Number of observed events and expectation from SM background for the preselection of electron candidate events in different data taking periods. The SM expectation is given including MC simulations for NC DIS both with CDM and MEPS. The expectation only from single W production and the efficiency for the single top signal MC is also shown. The quoted uncertainties are the statisticial uncertainties due to the limited number of generated MC events.

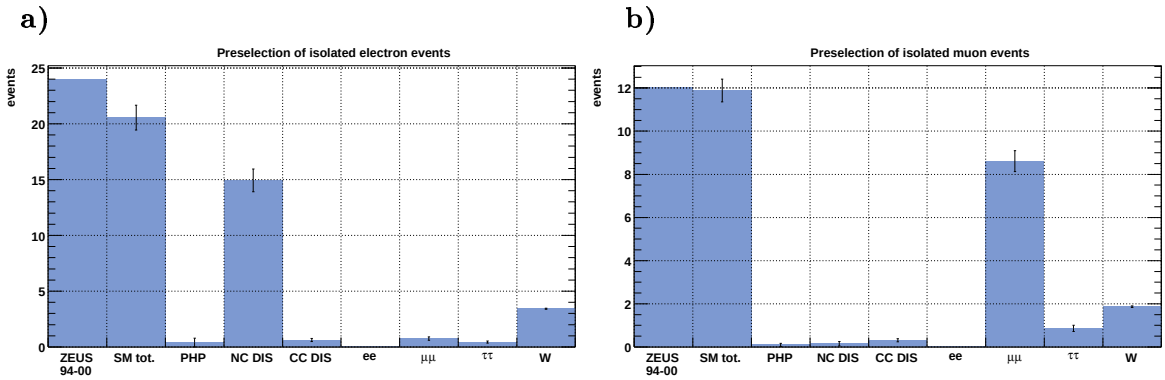

Figure 7.13: Event yields for the preselection of a) isolated electrons and b) isolated muons in the data from 1994-2000 and for the different sources of simulated SM background. Only ARIADNE CDM is shown for NC DIS. The event yields for the SM background are scaled to the data luminosity. The error bars indicate the statistical uncertainties on the SM background expectations.

7.2.3 Muon candidates (preselection)

Figures 7.14 and 7.15 show the distributions of kinematic variables for the preselection of isolated muon events. The background estimation consists of the simulated events described in section 4.3.1. Only ARIADNE CDM was used for the simulation of NC DIS events. The background expectation is still dominated by Bethe-Heitler di-muon production. 12 events are observed in the data and 11.9 ± 0.5 events are expected from SM processes. The expectation from single W-boson production is 1.87 ± 0.03 events. The agreement between data and SM expectation is still good also for the muon preselection and the distributions are similar to the ones from the muon control selection discussed above. Table 7.5 summarises the event yields, background expectation and signal efficiencies for the preselection of muon events. The corresponding event yields

and background expectations for the individual sources of simulated SM background processes are shown in Fig. 7.13b).

Preselection muon candidates						
coll.	$\sqrt{s}$	$\mathcal{L}_{\text{int}}$	Obs.	SM exp.	W only	signal eff. (%)
e^+p	300 GeV	$47.9\,\text{pb}^{-1}$	0	4.2 ± 0.32	0.6 ± 0.02	4.41 ± 0.10
e^-p	318 GeV	$16.7\,\text{pb}^{-1}$	1	2.1 ± 0.18	0.3 ± 0.01	4.53 ± 0.10
e^+p	318 GeV	$65.5\,\text{pb}^{-1}$	11	5.6 ± 0.38	1.0 ± 0.02	4.38 ± 0.10
Total		$130.1\,\text{pb}^{-1}$	12	11.9 ± 0.53	1.9 ± 0.03	4.41 ± 0.10

Table 7.5: Number of observed events and expectation from SM background for the preselection of muon candidate events in different data taking periods. The expectation only from single W production and the efficiency for the single top signal MC is also shown. The quoted uncertainties are the statisticial uncertainties due to the limited number of generated MC events.

Figure 7.16 shows the distribution of muon events from the preselection in the $M_T^{l\nu}$-p_T^{hadr}-plane. Figure 7.17 shows the events in the p_T^{miss}-p_T^{mu}-plane. One data events sticks out in the distributions, which is found at very large values of $M_T^{l\nu} = 91\,\text{GeV}$, $p_T^{\text{hadr}} = 39.6\,\text{GeV}$ and $p_T^{\text{miss}} = 62\,\text{GeV}$. It is shown in Fig. B.6. The hadronic transverse momentum of this event, $p_T^{\text{hadr}} = 39.6\,\text{GeV}$, is very close to the final selection cut for single-top candidates of 40 GeV, which will be described in the next section. Apart from this event, no obvious deviation from the SM prediction was observed at this stage of the event selection in these two-dimensional distributions for muon candidate events.

Table 7.6 shows selected kinematic variables of all data events from the preselection.

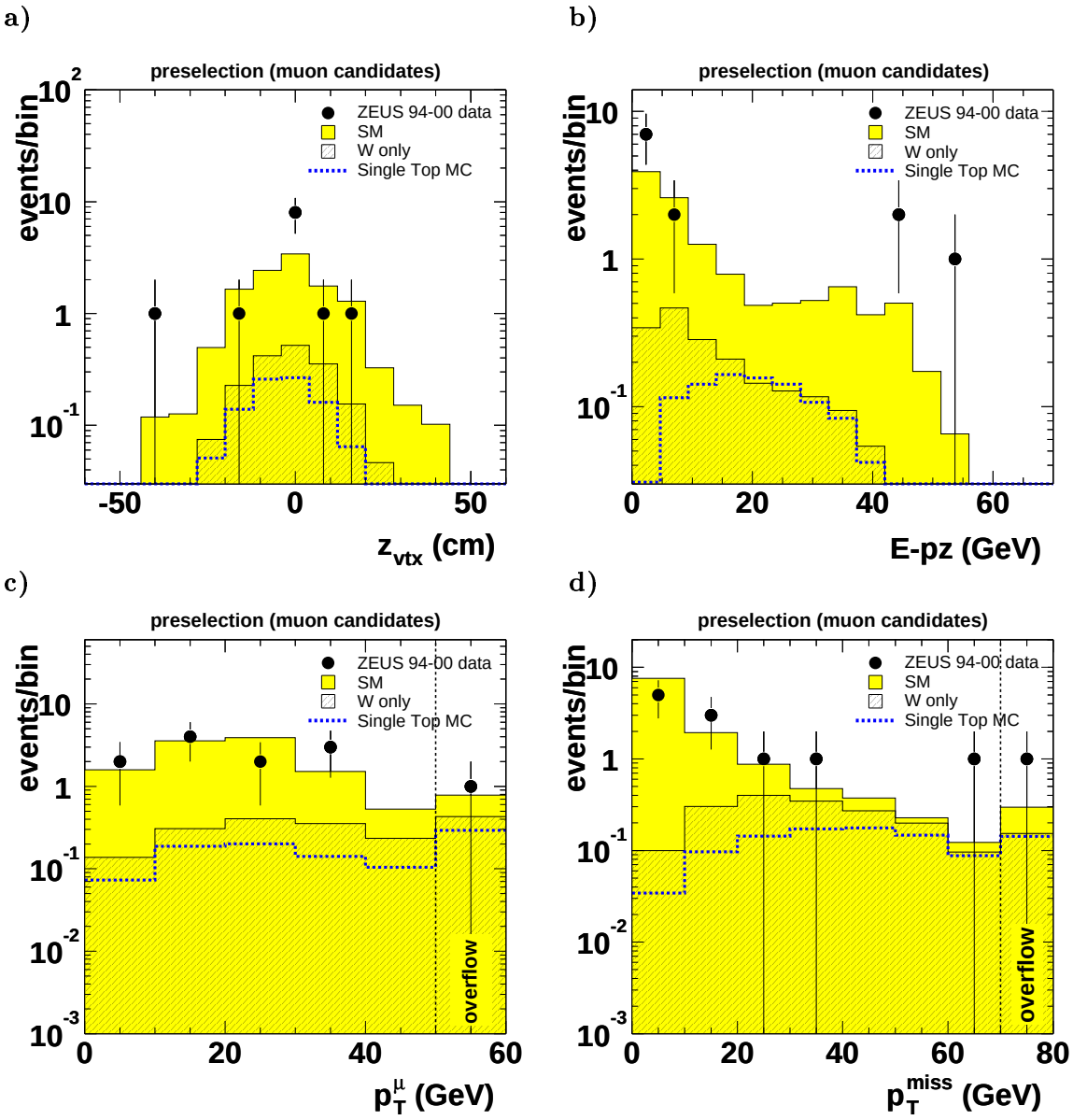

Figure 7.14: a) z-position of the event vertex, z_{vtx}, b) $E - p_z$, c) transverse momentum of the muon as measured in the CTD, p_T^{μ}, d) missing transverse momentum, $p_T^{\rm miss}$, for events with isolated muons, after the preselection cuts described in the text. The data points are compared to the expectation from simulated SM processes (solid histograms) and to a hypothetical single top signal (dashed lines). The single top signal was normalised to an integral of one event. In d) up to two mass solutions per event might appear.

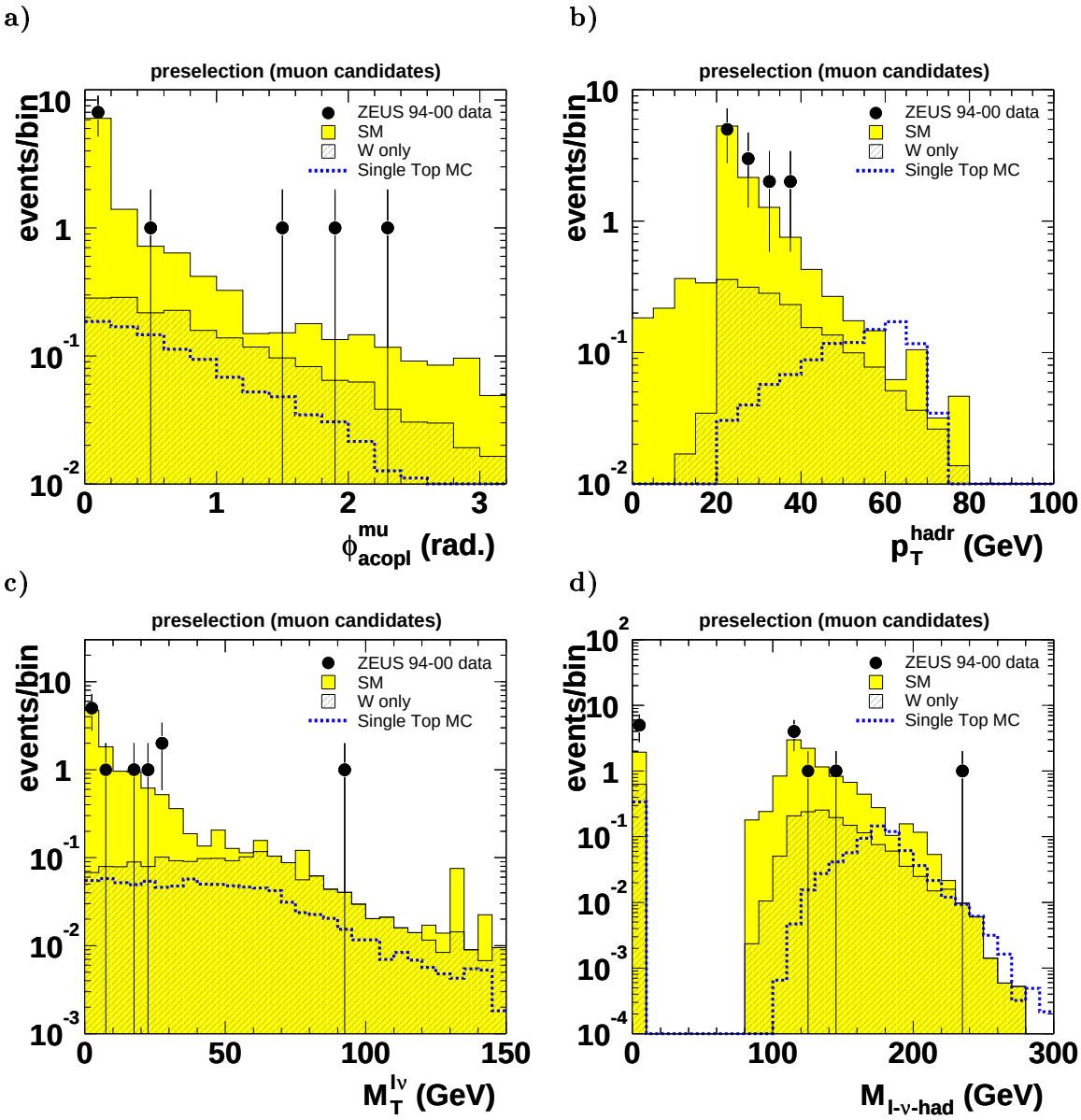

Figure 7.15: a) acoplanarity angle, $\phi^{\mathrm{mu}}_{\mathrm{acopl}}$, b) hadronic transverse momentum, p_T^{hadr}, c) transverse mass of the lepton-neutrino system, $M_T^{l\nu}$, d) reconstructed mass of the lepton-neutrino-hadron system, $M_{l-\nu-\mathrm{had}}$, for events with isolated muons, after the preselection cuts described in the text. The data points are compared to the expectation from simulated SM processes (solid histograms) and to a hypothetical single top signal (dashed lines). The single top signal was normalised to an integral of one event.

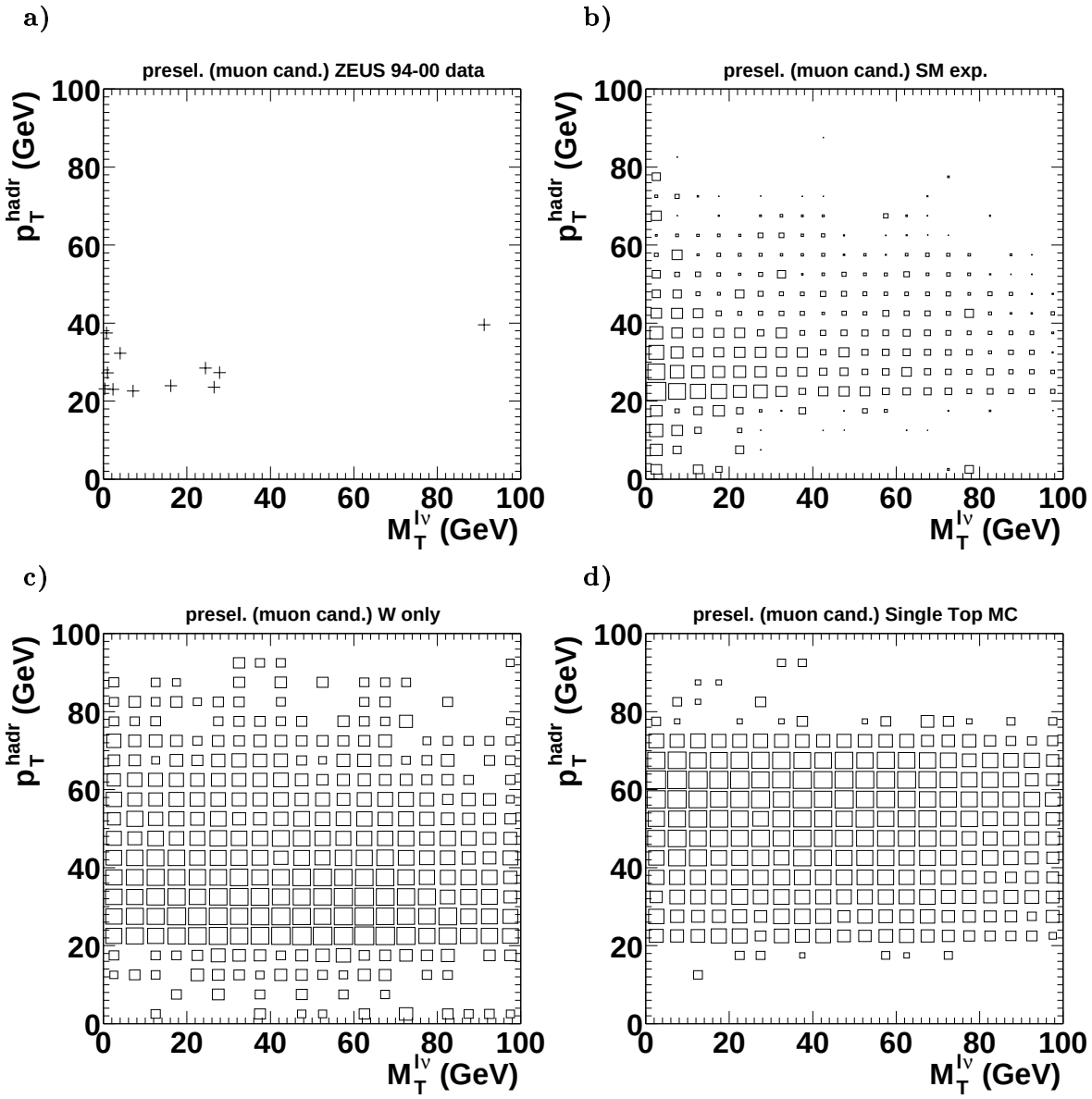

Figure 7.16: Distribution of the selected muon candidate events in the hadronic transverse momentum, $p_T^{\rm hadr}$, and the transverse mass of the lepton-neutrino system, $M_T^{l\nu}$, after applying the preselection cuts described in the text. The plots a), b), c) and d) show the data, the total SM background expectation, the expectation from only single W-boson production and the expectation from the arbitrarily normalized signal MC, respectively. The size of the boxes is proportional to the logarithm of the number of expected events.

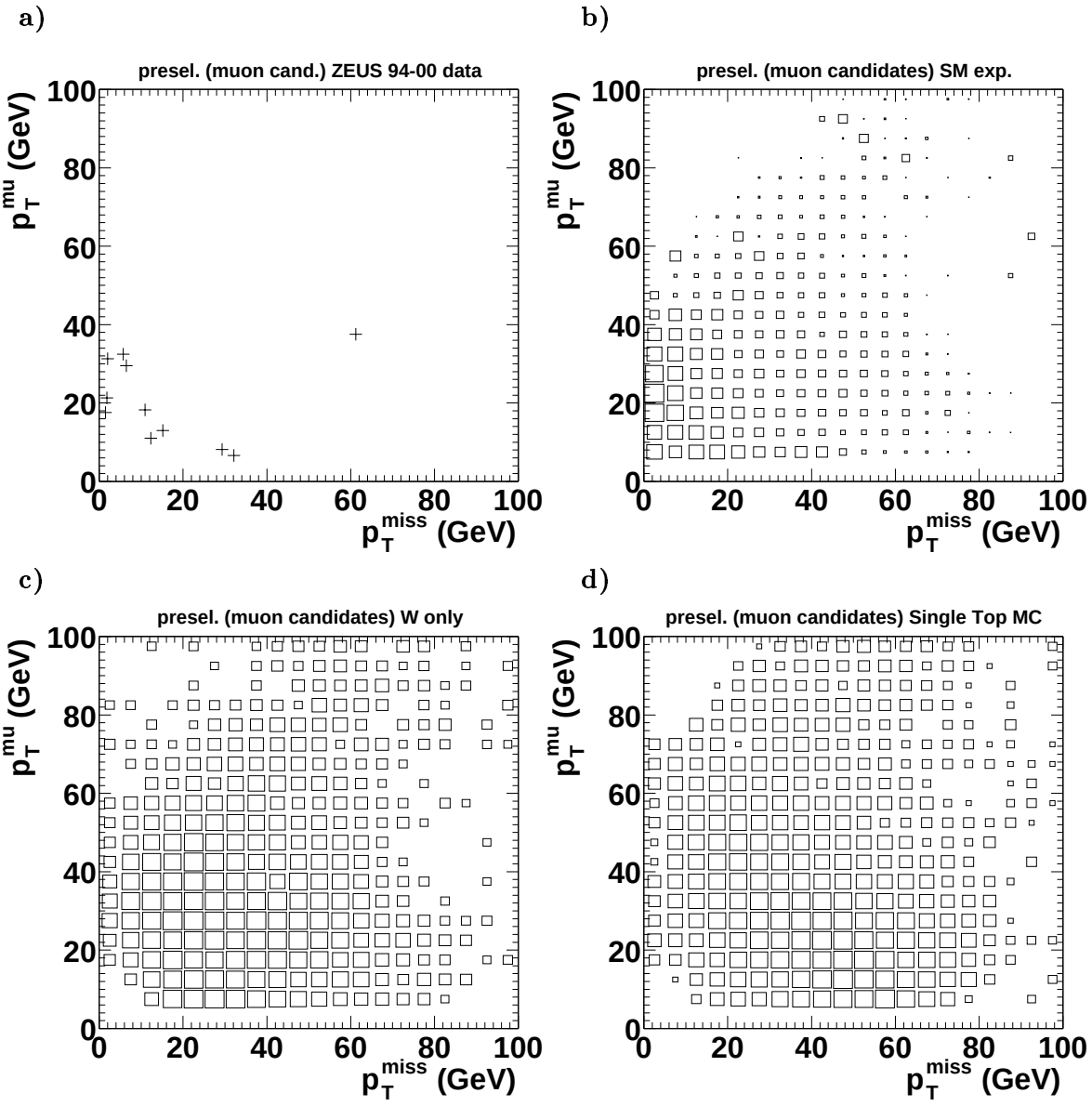

Figure 7.17: Distribution of the selected muon candidate events in the transverse momentum of the muon, p_T^{mu}, and the missing transverse momentum, p_T^{miss}, after applying the preselection cuts described in the text. The plots a), b), c) and d) show the data, the total SM background expectation, the expectation from only single W-boson production and the expectation from the arbitrarily normalized signal MC, respectively. The size of the boxes is proportional to the logarithm of the number of expected events.

#	e/μ	run	event	$p_T^{\rm CAL}$ (GeV)	$p_T^{\rm ex1IR}$ (GeV)	$p_T^{\rm miss}$ (GeV)	$p_T^{\rm hadr}$ (GeV)	$E-p_Z$ (GeV)	$\phi^{lept}_{\rm acopl}$ (rad)	$p_T^{\rm lept}$ (GeV)	$D_{\rm trk}$	$D_{\rm jet}$	$m_T^{l\nu}$ (GeV)
1994-1997, e^+p collisions, $\sqrt{s}=300\,\text{GeV}$, $\mathcal{L}_{\rm int}=47.9\,\text{pb}^{-1}$													
1	e^+	25282	27728	34.8	34.2	34.8	19.5	48.9	0.66	48.3	1.96	2.00	80.7
2	e^+	25394	20609	21.8	20.6	21.8	20.6	39.1	1.43	11.1	0.54	1.46	25.8
3	e^-	26461	3641	26.1	16.7	22.9	2.8	33.6	0.26	28.8	1.39	3.05	51.4
4	e^+	26560	138996	24.1	22.8	24.1	24.7	40.0	0.45	43.9	2.21	2.78	63.3
1998-1999, e^-p collisions, $\sqrt{s}=318\,\text{GeV}$, $\mathcal{L}_{\rm int}=16.7\,\text{pb}^{-1}$													
5	e^-	31052	6398	21.6	12.0	20.2	18.8	15.1	1.31	16.7	1.78	2.16	32.3
6	μ^-	31224	19966	27.4	23.5	32.1	27.4	43.7	2.33	6.4	0.68	1.10	27.0
7	e^-	31924	37714	24.0	28.0	24.0	32.9	55.8	0.32	52.9	2.19	3.64	69.5
8	e^-	31997	11353	21.9	19.4	21.9	11.0	37.1	0.60	30.2	1.02	1.42	51.0
9	e^-	32402	47518	23.0	23.8	23.0	7.1	46.6	0.20	30.0	1.23	3.18	52.5
10	e^-	32410	1937	22.3	23.4	22.3	10.1	45.6	0.29	31.8	1.70	3.29	53.2
11	e^+	32859	53874	22.4	21.4	22.4	33.1	41.1	0.75	25.5	1.04	1.97	34.8
12	e^+	32868	15723	31.0	31.2	31.0	19.4	36.5	0.68	43.2	2.00	3.26	71.5
1999-2000, e^+p collisions, $\sqrt{s}=318\,\text{GeV}$, $\mathcal{L}_{\rm int}=65.5\,\text{pb}^{-1}$													
13	e^-	33368	9275	20.5	18.0	20.5	15.2	46.7	0.15	35.3	1.81	3.06	53.6
14	μ^-	33399	11391	22.8	19.4	1.4	23.5	45.3	0.06	21.5	2.87	3.32	0.7
15	e^+	33468	36077	21.1	22.9	21.1	14.7	49.2	0.32	34.5	2.62	3.20	53.5
16	e^+	33483	15510	20.1	19.0	20.1	18.4	45.5	0.57	33.4	0.79	1.87	50.4
17	μ^-	33719	5856	30.2	26.3	751	30.2	9.0	0.07	780.6	2.33	2.94	1531
18	e^+	34015	14817	20.4	19.4	20.4	13.0	53.0	0.82	27.1	1.88	2.36	45.7
19	μ^+	34266	35962	33.0	24.3	1.4	33.0	3.5	0.02	31.8	1.66	3.39	3.0
20	μ^+	34348	9897	27.8	17.2	15.0	27.8	3.0	0.01	12.8	1.82	3.15	0.2
21	e^+	34460	38098	32.2	25.6	32.2	13.4	35.6	2.34	21.7	0.65	1.17	52.2
22	μ^+	35081	34896	39.6	34.3	61.9	39.6	3.6	1.86	37.7	1.76	2.32	91.3
23	μ^+	35092	49609	28.8	23.6	29.5	28.8	4.4	1.52	8.1	0.53	1.88	24.2
24	e^+	35194	22193	27.8	16.7	18.6	3.0	33.4	1.98	26.4	2.13	3.02	44.3
25	e^+	35365	777	21.1	21.4	21.1	8.6	46.2	0.17	29.7	2.03	3.05	50.0
26	μ^-	35668	4016	23.3	14.2	12.4	23.3	7.1	0.09	11.0	1.33	2.03	2.1
27	μ^-	35699	21924	23.9	17.9	1.4	22.8	52.9	0.10	18.0	0.60	3.26	7.8
28	μ^-	35854	98486	23.7	17.4	11.0	23.7	3.7	0.46	18.1	2.02	3.11	16.7
29	e^+	35899	24168	23.1	24.0	23.1	41.3	54.1	0.43	53.5	1.94	2.38	64.6
30	μ^-	35906	112642	23.5	19.2	6.1	23.5	3.8	0.01	29.6	1.75	3.26	26.8
31	μ^+	36305	29954	37.3	29.2	5.1	37.3	4.5	0.01	32.2	3.21	3.65	0.5
32	e^+	36544	24240	20.2	23.9	20.2	29.9	44.0	0.41	43.7	3.08	3.23	56.5
33	e^+	36688	87264	20.9	15.9	5.7	9.9	20.1	2.26	13.2	2.57	2.55	17.3
34	e^+	36826	112565	20.1	14.5	16.2	11.0	32.7	0.46	29.2	2.42	2.90	43.2
35	e^+	36956	83996	32.1	20.7	7.9	5.7	35.2	0.21	37.6	2.50	3.09	34.5
36	e^+	37511	9392	32.7	32.5	32.7	21.8	42.4	1.97	17.4	2.13	2.15	45.1

Table 7.6: Selected kinematic variables of candidate data events for the preselection of isolated electrons and muons.

7.3 Final selection of top decay candidates

A final set of cuts was applied to select candidate events for the signal process. The main goal of this selection was to reduce the NC DIS background in the electron channel and the di-muon background in the muon channel. On the other hand the cuts had to be chosen such that a high efficiency for single-top production remained.

7.3.1 Optimisation of the final selection cuts

The following variables were considered for the final selection:

- p_T^{CAL}. The missing transverse momentum in the CAL was used already for the preselection ($p_T^{\mathrm{CAL}} > 20\,\mathrm{GeV}$). This cut was considered for the final selection again, since the p_T^{CAL} distribution falls steeply for the background events.
- p_t^{hadr}. Signal events are characterized by a jet with large transverse momentum from the hadronisation of the b quark. None of the considered background processes has a similar signature.
- $E - p_z$ for electron-type events. The $E - p_z$ distribution for NC DIS events peaks at two times the electron beam energy. For signal events, on the other hand, the corresponding distribution is shifted towards lower values, due to the undetected neutrino in the final state.
- p_T^{miss} for muon-type events. Bethe-Heitler di-muon events can have large missing momentum in the CAL, but usually have small missing momentum, when taking into account also the momenta of muons, as measured by the CTD. The missing momentum in signal events is mainly caused by the momentum of the undetected neutrino and therefore p_T^{miss} is expected to be large.
- Number of muons for muon-type events. Most signal events are characterized by one muon in the final state, while in the Bethe-Heitler process two muons are produced. There can be additional muons from the decay of the b-quark for signal events. Only in 2% of the signal events after the selection of isolated muons there are two muons detected. On the other hand, also in two thirds of the Bethe-Heitler di-muon events, after the isolated muon selection, only one of the two Bethe-Heitler muons is detected.

The final values for these variables were chosen using only MC events to optimise the background suppression and signal efficiency at the same time. The method, which was chosen for this, optimises the expected Baysean upper limit on the signal in the presence of background. Assuming that all observed events, N_{obs}, originate from background, N_{obs} is expected to follow a Poisson distribution $P(N_{\mathrm{obs}}, n_b)$, where n_b is the expected number of background events. For a single given value for N_{obs}, the 95% confidence

level (C.L.) upper limit on the signal $N_{95\%}(N_{\rm obs}, N_{bg})$ can be obtained by solving the following equation numerically:

$$0.95 = 1 - \frac{e^{-N_{bg}-N_{95\%}} \sum_{n=0}^{N_{\rm obs}} \frac{(N_{bg}+N_{95\%})^n}{n!}}{e^{-N_{bg}} \sum_{n=0}^{N_{\rm obs}} \frac{{N_{bg}}^n}{n!}}$$

Assuming that all possible values for $N_{\rm obs}$ are a priori equally probable, the expected upper limit value, $< N_{95\%} >$ is given by the sum

$$< N_{95\%}(N_{bg}) >= \sum_{N_{\rm obs}=0}^{\infty} P(N_{\rm obs}, N_{bg}) N_{95\%}(N_{\rm obs}, N_{bg}).$$

For the expectation value of the 95% C.L. upper limit on the cross section for signal production $< \sigma_{95\%} >$ it follows:

$$< \sigma_{95\%} >= \frac{< N_{95\%}(N_{bg}) >}{\epsilon \mathcal{L}_{\rm int}},$$

where ϵ is the selection efficiency for the signal and $\mathcal{L}_{\rm int}$ is the integrated luminosity. The choice of the selection cuts affects both $< N_{95\%}(N_{bg}) >$ and ϵ. An optimised set of cuts is obtained by minimizing $< \sigma_{95\%} >$.

The optimisation is performed by varying each of the final selection cuts within a grid of 10 values, while keeping all other cuts at the optimised values. For each combination of cut values, the efficiency for the signal MC and the number of observed background events is evaluated and $< \sigma_{95\%} >$ is calculated[1]. Electron and muon channel were treated separately. The distribution of $< \sigma_{95\%} >$ for the selected set of variables is shown in Fig. 7.18 for the electron channel and in Fig. 7.19 for the muon channel. These distributions were used as a guideline for chosing the final values of the single top selection cuts. For $p_T^{\rm CAL}$ no significant dependence of the expected upper limit on the final cut value was observed within the statistical uncertainty of the MC expectation (Fig. 7.18a) and 7.19a). Also a rejection of events with more than one muon candidate has no significant impact on the expected upper limit (Fig. 7.19d). A significant dependence of the expected upper limit on the value of the final selection cut was observed for $E - p_z$ (electron channel, Fig. 7.18b), $p_T^{\rm miss}$ (muon channel (Fig. 7.19c) and $p_T^{\rm hadr}$ (both channels, Fig. 7.18b) and 7.19b). The following cut values were chosen for the final selection of single-top candidate events:

- $p_T^{\rm hadr} > 40\,{\rm GeV}$ for the electron and muon channel.
- $E - p_z < 47\,{\rm GeV}$ for the electron channel.
- $p_T^{\rm miss} > 10\,{\rm GeV}$ for the muon channel.

To ensure a disjunctive selection, events were accepted as electron candidates only if they were not at the same time passing all cuts of the final muon selection.

[1]For this optimisation, only the signal sample for the run period 1999-2000 ($\sqrt{s} = 318\,{\rm GeV}$, e^+p) was used and scaled to the total data luminosity of $130\,{\rm pb}^{-1}$.

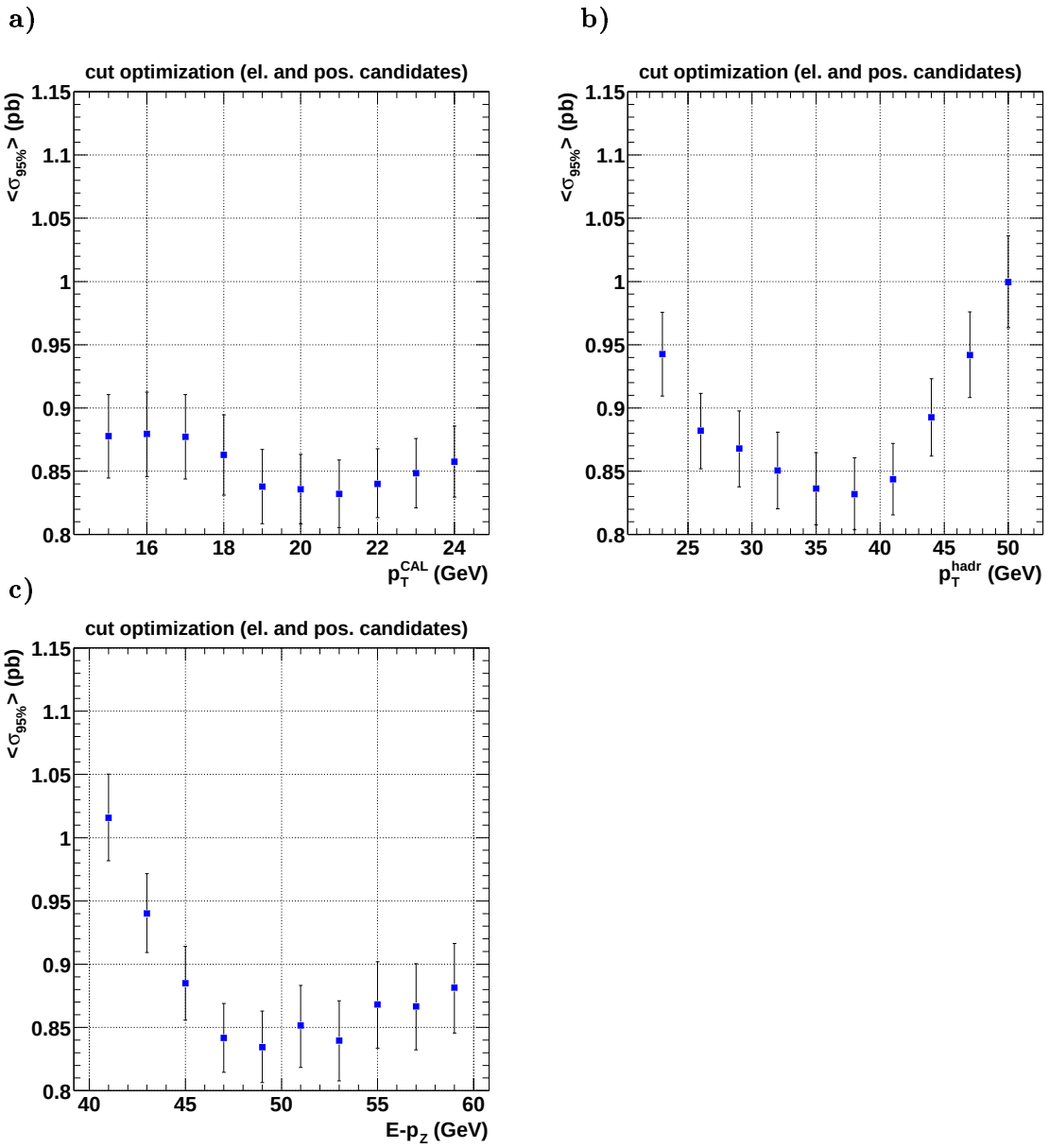

Figure 7.18: Expected 95% C.L. upper limit on the cross section for single top-quark production, obtained from electron and positron candidate events, as a function of the final selection cut on a) the missing transverse momentum in the CAL, p_T^{CAL}, b) the transverse momentum of the hadronic system, p_T^{hadr}, c) $E - p_Z$. While the corresponding selection cut was varied, the values of all other cuts were fixed to the optimised final values described in the text. The error bars indicate the statistical uncertainties on the MC simulation.

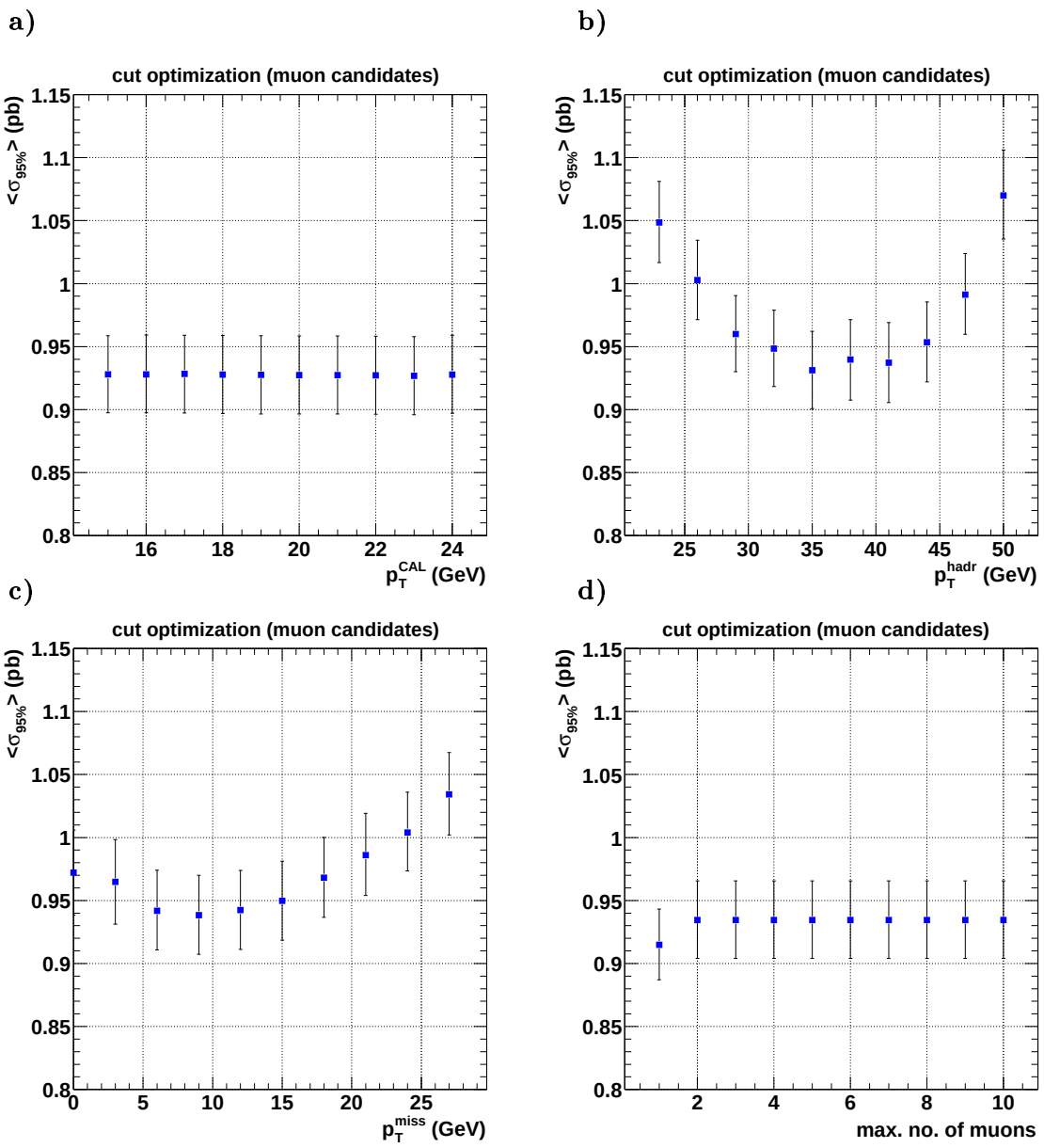

Figure 7.19: Expected 95% C.L. upper limit on the cross section for single top quark production, obtained from muon candidate events, as a function of the final selection cut on a) the missing transverse momentum in the CAL, p_T^{CAL}, b) the transverse momentum of the hadronic system, p_T^{hadr}, c) the missing transverse momentum, p_T^{miss}, d) the maximal number of allowed muon candidates in the event. While the corresponding selection cut was varied, the values of all other selection cuts were fixed to the optimised final values described in the text. The error bars indicate the statistical uncertainties on the MC simulation.

7.3.2 Results of the final single-top selection

After the final single top selection cuts, no event remained in the data, while 0.94 ± 0.10 electron events and 0.95 ± 0.10 muon events are expected from SM processes. The expectation from single W-boson production is 0.57 ± 0.02 electron events and 0.59 ± 0.02 muon events. The selection efficiency for the single top signal MC was $3.569\% \pm 0.088$ in the electron channel and $3.450\% \pm 0.086$ in the muon channel.

Figure 7.20 shows the event yields of final electron and muon candidates for the data from 1994 to 2000 and for the simulated SM background processes. For comparison with earlier results, also the numbers for a lower value of the cut on the hadronic transverse momentum ($p_T^{\mathrm{hadr}} > 25\,\mathrm{GeV}$) is given. Table 7.7 summarises the event yields, background expectation and signal efficiencies for the final selection of electron and muon candidate events. Event displays of the two electron candidates and five muon candidates, which were selected with the reduced cut on the hadronic transverse momentum of $p_T^{\mathrm{hadr}} > 25\,\mathrm{GeV}$, are shown in appendix B.

Final selection electron candidates ($p_T^{\mathrm{hadr}} > 25\,\mathrm{GeV}$)						
coll.	$\sqrt{s}$	$\mathcal{L}_{\mathrm{int}}$	Obs.	SM exp.	W only	signal eff. (%)
e^+p	300 GeV	$47.9\,\mathrm{pb}^{-1}$	0	0.72 ± 0.127	0.40 ± 0.012	4.31 ± 0.096
e^-p	318 GeV	$16.7\,\mathrm{pb}^{-1}$	1	0.64 ± 0.148	0.17 ± 0.011	4.39 ± 0.097
e^+p	318 GeV	$65.5\,\mathrm{pb}^{-1}$	1	1.54 ± 0.194	0.73 ± 0.021	4.48 ± 0.098
Total		$130.1\,\mathrm{pb}^{-1}$	2	2.90 ± 0.275	1.30 ± 0.026	4.402 ± 0.097
Final selection muon candidates ($p_T^{\mathrm{hadr}} > 25\,\mathrm{GeV}$)						
e^+p	300 GeV	$47.9\,\mathrm{pb}^{-1}$	0	0.78 ± 0.097	0.44 ± 0.012	4.12 ± 0.094
e^-p	318 GeV	$16.7\,\mathrm{pb}^{-1}$	1	0.45 ± 0.075	0.19 ± 0.012	4.27 ± 0.096
e^+p	318 GeV	$65.5\,\mathrm{pb}^{-1}$	4	1.53 ± 0.149	0.73 ± 0.021	4.11 ± 0.094
Total		$130.1\,\mathrm{pb}^{-1}$	5	2.75 ± 0.192	1.37 ± 0.027	4.14 ± 0.094
Final selection electron candidates ($p_T^{\mathrm{hadr}} > 40\,\mathrm{GeV}$)						
e^+p	300 GeV	$47.9\,\mathrm{pb}^{-1}$	0	0.23 ± 0.050	0.16 ± 0.008	3.47 ± 0.086
e^-p	318 GeV	$16.7\,\mathrm{pb}^{-1}$	0	0.16 ± 0.056	0.08 ± 0.007	3.48 ± 0.087
e^+p	318 GeV	$65.5\,\mathrm{pb}^{-1}$	0	0.54 ± 0.069	0.33 ± 0.014	3.67 ± 0.089
Total		$130.1\,\mathrm{pb}^{-1}$	0	0.94 ± 0.102	0.57 ± 0.017	3.57 ± 0.088
Final selection muon candidates ($p_T^{\mathrm{hadr}} > 40\,\mathrm{GeV}$)						
e^+p	300 GeV	$47.9\,\mathrm{pb}^{-1}$	0	0.26 ± 0.044	0.18 ± 0.008	3.43 ± 0.086
e^-p	318 GeV	$16.7\,\mathrm{pb}^{-1}$	0	0.08 ± 0.008	0.08 ± 0.008	3.55 ± 0.088
e^+p	318 GeV	$65.5\,\mathrm{pb}^{-1}$	0	0.61 ± 0.089	0.32 ± 0.013	3.44 ± 0.086
Total		$130.1\,\mathrm{pb}^{-1}$	0	0.95 ± 0.099	0.59 ± 0.017	3.45 ± 0.086

Table 7.7: Number of observed events and expectation from SM background for the final selection of electron and muon candidate events at large values of p_T^{hadr} in different data taking periods. The values are given for both, a cut at $p_T^{\mathrm{hadr}} > 25\,\mathrm{GeV}$ and for the final selection of single-top candidates at $p_T^{\mathrm{hadr}} > 40\,\mathrm{GeV}$. The expectation only from single W production and the efficiency for the single top signal MC is also shown. The quoted uncertainties are the statisticial uncertainties due to the limited number of generated MC events.

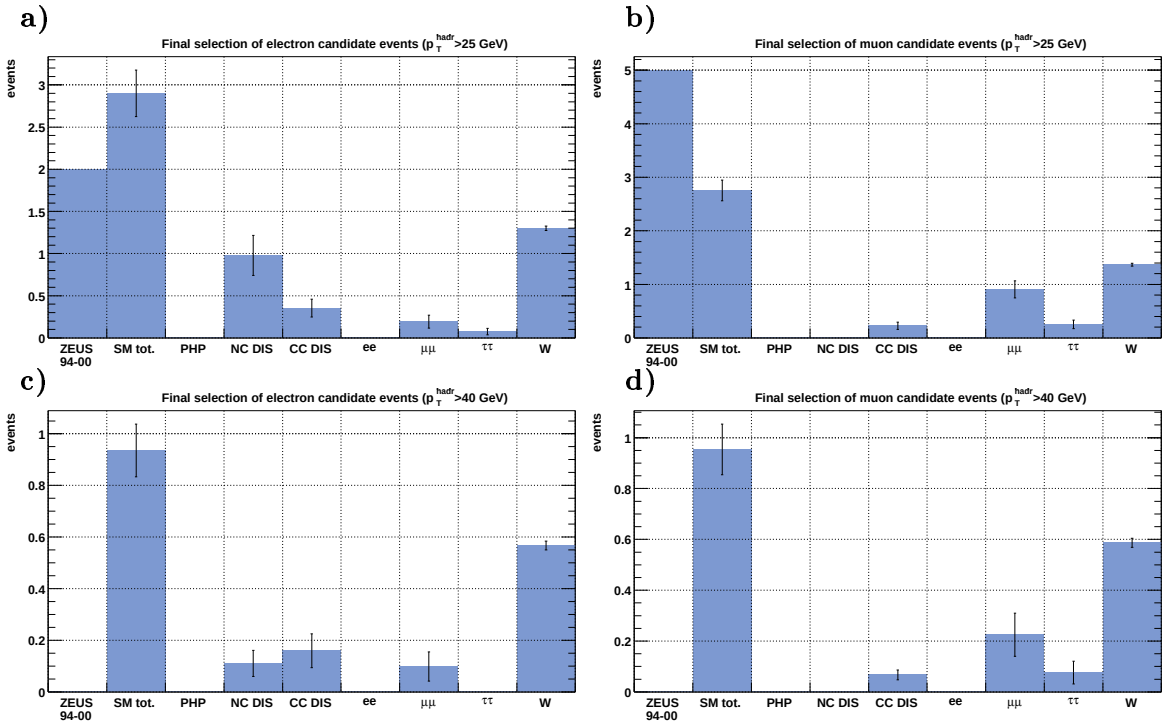

Figure 7.20: Event yields for the final selection of single-top candidate events: a) electron candidates and b) muon candidates with $p_T^{\mathrm{hadr}} > 25\,\mathrm{GeV}$, c) electron candidates and d) muon candidates with $p_T^{\mathrm{hadr}} > 40\,\mathrm{GeV}$. The event yields are shown for the data from 1994-2000 and for the different sources of simulated SM background. The event yields for the SM background are scaled to the data luminosity. The error bars indicate the statistical uncertainties on the SM background expectations.

7.3.3 Cross efficiencies

In some cases for the signal MC, the events selected in the electron or muon channel of the analysis were not originating from the corresponding channel of the W boson decay, as it was obtained from the MC generator information. These "cross efficiencies" for the different decay channels of the W boson in the signal MC are given in Tab. 7.8 for the final selection of electron and muon candidate events.

Events from muonic W decays entered the electron channel in cases were the muon was not detected as isolated muon and instead the scattered electron was observed as isolated electron in the detector.

Events from the decay $W^+ \to \tau^+\nu_\tau$ can lead to an isolated electron or muon in the detector in cases were the τ^+ decays leptonically ($BR(\tau^+ \to e^+\nu_e\bar{\nu_\tau}) = BR(\tau^+ \to \mu^+\nu_\mu\bar{\nu_\tau}) = 18\%$). Also tau leptons that decay hadronically with one charged particle ($BR(\tau^+ \to h^+\bar{\nu}_\tau \geq 0$ neutrals$) = 50\%$) can be misidentified as isolated electrons (see chapter 9).

Events from the hadronic decay chain $t \to W^+b$, $W^+ \to$ hadr. with three jets in the final state contribute with approximately 1% to the electron channel. Such events had

the scattered electron detected as isolated lepton and the missing transverse momentum was caused by a muon inside one of the QCD jets (e.g. from $B^0 \to D^{*+}\mu^-\bar{\nu_\mu}$).

The cross efficiencies did not affect the sensitivity of the search, since events were only accepted as electron candidates, if they were not selected as muon candidate events at the same time.

Candidate type	$W^+ \to e^+\nu_e$	$W^+ \to \mu^+\nu_\mu$	$W^+ \to \tau^+\nu_\tau$	$W^+ \to$ hadr.
electron	70%	8%	21%	1%
muon	0%	86%	14%	0%

Table 7.8: Cross efficiencies from different decay channels of the W boson for final electron and muon candidate events from the single-top signal MC.

7.3.4 Single-top efficiencies

The sensitivity for the single-top signal process with different production- and decay-modes for the top quark was studied with dedicated MC samples for these processes.

Table 7.9 compares the efficiencies in the final selection ($p_T^{\text{hadr}} > 40\,\text{GeV}$) for all considered combinations of production- and decay-modes. All samples were produced for e^+p scattering, $\sqrt{s} = 318\,\text{GeV}$ and $M_{\text{top}} = 175\,\text{GeV}$. The final selection efficiency for the signal MC with anomalous decay $t \to uZ$ was $1.22\% \pm 0.08$ in the electron channel and $1.80\% \pm 0.10$ in the muon channel. The leptonic decay channels of the Z boson, $Z \to l^+l^-$ have a branching ratio of only 3.4% per channel. Thus in most of the selected electron-candidate events in this sample the scattered beam electron was detected as an isolated lepton. Most of the muon events were from muonic b-decays. For single top production through Z^0 exchange, two MC samples with anomalous vector coupling v_{tuZ} at the $t - u - Z^0$ vertex and different decay modes were considered. For the SM decay $t \to bW^+$, the efficiency in the electron channel was $8.53\% \pm 0.29\%$ and in the muon channel $3.06\% \pm 0.18\%$. For the sample with anomalous vector coupling v_{tuZ} also at the decay vertex ($t \to uZ$), the efficiency in the electron channel was $8.92\% \pm 0.30\%$ and in the muon channel $2.02\% \pm 0.14\%$. The higher efficiency in the electron channel for single-top production through Z^0 exchange is due to the fact that in many events the beam positron is scattered under larger angles and thus can be detected as an isolated lepton. In the muon channel however the efficiency is smaller than for the nominal sample with production through γ exchange and SM decay of the top quark, for which the event selection was optimised.

Production	decay	eff. el. channel	eff. muon channel
$\kappa_{tu\gamma}$	$t \to bW$	3.67 ± 0.09	3.44 ± 0.09
$\kappa_{tu\gamma}$	$t \to uZ$	$1.22\% \pm 0.08$	$1.80\% \pm 0.10$
v_{tuZ}	$t \to bW$	$8.53\% \pm 0.29\%$	$3.06\% \pm 0.18\%$
v_{tuZ}	$t \to uZ$	$8.92\% \pm 0.30\%$	$2.02\% \pm 0.14\%$

Table 7.9: Comparison of the single-top efficiencies in the final top selection ($p_T^{\mathrm{hadr}} > 40\,\mathrm{GeV}$) for various combinations of production- and decay-modes of the single-top quark. All MC samples were produced for e^+p-scattering, $\sqrt{s} = 318\,\mathrm{GeV}$ and $M_{\mathrm{top}} = 175\,\mathrm{GeV}$.

7.4 Statistical and systematic uncertainties

The statistical uncertainties, σ_{stat}, were obtained by adding the individual uncertainties for the different MC samples in quadrature:

$$\sigma_{\mathrm{stat}} = \sqrt{\sum_i N^i_{\mathrm{MC,sel}} \left(\frac{\mathcal{L}_{\mathrm{data}} \sigma^i_{\mathrm{MC}}}{N^i_{\mathrm{MC,tot}}} \right)^2}, \tag{7.2}$$

where i runs over all MC samples of the corresponding data taking period, $N^i_{\mathrm{MC,tot}}$, $N^i_{\mathrm{MC,sel}}$ and σ^i_{MC} are the total number of events, the number of selected events and the cross section of the corresponding MC sample, respectively, and $\mathcal{L}_{\mathrm{data}}$ is the integrated luminosity of the corresponding data taking period. For the overall statistical uncertainty on the background expectation, the data taking from 1994 to 2000 was treated as one data set. The overall statistical uncertainty of the signal efficiency, $\sigma^{\mathrm{eff}}_{\mathrm{stat}}$, was obtained as the average of the efficiency in the individual data taking periods, weighted by the corresponding luminosities:

$$\sigma^{\mathrm{eff}}_{\mathrm{stat}} = \frac{\mathcal{L}_{94-97}\sigma^{\mathrm{eff},94-97}_{\mathrm{stat}} + \mathcal{L}_{98-99}\sigma^{\mathrm{eff},98-99}_{\mathrm{stat}} + \mathcal{L}_{99-00}\sigma^{\mathrm{eff},99-00}_{\mathrm{stat}}}{\mathcal{L}_{94-00}}. \tag{7.3}$$

The statistical uncertainty for the combination of electron and muon channel was obtained by adding the corresponding statistical uncertainties for electron and muon channel in quadrature.

Systematic uncertainties for background expectations and signal efficiencies result in a change of the number of expected background and signal events. Positive and negative systematic uncertainties σ^+_{syst} and σ^-_{syst} for background expectation and signal efficiency were taken into account:

$$\sigma^+_{\mathrm{syst}} = \frac{\sum_i \frac{\mathcal{L}_{\mathrm{data}}\sigma^i_{\mathrm{MC}}}{N^i_{\mathrm{MC,tot}}} (N^{i+}_{\mathrm{MC,sel}} - N^i_{\mathrm{MC,sel}})}{\sum_i \frac{\mathcal{L}_{\mathrm{data}}\sigma^i_{\mathrm{MC}}}{N^i_{\mathrm{MC,tot}}} N^i_{\mathrm{MC,sel}}}, \tag{7.4}$$

$$\sigma^-_{\mathrm{syst}} = \frac{\sum_i \frac{\mathcal{L}_{\mathrm{data}}\sigma^i_{\mathrm{MC}}}{N^i_{\mathrm{MC,tot}}} (N^i_{\mathrm{MC,sel}} - N^{i-}_{\mathrm{MC,sel}})}{\sum_i \frac{\mathcal{L}_{\mathrm{data}}\sigma^i_{\mathrm{MC}}}{N^i_{\mathrm{MC,tot}}} N^i_{\mathrm{MC,sel}}}, \tag{7.5}$$

where i runs over all background (signal) MC samples of the corresponding data taking period and $N^{i+(-)}_{MC,sel}$ are the number of selected MC events for a positive (negative) effect of the corresponding systematic variation ($N^{i+(-)}_{MC,sel} > (<) N^{i}_{\mathrm{MC,sel}}$).

The total positive (negative) systematic uncertainties for each data taking period were obtained by adding all positive (negative) systematic uncertainties for the corresponding data taking period in quadrature. In cases where the systematic variation of a parameter around the nominal value lead to a change in only one direction, the maximum of the two numbers was taken as the systematic uncertainty for that direction. The uncertainty in the other direction was in these cases set to zero. For the overall positive and negative systematical uncertainty on the background expectation, the data taking from 1994 to 2000 was treated as one data taking period. The positive (negative) systematic uncertainties for the signal efficiency for the combined period from 1994-2000 were obtained by averaging the positive (negative) systematic uncertainties for the individual periods, weighted by the data luminosity in the corresponding period:

$$\sigma^{\mathrm{eff}+(-)}_{\mathrm{syst}} = \frac{\mathcal{L}_{94-97}\sigma^{\mathrm{eff}+(-),94-97}_{\mathrm{syst}} + \mathcal{L}_{98-99}\sigma^{\mathrm{eff}+(-),98-99}_{\mathrm{syst}} + \mathcal{L}_{99-00}\sigma^{\mathrm{eff}+(-),99-00}_{\mathrm{syst}}}{\mathcal{L}_{94-00}}. \qquad (7.6)$$

The total positive (negative) uncertainty in each case was obtained as the quadratic sum of the statistical uncertainty and all positive (negative) systematic uncertainties. The systematic uncertainties for the combination of electron and muon channels were obtained in the same way as described for the individual channels, but after adding the number of expected background events and the efficiencies from electron and muon channel.

The following systematic effects were taken into account:

- *CAL scale*
  The uncertainty in the absolute energy scale of the CAL was assumed to be $\pm 1\%$ for FCAL and BCAL and $\pm 2\%$ for RCAL. For the systematic effect on the single-top signal MC efficiency, the energy of each CAL cell in the MC data was varied by $\pm 1\%$ and $\pm 2\%$ for the corresponding CAL section. For the systematic effect on the background MC expectation, the values of all CAL energy dependent selection cuts were varied by $\pm 1\%$, thus neglecting partly the influence of the CAL scale on the electron, muon and jet finding efficiency.

- *QCD-radiation model for NC DIS background*
  The use of LEPTO MEPS instead of ARIADNE CDM for the simulation of the NC DIS background was treated as a systematic uncertainty for the background expectation.

- *Parton density function*
  In order to evaluate the effect of the chosen PDF on the signal selection efficiency, the signal MC events, which were created with the MRS (A) PDF, were reweighted to the PDF, which was obtained from a recent ZEUS NLO QCD analysis of DIS data [92].

- *Mass of the top quark*
  The nominal value of 175 GeV for the top mass was varied by ±5 GeV in the signal MC. The resulting change in the signal efficiency was the dominating systematic uncertainty. This effect was taken into account by calculating the exclusion limit on single top-quark production for all three masses, 170 GeV, 175 GeV, 180 GeV.

Table 7.10 and 7.11 present the statistical and systematic uncertainties for the preselection and for the final selection of single top-quark candidates, respectively. A summary of the observed and expected event yields in the search for isolated electron and muon events is shown in Tab. 7.12, where the indicated uncertainties include the statistical uncertainties as well as the CAL scale uncertainty and the uncertainty due to the hadronisation model for the NC DIS background.

Preselection of isolated leptons									
effect	Electron				Muon				El.+Mu.
	94-97	98-99	99-00	94-00	94-97	98-99	99-00	94-00	94-00
stat.err. BG	±10.0%	±12.5%	±7.5%	±5.5%	±7.7%	±8.6%	±6.7%	±4.5%	±3.8%
stat.err. sig.	±1.9%	±1.9%	±1.9%	±1.9%	±2.2%	±2.2%	±2.2%	±2.2%	±1.5%
CAL-scale + BG	+4.8%	+13.9%	+4.1%	+5.9%	+3.4%	+1.6%	+2.5%	+2.7%	+4.7%
CAL-scale + sig	+0.4%	+0.3%	+0.6%	+0.5%	+0.1%	±0.0%	±0.0%	±0.0%	+0.3%
CAL-scale - BG	−1.8%	−4.7%	−4.9%	−3.8%	−1.1%	−7.3%	−3.6%	−3.4%	−3.6%
CAL-scale - sig	−0.5%	−0.6%	−0.5%	−0.5%	+0.1%	−0.1%	±0.0%	±0.0%	−0.1%
MEPS BG	−27%	−27%	−16%	−22%	−1.4%	+0.9%	±0.0%	−0.3%	−13.8%
$M_{\mathrm{top}} = 170\,\mathrm{GeV}$ sig.	−2.7%	−4.5%	−0.4%	−1.8%	−5.0%	−5.2%	−1.4%	−3.3%	−2.4%
$M_{\mathrm{top}} = 180\,\mathrm{GeV}$ sig.	−0.9%	−0.7%	+2.1%	+0.6%	−0.3%	−3.4%	−0.8%	−0.9%	±0.0%
tot. syst. BG +	+4.8%	+13.9%	+4.1%	+5.9%	+3.4%	+1.6%	+2.5%	+2.7%	+4.7%
tot. syst. BG -	−27%	−27%	−17%	−22%	−1.8%	−7.4%	−3.6%	−3.4%	−14.3%

Table 7.10: Statistical and systematic uncertainties for the preselection of isolated electron and muon events.

Final selection of single-top candidates ($p_T^{\mathrm{hadr}} > 40\,\mathrm{GeV}$)									
effect	Electron				Muon				El.+Mu.
	94-97	98-99	99-00	94-00	94-97	98-99	99-00	94-00	94-00
stat.err. BG	±21%	±34%	±13%	±11%	±19%	±9.3%	±13.2%	±10.1%	±7.4%
stat.err. sig.	±2.5%	±2.5%	±2.4%	±2.5%	±2.5%	±2.5%	±2.5%	±2.5%	±1.75%
CAL-scale + BG	+0.8%	+3.0%	+3.1%	+2.5%	+2.8%	+60%	+5.3%	+9.2%	+6.0%
CAL-scale + sig	−0.5%	−0.9%	−0.5%	−0.6%	+0.6%	+1.4%	+0.2%	+0.5%	−0.1%
CAL-scale - BG	−4.4%	−3.0%	−4.4%	−4.2%	−1.6%	±0.0%	−1.7%	−1.6%	−2.8%
CAL-scale - sig	+1.1%	+0.5%	+0.7%	+0.8%	−1.7%	−0.9%	−0.7%	−1.1%	−0.1%
MEPS BG	−1.2%	−10.2%	+0.9%	−1.5%	±0.0%	±0.0%	±0.0%	±0.0%	−0.7%
PDF sig.	+0.5%	+0.9%	+0.5%	+0.6%	+1.0%	+1.1%	+1.0%	+1.0%	+0.8%
$M_{\mathrm{top}} = 170\,\mathrm{GeV}$ sig.	−3.5%	−4.4%	−6.4%	−5.1%	−8.1%	−10.0%	−4.1%	−6.4%	−6.8%
$M_{\mathrm{top}} = 180\,\mathrm{GeV}$ sig.	+4.1%	+7.0%	+3.9%	+4.4%	+4.7%	+0.8%	+1.9%	+2.7%	+3.6%
tot. syst. BG +	+4.8%	+13.9%	+4.1%	+5.9%	+3.4%	+1.6%	+2.5%	+2.7%	+4.7%
tot. syst. BG +	+0.8%	+3.0%	+3.1%	+2.5%	+2.8%	+60%	+5.3%	+9.2%	+6.0%
tot. syst. BG -	−4.6%	−10.7%	−4.5%	−4.4%	−1.6%	±0.0%	−1.7%	−1.6%	−2.9%

Table 7.11: Statistical and systematic uncertainties for the final selection of single-top candidates.

Leptonic channel	Positron channel obs./expected (W)	Muon channel obs./expected (W)
Preselection		
e^+p, $\sqrt{s} = 300$ GeV ($\mathcal{L} = 47.9\,\mathrm{pb}^{-1}$)	$4 \;/\; 7.3^{+0.8}_{-2.1}$	$0 \;/\; 4.2^{+0.4}_{-0.3}$
e^-p, $\sqrt{s} = 318$ GeV ($\mathcal{L} = 16.7\,\mathrm{pb}^{-1}$)	$7 \;/\; 3.2^{+0.6}_{-1.0}$	$1 \;/\; 2.1^{+0.2}_{-0.2}$
e^+p, $\sqrt{s} = 318$ GeV ($\mathcal{L} = 65.5\,\mathrm{pb}^{-1}$)	$13 \;/\; 10.1^{+0.9}_{-1.9}$	$11 \;/\; 5.6^{+0.4}_{-0.4}$
Total ($\mathcal{L} = 130.1\,\mathrm{pb}^{-1}$)	$24 \;/\; 20.6^{+1.7}_{-4.6}$ (17%)	$12 \;/\; 11.9^{+0.6}_{-0.7}$ (16%)
Final selection ($p_T^{\mathrm{had}} > 25$ GeV)		
e^+p, $\sqrt{s} = 300$ GeV ($\mathcal{L} = 47.9\,\mathrm{pb}^{-1}$)	$0 \;/\; 0.72^{+0.27}_{-0.13}$	$0 \;/\; 0.78^{+0.10}_{-0.10}$
e^-p, $\sqrt{s} = 318$ GeV ($\mathcal{L} = 16.7\,\mathrm{pb}^{-1}$)	$1 \;/\; 0.64^{+0.28}_{-0.20}$	$1 \;/\; 0.45^{+0.07}_{-0.07}$
e^+p, $\sqrt{s} = 318$ GeV ($\mathcal{L} = 65.5\,\mathrm{pb}^{-1}$)	$1 \;/\; 1.54^{+0.33}_{-0.32}$	$4 \;/\; 1.53^{+0.17}_{-0.16}$
Total ($\mathcal{L} = 130.1\,\mathrm{pb}^{-1}$)	$2 \;/\; 2.90^{+0.59}_{-0.32}$ (45%)	$5 \;/\; 2.75^{+0.21}_{-0.21}$ (50%)
Final selection ($p_T^{\mathrm{had}} > 40$ GeV)		
e^+p, $\sqrt{s} = 300$ GeV ($\mathcal{L} = 47.9\,\mathrm{pb}^{-1}$)	$0 \;/\; 0.23^{+0.05}_{-0.05}$	$0 \;/\; 0.26^{+0.04}_{-0.04}$
e^-p, $\sqrt{s} = 318$ GeV ($\mathcal{L} = 16.7\,\mathrm{pb}^{-1}$)	$0 \;/\; 0.16^{+0.06}_{-0.06}$	$0 \;/\; 0.08^{+0.05}_{-0.01}$
e^+p, $\sqrt{s} = 318$ GeV ($\mathcal{L} = 65.5\,\mathrm{pb}^{-1}$)	$0 \;/\; 0.54^{+0.07}_{-0.07}$	$0 \;/\; 0.61^{+0.10}_{-0.09}$
Total ($\mathcal{L} = 130.1\,\mathrm{pb}^{-1}$)	$0 \;/\; 0.94^{+0.11}_{-0.10}$ (61%)	$0 \;/\; 0.95^{+0.14}_{-0.10}$ (61%)

Table 7.12: Number of observed and expected events for different selection stages in the search for isolated electron and muon events. The percentage of single W production included in the expectation is indicated in parentheses. The statistical and systematic uncertainties added in quadrature are also indicated.

7.5 Search for single-top production in the hadronic channel

The ZEUS collaboration has also performed a search for single top-quark production through FCNC $tu\gamma$ coupling in the hadronic-decay channel of the W boson [55,56]. The expected signature in this channel consists of three jets with large transverse energy and no significant missing transverse momentum. The event selection required three jets with $E_T^{\mathrm{jet}1} > 40\,\mathrm{GeV}$, $E_T^{\mathrm{jet}2} > 25\,\mathrm{GeV}$ and $E_T^{\mathrm{jet}3} > 14\,\mathrm{GeV}$. The photoproduction background was reduced by requiring one of the 2-jet masses and the 3-jet mass to be compatible with the W boson mass and the top mass, respectively. The number of observed events was found to be in agreement with SM expectations. The efficiency for detecting FCNC induced single-top quarks from hadronic decays of the W boson was 24%.

Chapter 8

Exclusion limits on single-top production

No events compatible with single top-quark production were found, both in the leptonic and hadronic channels of the W decay. Therefore exclusion limits on the values of the effective coupling constants $\kappa_{tu\gamma}$ and v_{tuZ} for the anomalous FCNC interactions were set, which are presented in this chapter.

8.1 Limit setting procedure

The effective Lagrangian (3.16) describes the possible production and decay of single top quarks through anomalous couplings of strength $\kappa_{tu\gamma}$ and v_{tuZ} at the $t-u-\gamma$ and the $t-u-Z^0$ vertex, respectively. The values of $\kappa_{tu\gamma}$ and v_{tuZ} determine both, the production cross section and decay width of the single top quark. They were treated as free parameters and limits were set in the $\kappa_{tu\gamma}$-v_{tuZ}-plane. A two dimensional likelihood, L, was defined in this plane as

$$L(N_{\text{obs}}|\kappa_{tu\gamma}, v_{tuZ}) = \frac{(N_{\text{sig}}(\kappa_{tu\gamma}, v_{tuZ}) + N_{SM})^{N_{\text{obs}}} \cdot e^{-(N_{\text{sig}}(\kappa_{tu\gamma}, v_{tuZ})+N_{SM})}}{N_{\text{obs}}!}, \qquad (8.1)$$

where L is the probability to observe N_{obs} events, when N_{SM} events are expected from SM background and N_{sig} events are expected from single top-quark production for a given pair of $\kappa_{tu\gamma}$ and v_{tuZ}. The production cross section, $\sigma_{\text{single top}}(\kappa_{tu\gamma}, v_{tuZ})$, was determined for each pair of $\kappa_{tu\gamma}$ and v_{tuZ} from eq. 3.17, neglecting the very small interference term $c_{\gamma Z}$. The number of expected signal events, N_{sig}, depends on:

- the production cross sections for γ and Z^0 exchange:
  $\sigma_{\text{single top},\gamma} = \sigma_{\text{single top}}(\kappa_{tu\gamma}, 0)$,
  $\sigma_{\text{single top,Z}} = \sigma_{\text{single top}}(0, v_{tuZ})$;
- the decay branching ratios $BR(t \to bW)$ and $BR(t \to uZ)$;

- the selection efficiencies for the considered production and decay channels $\epsilon_{\gamma,bW}$, $\epsilon_{Z,bW}$, $\epsilon_{\gamma,uZ}$ and $\epsilon_{Z,uZ}$;
- the integrated luminosity $\mathcal{L}_{\text{int}}$.

N_{sig} is thus given as:

$$\begin{aligned} N_{\text{sig}} &= (\sigma_{\text{single top},\gamma} \cdot (BR(t \to bW) \cdot \epsilon_{\gamma,bW} + BR(t \to uZ) \cdot \epsilon_{\gamma,uZ}) \\ &\quad +(\sigma_{\text{single top,Z}} \cdot (BR(t \to bW) \cdot \epsilon_{Z,bW} + BR(t \to uZ) \cdot \epsilon_{Z,uZ}))) \cdot \mathcal{L}_{\text{int}}. \end{aligned} \tag{8.2}$$

The efficiencies $\epsilon_{\gamma,bW}$, $\epsilon_{Z,bW}$, $\epsilon_{\gamma,uZ}$ and $\epsilon_{Z,uZ}$ were obtained from the corresponding MC samples. Four partial likelihoods L_i were defined, based on the analysis in the leptonic and hadronic channels for the two independent data taking periods at $\sqrt{s} = 300\,\text{GeV}$ and $\sqrt{s} = 318\,\text{GeV}$. The total likelihood was obtained by multiplying the partial likelihoods.

A two dimensional probability density in the $\kappa_{tu\gamma}$-v_{tuZ} plane was obtained using a Bayesian approach to invert the likelihood and assuming a uniform a priori probability in $\kappa_{tu\gamma}$ and v_{tuZ}:

$$p(\kappa_{tu\gamma}, v_{tuZ}|N_{\text{obs}}) = \frac{\prod_i L_i(N_{\text{obs}}|\kappa_{tu\gamma}, v_{tuZ})}{\int_{\kappa_{tu\gamma}=0}^{\infty}\int_{v_{tuZ}=0}^{\infty}\prod_i L_i(N_{\text{obs}}|\kappa_{tu\gamma}, v_{tuZ})d\kappa_{tu\gamma}dv_{tuZ}}. \tag{8.3}$$

The 95% C.L. limit in the $\kappa_{tu\gamma}$-v_{tuZ} plane was defined as the set of points $p(\kappa_{tu\gamma}, v_{tuZ}|N_{\text{obs}}) = p_0$, for which the following relation holds:

$$\int\limits_{p(\kappa_{tu\gamma},v_{tuZ}|N_{\text{obs}})>p_0} p(\kappa_{tu\gamma}, v_{tuZ}|N_{\text{obs}})d\kappa_{tu\gamma}dv_{tuZ} = 0.95. \tag{8.4}$$

For $v_{tuZ} = 0$ and $\kappa_{tu\gamma} = 0$, one dimensional probability distributions can be defined accordingly. In this case one can start from a uniform a priori probability in the cross section σ. The resulting cross section limits can then be transformed into the corresponding limits on the coupling constants, $\kappa_{tu\gamma}$ and v_{tuZ}. For this case one dimensional probability distributions are defined as:

$$\begin{aligned} p(\sigma, v_{tuZ} = 0|N_{\text{obs}}) &= \frac{\prod_i L_i(N_{\text{obs}}|\sigma, k_g(\sigma))}{\int_{\sigma=0}^{\infty}\prod_i L_i(N_{\text{obs}}|\sigma)d\sigma}, \\ p(\sigma, k_g = 0|N_{\text{obs}}) &= \frac{\prod_i L_i(N_{\text{obs}}|\sigma, v_{tuZ}(\sigma))}{\int_{\sigma=0}^{\infty}\prod_i L_i(N_{\text{obs}}|\sigma).d\sigma} \end{aligned} \tag{8.5}$$

The 95% C.L. limit on the cross section are defined as the values $\sigma^{\text{lim}}_{\kappa_{tu\gamma}}$ and $\sigma^{\text{lim}}_{v_{tuZ}}$, for which the following relations hold:

$$\begin{aligned} \int\limits_{\sigma=0}^{\sigma^{\text{lim}}_{\kappa_{tu\gamma}}} p(\sigma, v_{tuZ} = 0|N_{\text{obs}})d\sigma &= 0.95. \\ \int\limits_{\sigma=0}^{\sigma^{\text{lim}}_{v_{tuZ}}} p(\sigma, \kappa_{tu\gamma} = 0|N_{\text{obs}})d\sigma &= 0.95. \end{aligned} \tag{8.6}$$

8.2 Exclusion limits in the $\kappa_{tu\gamma}$-v_{tuZ} plane

Equation (8.4) was used to constrain the values of the coupling constants $\kappa_{tu\gamma}$ and v_{tuZ}. Since the dominant theoretical uncertainty was the uncertainty on M_{top}, the calculation was performed for three different values of $M_{\text{top}} = 170,\ 175$ and 180 GeV. Table 8.1 summarises the parameters, which enter in the calculation of the exclusion limit. The resulting limit curves are shown in Fig. 8.1 for the leptonic channels and for the combination of both, the leptonic and the hadronic channels. The exclusion limits obtained from the CDF [50] and L3 [54] analyses are also shown in the figure, assuming no anomalous coupling of the top quark to c quarks. Therefore the published L3 limits on the coupling constants were rescaled by a factor of $\sqrt{2}$ for the figure (see section 4.2.1). For the ZEUS measurement the sensitivity for the coupling $\kappa_{tu\gamma}$ is much higher than for the vector coupling v_{tuZ}, due to the suppression of the Z^0 exchange at the production vertex and due to the reduced efficiency in the hadronic channel for all cases where v_{tuZ} is involved in the production or decay of the top quark. The ZEUS results excludes a substantial region in $\kappa_{tu\gamma}$ not constrained by previous experiments.

8.3 One-dimensional exclusion limits

Exclusion limits on $\kappa_{tu\gamma}$ for $v_{tuZ} = 0$ and on v_{tuZ} for $\kappa_{tu\gamma} = 0$ were obtained from Fig. 8.1 as the intersection of the exclusion line with the $\kappa_{tu\gamma}$ and v_{tuZ} axis, respectively. The resulting values can be tranformed into cross section limits using equation (3.17) for a given CMS energy. The one dimensional integrations according to (8.6) (assuming a uniform a priori probability in the cross section) lead to slightly different values of the exclusion limits. The obtained values for the combination of the leptonic and the hadronic channels are compared in Tab. 8.2. The values from the different calculation approaches agree within 10%.

In the leptonic channels of the ZEUS analysis the background expectation is smaller than in the hadronic channel. On the other hand the efficiency for the single-top signal is also smaller than in the hadronic channel. The resulting sensitivity for $\kappa_{tu\gamma}$ is therefore similar in both channels: for $M_{\text{top}} = 175\,\text{GeV}$, assuming a uniform a priori probability in the cross section, the exclusion limit from the leptonic channels alone is $\kappa_{tu\gamma} < 0.247$. The corresponding value from the analysis in the hadronic channel is $\kappa_{tu\gamma} < 0.268$.

8.4 Exclusion limits based on NLO calculations

For $v_{tuZ} = 0$, the NLO QCD calculations from section 3.4.4 for single-top production through photon exchange were used to obtain a more precise value for the limit on $\kappa_{tu\gamma}$

Parameter	$\sqrt{s}$ (GeV)	$M_{\text{top}} = 170\,\text{GeV}$	$M_{\text{top}} = 175\,\text{GeV}$	$M_{\text{top}} = 180\,\text{GeV}$
Model parameters				
c_γ	300	5.451	4.300	3.370
	318	7.520	6.076	4.886
c_Z	300	0.1808	0.1433	0.1123
	318	0.2861	0.2340	0.1899
$\Gamma_{t\to bW^+}$	-	1404 MeV	1554 MeV	1713 MeV
$\Gamma_{t\to u\gamma}$	-	$293\,\text{MeV}\cdot\kappa^2_{tu\gamma}$	$302\,\text{MeV}\cdot\kappa^2_{tu\gamma}$	$310\,\text{MeV}\cdot\kappa^2_{tu\gamma}$
$\Gamma_{t\to uZ}$	-	$1297\,\text{MeV}\cdot v^2_{tuZ}$	$1449\,\text{MeV}\cdot v^2_{tuZ}$	$1610\,\text{MeV}\cdot v^2_{tuZ}$
Parameters for the leptonic channels				
$\epsilon_{\gamma,bW}$	300	6.49	6.90	7.20
	318	6.69	7.09	7.31
$\epsilon_{Z,bW}$	300	11.07		
	318	11.51		
$\epsilon_{\gamma,uZ}$	300,318	3.03		
$\epsilon_{Z,uZ}$	300	10.25		
	318	10.63		
N_{obs}	300	0		
	318	0		
N_{SM}	300	0.49		
	318	1.40		
luminosity (pb^{-1})	300	47.9		
	318	82.2		
Parameters for the hadronic channel				
$\epsilon_{\gamma,bW}$	300	11.3	16.6	14.0
	318	12.5	16.5	16.5
$\epsilon_{Z,bW}$	300,318	0		
$\epsilon_{\gamma,uZ}$	300	11.3	16.6	14.0
	318	12.5	16.5	16.5
$\epsilon_{Z,uZ}$	300,318	0		
N_{obs}	300	2	5	3
	318	6	9	8
N_{SM}	300	1.4	3.3	1.0
	318	10.6	14.3	11.3
luminosity (pb^{-1})	300	45.0		
	318	82.2		

Table 8.1: Values of the parameters, which enter the calculation of the exclusion limit for single-top quark production. c_γ and c_Z refer to the cross section parametrisation $\sigma_{\text{single top}} = c_\gamma \cdot \kappa^2_{tu\gamma} + c_Z \cdot v^2_{tuZ} + c_{\gamma Z} \cdot \kappa_{tu\gamma} \cdot v_{tuZ}$, obtained in LO with the MRST PDF and including ISR according to the Weizsäcker-Williams approximation (see section 3.4.3). In cases, where the efficiency was only evaluated for $\sqrt{s} = 318\,\text{GeV}$, the corresponding value was used also for $\sqrt{s} = 300\,\text{GeV}$ (indicated as "300,318").

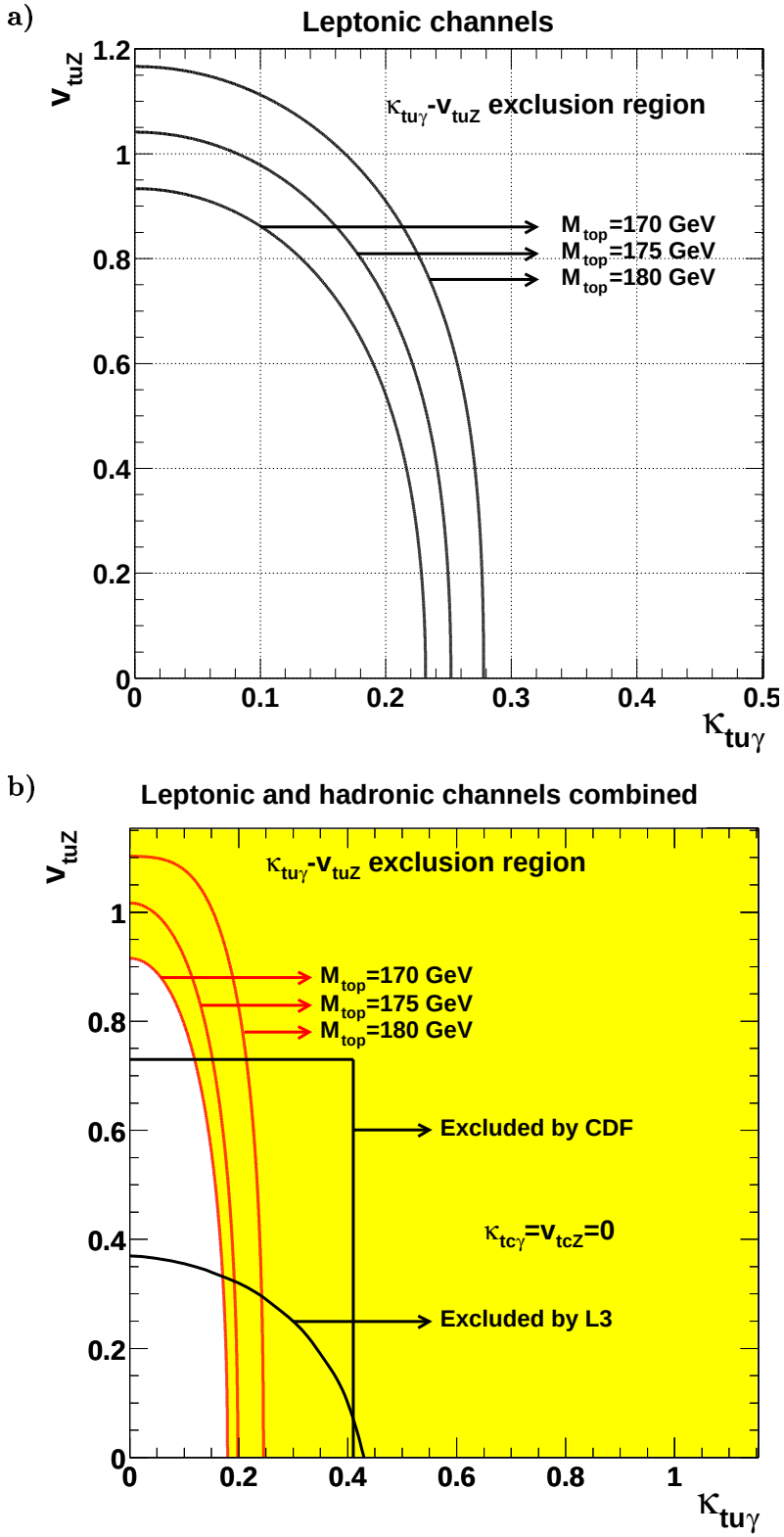

Figure 8.1: 95% C.L. limit in the $\kappa_{tu\gamma}$-v_{tuZ}-plane for single top-quark production a) for the leptonic decay channels and b) for the combination of the leptonic and the hadronic decay channels of the W boson. The arrows indicate the excluded region. The exclusion limits from the CDF and L3 analyses are also shown in b), assuming no anomalous coupling of the top quark to the c-quark.

M_{top}	method	$\kappa_{tu\gamma}^{\text{lim}}$	$\sigma_{\kappa_{tu\gamma}}^{\text{lim}}$	v_{tuZ}^{lim}	$\sigma_{v_{tuZ}}^{\text{lim}}$
170 GeV	2-dim	0.179	0.241	0.915	0.240
	1-dim	0.174	0.228	0.923	0.244
175 GeV	2-dim	0.198	0.238	1.017	0.242
	1-dim	0.192	0.224	1.021	0.244
180 GeV	2-dim	0.245	0.293	1.102	0.231
	1-dim	0.232	0.264	1.143	0.248

Table 8.2: 95% C.L. exclusion limits on the coupling constants, $\kappa_{tu\gamma}$ and v_{tuZ}, and on the cross sections, $\sigma_{\kappa_{tu\gamma}}^{\text{lim}}$ and $\sigma_{v_{tuZ}}^{\text{lim}}$, calculated at $\sqrt{s} = 318\,\text{GeV}$, for different top masses, M_{top}, and for the different calculation methods described in the text. The values were obtained from the combination of the analyses in both the leptonic and the hadronic decay channels of the W boson.

from the 1-dimensional cross-section limits:

$$M_{\text{top}} = 170\,\text{GeV}: \quad \kappa_{tu\gamma}(NLO) < 0.158 \text{ at } 95\% \text{ C.L.} \tag{8.7}$$
$$M_{\text{top}} = 175\,\text{GeV}: \quad \kappa_{tu\gamma}(NLO) < 0.174 \text{ at } 95\% \text{ C.L.} \tag{8.8}$$
$$M_{\text{top}} = 180\,\text{GeV}: \quad \kappa_{tu\gamma}(NLO) < 0.210 \text{ at } 95\% \text{ C.L..} \tag{8.9}$$

The exclusion limits obtained from LO and NLO calculations agree within 10%. The obtained exclusion limit of $\kappa_{tu\gamma} < 0.174$ for $M_{\text{top}} = 175\,\text{GeV}$ improves the result from CDF by more than a factor of two.

Chapter 9

Search for isolated tau leptons

This chapter describes the search for isolated tau leptons in events with missing transverse momentum, following the search for isolated electron and muon events described in the previous chapters. A tau-identification method based on observables describing the internal jet structure was used to discriminate between hadronic tau decays and quark- and gluon-induced jets. A more restrictive selection was applied to isolate tau leptons produced together with a hadronic final state with high transverse momentum, as expected from the decay of a heavy particle.

9.1 Tau identification

The search for tau leptons was based on the hadronic decays with one charged particle detected in the CTD. The narrow, "pencil-like", shape and the low charged-particle multiplicity of the tau jets were used to distinguish them from quark- and gluon-induced jets [93].

9.1.1 Properties of the tau lepton

The tau lepton is the heaviest lepton known to date ($M_\tau = 1776.99^{+0.29}_{-0.26}\,\mathrm{MeV}$ [26]). Unlike the electron and muon, which have a rest mass lower than the pion mass, it can decay into hadrons. The mean lifetime of $\tau = (290.6 \pm 1.1) \cdot 10^{-15}\,\mathrm{sec}$ [26] corresponds to a decay length of $c\tau = 87\,\mu\mathrm{m}$. The main decay modes of the tau lepton are given in Tab. 9.1. The total decay branching ratio to electrons or muons is about 35%. In almost all other cases ($\approx 65\%$) it decays into one (1-prong), three (3-prong) or five (5-prong) charged hadrons ($\pi^\pm$ or $K^\pm$), a tau neutrino (ν_τ) and zero or more neutral hadrons (π^0 or K^0).

The search for isolated tau leptons that is described in the following sections started from a sample of isolated tracks. The main contribution to the signal is thus expected to come from the 1-prong hadronic decay modes of the tau lepton. The mean decay length

Decay mode			BR
τ^-	$\rightarrow$	$e^-\bar{\nu}_e\nu_\tau$	17.8%
τ^-	$\rightarrow$	$\mu^-\bar{\nu}_\mu\nu_\tau$	17.4%
τ^-	$\rightarrow$	$h^-\nu_\tau \geq 0$ neutrals	49.5%
τ^-	$\rightarrow$	$2\ h^-\ h^+\nu_\tau \geq 0$ neutrals	15.2%
τ^-	$\rightarrow$	$3\ h^-\ 2\ h^+\nu_\tau \geq 0$ neutrals	0.1%

Table 9.1: The main decay modes of the tau lepton and the corresponding branching ratios, BR. $h^\pm$ and neutrals denote charged and neutral hadrons, respectively. The decay modes for the τ^+ lepton can be written in an analogous way and the branching ratios agree within the given precision.

of 87 µm would lead to a secondary vertex, which in principle can be used to identify tau decays. The resolution necessary for this was however beyond the capability of the ZEUS tracking system that was installed in the considered data taking periods[1].

The hadronic decay products of the tau lepton can be detected as jets in the CAL. For tau leptons produced at high momentum, the decay particles are strongly boosted in the direction of the tau lepton. The tau lepton is colour neutral, such that quark and gluon radiation is inhibited and the emerging energy depositions in the CAL are thus expected to have a narrow, pencil-like shape. Quark- and gluon-induced jets, on the other hand, are expected to be less collimated, since they can radiate gluons in the fragmentation phase. In addition, for such jets the colour connection to the rest of the final state enhances the spread of particles emerging from the hadronisation.

Figure 9.1a) shows an example of the response of the ZEUS detector to a QCD-jet originating from a simulated photoproduction process. Many tracks are pointing to a large cluster of energy depostions in the CAL. In Fig. 9.1b) the corresponding picture of a jet originating from a simulated $W \rightarrow \tau\nu_\tau$ event with 1-prong hadronic decay of the tau lepton is shown. It is characterized by a narrow cluster of energy depositions with one associated track.

9.1.2 Inclusive CC DIS control selection

An independent control analysis was performed to setup the tau identification. MC events from single W production, where the W decays to a tau lepton and a neutrino ($W \rightarrow \tau\nu_\tau$) and the tau lepton subsequently decays into hadrons, were used as signal. The background simulation was based on an inclusive selection of CC DIS events. An inclusive CC DIS data sample was used to monitor the quality of the simulation. The selection was based on the e^+p data taking period from 1999 to 2000 with an integrated luminosity of $\mathcal{L}_{\text{int}} = 65.5\,\text{pb}^{-1}$. The selection required mainly large missing transverse momentum [96]. The online selection and the non-ep background rejection cuts were

[1]The recently installed and commissioned Silicon Micro Vertex Detector (MVD) is capable of measuring impact parameters of $\mathcal{O}(100\,\mu\text{m})$ [94, 95]. If the designed precision of the MVD will be reached, the identification via a displaced impact parameter might become in reach.

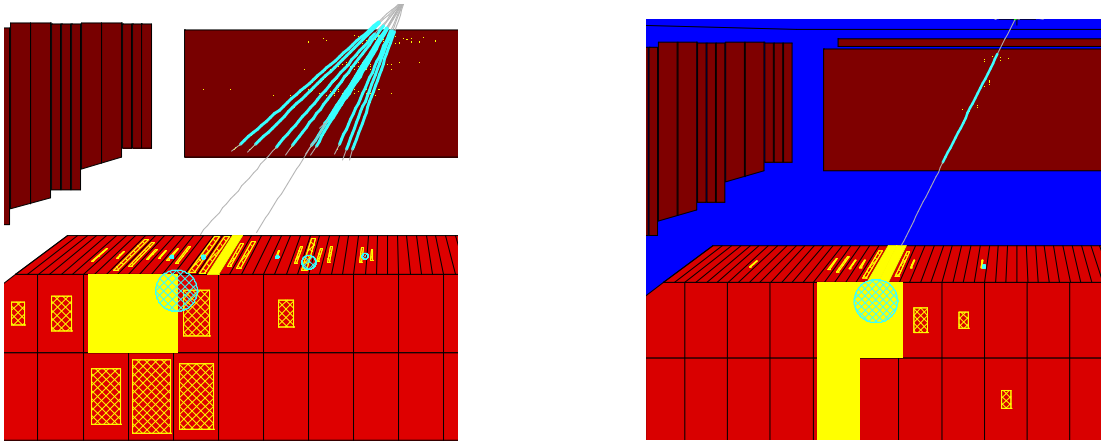

Figure 9.1: Response of the ZEUS tracking system and calorimeter to a) a QCD-jet from a photoproduction process and b) a jet from a $W \to \tau\nu_\tau$ decay with subsequent 1-prong hadronic decay of the tau lepton.

very similar to the ones used in the search for isolated leptons. The following list briefly describes the selection requirements that were applied to ensure a clean sample of CC DIS events. Only those cuts that were not also used in the search for isolated leptons are explained in more detail.

- *DST bit selection.* The charged current trigger bit DST B34 was required, selecting events selects events with $p_T^{\mathrm{ex1IR}} > 7\,\mathrm{GeV}$.
- *Non-ep rejection.*
  - CAL timing veto (for data only)
  - $|z_{vtx}| < 50\,\mathrm{cm}$
  - $n_{\mathrm{trk}}^{\mathrm{good}} > 0.2 \cdot n_{\mathrm{trk}} - 20$
  - Two-tracks cosmics rejection (3d-opening angle $< 178^o$)
  - The energy deposition in the hadronic part of the BCAL and RCAL was required not to exceed a fraction of 90% of the total energy deposition in the corresponding CAL section, if the total energy deposition exceeded a threshold of 5 GeV.
  - Rejection of cosmic muon events after visual scan.
- *Large missing transverse momentum*:
  - Transverse momentum in the CAL[2]: $p_T^{\mathrm{CAL}} > 20\,\mathrm{GeV}$.

[2]The transverse momentum used in this CC DIS control selection was not corrected for detector effects.

  - Transverse momentum outside the first inner ring of the FCAL: $p_T^{\mathrm{ex1IR}} > 9\,\mathrm{GeV}$

- *NC DIS and photoproduction rejection.* Events from NC DIS and photoproduction interactions were vetoed based on their characteristic event topology and on CAL energy-momentum-relations.

  - $\phi^{el}_{\mathrm{acopl}} > 0.2$
  - $p_T^{\mathrm{CAL}}/E_T^{\mathrm{CAL}} > 0.5$
  - $E - p_Z < 40\,\mathrm{GeV}$

- *Jet selection and electron rejection.* Only well reconstructed jets inside the CTD acceptance were considered. Remaining electrons were rejected based on the fraction of electromagnetic energy in the jet and the fraction of the jet energy carried by the most energetic track inside the jet. Only those events were accepted that contained at least one jet fulfilling all of the following requirements:

  - $E_T^{\mathrm{jet}} > 5\,\mathrm{GeV}$
  - $15^o < \theta_{\mathrm{jet}} < 164^o$
  - $ltf > 0$
  - $ltf + emfrac < 1.6$
  - $0.05 < emfrac < 0.95$
  - For the signal MC sample ($W \to \tau\nu_\tau$) it was additionally required that the reconstructed jet pointed within a radius of one in the $\eta - \phi$ plane into the direction of a hadronically decaying tau lepton, as obtained from the MC generator. This cut ensured a well defined signal sample that was used for the optimization of the tau finding technique.

Figure 9.2 shows control plots of global event variables for the inclusive CC DIS selection. The data are compared to the expectation from the simulation of CC DIS events and to the $W \to \tau\nu_\tau$ signal. Good agreement between data and CC DIS simulation can be observed for p_T^{CAL}, $E - p_Z$, $p_T^{\mathrm{CAL}}/E_T^{\mathrm{CAL}}$ and z_{vtx}. The signal falls far below the data for this inclusive CC DIS selection. 871 events were observed in the data, while 858 ± 2.18 events were expected from the simulation of CC DIS events. The expected number of events from the signal process was 1.14 ± 0.0083 events.

9.1.3 Jet shape observables

Previous analyses at HERA showed that the internal jet structure is generally well described by MC simulations [97,98]. For this analysis six observables were selected to distinguish tau jets from quark- and gluon-induced jets:

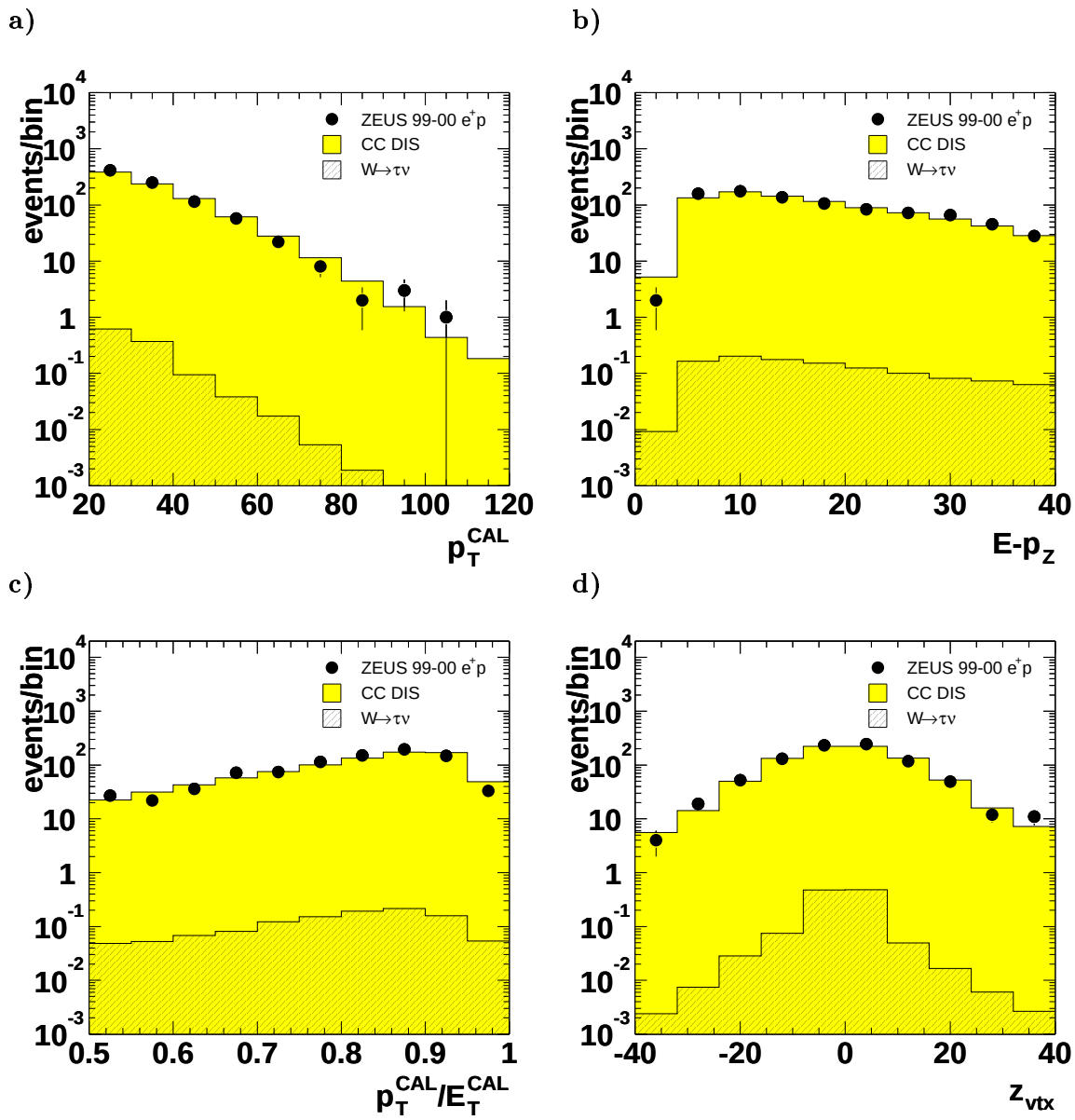

Figure 9.2: Global event variables for an inclusive selection of CC DIS events: a) Missing transverse momentum in the CAL, $p_T^{\rm CAL}$, b) $E - p_Z$, c) the ratio of missing transverse momentum to the total transverse energy, $p_T^{\rm CAL}/E_T^{\rm CAL}$, and d) the z-position of the event vertex, $z_{\rm vtx}$. Shown are the data (dots), a simulation of CC DIS events (shaded histograms) and the simulation of the single W-production signal $W \to \nu\tau$, where the τ decays hadronically (hatched histograms).

- the first moment of the radial extension of the jet energy deposition

$$\text{rmean} = \langle R \rangle = \frac{\sum_i E_i \cdot R_i}{\sum_i E_i},$$

  where the sum runs over the calorimeter cells associated to the jet, E_i is the energy of the cell i and R_i is defined as $R_i = \sqrt{\Delta\phi_i^2 + \Delta\eta_i^2}$, where $\Delta\phi_i$ ($\Delta\eta_i$) is the difference between the azimuthal angle (pseudorapidity) of the calorimeter cell i and the jet axis;

- the second moment of the radial extension of the energy deposition

$$\text{rrms} = \sqrt{\frac{\sum_i E_i (\langle R \rangle - R_i)^2}{\sum_i E_i}};$$

- the first moment of the projection of the energy depositions on the jet axis

$$\text{lmean} = \langle L \rangle = \frac{\sum_i L_i}{\sum_i E_i}, \text{ with } L_i = E_i \cdot \cos\theta_i^{\text{jet}},$$

  where L_i is the projection of the energy of the cell i on the jet axis and θ_i^{jet} is the angle between the direction of the cell i and the jet axis;

- the second moment of the projection of the energy depositions on the jet axis

$$\text{lrms} = \sqrt{\frac{\sum_i E_i (\langle L \rangle - \cos\theta_i^{\text{jet}})^2}{\sum_i E_i}};$$

- the number of subjets, subj, with a y_{cut} of $5 \cdot 10^{-4}$.
  The subjet multiplicity identifies the number of localised energy depositions within a jet that can be resolved using a resolution-criterion y_{cut}. The number of subjets was found by applying the same algorithm as was initially used to find jets. An exact definition can be found elsewhere [98–100];

- the invariant mass, $m_{\text{jet}}^{\text{obs}}$, of the jet calculated from the associated cells

$$m_{\text{jet}}^{\text{obs}} = \sqrt{(\sum_i E_i)^2 - (\sum_i p_x^i)^2 - (\sum_i p_y^i)^2 - (\sum_i p_z^i)^2},$$

  with $p_x^i = E_i \sin\theta_i \cos\phi_i$, $p_y^i = E_i \sin\theta_i \sin\phi_i$, $p_z^i = E_i \cos\theta_i$. θ_i and ϕ_i are the polar and azimuthal angle of cell i, respectively.

Figure 9.3 compares the inclusive CC DIS event sample to the MC simulation in each of the six observables. A logarithmic presentation was chosen for rmean, rrms, lmean and lrms to ensure a uniform and narrow distribution in the corresponding observable space and to avoid steeply rising or falling edges. For each event only the jet with

the largest value of the discriminant, D, as defined in the next section, enters the plot. The agreement between data and MC simulation is good. For each of the six observables a separation between the signal and the CC DIS selection can be seen. The expected signal however is very small and therefore a a multi-variate discrimination technique was used to fully exploit the information contained in the observables and their correlations.

9.1.4 Tau discriminant

To optimize the separation of the signal from the background, the six observables were combined in a discriminant, D, given for any point in the phase space

$$\vec{x} = (-\log(\text{rmean}),\ -\log(\text{rrms}),\ -\log(1-\text{lmean}),\ -\log(\text{lrms}),\ \text{subj},\ \text{m}_{\text{jet}})$$

as:

$$D(\vec{x}) = \frac{\rho_{\text{sig}}(\vec{x})}{\rho_{\text{sig}}(\vec{x}) + \rho_{\text{bg}}(\vec{x})},$$

where ρ_{sig} and ρ_{bg} are the density functions of the signal and the background events, respectively. The signal and background densities, sampled using MC simulations, were calculated for any point in the phase space using a method to estimate probability densities, which is based on range searching (PDE-RS) [101,102]. Figure 9.4 illustrates the calculation of D for an arbitary 2-dimensional jet-observable space[3] (x, y). The observable space is filled with a large number of jets from the MC generated signal and background samples. The value of D for any given jet with observable values (x_j, y_j) is calculated as the number of signal jets divided by the total number of jets in a small box around (x_j, y_j). As can be seen from this example, it is important to ensure a dense population of the observable space with both, signal and background jets, and to adjust the box size such that for any jet to be classified there are enough signal and background events in the box. The logarithmic representation for rmean, rrms, lmean and lrms minimizes those regions in the phase space, which are sparsely populated with signal or background jets. The minimum number of signal plus background jets in a box around the phase space point to be classified was set to 15. The values chosen for the edge length of the classification box were:

Observable	edge length
-log(rmean)	0.4
-log(rrms)	0.4
-log(1-lmean)	0.4
-log(lrms)	0.4
subj	1
m_{jet}	1.0 GeV

[3]The discriminant method can be used with any set of discriminating variables and is not restricted to jets. In this analysis however only jet-shape observables were considered for the discriminant.

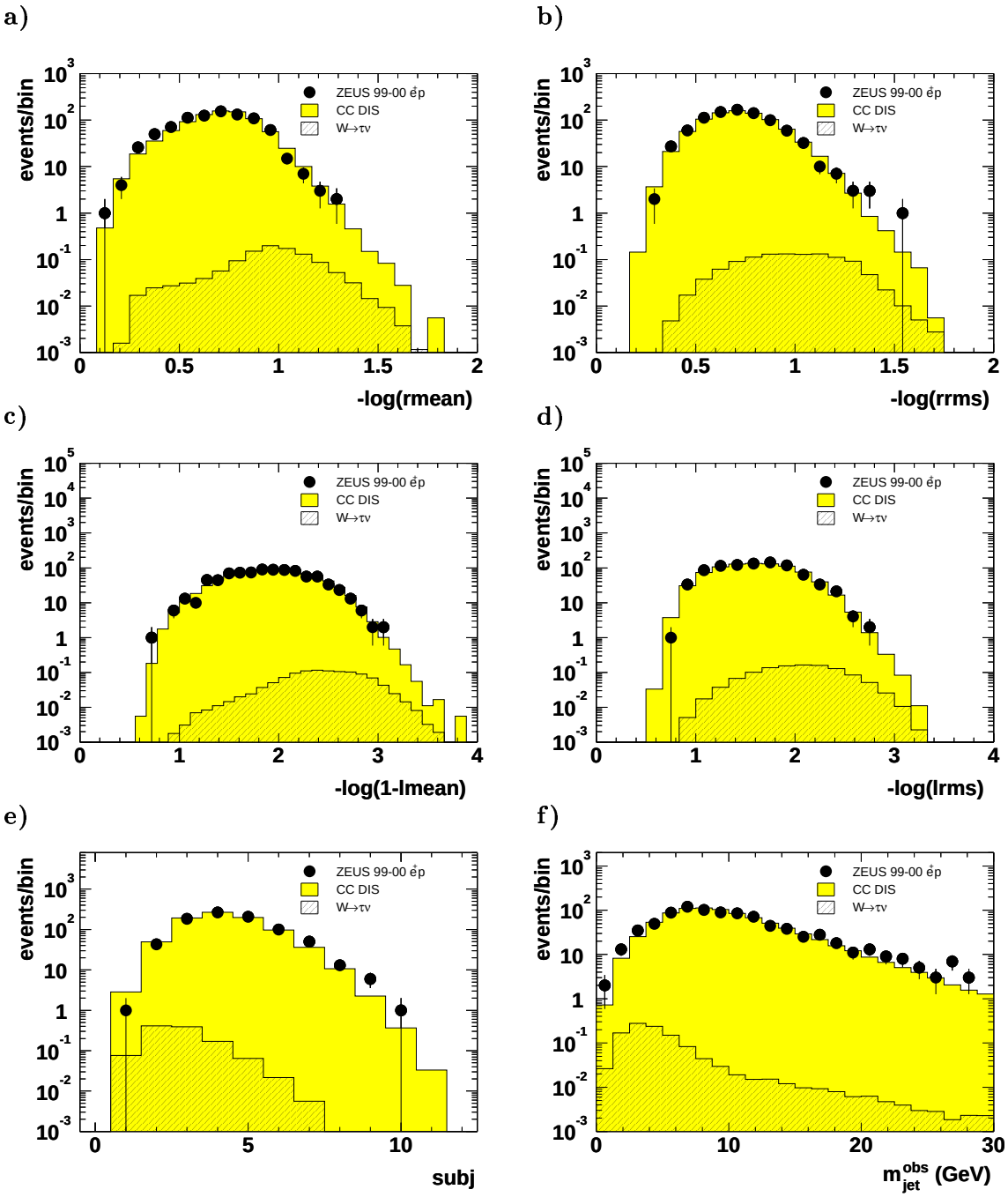

Figure 9.3: Observables characterising the internal jet structure for an inclusive selection of CC DIS events (see text for definitions). Shown are the data (dots), a simulation of CC DIS events (shaded histograms) and the simulation of the single W-production signal $W \to \nu\tau$, where the τ decays hadronically (hatched histograms).

A binary tree structure was used to store the information on the 6 jet-shape observables for the signal and background MC samples. The number of signal- and background-jets in the vicinity of a a given point in the 6-dimensional phase space were evaluated with an algorithm based on range searching, as explained in detail in [102].

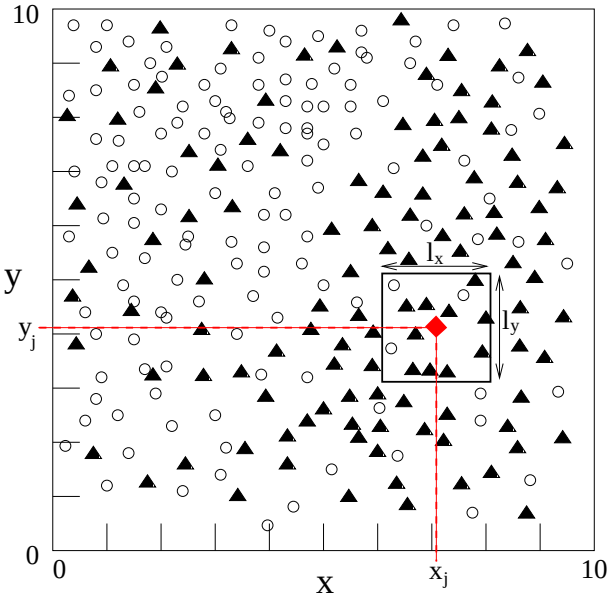

Figure 9.4: Example for the calculation of the discriminant D in an arbitrary 2-dimensional jet-observable space (x, y). The circles represent the simulated jets from the background sample, while the filled triangles represent the jets from the signal sample. The filled diamond represents the jet (x_j, y_j) to be classified. The disriminant D for this jet is given as the number of signal jets divided by the total number of jets inside the a box centered around (x_j, y_j) with edge length l_x and l_y.

Figure 9.5 shows the distribution of D for the MC-generated signal and background events and for the inclusive CC DIS data selection. The data is well described by the MC simulation for this inclusive selection. However, an excess of data events at large values of the discriminant can be observed already at this stage. The tau signal is clearly separated from the CC DIS background. The fraction of events, that passed all selection cuts, but could not be classified, was 0.7% for the CC DIS MC and 0.3% for the signal MC. Events were not classified, if the minimum number of 15 jets in the box around the corresponding phase space point was not reached.

The quality of the classification is characterized by the efficiency of the signal selection, ϵ_{sig}, the rejection of the background, R, and the signal-to-background ratio (separation power), S, which are defined for a given cut on the discriminant, D_{cut}, as follows:

$$\epsilon_{\text{sig}} = N_{\text{sig,selected}}/N_{\text{sig,total}}, \tag{9.1}$$

$$R = N_{\text{bg,total}}/N_{\text{bg,selected}}, \tag{9.2}$$

$$S = \sqrt{R} \cdot \epsilon_{\text{sig}}. \tag{9.3}$$

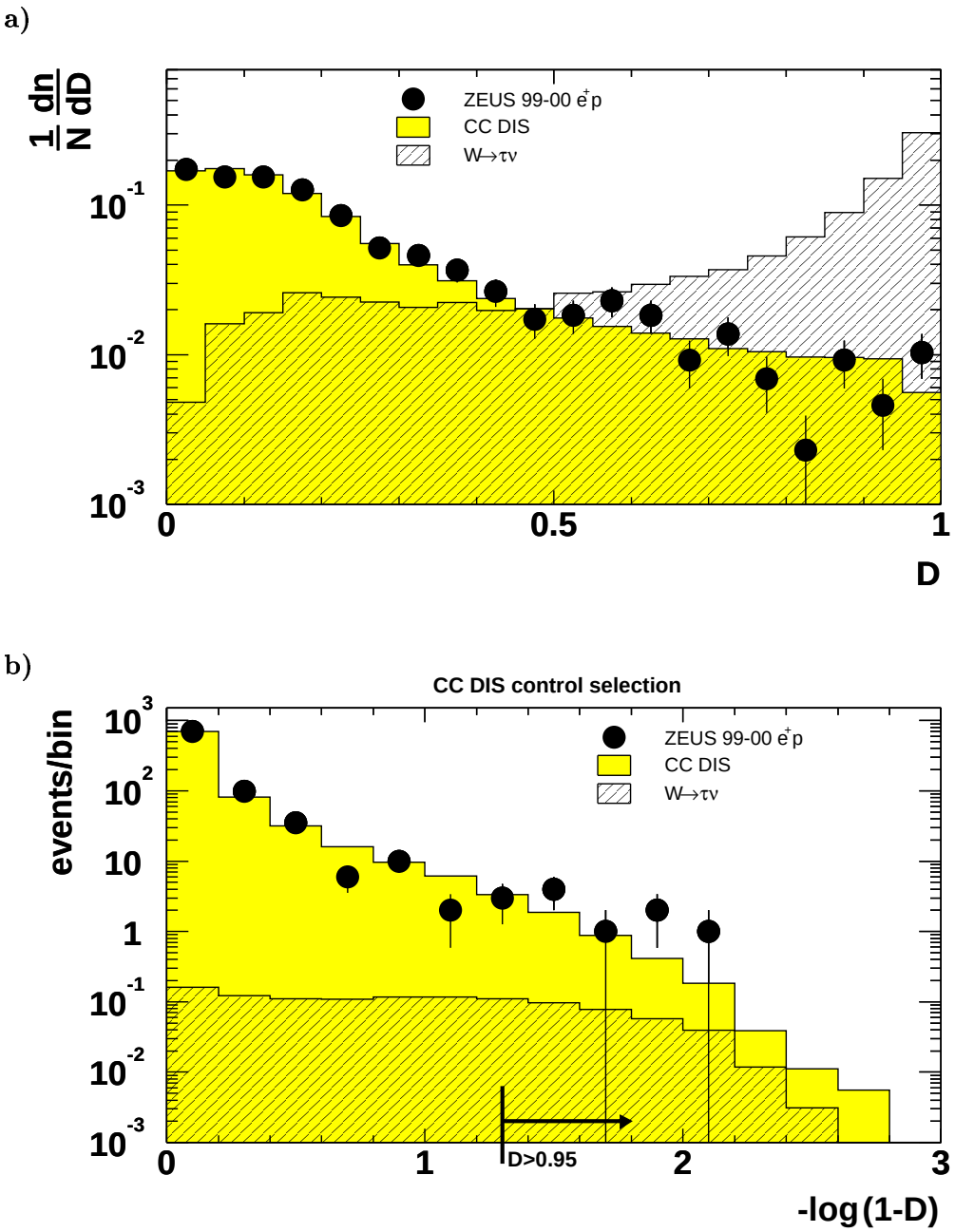

Figure 9.5: Distribution of the tau discriminant, D, for an inclusive selection of CC DIS data events, a simulation of CC DIS events and the simulation of the single W-production signal $W \to \nu\tau$, where the τ decays hadronically. In each event only the jet with the highest value of the discriminant enters. The histograms are normalized a) to the total number of events N and b) to the data luminosity. In b) the $-\log_{10}(1-D)$ distribution is displayed to show the region in which the tau lepton signal is expected more clearly.

$N_{\text{sig,total}}$ and $N_{\text{bg,total}}$ are the total number of signal and background events, respectively. $N_{\text{sig,selected}}$ and $N_{\text{bg,selected}}$ are the number of signal and background events with a value of $D > D_{\text{cut}}$, respectively. Figure 9.6a) shows the values of ϵ_{sig} and S as a function of the cut value on the discriminant D_{cut} for the CC DIS control selection. An optimal separation between signal and background is observed for a cut at approximately $D > 0.95$. For $D > 0.95$, a signal efficiency $\epsilon_{\text{sig}} = 31 \pm 0.2\%$, a background rejection $R = 179 \pm 6$ and a separation power $S = 4.1 \pm 0.1$ were obtained. The quoted uncertainties are the statistical uncertainties due to the limited number of generated MC events. Figure 9.6b) shows the values of ϵ_{sig} and S for the CC DIS control selection with the additional requirement that exactly one track had to be associated to the jet inside a radius of one in the $\eta - \phi$ plane. This additional requirement is relevant for the following search for one-prong hadronic tau decays. Also in this case an optimal separation between signal and background is observed for $D > 0.95$. The resulting signal efficiency was $\epsilon_{\text{sig}} = 22 \pm 0.2\%$, the background rejection $R = 637 \pm 41$ and the separation $S = 5.5 \pm 0.2$.

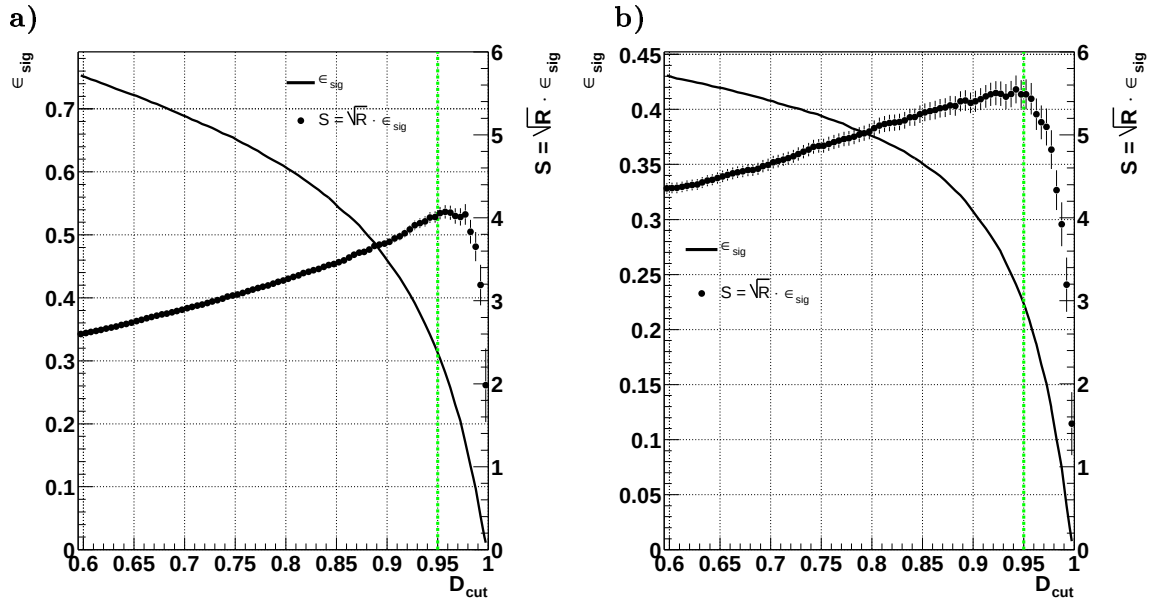

Figure 9.6: Signal Efficiency, ϵ_{sig} and separation, S, as a function of the cut value on the tau discriminant, D_{cut}, for the CC DIS control selection described in the text. The statistical uncertainty due to the limited number of generated MC events is shown for S. The vertical line indicates the cut value $D > 0.95$, which was used in this analysis. In a) there is no restriction on the number of tracks inside the jet, while in b) only jets with one track associated to the jet contribute.

Electrons can have a similar signatur in the detector as jets from hadronic 1-prong tau decays. The electron track is matched with a narrow cluster of energy depositions in the CAL. As opposed to tau-jets, the energy deposition is expected to be almost fully contained in the electromagnetic part of the CAL. Due to the absence of neutral decay

products, the transverse momentum of the electron track matches with the transverse momentum calculated from the energy deposition in the CAL. The tau discrimination method was optimized for separating tau-jets from quark- and gluon-induced jets. In addition, an efficient electron rejection has to be applied to avoid misidentification of electron-induced jets as tau jets. The efficiency of the electron rejection for electrons from NC DIS events was determined by studying a selection of NC DIS data events and samples of simulated NC DIS events. The following cuts were applied to reject the electron induced fake jets in this sample:

- $\phi^{el}_{\text{acopl}} > 0.2$
- $ltf > 0$
- $ltf + emfrac < 1.6$
- $0.05 < emfrac < 0.95$

An upper limit on the fraction of electrons, that passed these rejection cuts, of 3×10^{-6} was found. The same selection was used for an additional evaluation of the misidentification probability of QCD jets as tau jets. The rejection of one-track QCD jets from the NC DIS sample was found to be $R > 500$, in agreement with the results from the CC DIS selection. No significant dependence of the rejection on the transverse energy of the jets was found [103].

9.2 Preselection of tau candidate events

The sample of isolated tracks in events with missing transverse momentum, where the track was not identified as electron or muon (cf. section 7.2.1), was the starting point in the search for isolated tau leptons. After the electron and muon identification, 17 unidentified tracks remained in the data, while 10.3 ± 2.33 events where expected from all SM sources (0.80 ± 0.02 from single W production). The SM expectation consists mainly of badly reconstructed NC DIS events and of 2-jet CC DIS events. A visual scan of the 17 data events revealed that most of them have an event topology that is consistent with an NC DIS event, in which a high-energy scattered electron was not identified by the electron finder and the apparent missing transverse momentum was produced by a mismeasurement of the energy due to loss in dead material. Such events are not expected to be well reproduced by the detector simulation and therefore a reasonable agreement between the observed number of events and the expectation from simulated SM sources can be concluded for this small sample of isolated tracks remaining after the identification of electron and muon candidates. Figure 9.7a) shows the distribution of the acoplanarity angle, $\phi^{\text{trk}}_{\text{acopl}}$, for all unidentified isolated tracks. Most of the data events are observed at low values of the acoplanarity. The fraction of electromagnetic energy in the jet, $emfrac$, and the sum of the electromagnetic fraction and the leading track fraction, $emfrac{+}ltf$, are shown in Fig. 9.7b) and c) for the jets

associated to the isolated tracks. Remaining electron-induced fake jets are expected to have a large electromagnetic fraction and large leading track fraction. Another source of background are QCD jets from CC DIS events with a second jet from final state radiation. For such events the second jet is expected to be close to the main jet. Figure 9.7d) shows the distribution of the distance to the closest remaining jet in the event, $D_{\rm jet}$ for all unidentified tracks with associated jets. A cluster of simulated background events at low values of $D_{\rm jet}$, just above the isolation requirement for isolated tracks of $D_{\rm jet} > 1.0$ can be observed. The rate and kinematics of 2-jet events from CC DIS final state radiation, which are located at the very tail of the corresponding distributions, are challenging for the MC simulation and not expected to be precisely in agreement with the observation in the data.

The following selection cuts were designed to isolate candidate events for 1-prong hadronic tau decays by further reducing the background from badly reconstructed NC DIS events and from CC DIS events.

- *Track-jet-match.* Only those isolated tracks were considered for the following tau identification that were matched with a jet in the CAL ($D_{\rm jet} < 0.1$). The hadronic transverse momentum, $p_T^{\rm hadr}$, was recalculated after subtracting the momentum of this jet from the hadronic system.

- *NC DIS rejection.* The background from NC DIS events, where the scattered electron was not found by the electron finder, was reduced by applying the acoplanarity cut from the electron channel also to the unidentified isolated tracks:

$$\phi_{\rm acopl}^{\rm trk} > 0.14 \text{ rad.}$$

- *Rejection of not identified electrons.* Electrons, that were not identified by the electron finder, were rejected by the following requirements, which were based on an optimization performed for the CC DIS control selection from section 9.1.2 [93]:

$$emfrac < 0.95$$

$$ltf + emfrac < 1.6.$$

- *CC DIS rejection.* CC DIS events with an additional jet from final state radiation were rejected by a tighter cut on the distance of the isolated track to the closest remaining jet in the event:

$$D_{\rm jet} > 1.8.$$

Seven events remained after these additional cuts, while 2.18 ± 0.18 are expected from SM background (0.39 ± 0.015 from single W production). The distribution of the tau discriminant D is shown in Fig. 9.8 for this stage of the event selection. Three of the data events have a tau discriminant $D > 0.95$, and are therefore likely to come from tau decay. Pictures of the three tau candidate events from the ZEUS event display are shown in appendix C. Some selected event variables for the three tau candidate events are given in Tab. 9.2. The total expected SM background is 0.40 ± 0.096 (0.17 ± 0.010

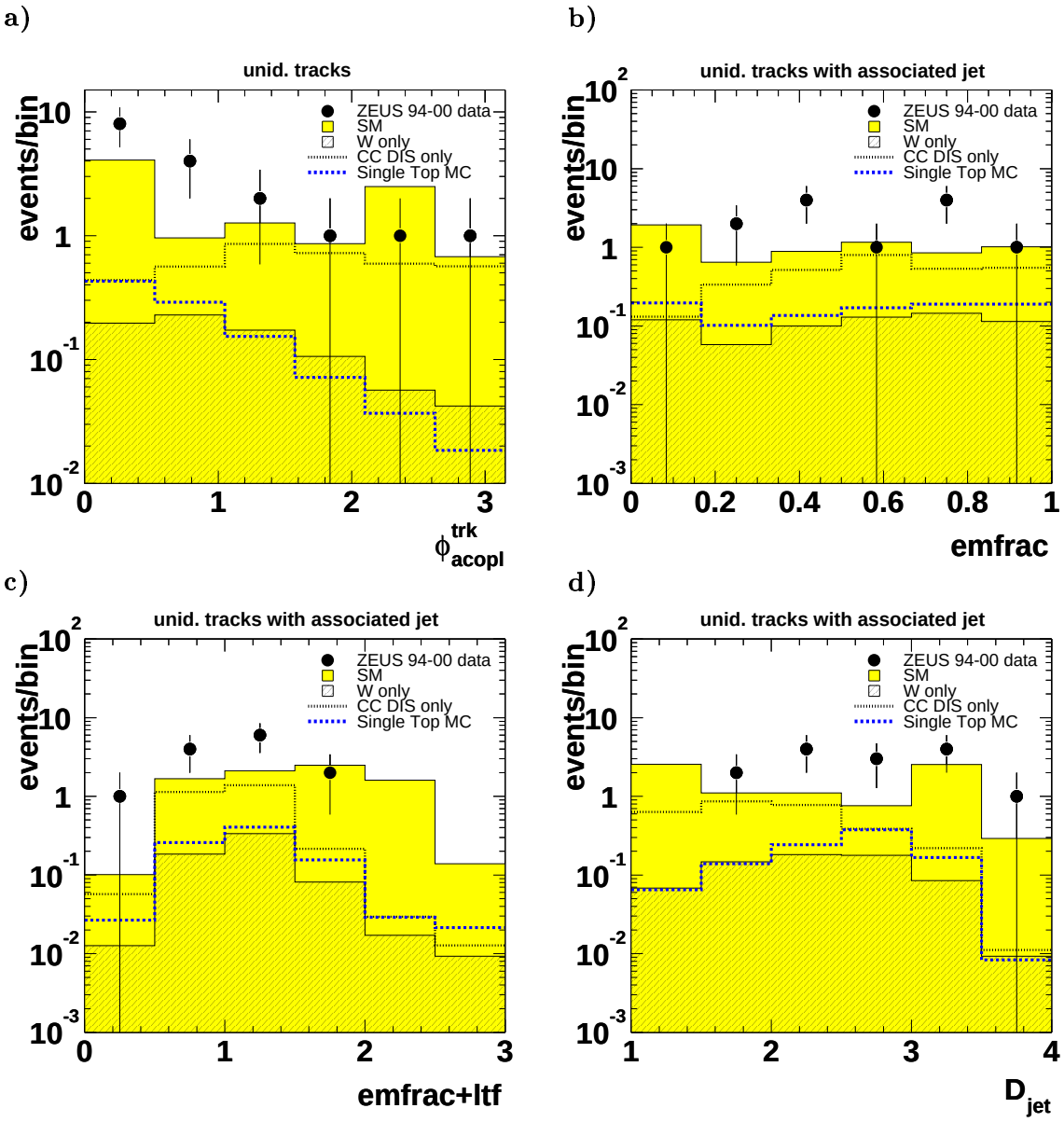

Figure 9.7: a) Acoplanarity angle, $\phi^{\mathrm{trk}}_{\mathrm{acopl}}$, b) electromagnetic fraction, $emfrac$, c) sum of electromagnetic fraction and leading track fraction, $emfrac + ltf$, and d) distance to the closest jet, D_{jet}, for all isolated tracks and their associated jets that remained unidentified after the electron and muon identification. The data (points) are compared to the SM expectations (shaded histograms). The hatched histograms represent the contribution from single W boson production in the SM. The dotted lines represent the contribution from CC DIS. The dashed lines represent the distribution of the single-top MC, including all decay channels of the W boson, normalized to an integral of one event.

	Tau 1	Tau 2	Tau 3
Centre of mass energy, $\sqrt{s}$	318 GeV	318 GeV	318 GeV
Collision type	e^-p	e^+p	e^+p
Run no., event no.	31173,6970	33358,19167	34169,5711
Transverse momentum in the CAL, $p_T^{\rm CAL}$	39 GeV	37 GeV	39 GeV
Hadronic transverse momentum, $p_T^{\rm hadr}$	9 GeV	48 GeV	38 GeV
Transv. momentum of the tau jet, $p_T^{\rm jet}$	45 GeV	21 GeV	41 GeV
Transv. momentum of the tau track, $p_T^{\rm trk}$	18 GeV	9 GeV	27 GeV
Charge of the tau track, q	-1	-1	+1
Azimuth angle of the tau track, $\phi_{\rm trk}$	9^o	256^o	205^o
Acoplanarity of the tau track, $\phi_{\rm acopl}^{\rm trk}$	40^o	45^o	55^o
Transverse mass, M_T	83 GeV	32 GeV	70 GeV
Reconstr. lept.-neutrino-hadr mass, $M_{l-\nu-{\rm had}}$	101 GeV; 130 GeV	181 GeV	126 GeV
Discriminant, D	0.956	0.994	0.977

Table 9.2: Kinematic variables for the tau-candidate events with $D > 0.95$. For the reconstructed lepton-neutrino-hadrons mass, $M_{l-\nu-{\rm had}}$, all physical solutions are given (cf. section 6.2.10).

from single W production). Figure 9.9a) shows the distribution of the transverse momentum of the hadronic system, $p_T^{\rm hadr}$, after applying the cut at $D > 0.95$. The value of $p_T^{\rm hadr}$ was obtained by subtracting the four-momentum of the tau-candidate from $p_T^{\rm CAL}$. The transverse momentum of the tau-track and of the tau-jet are shown in Fig. 9.9b) and Fig. 9.9c), respectively. Figure 9.9d) shows the distribution of the transverse mass, M_T, as obtained from the tau-jet and the missing transverse momentum:

$$M_T = \sqrt{2 p_T^{\rm jet} p_T^{\rm miss} (1 - \cos(\delta\phi_{\rm jet}^{\rm miss}))},$$

where $\delta\phi_{\rm jet}^{\rm miss}$ is the angular difference in the azimuthal plane between the tau jet and the direction of the missing transverse momentum.

9.3 Selection of events with large hadronic transverse momentum

A large value of the hadronic transverse momentum, $p_T^{\rm hadr}$, would be naturally obtained in a heavy particle decay in addition to the observed tau-candidate. An example of a heavy particle is a top quark produced in a flavour changing neutral current interaction. For such a signal a large value of $p_T^{\rm hadr}$ is expected. As seen in Fig. 9.9a), the SM background expectation is very low for large values of $p_T^{\rm hadr}$. The $p_T^{\rm hadr}$ distribution of the signal from the top decay on the other hand peaks at a value of approximately 60 GeV. As in the electron and muon channel, a final selection of events at large values

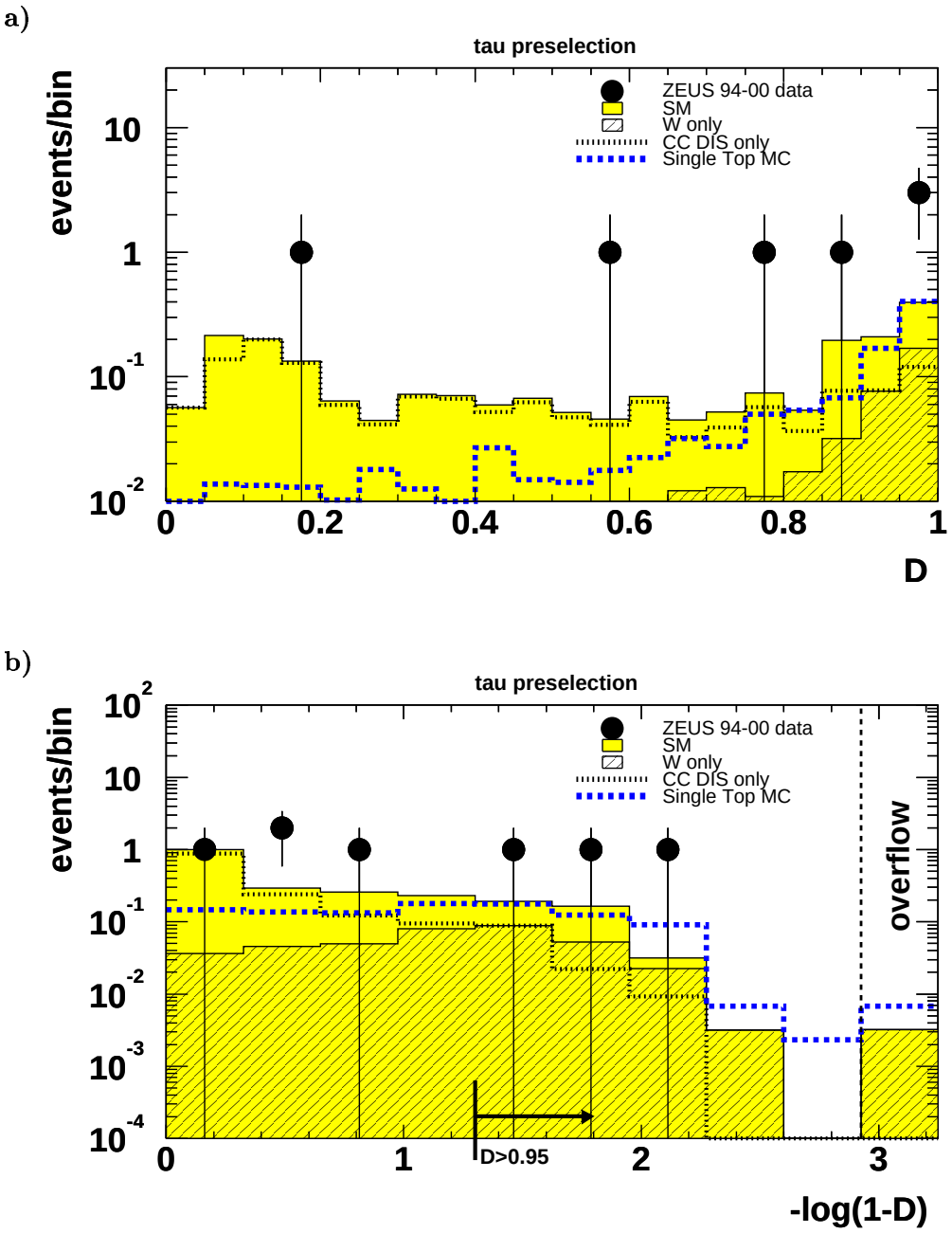

Figure 9.8: Distribution of the tau discriminant, D, for the tau preselection before applying the cut $D > 0.95$. The data (points) are compared to the SM expectations (shaded histogram). The hatched histograms represent the contribution from W boson production in the SM. The dashed lines represent the distribution of the single-top MC, including all decay channels of the W boson, normalized to an integral of one event. In a) the discriminant D is shown in a linear scale, while for b) the $-\log_{10}(1-D)$ distribution was chosen to show the region in which the tau lepton signal is expected more clearly. The last bin in b) contains also all events with a discriminant value above the upper edge of the bin.

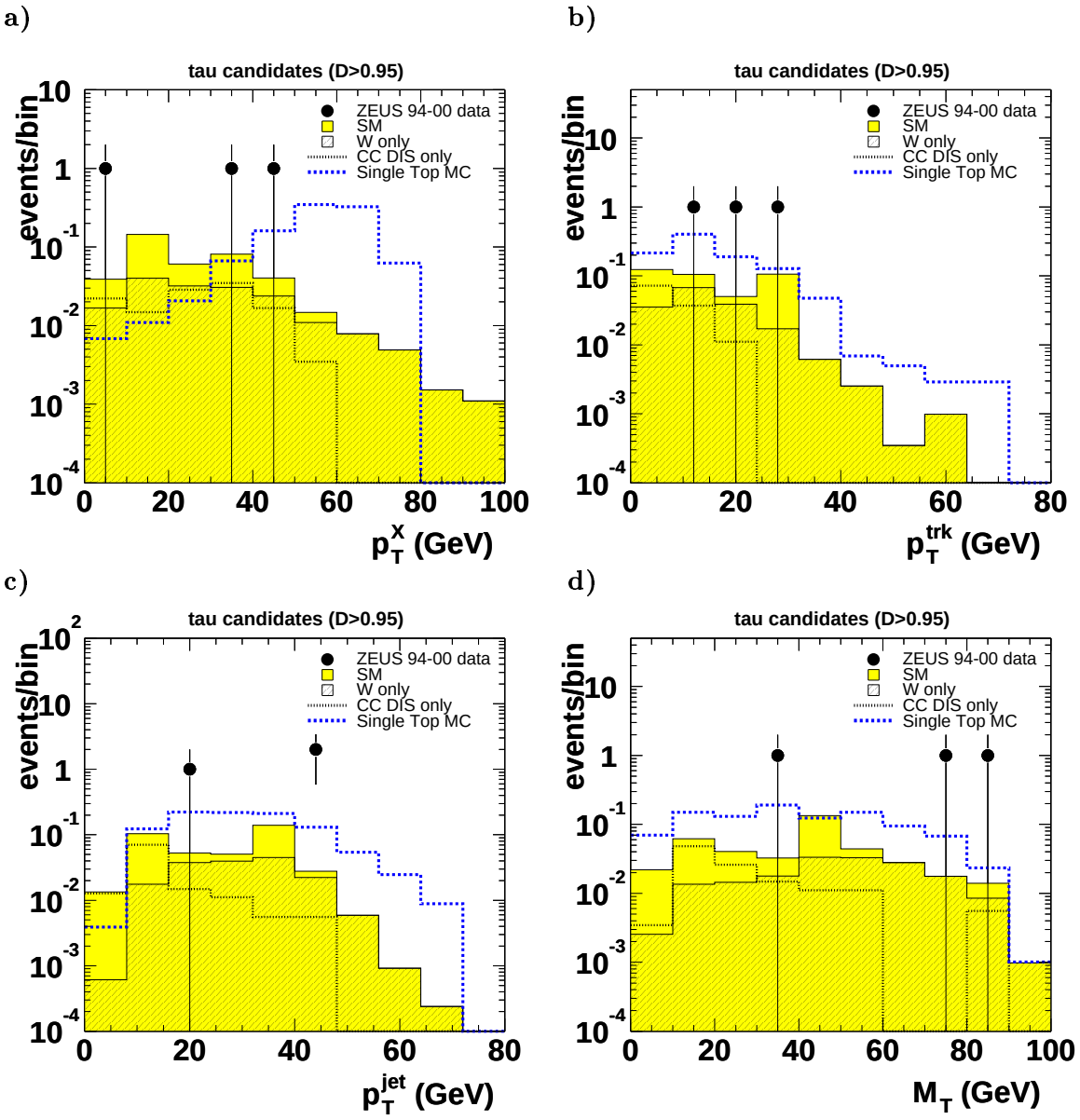

Figure 9.9: a) Hadronic transverse momentum, p_T^{hadr}, b) transverse momentum of the tau-track, p_T^{trk}, c) transverse momentum of the tau-jet, p_T^{jet} and d) transverse mass of the jet and the missing transverse momentum, M_T, for the tau preselection after applying the cut $D > 0.95$. The data (points) are compared to the SM expectations (shaded histograms). The hatched histograms represent the contribution from single W boson production in the SM. The dotted lines represent the contribution from CC DIS. The dashed lines represent the distribution of the single-top MC, including all decay channels of the W boson, normalized to an integral of one event.

Selection stage	Obs.	SM exp.	W only	s.-top eff. (%)
Unidentified tracks	17	10.3±2.33	0.80±0.02	1.76 ± 0.06
Tracks with associated jet	14	8.4±2.31	0.67±0.02	1.23 ± 0.05
$\phi^{\rm trk}_{\rm acopl} > 0.14$	11	6.9 ±1.86	0.74±0.02	1.55 ± 0.06
$D_{\rm jet} > 1.8$, $emfrac < 0.95$, $emfrac + ltf < 1.6$	7	2.2±0.18	0.39±0.02	0.68 ± 0.04
Discriminant $D > 0.95$	3	0.40±0.10	0.17±0.01	0.27 ± 0.02
$p_T^{\rm hadr} > 25\,{\rm GeV}$ (final selection)	2	0.20±0.03	0.10±0.01	0.27 ± 0.02
$p_T^{\rm hadr} > 40\,{\rm GeV}$	1	0.07±0.01	0.05±0.01	0.25 ± 0.02

Table 9.3: Event yields for the data from 1994-2000, corresponding background expectations and efficiencies for the single-top MC at different selection stages in the search for isolated tau leptons.

of $p_T^{\rm hadr}$ was performed. To design the final cut for events with high $p_T^{\rm hadr}$, the single-top MC was used as a template.

Following the analysis in the electron and muon channels, a final cut on the hadronic transverse momentum, $p_T^{\rm hadr}$, was applied to select events in a phase-space region where events involving decay products of a heavy particle would be expected and where the SM background is negligible. The very low number of expected background events in the final sample of tau candidates did not allow for a meaningful optimization of the final cut on $p_T^{\rm hadr}$ in the same way as it was performed in the electron and muon channels. In the tau channel only the SM expectation from single W production is obtained with a sufficient number of events to be compared with the expectation from signal production as function of a final cut value on $p_T^{\rm hadr}$ (Fig. 9.9a)). A final cut value of $p_T^{\rm hadr} > 25\,{\rm GeV}$ gives a good separation between the single-top signal and the expected number of events from single W boson production. For the final selection two events remained in the data, while 0.20 ± 0.03 events are expected from the SM, mainly from the production of single $W^{\pm}$ bosons (0.0966 ± 0.0072) and CC DIS. With a higher cut at $p_T^{\rm hadr} > 40\,{\rm GeV}$, one event remains in the data, while 0.07 ± 0.01 events are expected from the SM (0.050 ± 0.0051 from single W production). Table 9.3 summarises the event yields in the search for isolated tau leptons at all stages of the event selection. A comparison of the observed event yields with the expected number of events from the different SM background sources is shown in Fig. 9.10 for several stages of the event selection. Various background sources contribute for the early stages of the event selection, while for the final selection stages only CC DIS and W production lead to a sizeable contribution.

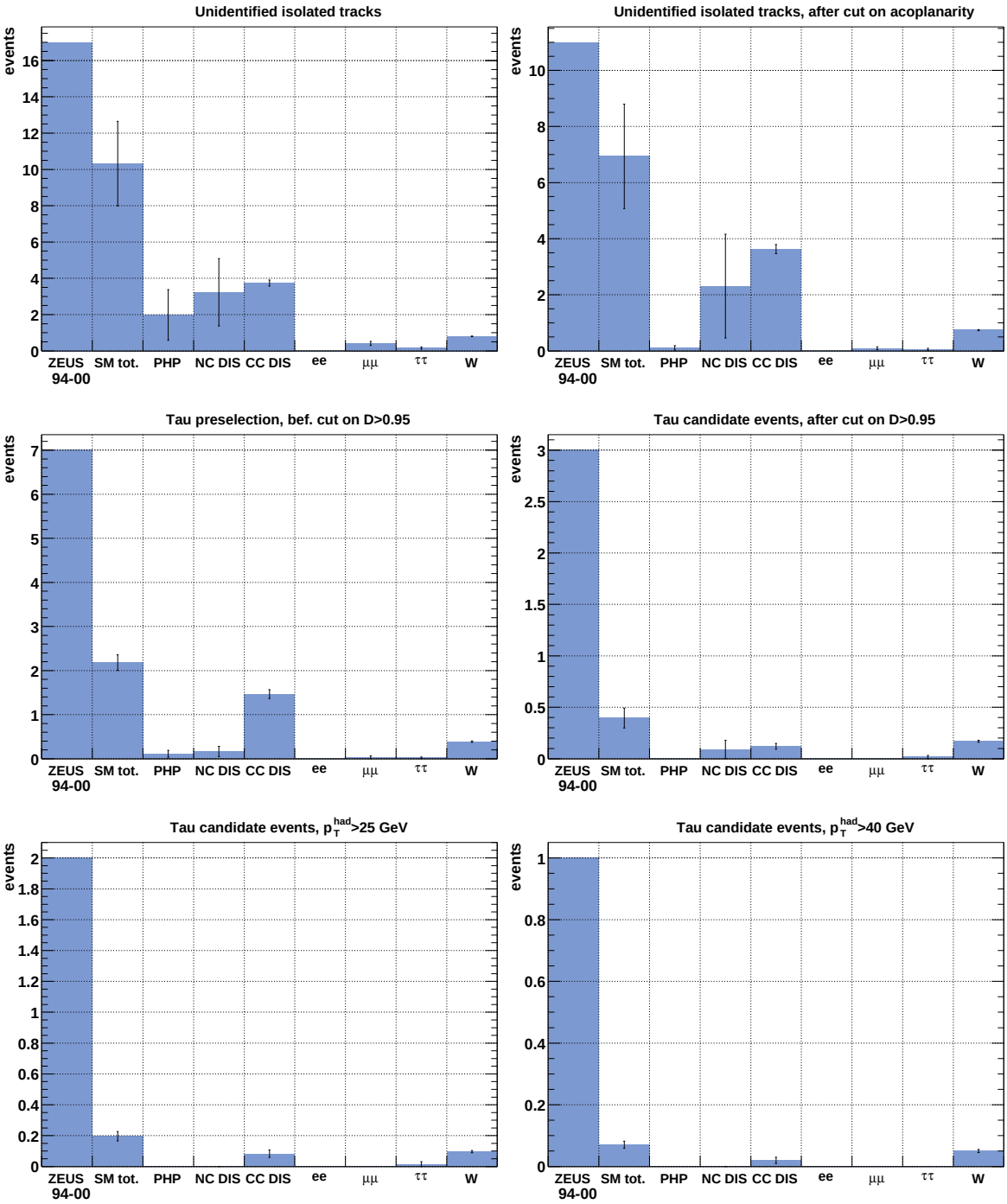

Figure 9.10: Event yields at different selection stages in the search for isolated tau leptons. Shown are the number of events in the data from 1994-2000 and the expected number of events for the different sources of simulated SM background. Only ARIADNE CDM is shown for NC DIS. The event yields for the SM background are scaled to the data luminosity. The error bars indicate the statistical uncertainties on the SM background expectation.

9.4 Systematic uncertainties

The errors quoted in the previous sections include only the statistical uncertainties due to the limited number of generated MC events. For an estimation of the systematic uncertainties, the following effects were taken into account:

- *Calorimeter energy scale.* An uncertainty of $\pm 1\%$ on the absolute energy scale of both the electromagnetic and the hadronic part of the FCAL and BCAL, which are the relevant CAL sections for this analysis, was assumed [80]. The effect of this uncertainty on the SM background expectation was estimated by varying all CAL energy related selection cuts by $\pm 1\%$. The resulting change in the background expectation was up to approximately $\pm 4\%$;

- *Simulation of the QCD cascade.* As in the electron and muon channel, the background from NC DIS and CC DIS events is expected to depend on the simulation model for the QCD cascade. Previous studies of NC DIS and CC DIS selections showed that the colour dipole model implemented in ARIADNE in general gives a better description of the final state [74,75]. It was thus chosen as the default for the simulation of NC DIS and CC DIS events. The dependence of the expected number of events on the choice of the simulation model was estimated by repeating the analysis using LEPTO-MEPS instead of ARIADNE to estimate both the NC DIS and CC DIS background. In the preselection of tau candidate events, a change of -20% in the total background estimation was observed. For the final selection at large values of p_T^{hadr} however, the limited number of remaining MC events did not allow for a reliable estimation of the change in the expected number of background events. The systematic uncertainty due to the simulation of the QCD cascade for the final selection stages was therefore estimated by scaling the -20% change in the expectation for the preselection with the corresponding contribution from NC DIS and CC DIS events;

- *Track selection.* A variation of the track-quality requirements and the angular range of the track selection resulted in changes of up to $\pm 15\%$ in the background estimation. Two variations were performed independently: a) the sample of tracks was restricted to those tracks with transverse momentum above 200 MeV (nominal value: 100 MeV) and b) the tracks considered as isolated tracks had to pass at least 5 radial superlayers of the CTD, corresponding to a restriction of the polar angle range to $\theta \gtrsim 25^o$ (nominal value: 3 radial superlayers, $\theta \gtrsim 17^o$);

- *W cross section.* The uncertainty for the cross section of single W-boson production was estimated to be $\pm 15\%$ [18–21], resulting in changes of up to $\pm 8\%$ in the total background expectation.

- *Tau discriminant method.* Both, the CC DIS control analysis from section 9.1.2 and the tau search analysis were repeated with modified sets of jet-shape observables for the tau-discriminant and different parameters for the box-sizes. The results were found to be stable. Hence no systematic uncertainty was assigned to the tau discriminant method.

Table 9.4 shows the resulting systematic uncertainties in percent of the total background estimation for the preselection of tau candidates (before the cut on $D > 0.95$) and for the final selection of tau candidates at large values of p_T^{hadr}. The statistical uncertainties and the resulting total uncertainties are also shown.

Systematic effect	tau preselection	$p_T^{\mathrm{hadr}} > 25\,\mathrm{GeV}$
CAL scale $\pm 1\%$	$\pm 3.5\%$	$\pm 4\%$
MEPS instead of CDM	-20%	-12%
Track selection	$\pm 15\%$	$\pm 15\%$
W cross section	$\pm 3\%$	$\pm 8\%$
Total systematic uncertainty	$^{+16}_{-25}\%$	$^{+17}_{-21}\%$
Total statistical uncertainty	$\pm 8\%$	$\pm 15\%$
Total systematic + statistical uncert.	$^{+17}_{-27}\%$	$^{+23}_{-26}\%$

Table 9.4: Systematic and statistical uncertainties in percent of the total number of expected background events for the preselection of tau candidates (before the cut on $D > 0.95$) and for the final selection of events at large values of p_T^{hadr}. The total uncertainties were obtained as the quadratic sum of the corresponding individual uncertainties.

9.5 Results

Table 9.5 gives the result for the final selection in the tau channel and compares it to the results of the search in the electron and muon channel, where agreement with the SM prediction was observed. For the electron and muon channels the final cut value for p_T^{hadr} was set to 40 GeV. The quoted errors on the background estimation include the statistical uncertainties as well as the systematic uncertainties discussed in section 9.4. The Poisson probability to observe two or more events, when $0.20^{+0.05}_{-0.05}$ events are expected, is 1.8%. The uncertainty on the SM prediction was taken into account for calculating the Poisson probability. For the cut at $p_T^{\mathrm{hadr}} > 40\,\mathrm{GeV}$, the corresponding poisson probability to observe one event, when 0.07 ± 0.02 are expected, is 6.7%.

A detailed discussion of the results in all channels and a comparison to the corresponding results obtained by the H1 collaboration can be found in chapter 10.

ZEUS 1994-2000 $e^{\pm}p$ $\mathcal{L} = 130.1\,\mathrm{pb}^{-1}$	Electron obs./exp. (W)	Muon obs./exp. (W)	Tau obs./exp. (W)
$p_T^{\mathrm{hadr}} > 25\,\mathrm{GeV}$	2 / 2.90 $^{+0.59}_{-0.32}$ (45%)	5 / 2.75 $^{+0.21}_{-0.21}$ (50%)	2 / 0.20 $^{+0.05}_{-0.05}$ (49%)
$p_T^{\mathrm{hadr}} > 40\,\mathrm{GeV}$	0 / 0.94 $^{+0.11}_{-0.10}$ (61%)	0 / 0.95 $^{+0.14}_{-0.10}$ (61%)	1 / 0.07 $^{+0.02}_{-0.02}$ (71%)

Table 9.5: Summary of the results of searches for events with isolated leptons, missing transverse momentum and large p_T^{hadr}. The number of observed events is compared to the SM prediction. The W component is given in parentheses in percent. The statistical and systematic uncertainties added in quadrature are also indicated.

Chapter 10

Comparison to other searches for isolated lepton events at HERA

The results of the search for isolated electron and muon events, as presented in this thesis, were confirmed by an independent second analysis performed by another group inside the ZEUS collaboration and were published in [55, 56]. A further consistency check was performed by adapting the event selection of this analysis to earlier preliminary results, which were obtained by another group inside the ZEUS collaboration and were presented at the EPS 2001 conference [104]. The result of this comparison showed good agreement between the independent analyses. A detailed description of the comparison can be found in appendix D.

Preliminary results of the search for isolated tau leptons were also confirmed by an independent second analysis and were published in [105].

This chapter compares the obtained results with searches for isolated electron and muon events and for single-top quark production, which were performed by the H1 collaboration[1]. The different analyses are compared in view of possible signal processes beyond the SM. An outlook is given to the future HERA II data taking period.

10.1 Results from the H1 collaboration

The H1 collaboration had first reported on the observation of an isolated muon event at large hadronic transverse momentum in a data sample of $4\,\mathrm{pb}^{-1}$ in 1994 [106]. An accumulating excess of both muon and electron events at large hadronic transverse momenta has been observed over the following years [1–5]. While the present ZEUS analysis is based on an inclusive selection of isolated track events, the event selection in the recent H1 analysis was based on the search for events from single W-boson

[1] Up to now the results for isolated lepton searches published by the H1 collaboration do not include the tau channel.

production[2] [5]. Preliminary H1 results are available for a subsequent final selection of single top-quark candidate events [4].

10.1.1 Search for isolated electrons and muons in events with missing p_T

The main selection criteria for the H1 analysis are compared to the corresponding ZEUS selection of isolated electrons and muons in Tab. 10.1. The main differences are the lower cut on $p_T^{\rm CAL}$ and the larger polar-angle acceptance for the H1 analysis. Additional cuts on the ratio of the anti-parallel to parallel components of the measured calorimetric transverse momentum, with respect to the direction of the calorimetric transverse momentum, on $E - p_Z$ and on the electron kinematics were applied in the H1 analysis, which are not reported in the table. Those additional cuts reduced the background mainly from NC DIS events and thus compensated for the lower cut on $p_T^{\rm CAL}$. Table 10.2 summarises the event yields from the H1 search for isolated leptons

Variable	H1		ZEUS	
	Electron	Muon	Electron	Muon
$\theta_{\rm lept}$	$5^0 < \theta_{\rm lept} < 140^o$		$17^0 < \theta_{\rm lept} < 115^o$	
$p_T^{\rm lept}$	$> 10\,{\rm GeV}$		$> 5\,{\rm GeV}$	
$p_T^{\rm CAL}$	$> 12\,{\rm GeV}$		$> 20\,{\rm GeV}$	
$D_{\rm jet}$	> 1.0		> 1.0	
$D_{\rm trk}$	> 0.5 for $\theta_{el} \geq 45^o$	> 0.5	> 0.5	
$\phi_{\rm acopl}$	$> 20^o$	$> 10^o$	$> 8^o$	-

Table 10.1: Comparison of the main selection requirements for H1 and ZEUS in the electron and muon channels.

with missing transverse momentum in e^+p scattering and the comparison with the signal from SM W and Z production [5]. After all selection requirements, but without a cut on the hadronic transverse momentum, $p_T^{\rm hadr}$, 10 electron candidate events were observed, while 7.2 ± 1.2 events were expected from the signal of W- and Z-production and 2.68 ± 0.49 events were expected from background sources. In the muon channel 8 events were observed in the data, while 2.23 ± 0.43 events were expected from signal processes and 0.33 ± 0.08 from background sources. At $p_T^{\rm hadr} < 25\,{\rm GeV}$ the agreement between the observed events and the SM expectation is good, while for larger values of $p_T^{\rm hadr}$ an excess of data events above the signal and background expectation was observed. 10 lepton events were observed at $p_T^{\rm hadr} > 25\,{\rm GeV}$, while 2.9 ± 0.5 events were expected from all SM sources. For $p_T^{\rm hadr} > 40\,{\rm GeV}$, six lepton events were seen, where 1.08 ± 0.22 events were expected from all SM sources. The probability for the SM expectation to fluctuate to the observed number of events or more is 10% for the full

[2] Also single Z-boson production ($ep \to eZ(\to \nu\bar{\nu})X$) was considered as a signal process in the H1 analysis. The contribution from this process was found to be less than 3%. In the present ZEUS analysis the Z contribution to the SM background expectation is neglected.

$p_T^{\rm hadr}$ range, 0.15% for $p_T^{\rm hadr} > 25\,{\rm GeV}$ and 0.12% for $p_T^{\rm hadr} > 40\,{\rm GeV}$. The uncertainties on the SM predictions were taken into account in calculating these probabilities. The quoted Poisson probabilities correspond approximately to a 3σ deviation from the SM expectation.

For the $e^- p$ data sample, which is not included in the table, one electron and no muon events were observed in the data, while 1.69 ± 0.22 electron events and 0.37 ± 0.06 muon events were expected from all SM processes.

To facilitate comparison between the two experiments, H1 has repeated a preliminary version of the analysis with the additional requirement that the polar angle of the isolated lepton was restricted to the ZEUS angular range [107]. All events for $p_T^{\rm hadr} > 25\,{\rm GeV}$ from the nominal analysis were also found with the restricted angular range. The Standard Model expectation was reduced by $20 - 25\%$.

e^+p data, $104.7\,{\rm pb}^{-1}$	Electrons			Muons		
	obs.	SM exp.	SM signal	obs.	SM exp.	SM signal
$p_T^{\rm hadr} < 12\,{\rm GeV}$	5	6.40 ± 0.79	4.45 ± 0.70	-	-	-
$12\,{\rm GeV} < p_T^{\rm hadr} < 25\,{\rm GeV}$	1	1.96 ± 0.27	1.45 ± 0.24	2	1.11 ± 0.19	0.94 ± 0.18
$25\,{\rm GeV} < p_T^{\rm hadr} < 40\,{\rm GeV}$	1	0.95 ± 0.14	0.82 ± 0.13	3	0.89 ± 0.14	0.77 ± 0.14
$p_T^{\rm hadr} > 40\,{\rm GeV}$	3	0.54 ± 0.11	0.45 ± 0.11	3	0.55 ± 0.12	0.51 ± 0.12

Table 10.2: Observed and predicted event rates for electron and muon candidates in the H1 analysis of all e^+p data (from [5]).

10.1.2 Search for single-top production in the leptonic channel

A more restrictive selection was applied to the sample of isolated lepton events, in order to isolate events from single top-quark production. The following description of this search corresponds to preliminary results, which were presented at the EPS conference in 2002 [4]. The p_T of the highest-p_T jet had to exceed 25 GeV (35 GeV for a polar angle $\theta_{\rm jet} < 35^o$), thus assuring a large hadronic activity, as expected from the subsequent decay of the b-quark from the top decay. The corresponding cut in the ZEUS analysis required the hadronic transverse momentum to exceed 40 GeV. A positive lepton charge, as expected from the top decay $t \to W^+ b \to l^+ X$, was required. To reduce the contribution from processes with off-shell W bosons, the transverse mass, M_T, had to exceed 10 GeV. No restriction on the lepton charge and on the transverse mass was made in the ZEUS final top-quark selection. The ZEUS final selection additionally required $E - p_Z$ not to exceed 47 GeV in the electron channel, while the corresponding cut $E - p_Z < 50\,{\rm GeV}$ was already applied to the preselection of isolated electron events in case of the H1 analysis. For the whole HERA I dataset of $115.2\,{\rm pb}^{-1}$, 3 electron and 2 muon events were found by H1 after these additional cuts, while 1.8 events were expected from SM background. The efficiency for detecting events from the signal MC ($\epsilon \times BR$) was 3.97% in the electron channel and 4.76% in the muon channel. The Poisson probability to observe 5 or more events, when 1.8 events

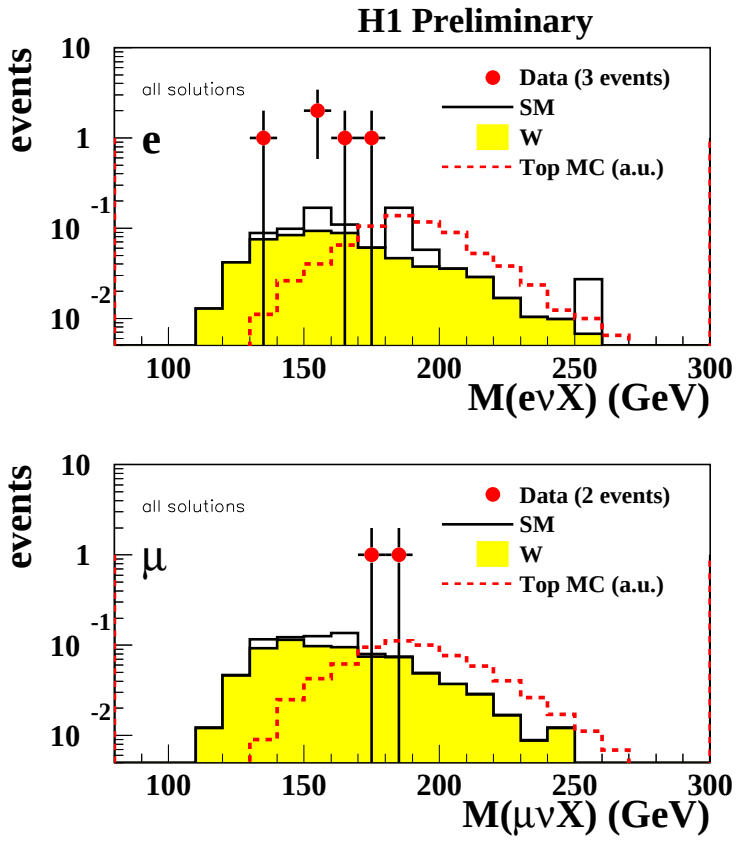

Figure 10.1: Distributions of the reconstructed invariant mass of the lepton-neutrino-hadron system for the H1 top candidates in the electron channel (upper plot) and in the muon channel (lower plot), compared to expectations from SM W boson production and a hypothetical single top-quark production signal, normalized to one event (from [4]).

are expected, is 2.6%. The observed excess is hence less significant than the one in the model independent search reported in the previous section.

Assigning the missing transverse momentum to a hypothetical neutrino and assuming the lepton-neutrino-system to originate from a W boson decay, the lepton-neutrino-hadron invariant mass $M_{l\nu X}$ of the H1 candidates was computed. The neutrino kinematics were obtained either from constraining the invariant mass of the lepton and neutrino to the W mass or from the energy-momentum-balance, if the scattered lepton was observed in the calorimeter. Two mass solutions were obtained for each event. For three of the candidate events only one solution is compatible with the kinematic constraints, while for the other two candidates both solutions are acceptable. The reconstructed mass is compatible with that of the top quark for most of the events, as shown in Fig. 10.1.

10.1.3 Search for single-top production in the hadronic channel

The H1 collaboration has also performed a search for single top-quark production in the hadronic decay channel of the W boson and presented the preliminary results at the EPS 2002 conference [4]. The event selection required three jets with transverse energies $E_T^{jet1} > 40\,\text{GeV}$, $E_T^{jet2} > 25\,\text{GeV}$ and $E_T^{jet3} > 20\,\text{GeV}$. The photoproduction background was reduced by requiring one of the 2-jet masses and the 3-jet mass to be compatible with the W boson mass and the top mass, respectively. The number of observed events in the hadronic channel was found to be in agreement with SM expectations, as in the corresponding ZEUS analysis. The sensitivity of the searches in the hadronic channel is however lower than for the leptonic channel, due to the larger expected background.

10.1.4 Exclusion limits on single-top production

The H1 results from the leptonic and the hadronic channels were, as in the ZEUS analysis, used to obtain an upper bound on the single top cross section, which is:

$$\sigma(ep \to etX, \sqrt{s} = 318\,\text{GeV}) < 0.43\,\text{pb} \quad \text{at } 95\%\ \text{C.L.}.$$

The corresponding upper limit on the anomalous $t-u-\gamma$ coupling, assuming all other anomalous FCNC couplings to be zero and $BR(t \to bW) = 100\%$, was:

$$\kappa_{tu\gamma} < 0.22.$$

The exclusion limits are less stringent than the corresponding ZEUS limits of $\sigma(ep \to etX, \sqrt{s} = 318\,\text{GeV}) < 0.225\,\text{pb}$ and $\kappa_{tu\gamma} < 0.174$, due to the excess observed by H1 in the leptonic channel.

The H1 limit contains both statistical and systematic uncertainties folded in channel-by-channel. In the present ZEUS analysis the uncertainty on the top mass was found to be the dominating one. The limit calculation was performed for three different values of the top mass, neglecting other sources of uncertainty.

The 95% C.L. upper limit on the single top-quark production cross section from the hadronic channel of the H1 analysis corresponds to an upper limit of 5.4 events from single top quark decays in the electron and muon channels of the e^+p dataset [4]. Therefore the interpretation of the five observed lepton events as anomalous top-quark production is not ruled out by the H1 analysis in the hadronic channel.

The ZEUS upper bound on the single-top cross section would correspond to a maximum of 2.0 observed top events in the leptonic channel of the H1 analysis. The observed number of 5 events in the H1 analysis is compatible with originating from the expectation value of 1.8 background events plus an additional signal of 2.0 events. The interpretation of the observed excess in the H1 leptonic analysis as anomalous top-quark production is therefore also not ruled out by the result of the ZEUS analysis.

10.2 Processes beyond the Standard Model

In the following the observed event yields in the H1 and ZEUS analyses are compared to the expectation from hypothetical signal processes beyond the SM. The discussion allows an evaluation of the respective significance of the deviations in the channels presented. In section 10.2.1 a general model assuming anomalous production of W bosons is considered as a possible source of high-p_T lepton events. Single top-quark production is chosen as a more specific model in section 10.2.2. Section 10.2.3 considers the anomalous production of tau leptons as a source for the excess in both the H1 electron/muon analysis and the ZEUS tau analysis.

10.2.1 Anomalous W production

Anomalous production of W bosons in a theory beyond the SM was considered as an explanation of the observed excess of electron and muon events at large p_T^{hadr} in the model independent search for isolated lepton events performed by the H1 collaboration [5]. In the following the expected event yields from such a signal process are compared to the observations in the H1 electron and muon channel for $p_T^{\mathrm{hadr}} > 40\,\mathrm{GeV}$ (6 events), in the ZEUS electron and muon channel for $p_T^{\mathrm{hadr}} > 40\,\mathrm{GeV}$ (0 events) and in the ZEUS tau channel for $p_T^{\mathrm{hadr}} > 25\,\mathrm{GeV}$ (2 events). It was assumed that the signal process would lead to the production of a W boson with a cross section $\sigma_{\mathrm{W,BSM}}$ and subsequent SM decay of the W boson. For this scenario the efficiency in the ZEUS tau channel is approximately 11 times lower than in both the ZEUS and H1 electron/muon channel.

The negative log-likelihood function F for the combination of i independent channels is defined as:

$$F(\sigma_{\mathrm{W,BSM}}) = -\sum_i \ln P_i(N^i_{\mathrm{obs}}, N^i_{\mathrm{BG}} + N^i_{\mathrm{exp}}(\sigma_{\mathrm{W,BSM}})), \tag{10.1}$$

where $P_i(N^i_{\mathrm{obs}}, N^i_{\mathrm{BG}} + N^i_{\mathrm{exp}}(\sigma_{\mathrm{W,BSM}}))$ is the Poisson probability for the observed number of events N^i_{obs} in channel i, if N^i_{BG} background events and $N^i_{\mathrm{exp}}(\sigma_{\mathrm{W,BSM}})$ signal events from a hypothetical signal process with cross section $\sigma_{\mathrm{W,BSM}}$ are expected[3]. The detection effeciency for the hypothetical W signal in the different channels was estimated from the corresponding efficiencies for SM single W-boson production. The uncertainties on the SM background expectations were taken into account in obtaining the Poisson probabilities.

Figure 10.2 a) shows $F(\sigma_{\mathrm{W,BSM}})$ for various combinations of the different channels. The minima of the $F(\sigma_{\mathrm{W,BSM}})$ curves, $F_{\mathrm{min}}(\sigma_{\mathrm{min}})$, correspond to the cross section with the highest probability for the observed event yields in the corresponding combination of channels. The values of $\sigma_{\mathrm{W,BSM}}$, for which $F(\sigma_{\mathrm{W,BSM}})$ has increased by 0.5 units above

[3] The considered full HERA I data sets contain data taking periods at CMS energies of both 300 GeV and 318 GeV. Hence the value of $\sigma_{\mathrm{W,BSM}}$ corresponds to the luminosity weighted average of a value at $\sqrt{s} = 300\,\mathrm{GeV}$ and one at $\sqrt{s} = 318\,\mathrm{GeV}$.

$F_{\min}$, define the 1σ confidence interval for $\sigma_{\min}$ [108], which is quoted as the uncertainty on the value of $\sigma_{\min}$ in the following.

For the ZEUS electron and muon channel analysis, where no events were observed, the most probable scenario corresponds to the SM background expectation, without additional contribution from a signal process: $\sigma_{\min}^{\mathrm{ZEUS-el/mu}} = 0^{+0.5}_{-0.0}\,\mathrm{pb}$. The most probable value of the anomalous W production cross section for the H1 measurement, where an excess of events above the SM prediction was observed, was obtained as $\sigma_{\min}^{\mathrm{H1-el/mu}} = 6.3^{+3.6}_{-2.7}\,\mathrm{pb}$. An even higher signal would be compatible with the ZEUS observation in the tau channel, where an excess above a very small background expectation was observed: $\sigma_{\min}^{\mathrm{ZEUS-tau}} = 22.1^{+21.7}_{-13.5}\,\mathrm{pb}$. The 1σ error on this estimated value is larger than in the analyses in the electron and muon channels, due to the smaller efficiency in the tau channel. The values of $\sigma_{\min}$ for the considered combinations of channels lie in between the corresponding values for the individual channels. For the combination of all H1 and ZEUS channels, a value of $\sigma_{\min}^{\mathrm{all}} = 2.8^{+1.8}_{-1.4}\,\mathrm{pb}$ was obtained.

The compatibility of the considered combinations of measurements was estimated from a Monte Carlo experiment. Event numbers were randomly generated for the individual channels, following a Poisson distribution with the corresponding value of $N^i_{\mathrm{BG}}+N^i_{\mathrm{exp}}(\sigma)$ used as expectation value. A Monte Carlo event for a given combination of n channels consists of a set of event numbers $(N_1, \ldots, N_n)$. For each of the Monte Carlo generated events the value of F is obtained in analogy to eq. 10.1 as a measure of the probability for this event to occur. A probability P_{obs} characterizing the actual observation in the corresponding channels was then defined as the fraction of generated Monte Carlo events with $F \geq F_{\min}$. A small value of P_{obs} corresponds to the conclusion that the actual observation has a low probability to occur when simulating the experiment with the given assumptions on the expected number of events. Table 10.3 shows the values for $\sigma_{\min}$, $P_{\mathrm{obs}}(\sigma_{\min})$ and $P_{\mathrm{obs}}(\sigma = 0)$ for the individual channels and all possible combinations. $P_{\mathrm{obs}}(\sigma_{\min})$ corresponds to the probability assuming the most probable cross section for the considered combination, while $P_{\mathrm{obs}}(\sigma = 0)$ corresponds to the probability assuming no signal. All combinations, that include the ZEUS electron/muon channel results have a low value of $P_{\mathrm{obs}}(\sigma_{\min})$ of the order of 1%, while the combination of the ZEUS tau channel and the H1 electron/muon channel analysis has a large value of $P_{\mathrm{obs}}(\sigma_{\min}) = 30\%$. This indicates that the observed excess in both the H1 electron/muon and the ZEUS tau analysis are compatible within 1σ, given the assumption of an anomalous W production signal, while the ZEUS electron/muon analysis is in contradiction to this assumption. The value of $P_{\mathrm{obs}}(\sigma = 0)$, which gives the probability for the observation assuming no signal, is large only for the ZEUS electron/muon analysis, where no excess was observed. For the H1 analysis alone a value of 0.12% was obtained, corresponding approximately to a 3σ significance. For the combination of all H1 and ZEUS measurements a very small probability of approximately 10^{-4}, corresponding to a 3.7σ significance, was obtained. This probability, though small, is not small enough to claim the observation of a deviation from the SM.

Anomalous W production			
channel	$\sigma_{\min}$	$P_{\text{obs}}(\sigma_{\min})$	$P_{\text{obs}}(\sigma = 0)$
ZEUS electron/muon	$0^{+0.5}_{-0.0}$ pb	28%	28%
H1 electron/muon	$6.3^{+3.6}_{-2.7}$ pb	100%	0.13%
ZEUS tau	$22.1^{+21.7}_{-13.5}$ pb	100%	1.8%
ZEUS electron/muon $\wedge$ ZEUS tau	$0^{+1.3}_{-0.0}$ pb	1.1%	1.1%
ZEUS electron/muon $\wedge$ H1 electron/muon	$2.1^{+1.6}_{-1.3}$ pb	1.2%	0.12%
ZEUS tau $\wedge$ H1 electron/muon	$7.7^{+3.7}_{-2.9}$ pb	30%	0.005%
ZEUS el./muon $\wedge$ H1 el./muon $\wedge$ ZEUS tau	$2.8^{+1.8}_{-1.4}$ pb	0.43%	0.011%

Table 10.3: Most probable cross-section values $\sigma_{\min}$ of a hypothetical W production signal for all possible combinations of the H1 and ZEUS analysis results in the different channels. The values of $P_{\text{obs}}(\sigma_{\min})$ and $P_{\text{obs}}(\sigma = 0)$, as explained in the text, are also given for each of the combinations.

10.2.2 Single-top production

Following the discussion in the previous section, a more specific model assumption on the anomalous W production process was made by comparing the obtained event yields with the prediction from anomalous single top-quark production with a cross section $\sigma_{\text{sing.top}}$. Here $\sigma_{\text{sing.top}}$ corresponds to the luminosity weighted average of a value at $\sqrt{s} = 300\,\text{GeV}$ and one at $\sqrt{s} = 318\,\text{GeV}$. In case of the H1 analysis, the preliminary results for the single-top production search were considered [4] to obtain the observed numbers of events, background expectation values and signal efficiencies for single-top producion. The considered observed event numbers and background expectations for the ZEUS channels were identical to the ones from the previous section, while for the signal efficiency the values for single-top production were used. For this scenario the efficiency in the ZEUS tau channel is approximately 24 times lower than in the ZEUS electron/muon channel and 30 times lower than in the H1 electron/muon channel. Figure 10.2 b) shows the value of the negative log-likelihood function $F(\sigma_{\text{sing.top}})$ as function of a hypothetical single-top-production cross section $\sigma_{\text{sing.top}}$. Also here the uncertainties on the SM background expectations were taken into account when calculating the Poisson probabilities. The values of $\sigma_{\min}$, $P_{\text{obs}}(\sigma_{\min})$ and $P_{\text{obs}}(\sigma = 0)$ for the individual channels and all considered combinations are given in Tab. 10.4. As expected from the very low efficiency for single-top quark production, the most probable single-top production cross section reaches a large value of $\sigma_{\min} = 4.8^{+4.7}_{-2.9}\,\text{pb}$ for the ZEUS tau channel. In this scenario, as can be seen from the values of $P_{\text{obs}}(\sigma_{\min})$, the combination of ZEUS electron/muon and ZEUS tau and the combination of all channels have a small probability, while the combination of ZEUS and H1 electron/muon and the combination of H1 electron/muon and ZEUS tau are compatible ($P_{\text{obs}}(\sigma_{\min}) = 6\%$ in both cases). The increased compatibility for the combinations, where the H1 electron/muon analysis is involved, corresponds to the fact that the observed excess in this dedicated top search analysis is less significant than the excess in the generic search for isolated electrons and muons, on which the results from the previous section were

based. The values of the probabilities for the no-signal hypothesis, $P_{\text{obs}}(\sigma = 0)$, are for the ZEUS analyses identical to the ones from the W hypothesis, where the same background expectations were used. For H1 the no-signal hypothesis gets a higher probability in the dedicated single-top search, where the excess is smaller and the expected SM background is larger than in the generic search for isolated electrons and muons. Hence the combinations of the channels, where the H1 electron/muon analysis is involved, have also a larger probability $P_{\text{obs}}(\sigma = 0)$ for the single-top hypothesis.

Anomalous single-top production			
channel	σ_{min}	$P_{\text{obs}}(\sigma_{\text{min}})$	$P_{\text{obs}}(\sigma = 0)$
ZEUS electron/muon	$0^{+0.06}_{-0.0}$ pb	28%	28%
H1 electron/muon	$0.33^{+0.26}_{-0.20}$ pb	100%	4.3%
ZEUS tau	$4.8^{+4.7}_{-2.9}$ pb	100%	1.8%
ZEUS electron/muon $\wedge$ ZEUS tau	$0^{+0.09}_{-0.0}$ pb	1.1%	1.1%
ZEUS electron/muon $\wedge$ H1 electron/muon	$0.07^{+0.14}_{-0.07}$ pb	6.3%	3.8%
ZEUS tau $\wedge$ H1 electron/muon	$0.43^{+0.3}_{-0.22}$ pb	6.4%	0.24%
ZEUS el./muon $\wedge$ H1 el./muon $\wedge$ ZEUS tau	$0.12^{+0.16}_{-0.12}$ pb	0.77%	0.29%

Table 10.4: Most probable cross-section values σ_{min} of a hypothetical single-top production signal for all possible combinations of the H1 and ZEUS analysis results in the different channels. The values of $P_{\text{obs}}(\sigma_{\text{min}})$ and $P_{\text{obs}}(\sigma = 0)$, as explained in the text, are also given for each of the combinations.

10.2.3 Anomalous tau production

Anomalous direct production of tau leptons in a process beyond the SM, as considered in section 3.3.2, could be the cause of both the two tau events observed in the ZEUS search and the excess of electron and muon events at large values of p_T^{hadr} in the H1 isolated lepton analysis. In this scenario the tau leptons do not originate from W decays and hence the expected signal in the electron/muon channel consists only of the electron/muon decay channel of the tau lepton, with a total branching ratio of 35%. In the following it is assumed that the decay products of the anomalously produced tau leptons are detected with the same efficiency as in the corresponding SM W-production channels. It follows that the expected number of events in the electron/muon channel of both the H1 and ZEUS electron/muon analysis is approximately the same as the one in the ZEUS tau channel.

Figure 10.2 c) shows the value of the negative log-likelihood function $F(\sigma_{\text{sing.top}})$ as function of the hypothetical tau-production cross section $\sigma_{\tau,\text{BSM}}$. The values of σ_{min}, $P_{\text{obs}}(\sigma_{\text{min}})$ and $P_{\text{obs}}(\sigma = 0)$ for the individual channels and all considered combinations are given in Tab. 10.5. The most probable cross-section value for the combination of all channels of $\sigma_{\text{min}} = 1.2^{+0.72}_{-0.56}$ corresponds to 2 expected signal events in the ZEUS tau channel as well as in the H1 and ZEUS electron/muon channels. Compared to the

anomalous W production scenario and the single-top production scenario, the compatibility of the ZEUS tau channel with the H1 electron/muon channel is increased, due to the fact that all channels have a similar efficiency in this scenario. The probabilities for the no-signal hypothesis, $P_{\rm obs}(\sigma = 0)$, are identical to the ones in the anomalous W production scenario, since the same background expectations were assumed. The probability for the combination of all observations, $P_{\rm obs}(\sigma_{\rm min}) = 3.0\%$, is higher in this scenario than for the previously discussed assumptions.

Anomalous tau production			
channel	$\sigma_{\rm min}$	$P_{\rm obs}(\sigma_{\rm min})$	$P_{\rm obs}(\sigma = 0)$
ZEUS electron/muon	$0^{+0.32}_{-0.0}$ pb	28%	28%
H1 electron/muon	$3.8^{+2.2}_{-1.6}$ pb	100%	0.13%
ZEUS tau	$1.2^{+1.2}_{-0.7}$ pb	100%	1.8%
ZEUS electron/muon $\wedge$ ZEUS tau	$0.5^{+0.57}_{-0.36}$ pb	7.6%	1.1%
ZEUS electron/muon $\wedge$ H1 electron/muon	$1.2^{+0.99}_{-0.76}$ pb	1.3%	0.12%
ZEUS tau $\wedge$ H1 electron/muon	$2.2^{+1.12}_{-0.88}$ pb	42%	0.005%
ZEUS el./muon $\wedge$ H1 el./muon $\wedge$ ZEUS tau	$1.2^{+0.72}_{-0.56}$ pb	3.0%	0.011%

Table 10.5: Most probable cross-section values $\sigma_{\rm min}$ of a hypothetical anomalous tau-production signal for all possible combinations of the H1 and ZEUS analysis results in the different channels. The values of $P_{\rm obs}(\sigma_{\rm min})$ and $P_{\rm obs}(\sigma = 0)$, as explained in the text, are also given for each of the combinations.

10.3 H1 and ZEUS isolated lepton events in the future

In this section it is investigated how the future HERA II data taking can help to clarify the origin of the excess of isolated electron and muon events at large values of $p_T^{\rm hadr}$ in the H1 analysis. An integrated luminosity of $1\,{\rm fb}^{-1}$ was originally anticipated within 5 years of HERA II data taking [109]. The recently started commissioning phase of the H1 and ZEUS data taking after the luminosity upgrade however has revealed serious problems with synchrotron radiation and particle backgrounds. Measures to improve the background situation have been adopted in an ongoing shutdown.

In the following it is assumed that both H1 and ZEUS will continuously analyse their new data in the same way as before and that the SM background rates and signal efficiencies will resume at the level of the combined 1994-2000 analyses. Also improvements in the detectors are not taken into account and the tau channel is not considered, due to its much lower efficiency as opposed to the electron and muon channels. Uncertainties on the expected event yields were taken into account by scaling the uncertainties of the 1994-2000 analyses with the expected future luminosity.

Figure 10.3 compares different scenarios for the observed event yields in the future H1 and ZEUS analysis of isolated lepton events. Shown are the probability to observe $N_{\rm obs}$ or more events, assuming that only SM background processes contribute to the observed number of events. The probability is displayed as a function of the additional HERA II luminosity. The starting point corresponds to the present situation of the 1994-2000 analyses. Three scenarios are shown:

- *Scenario 1: high rate.* The first scenario assumes that both experiments will observe events at a rate corresponding to the event rate $R_{\rm H1}$ of the 1994-2000 e^+p H1 analysis. For ZEUS, the corresponding rate $R_{\rm ZEUS}$ was obtained by scaling the H1 rate with the different luminosities and signal efficiencies:

$$R_{\rm ZEUS} = \frac{N_{bg}^{\rm ZEUS}}{\mathcal{L}_{\rm ZEUS}} + (N_{\rm obs}^{\rm H1} - N_{bg}^{\rm H1}) \cdot \frac{\epsilon_{\rm ZEUS}}{\epsilon_{\rm H1}\mathcal{L}_{\rm H1}},$$

  where $N_{bg}^{\rm ZEUS}$ and $N_{bg}^{\rm H1}$ are the 1994-2000 background expectation of the H1 and ZEUS analysis, respectively, $N_{\rm obs}^{\rm H1}$ is the number of observed events in the 1994-2000 H1 isolated lepton analysis, $\mathcal{L}_{\rm ZEUS}$ and $\mathcal{L}_{\rm H1}$ are the 1994-2000 luminosities, $\epsilon_{\rm ZEUS}$ is the single-top efficiency in the ZEUS analysis and $\epsilon_{\rm H1}$ is the efficiency for SM single W production for $p_T^{\rm hadr} > 40\,{\rm GeV}$ in the H1 isolated lepton analysis. The combined results for H1 and ZEUS were obtained by adding both the expected number of observed events and the expected number of background events from both experiments. The error used for the background observation in the combined result was calculated as the quadratic sum of the individual errors for the H1 and ZEUS analysis. In this scenario the significance of the excess observed by H1 increases from the starting point of approximately 3σ. Each step in the probability curve corresponds to the observation of a new candidate event. For an additional luminosity of $200\,{\rm pb}^{-1}$, approximately 10 new single-top candidate events are observed. The Poisson probability for the total number of observed or more events, assuming only background sources, drops to 10^{-9}, corresponding to a 5σ significance level for a deviation from the SM. Also ZEUS observes an excess above the SM background expectation in this scenario, which, however, is less significant due to the absence of single-top candidate events in the 1994-2000 data and due to the larger background expectation. The significance of a deviation from the SM in the ZEUS analysis is between 2σ and 3σ for an additional luminosity of $200\,{\rm pb}^{-1}$. For this value of the additional luminosity, the combined number of observed events in the H1 and ZEUS analysis corresponds already to a more significant excess than in the H1 analysis alone.

- *Scenario 2: medium rate.* The second scenario assumes that both experiments will observe events at the average of the previous H1 and ZEUS rates, corresponding to 50% of the excess observed by H1 in the 1994-2000 analysis. In this case a 5σ deviation from the SM for the H1 analysis is reached only after an additional luminosity of $800\,{\rm pb}^{-1}$. For the combination of the H1 and ZEUS results, this significance level is reached already at $500\,{\rm pb}^{-1}$. The ZEUS analysis alone reaches a significance level of 4σ only after the design value of the integrated luminosity of $1000\,{\rm pb}^{-1}$.

- *Scenario 3: SM background rate.* The third scenario assumes that both experiments will observe events at the rate of the SM background expectation. The excess in the H1 observation above the background expectation becomes less significant in this case with increasing luminosity. For an additional luminosity of $200\,\mathrm{pb}^{-1}$ it decreases from 3σ to 2σ. The ZEUS analysis stays in agreement with the SM expectation. The combined ZEUS and H1 result are within approximately 1σ in agreement with the SM expectation.

The expected results for the three scenarios show that the future HERA II data taking will help to clarify the significance of the excess observed by H1 in the 1994-2000 analysis. The sensitivity is expected to increase when including also the tau channel. The improvements in both the H1 and the ZEUS detector for the HERA II run period will allow to further improve the analyses, in particular with respect to the tracking in the forward direction.

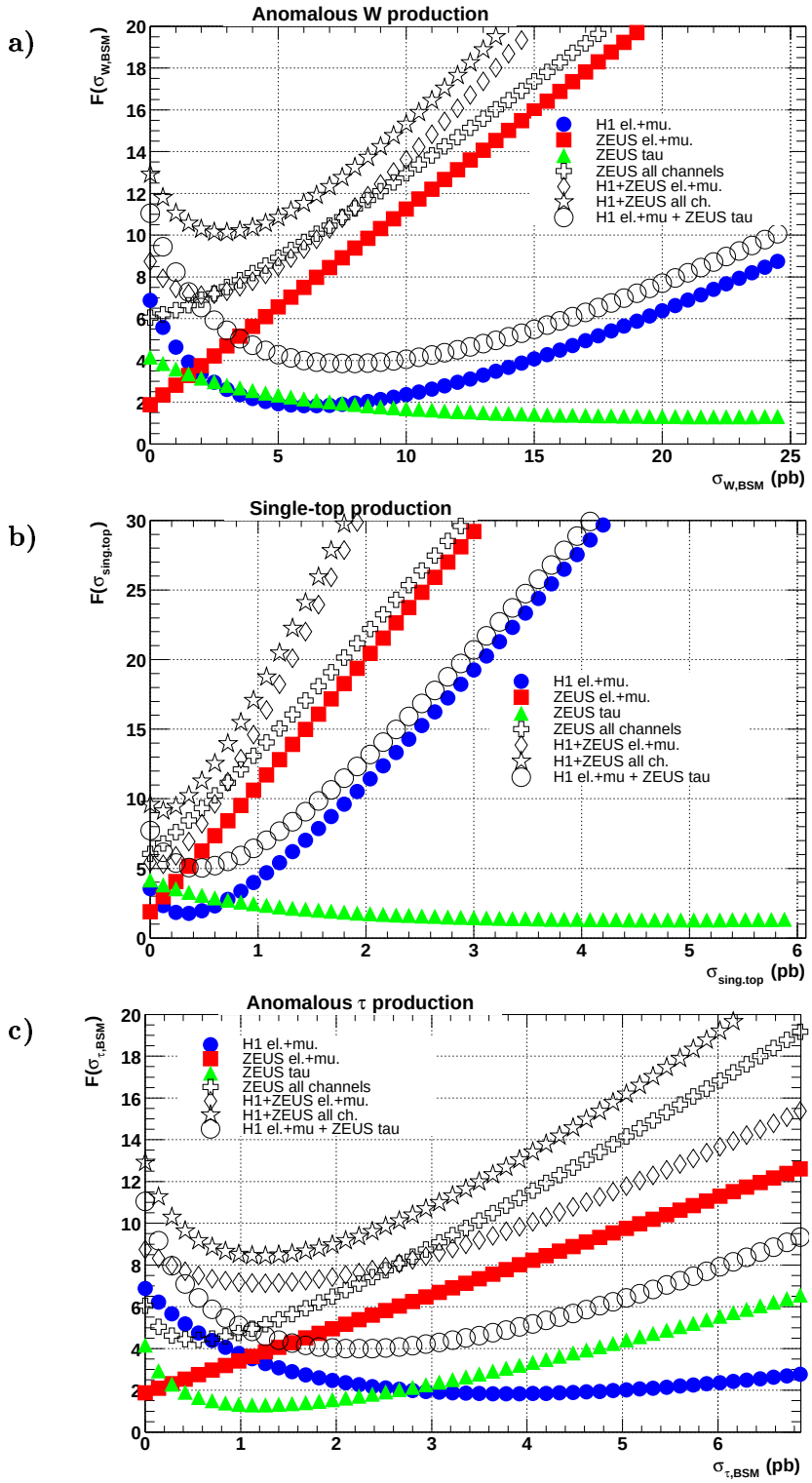

Figure 10.2: Value of the negative log-likelihood function, F, for the observed event yields in the H1 and ZEUS searches for isolated leptons, as a function of a) a hypothetical anomalous W production signal with cross section $\sigma_{\mathrm{W,BSM}}$, b) a hypothetical single-top production signal with cross section $\sigma_{\mathrm{sing.top}}$ and c) a hypothetical anomalous τ production singal with cross section $\sigma_{\tau,\mathrm{BSM}}$. The value of F for all possible combinations of the different search channels is also shown.

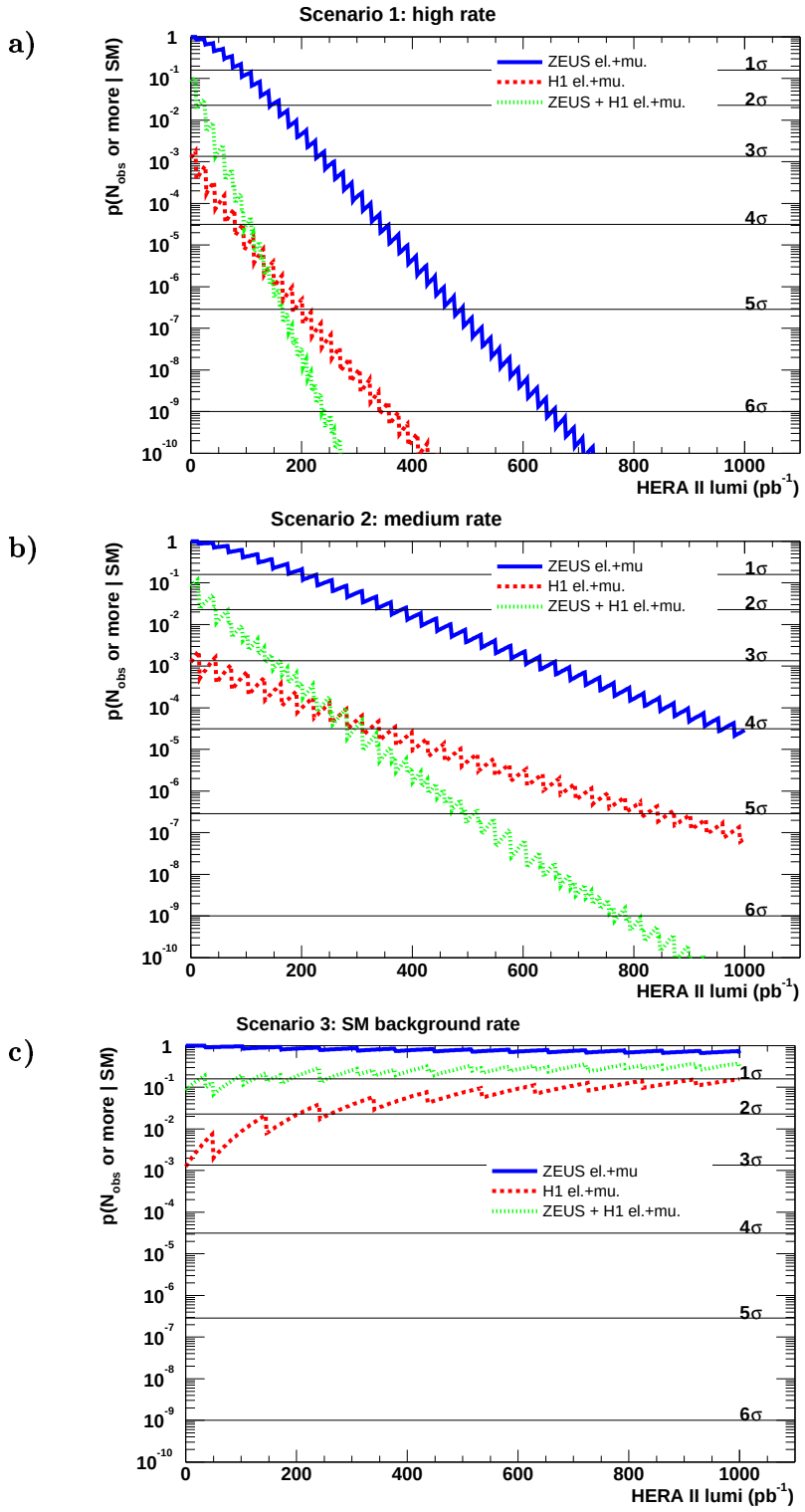

Figure 10.3: Poisson probabilities of future event yields in the H1 and ZEUS isolated electron and muon searches for three different scenarios of the future HERA II data taking, as explained in the text. Shown are the probabilities to observe $N_{\rm obs}$ or more events in the data, assuming that only SM background processes contribute. The horizontal lines indicate the 1σ to 6σ significance levels for a deviation from the SM.

Chapter 11

A radiation monitor for the ZEUS Micro Vertex Detector

A radiation monitoring system based on silicon PIN diodes and Radiation Field Effect Transistors (RadFETs) is described in this chapter. It has been designed and installed to protect the ZEUS Silicon Micro Vertex Detector (MVD) from radiation damage during HERA operation. The MVD is briefly introduced, followed by a description of the relevant types of background radiation in the HERA environment. The radiation hardness of the MVD is discussed, which leads to the requirements for a radiation monitoring system. The concept and layout of this radiation monitoring system are presented. First results from the commissioning phase of the HERA-II running period are shown, during which the radiation monitoring system has proven to be a reliable and highly necessary tool. The chapter ends with a short summary and conclusions.

11.1 The HERA upgrade and the ZEUS Micro Vertex Detector

The HERA collider underwent a major upgrade [109] during the years 2000-2001. The aims of the upgrade were to increase the maximum instantaneous luminosity from 1.5 to $7.5 \cdot 10^{31}$ cm^{-2} s^{-1} and to provide longitudinally polarised electrons for the collider experiments H1 and ZEUS, thus giving higher sensitivity to electro-weak physics and physics beyond the Standard Model.

The lepton and proton beam focussing system has been redesigned to move the separation of the two beams closer to the interaction region and thus help to increase the instantaneous luminosity. This included the installation of two superconducting magnets (GO and GG) inside the detector, extending from $z = 2.0$ m to $z = 5.2$ m (GO) and from $z = -3.3$ m to $z = -2.0$ m (GG).

The ZEUS experiment has been equipped with new tracking detectors extending in the proton beam direction, the Straw Tube Tracker (STT) and the Silicon Micro Vertex

Detector (MVD). They improve the precision of the existing tracking system and allow the identification of events with secondary vertices produced by the decay of long-lived states like hadrons with charm or bottom quarks and τ leptons.

The MVD is composed of a barrel (BMVD) and forward (FMVD) part, fitting inside a cylinder of 324 mm diameter defined by the inner wall of the Central Tracking Detector (CTD). The readout electronics, based on the HELIX 128-v3.0 [110] chip, have been mounted inside the active volume, close to the silicon sensors. The BMVD (FMVD) consists of 600 (112) sensors. The silicon strip sensors are made of high resistivity n-type silicon (3 kΩ·cm$< \rho <$ 8 kΩ·cm) with 300 μm active thickness. On one side p^+ strips are implanted with a strip pitch of 20 μm. The readout pitch is 120 μm, with five intermediate strips between two readout strips. More details on the MVD design and mechanical structure can be found elsewhere [111, 112].

11.2 Radiation background in the ZEUS interaction region

The three main sources of background radiation at HERA are direct and backscattered synchrotron radiation, off-momentum electrons or positrons and proton-beam-gas events. In addition, severe damage due to partial beam loss can occur. The irradiation from the primary *ep* interactions however is negligible. During the years of HERA-I operation (1992-2000) the experiments accumulated an average dose of 50 Gy/year [113]. Most of this dose was received during well identified accidents, while the average dose rate during good beam conditions was considerably lower. In the following the different sources of background radiation and their relation to the HERA machine operation are discussed.

11.2.1 Synchrotron radiation

Direct synchrotron radiation from the lepton beam contains photons at high energy, with a mean critical energy[1] of $E_{\mathrm{crit}} = 85\,\mathrm{keV}$ (for $E_{\mathrm{lept}} = 27.5\,\mathrm{GeV}$). Direct synchrotron radiation reaches the ZEUS detector in time with the lepton bunches. The central part of the detector is protected from direct synchrotron radiation by collimators inside the beampipe, by outer detector components and by additional material outside the beampipe. The main contribution of synchrotron radiation background is made up from photons which are backscattered into the central detector volume. Direct synchrotron radiation is scattered (main processes: Compton and Rayleigh scattering and Photoeffect) from collimators and additional reflecting surfaces and travels back to the interaction region, where it enters the central detector. The backscattered synchrotron radiation arrives delayed with respect to the lepton bunches. The Compton

[1] The critical energy of a spectrum is defined as the energy, above which half of the total power is contained.

scattering of the photons in the collimator, which is the dominating process, limits the photon energy to less than $M_e/2$ (for a scattering angle of 180°).

The actual level of synchrotron radiation during HERA operation depends on:

- *Lepton beam current and energy*
  The synchrotron radiation power is proportional to the lepton beam current, I_e and varies approximately as E_e^4.

- *Position and optimisation of collimators*
  Persisting high levels of direct and reflected synchrotron radiaton can occur due to misaligned collimators. Figure 11.1 shows a horizontal view of the HERA lepton beamline in the vicinity of the ZEUS interaction region, with its complex geometry and the various installed collimators and magnets influencing the synchrotron radiation background.

- *Orbit alignment*
  With the electrons or positrons on the design orbit, only a low, constant level of backscattered synchrotron radiation reaches the detector during normal running conditions. Deviations from this design orbit in position and angle can however lead to a larger spread of the normally collimated synchrotron radiation cone, due to the long lever arm of up to 100 m, leading to much higher levels of direct and backscattered synchrotron radiation in the detector.

11.2.2 Lepton beam-gas background

Off-momentum positrons, which have lost energy with respect to the primary beam e.g. due to interactions with residual gas in the beam pipe, start to oscillate around the design orbit. In the ZEUS interaction region most of these positrons are bent towards the ring centre ($+x$). They can produce electromagnetic showers in the central detector. Since the off-momentum positrons enter the interaction region from the forward direction, the rear parts of the inner detector components are most affected by this source of background. Moreover, due to the bending towards the ring centre, the background peaks at the inside of the ring.

The level of lepton beam-gas background depends on:

- *Lepton beam energy*
  The number of particles produced via showering is proportional to the energy of the lepton beam E_e.

- *Lepton beam current and vacuum in the beampipe*
  The number of electron or positron beam-gas scattering events for a given vacuum condition scales linearly with the lepton beam current. Experience has shown that also the beam-gas density itself is approximately linearly dependent on the lepton beam, such that the number of produced particles varies as I_e^2.

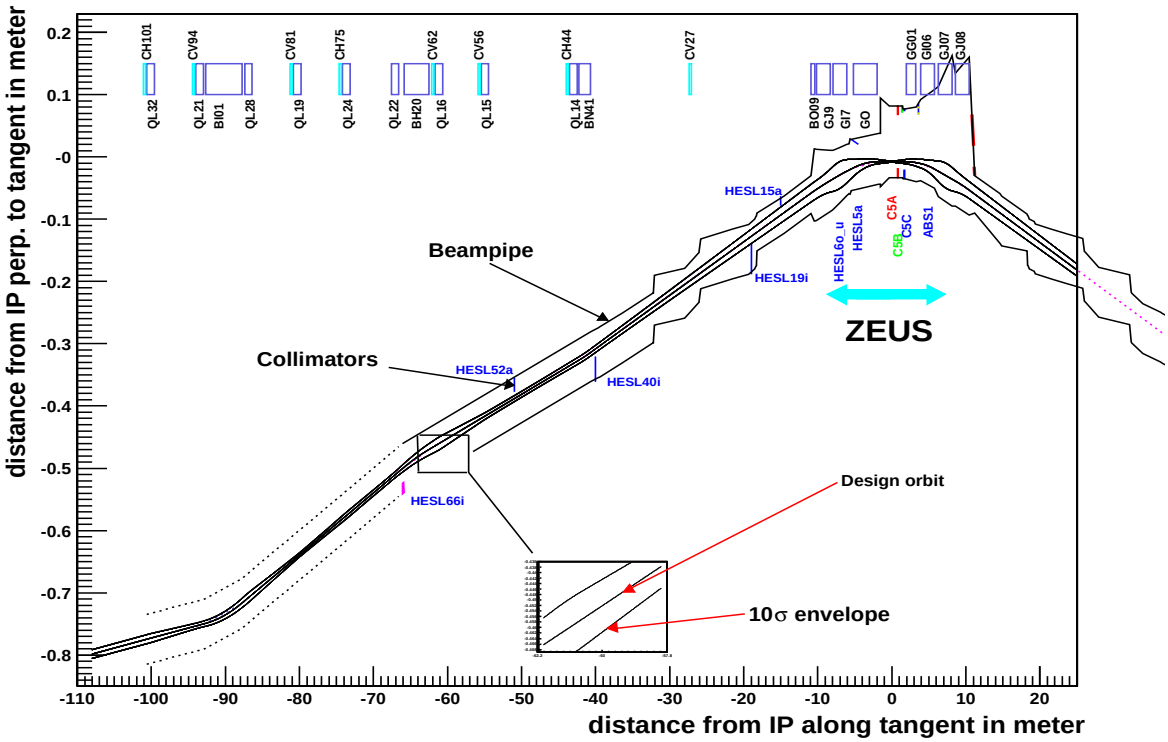

Figure 11.1: Horizontal view of the HERA lepton beamline in the vicinity of the ZEUS interaction region. Shown are the design positron orbit and its 10σ envelope, the beampipe and the collimators. The positron beam enters the interaction region from the left. At the top the z positions of the lepton magnets are shown. Note the highly distorted scale ($y : x = 1 : 100$) [114].

- *Orbit stability*
  The lepton injection phase, during which electrons or positrons of 12 GeV energy enter the beam within several minutes, is a critical operation, leading to oscillations and potential losses of the lepton beam, with sudden high particle rates. The normal background rate can be improved by tuning the orbit through changes in the magnet configuration. Failures in the magnet power supplies can lead to severe beam loss accidents. Also changes in the configuration of the experiment influence the beam stability, such as the closing of the ZEUS CAL or movements of the HERA-B proton targets. Finally also natural ground motion as well as cultural noise has an impact on the operation of the HERA machine[2].

[2]The HERA accelerator is located in an environment which is very challenging for a stable beam operation: in the direct vicinity of the ring there are several main roads, a highway, train tracks, a trotting course and two stadiums and their corresponding parking lots (see Fig. 2.1). A time dependent level of beam disturbance is thus observed, which is partly being compensated for by beam-based feedback.

11.2.3 Proton-beam background

Upstream interactions of protons from the beam with residual gas in the beam pipe are a significant source of proton-beam background, with similar effects and causes as the lepton beam-gas background described above. The proton beam is usually more stable than the lepton beam due to the larger mass and momentum of the protons and their smaller interaction cross sections. On the other hand, proton beam-loss accidents, which have happened in the past, are a source of very intense and collimated hadronic irradiation, which can lead to large local damage of the MVD detector system.

The electron-beam and synchrotron-radiation induced desorption of restgas and subsequent proton beam-gas interaction is one of the major sources of background for the experiment, contributing to high currents in the CTD and eventually to increased dead time of the data aquisition system.

11.3 Tolerable radiation dose for the MVD

The radiation hardness of the MVD sensors and its readout electronics have been tested using prototypes. Electrical measurements and an extensive electron testbeam program have been performed to study the effect of both hadronic and ionising irradiation on the detector performance [94, 112, 115, 116].

For neutron irradiation with 1 MeV-neutron-equivalent fluences up to $\phi_{eq}^{\max} = 1 \cdot 10^{13}$ n cm^{-2} (much higher than the hadronic background expected during the MVD lifetime), type inversion has not occurred and the influence of hadronic irradiation is limited to a change in the depletion voltage and an increase of the bulk generation current. No degradation of the detector performance has been observed in testbeam measurements for neutron irradiated sensors.

The effect of ionising radiation was tested with ^{60}Co photons for doses from 50 Gy up to 2.9 kGy (up to 5 kGy for the readout electronics). A large increase in the leakage current of the sensors has been found after photon irradiation. The increase in leakage current could be attributed to additional generation currents from the SiO_2 - Si interface [112]. No degradation of the detector performance was observed in the electron testbeam. For the readout electronics however a deterioration of the performance after irradiation was observed, and the single track resolution for perpendicular incidence in a single diode worsens from 7.2 µm before irradiation to 12.2 µm after 5 kGy photon irradiation. By optimising the programmable readout parameters, the resolution after irradiation improves to 10.6 µm. The resulting performance was thus still within the specified range [116].

The MVD is foreseen to operate for 5 years in the HERA environment. Here and in the following, one year is considered 10^7 seconds, corresponding to the approximate duty time of the HERA machine. The maximum tolerable dose of ionising radiation for the detector and its readout electronics was specified to be 3 kGy, after which the readout electronics will already show degradation of its performance. The acceptable

dose rate is thus 250 Gy/year (25 μGy/s), which is approximately five times higher than the average dose rate in the HERA-I data taking periods.

11.4 Requirements for the radiation monitor

The radiation monitor system for the ZEUS MVD was designed to protect the MVD from high levels of background radiation. The following restrictions and requirements were considered essential:

- *Space and material constraints*
  Due to the highly inhomogenous distribution and complex spectrum of the expected background radiation, the dose has to be measured inside the active volume of the detector, in the direct vicinity of the MVD. The available space in this region is limited and, in addition, any installed component has to be optimised for low radiation length with respect to the trajectories from the interaction point to the outer components.

- *Radiation hardness*
  The components of the radiation monitoring system have to stand the expected level of radiation over the projected lifetime of five years of HERA operation.

- *Automatic beam dump*
  In case of excessively high instantaneous dose-rates, an automatic dump procedure of the lepton beam has to be triggered immediately. (The proton beam dump procedure does not foresee a direct connection to the experiments.)

- *Online information*
  For both, the HERA and the ZEUS shift crews, an online information on the actual level of background radiation in the vicinity of the MVD has to be provided. This includes different levels of warning messages in case of increased dose-rates.

- *Measurement of integrated dose*
  The integrated dose has to be measured on a time scale from seconds up to the lifetime of the MVD detector system.

- *Post mortem information*
  The full information on the situation leading to a beam-dump request has to be stored to allow for debugging and correlation with data from other components, the other HERA experiments and the accelerator.

- *Independent readout*
  The system has to operate continuously, independent from other components such as the MVD itself, which is turned on only during stable beam conditions.

11.5 Components of the radiation monitor system

The dose rate measurement is based on the readout of the radiation induced signal currents of silicon PIN diodes. A precise temperature measurement allows for a correction of the temperature induced changes in the diode's leakage current. The leakage current adds as a constant offset to the total measured current of the reverse biased diodes. In addition to the measurement of the instantaneous dose-rate, the offset current measurement in periods without machine operation is used to estimate the bulk-damage component of the background radiation. Radiation-induced bulk damage in a diode and the following annealing of this damage leads to a predictable change of the offset leakage current on a time scale from seconds up to the lifetime of the MVD system. Thus monitoring the changes in the radiation induced leakage currents allows for an estimation the bulk damage component of the total radiation dose.

The online dose rate measurement of the silicon diodes is complemented by a system of radiation field effect transistors (RadFETs), which are sensitive to surface damage from ionising radiation.

In addition, thermoluminescent dosimeters (TLDs), read out monthly, allow for a calibration and control of the online measurements.

11.5.1 Layout

The layout of the radiation monitor system is sketched in Fig. 11.2. It consists of the following elements:

- *Silicon PIN diodes*
  16 reverse biased silicon PIN diodes, grouped in 8 modules, are mounted close to the ZEUS interaction point in the vicinity of the MVD. Figure 11.3a) shows the components of a module. It consists of two diodes (1 cm^2 size) mounted individually on printed-circuit-boards (PCB). The two PCBs are glued back-to-back, with 1 mm of lead shielding in between. An NTC temperature sensor is mounted on one of the PCBs, close to the diode. The back-to-back configuration of two independent diodes results in redundancy for the local dose-rate measurement, which is important for reliable beam-dump requests. The lead shielding separating the two PCBs absorbs very low-energy ionising radiation (1/10 attenuation for a photon beam of 80 keV energy). For radiation coming from only one direction, it thus allows for a separation of the contribution of the low-energy part of the spectrum. The module is electrically shielded by an aluminum case. The outer dimensions of a module are approximately 34 mm x 28 mm x 27 mm.

  Four forward modules are mounted on an aluminum flange, close to the FMVD, at $z = 110\,\text{cm}$, surrounding the beam pipe in the vertical plane (see Fig. 11.2). The modules are electrically isolated from the aluminum flange by a Kapton foil and plastic screws. The four rear modules are mounted in the same configuration, but close to the BMVD at $z = -100\,\text{cm}$. Figure 11.3b) shows a picture of two

of the rear modules after final assembly. The modules are not accessible during shutdowns and are foreseeen to stay in place for the lifetime of the MVD system.

All active components and the readout electronics are situated in racks outside the main detector. The total cable length from the diodes to the readout electronics is 33.2 m for the forward and 30.7 m for the rear modules.

- *Radiation field-effect transistors*
  The eight RadFETs are situated in the forward direction at $z = 200\,\text{cm}$ (four low-sensitivity modules, 100 nm gate oxide thickness) and in the rear direction at $z = -130\,\text{cm}$ (four high-sensitivity modules, 400 nm gate oxide thickness), as shown in Fig. 11.2a). At both z-positions, the four modules are surrounding the beam pipe and are directly attached to it, as sketched in Fig. 11.2b). The power supply and readout electronics for the RadFETs is also located outside the detector, connected through cables of 30 m (25 m) length for the forward (rear) modules.

- *Thermoluminescent dosimeters*
  In the rear region there are 6 plastic tubes glued on the inside of the MVD shielding, which are used to insert TLDs. They extend in the forward direction to the rear barrel flange, thus allowing to place TLDs at any position between $z = -37\,\text{cm}$ and $z = -140\,\text{cm}$. For the period considered in the following, all TLDs could only be placed at approximately $z = -120\,\text{cm}$.

- *Additional components*
  In addition to the measurements from the dedicated radiation monitoring system, information on the background radiation level is obtained from several other radiation-sensitive components of the ZEUS detector: The leakage currents in the MVD diodes have a similar dependence on the radiation level as have the currents of the silicon PIN diodes. The current drawn by the signal wires of the central tracking detector (a drift chamber) is related to the particle and synchrotron radiation rate traversing the chamber. A tungsten embedded scintillator counter (C5) outside the main detector, at $z = -130\,\text{cm}$, provides information on the lepton- and proton-beam-gas particle background.

11.5.2 Silicon PIN diodes

The diodes used for the radiation monitor system were produced by SINTEF [117]. The most important parameters of the diodes are summarised in Tab. 11.1. They are made from oxygen-enriched high-resistivity silicon and are n-type, 300 μm thick, with an active area of $1\,\text{cm}^2$, which is surrounded by one guard ring. The pad and guard ring are p^+ implanted and the complete backside is n^+ implanted. All implanted areas are aluminised to allow for contacting and reverse biasing. The guard ring is connected directly to ground, thus drawing the currents generated by defects and impurities at the detector edge and by defects at the $Si - SiO_2$−interface, which otherwise would

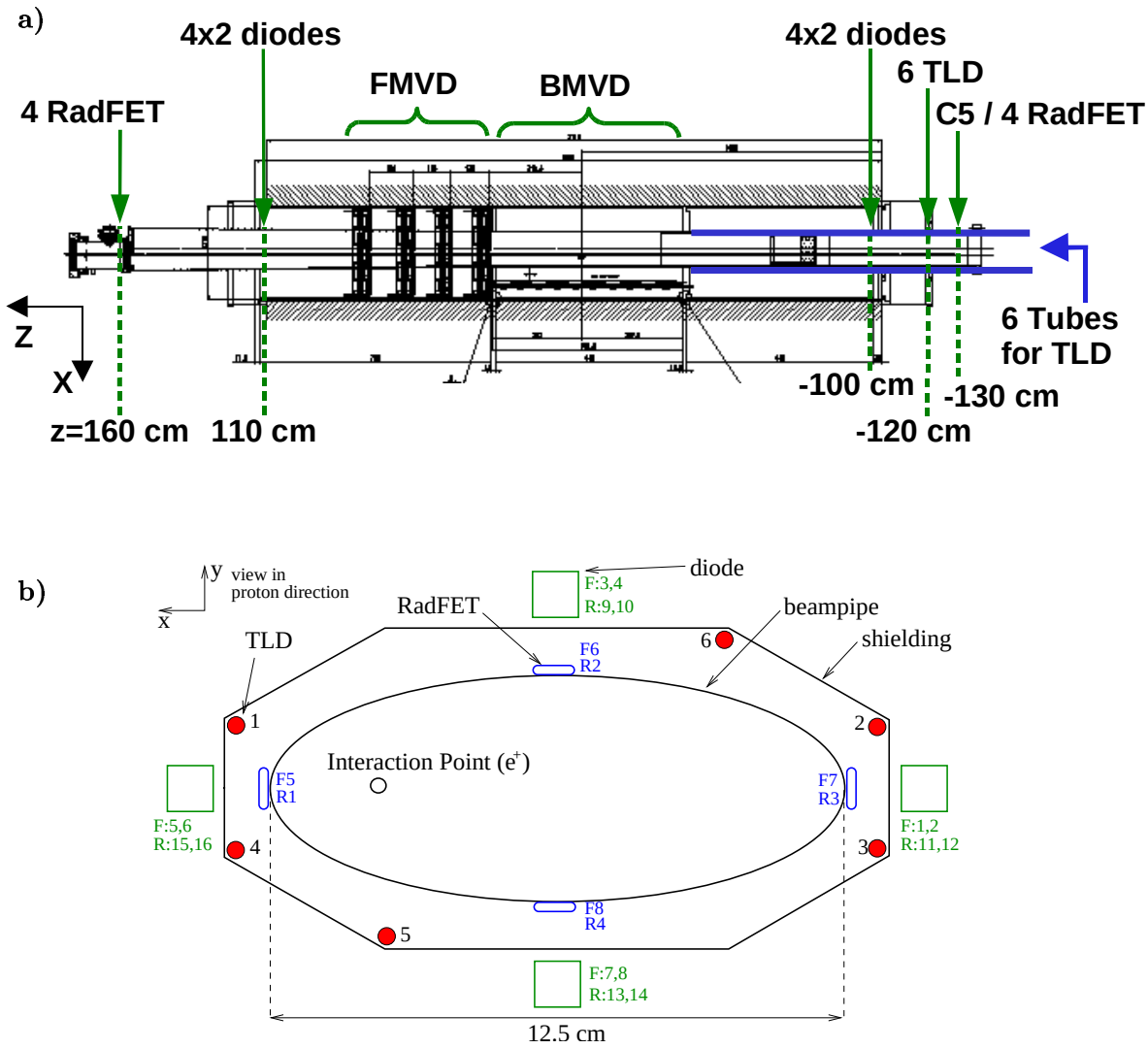

Figure 11.2: The radiation monitor system inside the ZEUS detector. In a) the position of the components along the beam direction is shown. In b) the position of the components in the x-y-plane is shown. The diodes are labeled from 1 to 16 and the RadFETs from 1 to 8. The letters F and R in front of the diode and RadFET numbers indicate the z position in the forward and rear region, respectively. The first diode number of each module corresponds to the upper diode (facing the interaction point), while the second diode number referes to the diode behind the lead shielding. The tubes for inserting the TLDs are labeled from 1 to 6.

add to the measured bulk current. The initial depletion voltage of the 8 diodes in the forward (rear) area was +75 V (+85 V). The depletion voltage is expected to decrease after moderate bulk damage. The initial operation bias voltage was +100 V, applied at the backside of the diodes. The 16 diodes were selected from a larger sample from two different wafers according to the long-term stability of their leakage current. The

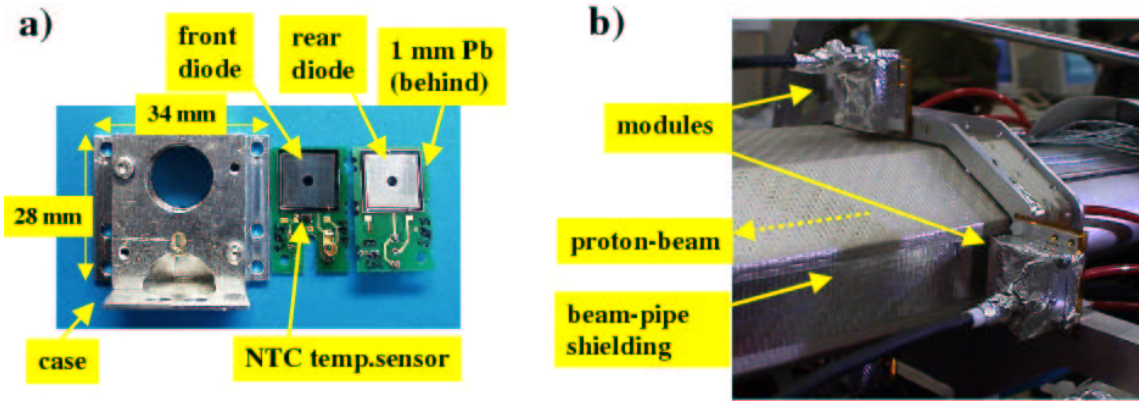

Figure 11.3: A radiation monitor module consisting of two silicon diodes and an NTC temperature sensor before assembly (a). In b) two of the rear modules are shown after final assembly.

initial bulk leakage current of the selected diodes was stable and below 1 nA at the test bias voltage of 120 V, which had been applied continuously for several weeks, as shown in Fig. 11.4.

Producer	SINTEF
Number of diodes	16
Type	n-type silicon, p^+ pad implant
Resistivity	rear diodes: 3.35 kΩcm, forward diodes: 3.80 kΩcm
Full depletion voltage	rear diodes: 85 V, forward diodes: 75 V
Active volume thickness	300 µm
Backplane	thick n^+ layer, aluminised
Number of guard rings	1
Biasing scheme	positive reverse biasing, guard-ring to ground
Operation bias voltage	$V_{\text{bias}} = +100$ V
Initial leakage current	$< 1nA$ at $V_{\text{bias}} = 120$ V and $T = 20°C$

Table 11.1: Parameters of the silicon diodes used for the radiation monitor.

The current measured in the reverse biased diodes depends mainly on:

- *Instantaneous radiation dose rate*
  The photo current induced by ionising photons and particles traversing one of the reverse biased radiation monitor diodes, I_{photo}, is proportional to the rate of the absorbed dose, $\dot{D}$:
  $$I_{\text{photo}} = \dot{D} \cdot \frac{M_{\text{diode}} \cdot e}{E_i}, \tag{11.1}$$
  where $M_{\text{diode}} = 7.0 \cdot 10^{-5}$ kg is the mass of the sensitive volume of a diode, $e = 1.60 \cdot 10^{-19}$C is the elementary charge and $E_i = 3.6$ eV is the energy required

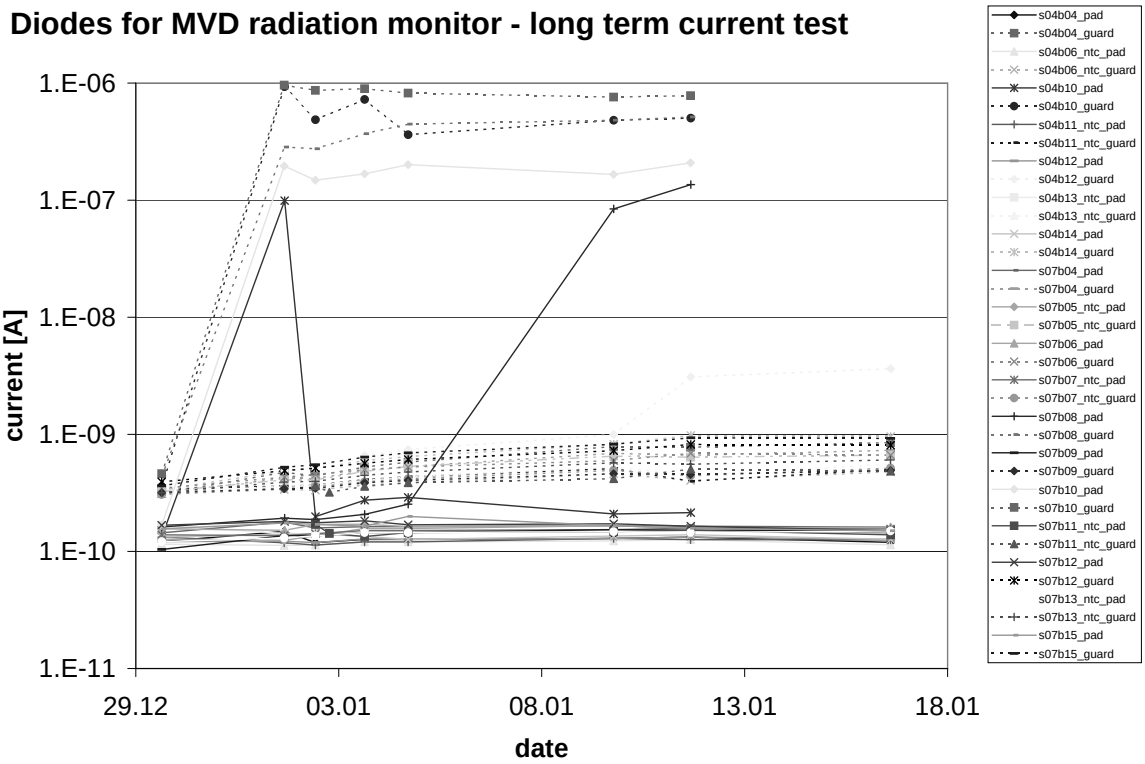

Figure 11.4: Long term test of the diode leakage current at a continuous bias voltage of 120 V. Shown are bulk current (solid lines) and the guard-ring current (dashed lines). Diodes with bulk leakage currents below 1 nA were selected for the radiation monitor.

to create an electron-hole pair in silicon. The obtained constant of proportionality relating the measured current to the absorbed dose rate is:

$$\dot{D}\ [\frac{\mathrm{Gy}}{\mathrm{s}}] = 5 \cdot 10^{-5} \cdot I_{\mathrm{photo}}\ [\mathrm{nA}] \tag{11.2}$$

- *Radiation damage and annealing*
  Low energy ionising radiation leads mainly to surface damage, resulting in additional current from generation centres at the $Si - SiO_2$-interface. This current is drawn by the guard ring of the radiation monitor diode and thus does not affect the measured pad current[3]. Irradiation from high energy particles however leads mainly to bulk damage, resulting in additional current measured through the pad of the diode. The bulk damage shows annealing after the irradiation. The radiation induced change of the leakage current is discussed in detail in section 11.6. Figure 11.5 shows the simulated current of a radiation monitor diode over the projected lifetime of 5 years for an assumed total equivalent fluence of

[3]The MVD sensors are more sensitive to damage from ionising radiation than the PIN diodes, due to the large number of $Si - SiO_2$ surface areas in between the approximately 3000 strips of each MVD sensor.

$\phi_{eq}^{\max} = 1 \cdot 10^{13}\ n\mathrm{cm}^{-2}$, which is collected in single steps of one irradiation per HERA operation week. In this scenario, where the dose corresponds to the previously tested maximum level of hadronic irradiation for the MVD system, the total leakage current of a radiation monitor diode at the end of the projected lifetime amounts to approximately 9 μA. The long-term annealing of the leakage current was taken into account according to the long-term parametrisation (11.7).

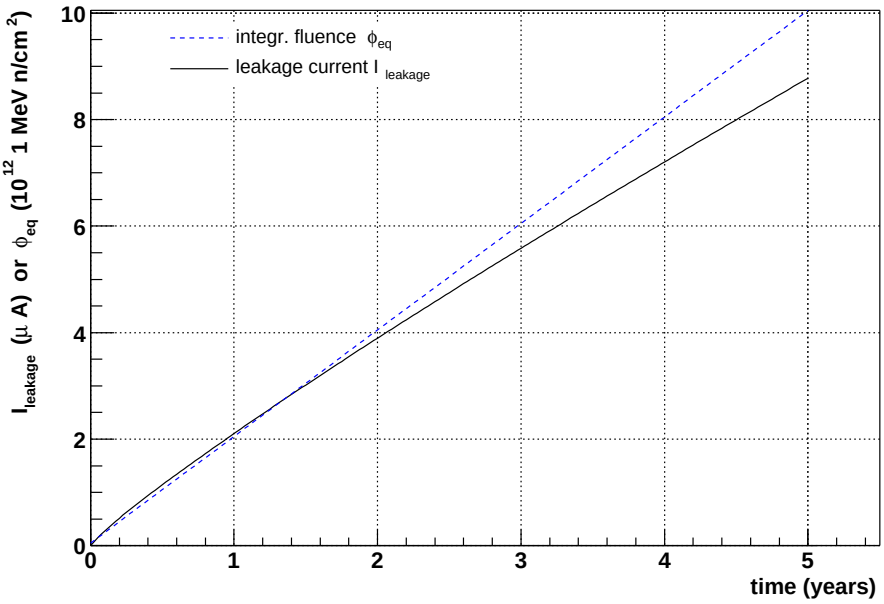

Figure 11.5: Integrated fluence and simulated resulting radiation induced leakage current for a radiation monitor silicon PIN diode over the projected lifetime.

- *Temperature*
  The leakage current offset in a silicon diode depends roughly exponentially on the temperature. The temperature in the vicinity of the MVD varies between 15°C and 25°C, depending on the status of the HERA machine, the MVD cooling system and the MVD readout electronics.

  All measured currents can be scaled to $T = 293\ K$ according to the equation

$$I(T = 293) = I_T \left(\frac{293}{T}\right)^2 \exp\left(\frac{E_g}{2}\frac{1}{k_b}\left(\frac{1}{T} - \frac{1}{293}\right)\right), \qquad (11.3)$$

  which corrects for the temperature dependence of bulk generation currents [118]. E_g is the effective energy gap at $T = 293\ K$, $E_g = 1.12$ eV, and k_b is the Boltzmann constant. For $T = 293\ K$, the change in current is about 8%/K.

  Resistors with negative temperature coefficient (NTC) are used to measure the temperature very close to the diodes (see Fig. 11.3). The resistance of the NTC,

R_{NTC}, depends exponentially on the temperature, T:

$$R_{\mathrm{NTC}}(T) = R_{ref} \cdot \exp(\beta \cdot (\frac{1}{T} - \frac{1}{T_{\mathrm{ref}}})), \tag{11.4}$$

where R_{ref} is the resistance of the NTC at a referenc temperature T_{ref} and β is a coefficient parametrising the exponential decrease of the resistance with increasing temperature. The nominal values for the NTCs in the radiation monitor modules are $R_{25} = 4.7$ kΩ at $T_{25} = 25^{\circ}$C and $\beta = 3300$.

The measured temperature T is used to obtain the actual value of the leakage-current offset in a diode $I_{\mathrm{leakage}}(T)$ from a reference measurement $I_{\mathrm{ref}}(T_{\mathrm{ref}})$ at T_{ref}:

$$I_{\mathrm{leakage}}(T) = I_{\mathrm{ref}}(T_{\mathrm{ref}} \cdot \exp(\beta_d(\frac{1}{T} - \frac{1}{T_{\mathrm{ref}}})). \tag{11.5}$$

The coefficient β_d parametrises the exponential temperature dependence of the leakage current in the diode. The temperature T is calculated with one fixed value of β and R_{25} for all NTCs. For the temperature correction of the leakage current offset however, a more precise correlation between the NTC resistance and the leakage current as function of the temperature is needed. Therefore one value for β_d was obtained for each diode by a fit to the observed relation between $R(T)$ and $I_{\mathrm{leakage}}(T)$ in the temperature range of interest.

11.5.3 Silicon diode and NTC readout

The connection scheme of a module is shown in Fig. 11.6. A cable combining two coax and one twisted pair cables connects the module, through a passive interface at a patchbox, with high-voltage supplies and readout electronics. A common shield is connected to the module case of the two diodes and connected to ground at the readout side. Each diode is individually biased from the backside through the outer shield of the corresponding coax cable. Iseg EHQ F0025 power supplies [119] are used, which are software controlled via a CAN interface. The inner conductors of the coax cables are connected to the pad of the corresponding diode, carrying the bulk current back to the readout amplifier. The NTC temperature sensor is connected to the readout electronics through a twisted pair cable. The ground connector of the NTC carries also the guard ring current of the two diodes. The total cable length from the diodes to the readout electronics boards is 33.2 m for the forward and 30.7 m for the rear modules.

The pad current of the diodes is sent to a two-stage integrating amplifier, with an integration time of 0.1 s. The output voltage of 10 mV/nA is connected to the 0 to 10 V input of two 12 bit ADCs (NS LM 12458). The resulting dynamic range allows current measurements up to 1000 nA with a resolution of 244 pA.

The NTC temperature resistor is connected to a current source delivering a constant current of 100 μA. The voltage drop over the resistor is amplified (10x gain) and the resulting output voltage of 1 V/kΩ is sent to another 12 bit ADC (NS LM 12458). The dynamic range of the resistance measurement allows resistance measurements up

to 10 kΩ with a resolution of 2.4 Ω. The corresponding temperature resolution is approximately 10 mK at 20°C.

The digitised signals from the ADCs are read out by a Motorola MVME 2600 CPU using a VME bus with 30 samplings in one second. All further signal processing is performed by software. Online histograms and acoustic warnings in case of high background levels are sent to the ZEUS and HERA control rooms. The histograms are archived on disc. In case of excessive background radiation, a trigger signal for an automatic dump of the lepton beam is sent to the HERA lepton beam-dump magnet system via a relay.

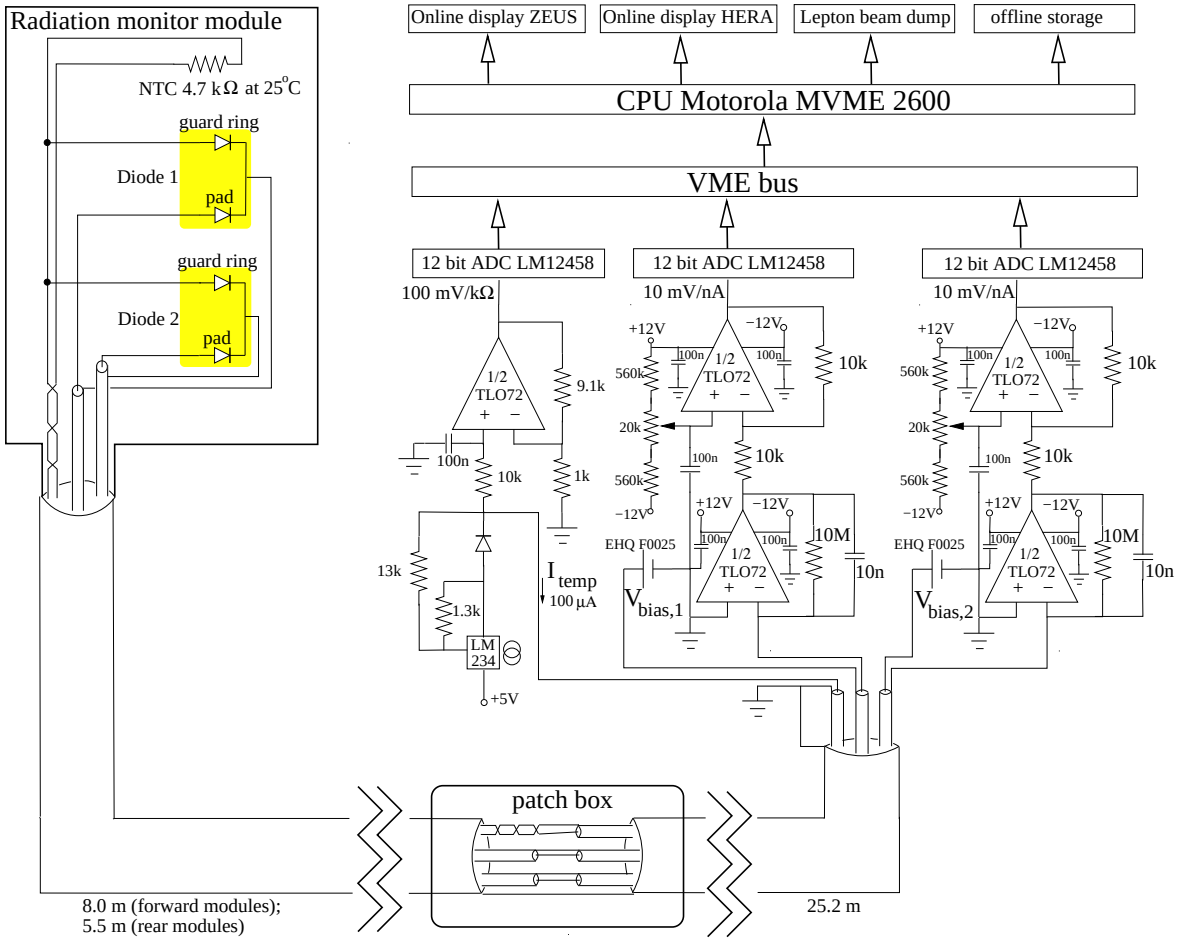

Figure 11.6: Connection scheme of a radiation monitor module.

11.5.4 Leaky bucket integrated dose measurement

The online radiation monitoring system adapts the so called leaky bucket concept, which is also used in the radiation monitor of the BaBar experiment [120]. The signal current of each diode, after subtracting the leakage-current offset, is integrated and

translated into a train of pulses. The pulse frequency is proportional to the input current, which itself is proportional to the instantaneous radiation dose rate. The pulses are used to increment a counter. At the same time, a constant count-down signal is sent to the counter, with a frequency tuned to compensate for the average acceptable background current. The counter is thus integrating the dose-rate above the tolerated level of radiation. Thresholds on the counter generate warning messages for the ZEUS and HERA shift crews as well as the trigger signal for the automatic beam dump. The system is sensitive to the integrated dose, rather than to instantaneous radiation peaks. To avoid beam dumps caused by a slow accumulation of counts, the count-down rate has to be set to a value well above the average background rate. This value, ϕ_f, is called "forgiveness rate", since any dose rate below will never cause a beam dump.

For the readout concept considered in the following, the handling of the counter was implemented in software. The parameters chosen were restricted by the dynamic range of the current measurement. The current value in nA, sampled at a rate of 1 Hz, is used to increment the counter. The forgiveness rate, ϕ_f, corresponds to 10 nA (0.5 mGy/s). The threshold counter value for triggering an automatic dump of the lepton beam is 4000 nAs, with a coincidence of at least two diodes exceeding this threshold. With the maximum current of 1000 nA (50 mGy/s), the resulting minimum time before a beam-dump request is 5 s. Figure 11.7 shows the time and integrated dose before a beam-dump request as function of the instantaneous dose rate. For low rates, close to the forgiveness rate, both time and integrated dose before a dump trigger increase steeply. For a dose-rate of 0.6 mGy/s, which is 20% above the forgiveness rate, the dump time is 30 minutes and the integrated dose is 1.2 Gy. For dose-rates above 3 mGy/s, the integrated dose reaches a plateau of 200 mGy. For high dose rates above the dynamic range of the readout (50 mGy/s), the dump-time reaches a minimum of 5 s, while the integrated dose increases linearly with the dose rate. For very high currents above 50 μA (2.5 Gy/s), the voltage source for the diode trips. In this case, the leaky bucket counter is immediately set to a value above the maximum, such that the time before the beam dump trigger decreases to 1 s, with a corresponding decrease in the integrated dose. To avoid beam dumps after problems with the power supplies, that are not related to the beam conditions, at least one of the power supplies is required to be operational.

A faster version of the readout is currently being tested, in which the leaky-bucket concept is implemented in programmable hardware, reducing the reaction time for a beam-dump request to a few milliseconds (cf. section 11.7.5).

11.5.5 Diode current readout parameters

The readout of the diode currents allows a measurement of the dose rates from 12.2 μGy/s (244 pA) up to 50 mGy/s (1 μA). The upper limit of the dose-rate measurement will decrease with increasing offset leakage current after radiation damage. The warning threshold for the ZEUS and HERA control room shifts is set to 0.5 mGy/s (10 nA),

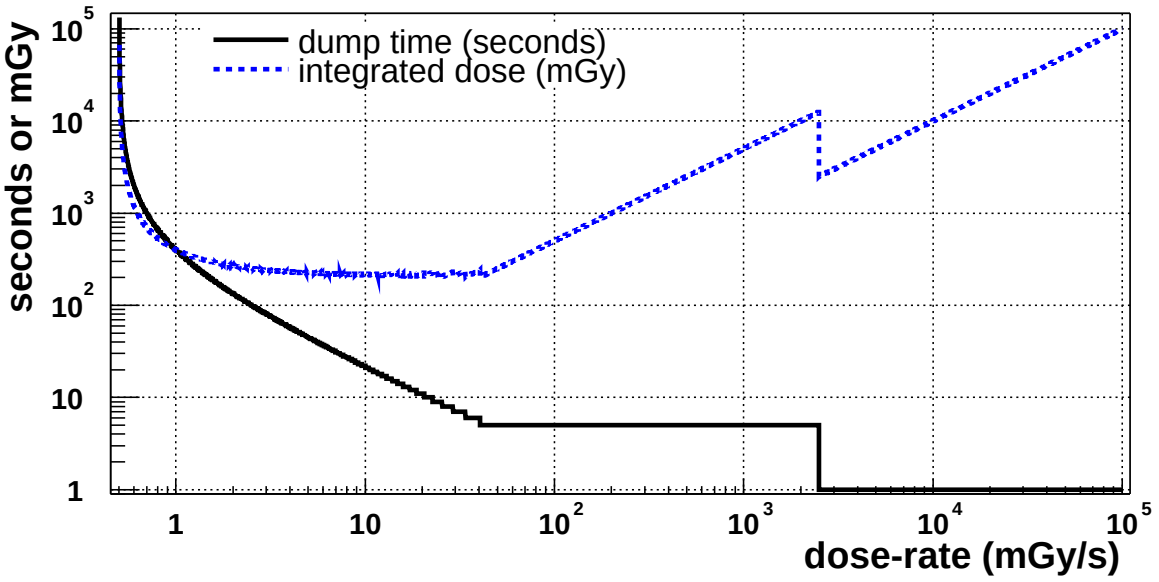

Figure 11.7: Time (solid line) and integrated dose (dashed line) before a beam-dump request as function of the instantaneous dose rate.

which is 20 times higher than the maximum tolerable average of 25 μGy/s (500 pA). The dynamic range and typical values for the dose-rate measurement are summarised in Tab. 11.2. The threshold values for warning and alarm signals to the ZEUS and HERA shifts and the threshold for beam-dump requests are also given.

Dynamic range		
resolution I_{min}	244 pA	12.2 μGy/s
maximum current I_{max}	1 μA	50 mGy/s
leaky bucket forgiveness rate	10 nA	0.5 mGy/s
Typical rates		
stable lumi operation	0-250 pA	0-12.5 μGy/s
maximum tolerable average	500 pA	25 μGy/s
energy ramping and beam tuning	2-3 nA	100-150 μGy/s
lepton injection spills	2-50 nA	0.1-2.5 mGy/s
Current measurement threshold		
warning for ZEUS and HERA	$>$ 10 nA	$>$ 0.5 mGy/s
Leaky bucket level threshold		
ZEUS alarm	1000 nAs	$\gtrsim$ 50 mGy
lepton beam dump	4000 nAs ($\geq$2 diodes)	$\gtrsim$ 200 mGy

Table 11.2: Readout parameters and typical values for the diode current and integrated dose measurement.

11.5.6 Radiation field-effect transistors

The integrated dose of ionizing radiation can be estimated from the changes in the surface properties of silicon devices. Ionising radiation creates electron-hole pairs in the silicon oxide layer of a field effect transistor. Holes that get trapped in defects at the $Si-SiO_2$ interface area form a positive space charge, which has to be compensated by a negative gate voltage [121]. The negative threshold voltage $V_{\rm th}$, which is necessary to create an inversion layer connecting the source and drain areas, is thus increasing with radiation (see Fig. 11.8).

For the MVD radiation monitoring system, eight p-type radiation field effect transistors (RadFETs) of two different gate-oxide thicknesses (100 nm and 400 nm) are used. The initial change in $V_{\rm th}$ is approximately 1.5 mV/Gy (18 mV/Gy) for 100 nm (400 nm) gate-oxide thickness. A non-linear calibration curve for doses between 1 Gy and 1 kGy has been obtained from measurements on a sample of seven RadFETs by the manufacturer [122]. During the irradiation no voltage was applied for these calibration measurements. The uncertainty on the dose determination from the measurement of $V_{\rm th}$ was estimated from a fit to the calibration measurements to be 55%.

The readout scheme of the RadFETs is shown in Fig. 11.9. A current source delivering a current of 18 μA is connected to each RadFET every 17 minutes for 32 seconds. At the end of this cycle, 64 voltage measurements are sampled, digitised by the ADC and converted to a measurement of $V_{\rm th}$. The integrated radiation dose is obtained from the change in $V_{\rm th}$, based on the calibration measurements for each of the two different types.

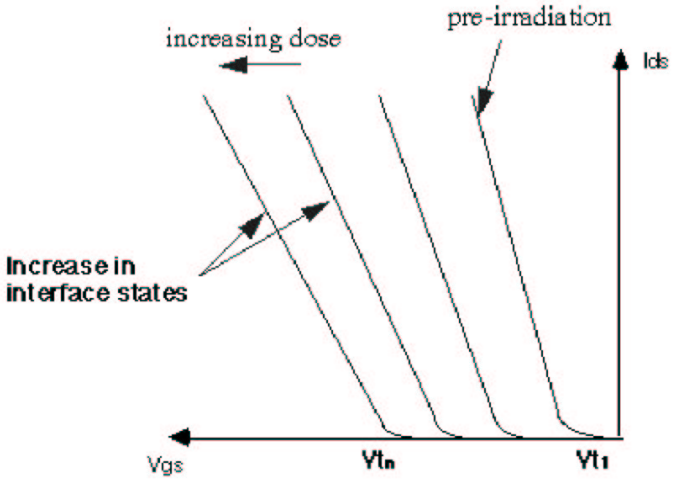

Figure 11.8: Change in the transfer characteristic of a RadFET after irradiation.

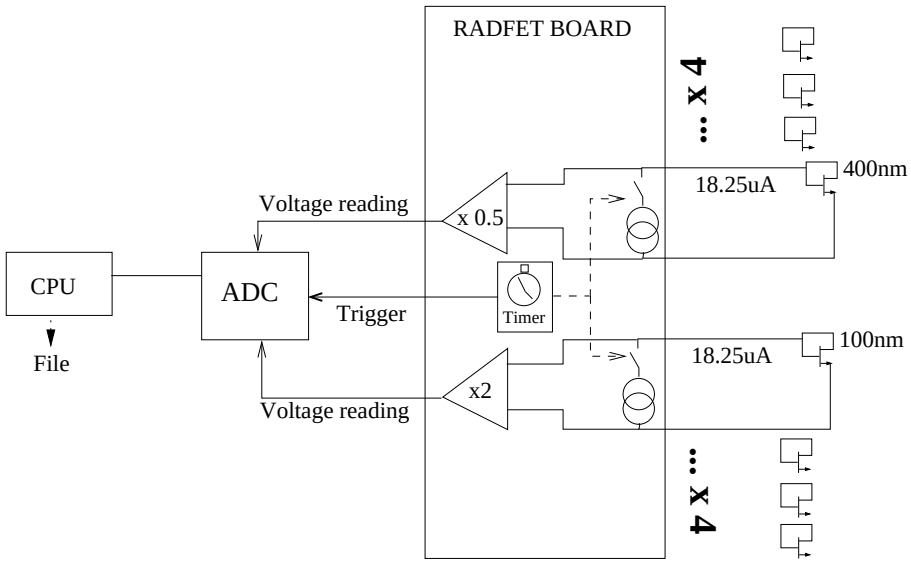

Figure 11.9: Schematic of the RadFET readout.

11.5.7 Thermoluminescent dosimeters

Electron and hole traps are filled in thermoluminescent materials during exposure to radiation. Heating frees electrons and holes from theses traps and visible photons are emitted when the electrons and holes recombine. The integrated light output has a known dependence of to the radiation dose. Two types of thermoluminescent dosimeters (TLDs) are used for radiation monitoring in the ZEUS detector: ^{6}LiF (TLD-600) being sensitive to thermal neutrons by means of the (n, α) $1/v$ capture cross section and ^{7}LiF (TLD-700) being sensitive to betas, photons and neutrons. The TLDs measure the integrated dose and are replaced and analysed during monthly shutdowns.

11.6 Bulk damage in silicon devices

Irradiation of silicon devices with high-energy particles or photons leads to damage in the bulk of the devices, with predictable changes in the macroscopic properties. In the following, the dependence of the radiation damage on the particle type and energy and the effect on the measured leakage current of silicon diodes is discussed. The results are used to estimate the radiation dose from the observed changes in the leakage currents of the radiation monitor diodes.

11.6.1 NIEL hypothesis

The so-called Non Ionising Energy Loss (NIEL) hypothesis [123] states that the displacement damage from different types of particles at different energies can be parametrised with a single hardness factor, k. The initial increase of the bulk generation current

in a silicon diode is approximately proportional to the product of this hardness factor with the fluence of particles. The value of k is set to 1 for neutrons of 1 MeV energy. Figure 11.10 shows the value of the k for different particles as function of the particle energy.

In the following, a hardness factor of $k = 0.62$, which had been obtained for protons of 24 GeV [124], is assumed for high-energy protons ($E_p \gtrsim 10\,\mathrm{GeV}$). For high-energy photons and electrons ($E \gtrsim 1\,\mathrm{GeV}$), a hardness factor of $k = 0.1$ is assumed [125].

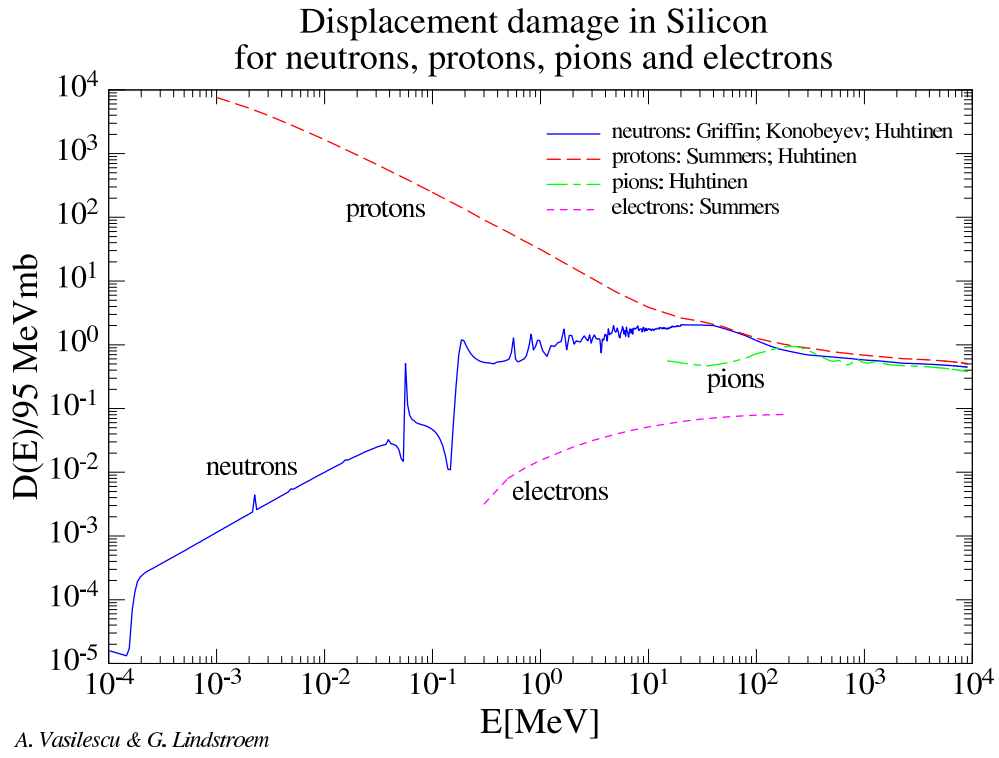

Figure 11.10: Displacement damage hardness factors for neutrons, protons, pions and electrons as function of the particle energy [123]. The quantity $D(E)/95$ MeVmb corresponds to the hardness factor k described in the text.

11.6.2 Leakage-current increase and long-term annealing

The total leakage current after a single radiation incident at $t = 0$ can be parametrised as [124, 126]:

$$\begin{aligned} I(t, \phi_{eq}) &= \alpha(t) \cdot \phi_{eq} \cdot V, \\ \alpha(t) &= \alpha_I e^{\frac{-t}{\tau_I}} + \alpha_0 - \beta \ln \frac{t}{t_0}, \end{aligned} \tag{11.6}$$

where $\phi_{eq} = \phi \cdot k$ is the fluence, scaled to the equivalent of 1 MeV neutrons/cm^2, V is the active volume of the diode and t is the time after irradiation. For the damage and

time constants α_I, α_0, β, τ_I and t_0, the following values are used [124]:

$$\begin{aligned} \alpha_I &= 1.23 \cdot 10^{-17} \frac{A}{\text{cm}} \\ \alpha_0 &= 7.07 \cdot 10^{-17} \frac{A}{\text{cm}} \\ \beta &= 3.29 \cdot 10^{-18} \frac{A}{\text{cm}} \\ \tau_I &= 1.4 \cdot 10^4 \,\text{min} \\ t_0 &= 1 \,\text{min} \end{aligned} \tag{11.7}$$

This parametrisation is valid for the long-term annealing starting from several hours after irradiation up to several years, assuming that the silicon devices are kept at room temperature ($\approx 20^\circ$C).

11.6.3 Short-term annealing

For the short-term annealing within seconds after irradiation, a new parametrisation was obtained from an experiment at the CERN PS proton irradiation facility [127]. Several radiation monitor diodes were irradiated with single spills ($t_{\text{spill}} \approx 180\ ms$) of 24 GeV protons. The bias voltage was applied during and after irradiation and the leakage current and temperature were continuously monitored. The fluence per spill was obtained from a secondary emission chamber (SEC) counter, which was calibrated with the measurement of the activation of an aluminum foil irradiated together with the corresponding diode. Figure 11.11 shows the change in the leakage current in one of the diodes, normalised to $T = 20^\circ$C, after receiving a single spill of $4.1 \cdot 10^{10}$ protons per cm^2. This fluence corresponds to $\phi_{eq} = 2.5 \cdot 10^{10}\ n\ \text{cm}^{-2}$, assuming $k = 0.62$ for 24 GeV protons [124]. For parametrising the annealing, a fit with three exponential functions in the range from 1 s to 6 hours after irradiation was performed. The long-term parametrisation (11.7) was included as an offset with fixed parameters (11.8) in the fit. The resulting formula for the leakage current after irradiation is thus given as:

$$I_{leakage}(t) = \phi_{eq} \cdot V \cdot (\alpha(t) + A_1 \exp(-t/t_1) + A_2 \exp(-t/t_2) + A_3 \exp(-t/t_3)), \tag{11.8}$$

where $I_{leakage}$ is the measured leakage current, scaled with (11.3) to $T = 20^\circ$C, ϕ_{eq} is the equivalent fluence of 1 MeV neutrons, V is the volume of the diode, $\alpha(t)$ is the long-term annealing parametrisation according to (11.7), $A1$, A_2 and A_3 are the damage parameters and t_1, t_2 and t_3 are the corresponding time constants. The parameters obtained from the fit are:

$$A_1 = 5.89 \cdot 10^{-8}\ \text{nA/cm} \tag{11.9}$$
$$t_1 = 6.9\ \text{s} \tag{11.10}$$
$$A_2 = 2.05 \cdot 10^{-8}\ \text{nA/cm} \tag{11.11}$$
$$t_2 = 187\ \text{s} \tag{11.12}$$
$$A_3 = 8.77 \cdot 10^{-9}\ \text{nA/cm} \tag{11.13}$$
$$t_3 = 5520\ \text{s} \tag{11.14}$$

The fit is compared to the data in Fig. 11.11. The long-term parametrisation according to (11.7) is also shown in the plot (dashed line). The new parametrisation is in good agreement with the data over the full range. The long-term parametrisation, however, underestimates the measured current for the shorter time-scales. For $t = 1\ s$, the predicted current according to the long-term parametrisation is approximately 50% lower than the measured one. For long annealing times, the long-term parametrisation agrees well with the data (within 10% at t=10 min and within 1% at t=6 hours). The new parametrisation is used to estimate the bulk damage from radiation received in single accidents during HERA operation, which leads to step-like increases in the leakage current of the radiation monitor diodes.

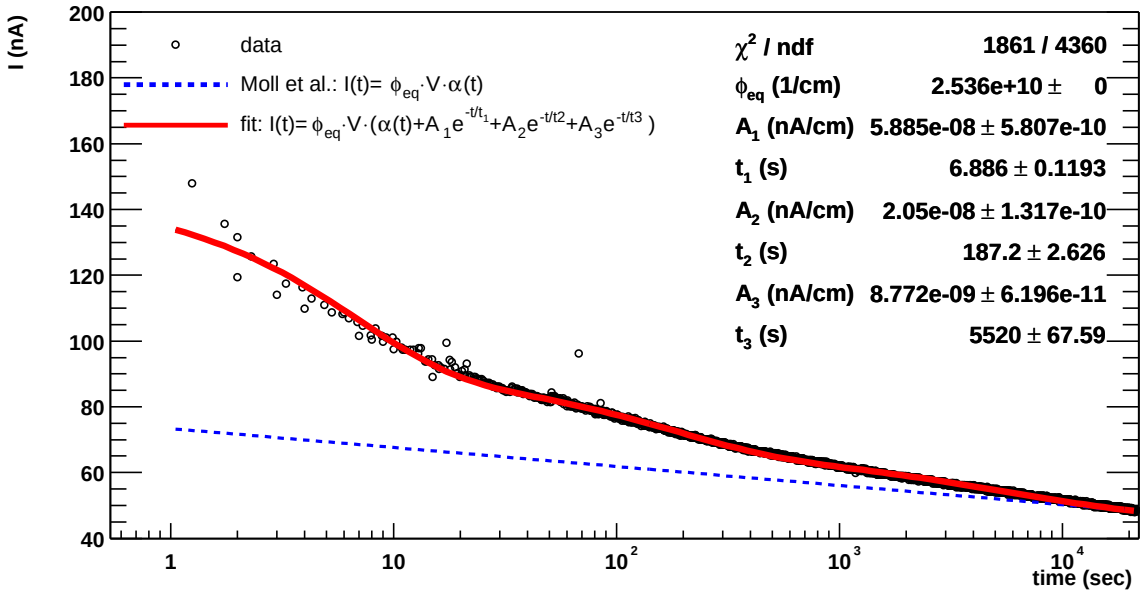

Figure 11.11: Leakage current annealing of a silicon diode after a single proton irradiation spill with $4.09 \cdot 10^{10}$ protons ($E = 24\,\mathrm{GeV}$) per cm^2 at $t = 0$. Shown are the data (circles), the standard parametrisation described in the text (dashed lines) and a fit to the data with the sum of the standard parametrisation and three exponential functions in the range [1 s, 6 hours] (solid lines). The initial current before irradiation (not shown in the plot) was below 1 nA.

11.6.4 Dose estimation

The absorbed dose, D, can be estimated from the equivalent fluence of high energy particle radiation, ϕ_{eq}, assuming that the radiation damage is caused by minimal ionising particles (MIPs) with known k-factor. The average number of created electron-hole-pairs per µm of a MIP traversing the silicon bulk of the diodes is $n_{eh} = 80/\,\mu\mathrm{m}$ [128]. The relation between the fluence of particles, $\phi = \phi_{eq}/k$, and the absorbed dose, D, is

thus:

$$D = \phi \cdot \frac{n_{eh} \cdot E_i \cdot e}{\rho_{\mathrm{Si}}}, \tag{11.15}$$

where $\rho_{\mathrm{Si}} = 2.33$ g/cm^3 is the density of silicon. The fluence corresponding to the maximal tested hadronic irradiation dose for the MVD system of $\phi_{eq}^{\max} = 1 \cdot 10^{13}/\mathrm{cm}^2$ corresponds to an absorbed dose of $D = 20$ kGy, assuming that the bulk damage will mainly be produced from electrons or positrons escaping the lepton beam ($E_e \lesssim 27.5\,\mathrm{GeV}$, $k \approx 0.1$).

11.7 Results from the HERA II commissioning phase

The upgraded HERA II machine and experiments were commissioned and used to take first data for 20 months from July 2001 to March 2003. During this period, instable background conditions and problems with high synchrotron- and particle-background radiation were observed and partially reduced [114]. The radiation monitor system for the ZEUS MVD has proven to be an indispensable tool to understand the cause of part of these problems and to limit the damage from excessively high background levels for the MVD system. In the following, examples of measurements of different components are presented and total dose estimates are compared.

11.7.1 Temperature correction

Figure 11.12 shows an example of the temperature variation in one of the NTCs during a period of 220 minutes. The temperature in this period shows large fluctuations in a range from 15°C to 21°C. The uncorrected leakage current measured in the corresponding diode is also shown, as well as the temperature corrected current. During this period the HERA machine was not operating, such that no radiation induced current was present. The uncorrected current varies in a range of approximately 30% with a strong temperature correlation, while the corrected current is stable within 0.2%. The largest variations in the corrected current are observed for high temperature gradients (in this example at t=50 min, when the MVD detector and its cooling system were switched on). Measurements revealed that the the temperature correction coefficients β_d from equation (11.5) change with the accumulated radiation damage in the diodes. Fits to obtain the values of β_d have been performed repeatedly within the HERA II commissioning period.

11.7.2 Dose rate and leaky bucket measurements

During stable luminosity operation, the instantaneous radiation dose, measured through the currents in the diodes, has been low, close to the readout resolution (≈ 10 μGy/s). Spikes in the current measurement have been observed during injection of the lepton

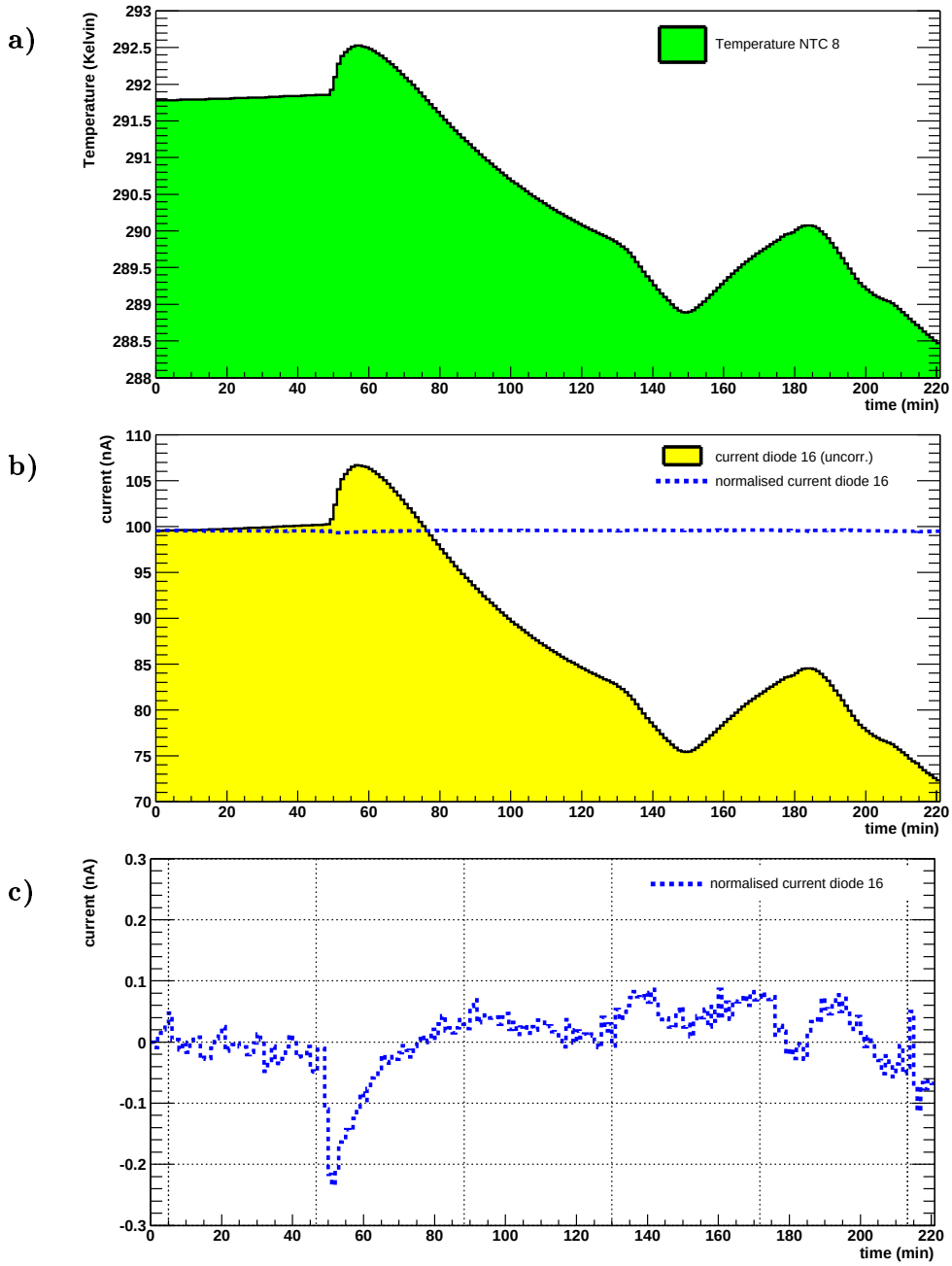

Figure 11.12: Temperature, as measured in one of the NTC resistors (a) and leakage current current in the corresponding diode (b and c). For the leakage current, both the uncorrected measurement (filled histogram) and the values after temperature correction (dashed line) are shown in b). In c), the corrected current is displayed in an enlarged scale, with the offset current value at $t = 0$ subtracted.

beam and during energy ramping and beam tuning phases. Large dose rates have normally been observed only for the rear diodes mounted in the horizontal plane (11/12 and 15/16, cf. Fig. 11.2). The highest dose rates have been measured for the diode pair mounted towards the center of the HERA ring (15/16). Most of the off-momentum positrons are expected to be deflected in this direction.

The measured dose rate in one of the radiation monitor diodes during a typical positron injection is shown in Fig. 11.13. Six positron spills were injected over a period of 12 minutes, resulting in a total positron current of 30 mA in HERA. The injection of each spill leads to a disturbance of the beam-orbit with an increased number of lost positrons, visible as a peak in the measured background rate. For normal injection, as in this example, the measured rate is of the order of 0.5 mGy/s (corresponding to a current in the diode of 10 nA).

Figure 11.14 shows the instantaneous dose rate and the leaky bucket level for one of the diodes during an instable positron-beam injection. High background rates fill the leaky bucket and lead to an automatic dump of the positron beam. A first radiation peak at t=2 s leads to a moderate increase of the leaky-bucket counter well below the beam-dump threshold of 220 mGy. The count-down rate sets back the level of the leaky bucket to zero within 30 s. The second high-radiation phase started at t=-51 s and resulted in a fast increase of the leaky-bucket counter. The beam-dump threshold of 200 mGy for the integrated dose is reached within 16 s and the automatic dump of the positron beam is triggered at t=67 s.

11.7.3 Offset current measurements

The long-term monitoring of the offset leakage currents in the diodes allows an estimation of the bulk-damage component of the accumulated radiation dose. In addition, steps in the leakage current after instantaneous beam-loss accidents have been observed, with subsequent decrease of the current, indicating annealing of the created bulk damage in the diodes.

Figure 11.15 shows an example for the change in the leakage current of one of the rear diodes after a positron beam loss accident. The current is normalised to a temperature of $T = 20°C$ and the initial offset value of 42 nA is subtracted. The positron beam was lost at $t = 0$, at an energy of almost 27.5 GeV [129]. The beam loss was initiated by a failure in one of the superconducting vertical correction magnets, located at the north side of the HERA ring. The resulting orbit disturbance lead to an excursion of the beam with a maximum amplitude reached at the position of the ZEUS GO magnet ($z \approx 2$ m). The current in the radiation monitor diode shows a step-like increase at $t = 0$ with subsequent annealing of the leakage current over a period of 17 minutes, during which no positron beam was present in the machine.

Diode 13, which is shown in the plot, is located in the rear area, at the bottom of the beampipe (cf. Fig. 11.2). Also all other radiation monitor diodes showed a spike at $t = 0$ for this accident. A similar increase of the leakage current offset was seen in the

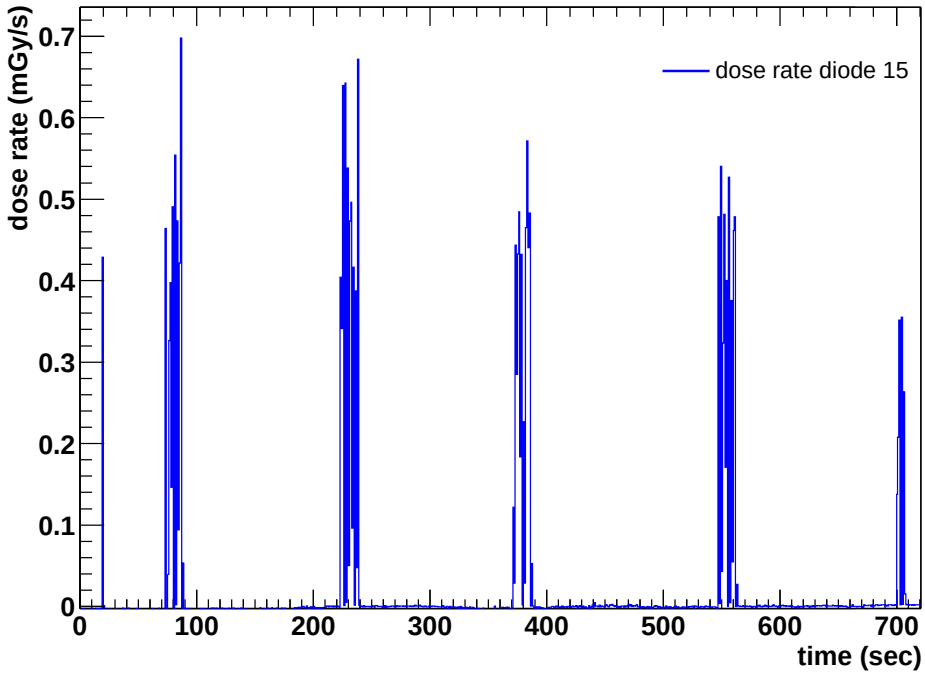

Figure 11.13: Dose rate for one of the silicon PIN diodes during a positron injection at Feb-14-2003, 23:33. The six spikes correspond to the injection of single positron spills leading to a total positron current of 30 mA in HERA.

rear diode pair 11/12 (located towards the outside of the ring). For the rear diode pair 9/10 (located on top of the beampipe) the increase of the current was approximately 50% larger, with a similar shape of the resulting curve. The rear diode pair 15/16 (located towards the inside of the ring) showed an increase in the current of only about 10% of the value measured in diode 13. None of the eight front diodes showed a sizeable rise of the leakage current offset following this accident.

Of the RadFETs, only RadFET 3 (located in the rear, at the bottom of the beampipe) observed a sizeable increase of the integrated dose (approximately 1 Gy).

A fit with the parametrisation (11.8) is also shown in the plot for diode 13. The parameters (11.14) were used, as obtained from the proton irradiation at the CERN PS. The fit was performed for the equivalent fluence ϕ_{eq} in the time range from 500 s to 1000 s. The resulting fit line corresponds to an equivalent fluence of $\phi_{eq} = 1.2 \cdot 10^8\ n\ \mathrm{cm}^{-2}$. The fit though does not reproduce the observed initial steep decay of the current in the data. Similar results were obtained for other beam-loss accidents, where increased leakage currents and subsequent annealing with very short time constants were observed in the radiation monitor diodes, as opposed to the measurements after proton irradiation at the CERN PS. The following influencing factors were considered as possible explanations for the observed difference:

- *Radiation type.* The damage mechanisms leading to increased leakage currents

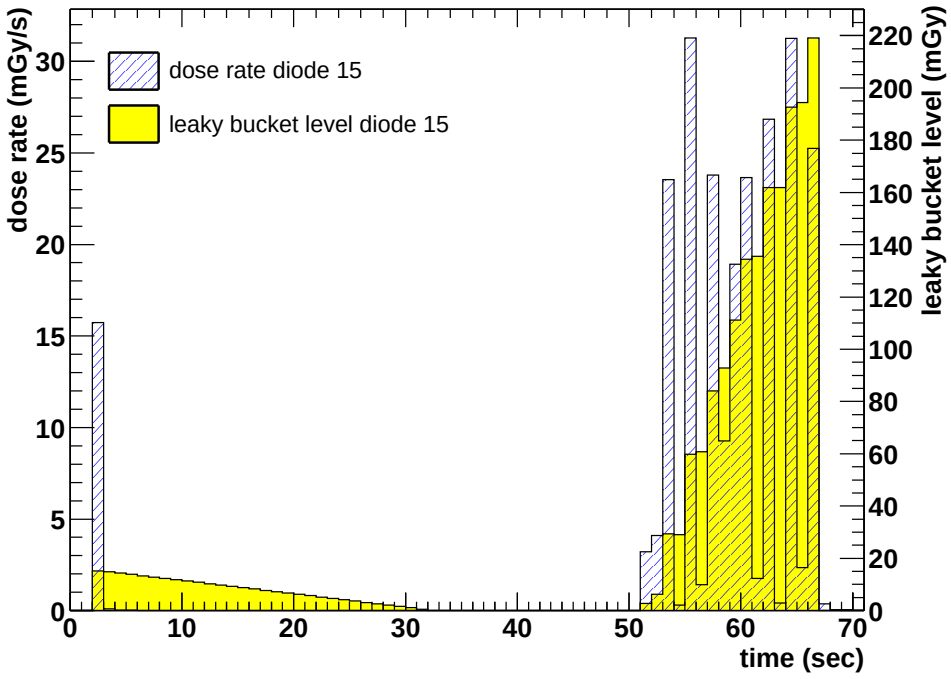

Figure 11.14: Dose rate and leaky-bucket level for one of the silicon PIN diodes during instable HERA operation at May-21-2002, 23:57, leading to an automatic dump of the lepton beam at t=66 s.

after high-energy electron irradiation during a beam-loss accident are expected to be similar to the ones for high-energy proton irradiation, as discussed in section 11.6. The effect of possible surface damage should, in both cases, be absorbed by the guard ring of the diode. A dedicated irradiation experiment with electrons at HERA energies is however necessary to exclude that a difference between electrons and protons exists concerning bulk-damage induced leakage-current increase and its short-term annealing.

- *Temperature.* In both cases the temperature was measured continuously and close to the position of the diode, and all measured currents were scaled to $T = 20°C$. For the measurements at the CERN PS, the temperature was at approximately 25°C, while during and after this beamloss accident at HERA the temperature was at approximately 15°C. The leakage-current annealing, however, is generally expected to proceed faster for higher temperatures [130], in contrast to the observed slower annealing for the proton-irradiation experiment.

- *Setup.* The configuration of the diodes in the ZEUS experiment and their readout was similar with respect to the proton irradiation experiment performed at the CERN PS. In both cases it was confirmed that the connection to the readout through long cables does not affect the fall-time of the signal on a time scale of seconds.

- *Activation.* The creation of short-lived radioactive nuclei in the vicinity of the diodes could affect the measured current. The ionising radiation from activated nuclei could lead to additional current measured in the diodes. Activation effects are expected to be more pronounced after irradiation with hadrons as opposed to electrons. A possible scenario would be the creation of nuclei with half-lifes of the order of minutes to hours in the setup of the CERN PS irradiation experiment or in the silicon diodes themselves, which are not created after lepton beam-loss accidents at HERA. In this case, the observed time-constants for the CERN PS irradiation experiment would be due to a mixture of leakage current annealing and radiation-induced photo current. Further investigation are necessary to clarify whether short-term activation effects are the cause of the observed difference.

The observed difference in the fall time of the measured current between the proton irradiation experiment and the situation after lepton beam-loss accidents at HERA thus prevents a profound quantitative estimation of the received fluence. However, for long annealing times ($\gtrsim$ 10 minutes) the measured absolute value of the current after the proton irradiation experiment was found to be in good agreement with the predictions from independent long-term annealing experiments (cf. the parametrisation (11.7)). The value of $\phi_{eq} = 1.2 \cdot 10^8$ n cm^{-2}, obtained from the fit in the time range from 500 s to 1000 s, can thus be considered an approximate upper limit on the fluence of high-energy radiation received for this positron beam-loss accident.

11.7.4 Total dose estimates

The total radiation dose received by the different components of the radiation monitor system and by the MVD itself depends on the position of the corresponding component. Furthermore, a direct comparison is complicated, as the components are sensitive to different parts of the complex spectrum of radiation in the HERA environment. In the following, estimates are presented for the total dose (or equivalent fluence) received by the components during the first HERA II commissioning phase.

- *RadFETs.* The accumulated dose of ionising radiation received by the eight RadFETs, as estimated from the change in the flatband voltage, is shown in Fig. 11.16 for the last 430 days of the commissioning phase. In addition to several step-like increases, a steady accumulation of radiation can be observed. RadFET number 1, which was placed at the ring-inside in the rear region, integrated the highest dose (approximately 1.3 kGy). The other RadFETs have received only moderate radiation doses between approximately 50 Gy and 300 Gy.

- *PIN diodes.* The total bulk damage in the PIN diodes was estimated from the increase in the leakage current offset, as shown in Fig. 11.17. A very high increase in the leakage current from $<$ 1 nA before HERA startup to 25-70 nA was observed during the first days of HERA II commissioning. In this period, technical problems during proton injections caused several severe proton-beam

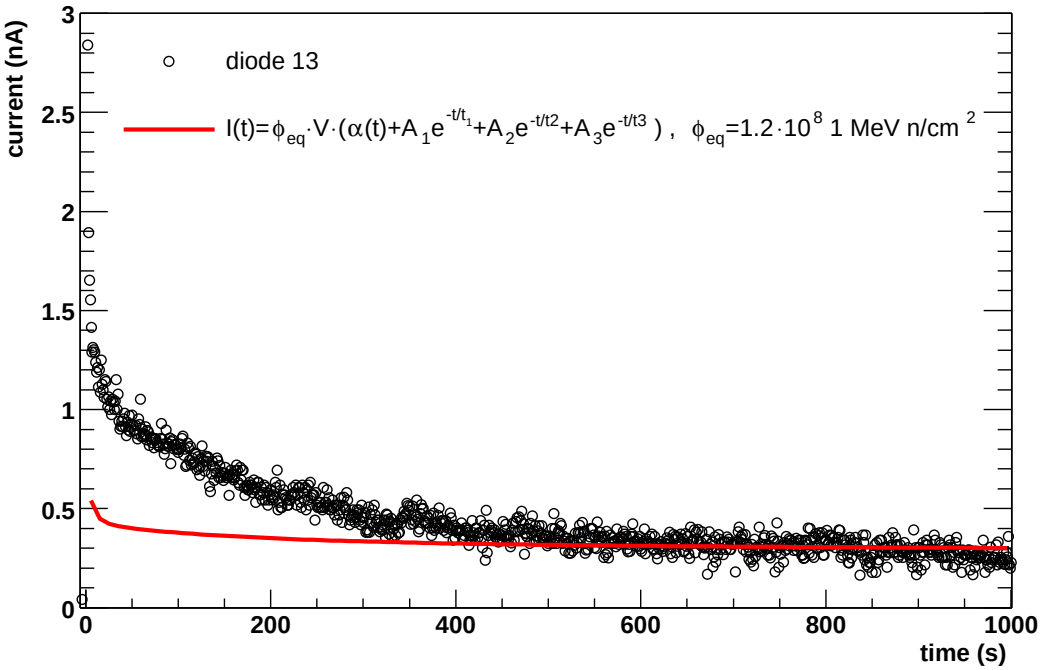

Figure 11.15: Current increase and the following annealing in one of the radiation monitor diodes after a positron beam-loss accident at Jun-14-2002, 23:41. The circles correspond to the leakage current measured in the diode, scaled to a temperature of $T = 20°\mathrm{C}$. The value of the leakage current before the beam loss is subtracted. The line represents a fit for the equivalent fluence with the parametrisation (11.8) in the range from 500 s to 1000 s. The equivalent fluence corresponding to this fit is $\phi_{eq} = 1.2 \cdot 10^8\ n\mathrm{cm}^{-2}$.

losses with energies ranging from 40 GeV to 500 GeV. From the parametrisation of the leakage current increase (11.7), the equivalent fluence of high-energy irradiation in the diodes caused by this series of beam-losses was estimated to range from $\phi_{eq} = 1.7 \cdot 10^{10}\ n\ \mathrm{cm}^{-2}$ to $\phi_{eq} = 4.8 \cdot 10^{10}\ n\ \mathrm{cm}^{-2}$. The equivalent fluence estimates were translated to estimates of the absorbed dose of high-energy ionising radiation according to (11.15), assuming a hardness factor of $k = 0.62$ for protons. The resulting dose estimate ranges from 5 Gy to 15 Gy. During the months following this short period of frequent beam-loss accidents, annealing with an overlay of accumulating radiation damage can be observed in the diode currents. As expected, the diodes belonging to the same module show very similar currents. A larger radiation damage is observed for the diodes placed in the rear region than for the ones in the forward region. This shows that the proton beam-loss accidents took place outside of the ZEUS detector and only the extended shower reached the centre of the detector. Furthermore, the diodes 15/16 and 3/4, which are placed towards the inside of the HERA ring, show the highest current among the corresponding modules at the same z-position. The current at the end of the commissioning phase varies from approximately 20 nA to 120 nA,

depending on the position of the corresponding module. The contribution of the proton beam-loss accident at the beginning of the commissioning phase to the final leakage current values, after 19 months of annealing, is approximately from 10 nA to 40 nA. The equivalent fluence of irradiation in this period can be estimated from the leakage current increase, taking into account also the annealing during the commissioning phase according to the parametrisation (11.7). The resulting fluence estimates for the period after the proton beam-loss accident, assuming 1.5 years of continuous irradiation, are from $\phi_{eq} = 7 \cdot 10^9$ n cm^{-2} to $\phi_{eq} = 8.3 \cdot 10^{10}$ n cm^{-2}. The maximal total accumulated fluence was thus in the order of 1 % of the maximum tested fluence for the diodes of the MVD ($\phi_{eq}^{\max} = 1 \cdot 10^{13}$ n cm^{-2}). The corresponding dose, assuming a k-factor of 0.1 for electrons, ranges approximately from 14 Gy to 160 Gy.

- *TLDs.* The total dose estimate obtained from the monthly readout of the TLDs is summarised in Tab. 11.3 for the six different TLD positions. The values from 25 Gy to 300 Gy for the TLD-700, which are sensitive to photons, electrons and neutrons, are in rough agreement with the dose estimates from the RadFET modules. The corresponding measurements for the TLD-600, which are sensitive to neutrons, resulted in very low total dose estimates of approximately 1 Gy to 2 Gy, accumulated only in the first month of HERA operation, in which the proton beam-loss accident had occured. The data obtained from the analysis of the TLD-600 were calibrated for thermal neutrons. Therefore the dose estimates given in the table were obtained after applying a scale-factor of 6 to the original measurements, to take into account the lower sensitivity for fast neutrons, which are expected for HERA energies [131].

- *MVD.* The surface radiation damage in the MVD readout electronics was estimated from the decrease of the signal-to-noise ratio during the commissioning phase. The largest decrease of up to 8% was observed for the modules at the inside of the ring, closest to the beam-pipe. From irradiation tests performed with a ^{60}Co source [116], the dose of low-energy ionising radiation, which corresponds to this decrease of the signal-to-noise ratio, was estimated to be approximately 250 Gy to 500 Gy. The dose received by the MVD modules with highest radiation damage is thus in rough agreement with the dose measured by the RadFET modules.

The dose estimates from the different components agree qualitatively. For a detailed quantitative comparison, Monte Carlo simulation studies are necessary. The obtained values can be used as input parameters.

11.7.5 Outlook

The radiation monitor system has been used successfully to protect the MVD from excessive levels of ionising radiation and to monitor the accumulated radiation dose during the HERA II commissioning phase. For the future high-luminosity HERA II

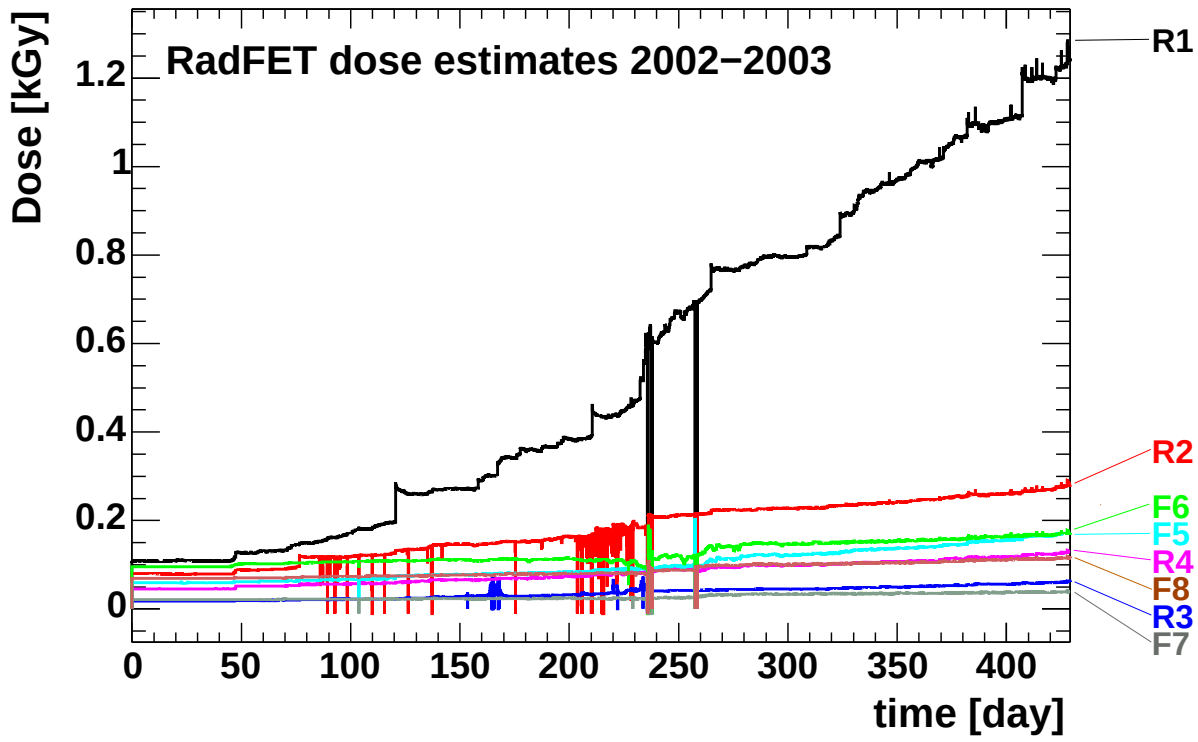

Figure 11.16: Integrated dose estimates from the RadFET measurements for the period from January 2002 until the end of the first HERA II commissioning phase in March 2003.

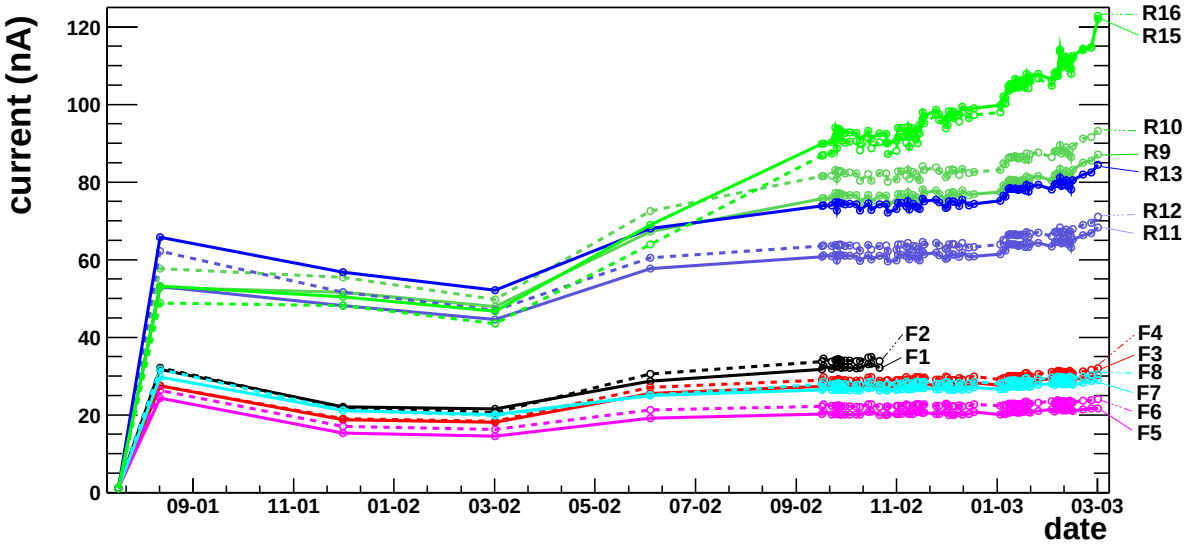

Figure 11.17: Offset leakage current in the radiation monitor diodes during the HERA II commissioning phase from August 2001 until March 2003.

TLD	TLD-700 (e, γ, n)	TLD-600 (n)
1	62 Gy	7 Gy
2	301 Gy	10 Gy
3	64 Gy	6 Gy
4	111 Gy	-
5	25 Gy	11 Gy
6	29 Gy	8 Gy

Table 11.3: Integrated dose estimates from the readout of the TLDs.

data taking, improvements of the existing equipment as well as additional devices are planned to increase both the sensitivity and the reaction time of the radiation monitoring. The following changes are foreseen:

- *Readout electronics*
  The readout system for the currents of the diodes has proven to be robust and flexible. It is however only sufficient up to moderate levels of accumulated bulk damage, since for high offset values of the diode leakage currents both a larger dynamic range and a more accurate compensation for temperature induced changes in the currents will be required. An upgraded version of the readout electronics has been developed that includes dedicated ADCs for low- and high-rate-measurements. The full scale is 1 μA (100 μA) and the resolution is 10-15 pA (25 nA) for the low-range (high-range) ADCs. The full scales will be kept effective also for high offset currents, towards the end of the HERA running time, by using a DAC to remove a pedestal current of up to 5 μA, with a nominal resolution of 6 pA. The leaky-bucket concept is implemented in programmable hardware. Furthermore, the gaps of 1.5 μs in the HERA bunch train, with no particles passing ZEUS, will be used to continuously measure the leakage-current offset during HERA operation. The current signal at the end of every empty-bunch window is sampled and hold and the sampled signal is integrated over several milliseconds. The full scale is 100 nA and the design resolution is 1.5 pA. Using the new readout electronics, the time before an automatic lepton-beam-dump request will decrease to approximately 10 ms, with a corresponding decrease in the integrated dose before the dump. The beam-dump signal will be transmitted via a fibre optic cable. First final versions for the new readout are currently being tested.

- *RadFETs*
  In addition to the existing 8 RadFETs, 16 new high-sensitivity RadFETs have been installed closer to the interaction point: 8 devices at $z = -0.5$ m, and 8 devices at $z = -1.1$ m. 4 of the new devices at both z-position will have a faster readout ($\approx$ 1 s). The new RadFETs are produced with implanted gate oxide (400 nm oxide thickness) and the initial change in $V_{\rm th}$ is approximately 50 mV/Gy [122].

- *TLDs*
  The insertion system has been improved, such that TLDs can be placed closer to the interaction point than before, ranging from $z = -37\,\mathrm{cm}$ to $z = -140\,\mathrm{cm}$.

Chapter 12

Summary

This thesis has presented a search for isolated leptons in events with large missing transverse momentum at HERA, covering an integrated luminosity of $130\,\mathrm{pb}^{-1}$ at $\sqrt{s} = 300\,\mathrm{GeV}$ and $318\,\mathrm{GeV}$. Improvements with respect to earlier ZEUS results include an extended acceptance, a better simulation of the signal and background processes in all data taking periods and the extension of the search to isolated tau leptons.

The main contribution from the SM to the signature of interest comes from production of single W bosons with subsequent leptonic decay: $ep \to eWX$, $W \to e\nu$, $\mu\nu$, $\tau\nu$. A more precise estimate of this contribution was obtained by reweighting the EPVEC LO MC simulation with recently published calculations that included NLO corrections to the photoproduction part of the cross section. The resulting total cross section is $1.0\,\mathrm{pb}$ (1.2) for $\sqrt{s} = 300\,\mathrm{GeV}$ ($\sqrt{s} = 318\,\mathrm{GeV}$). NC DIS events with large apparent transverse momentum due to a mismeasurement of the electron or the hadronic system contribute as background to the electron channel. The Bethe-Heitler muon-pair production process leads to isolated muon events in cases where only one of the muons is detected and a mismeasurement of the hadronic system results in apparent missing transverse momentum.

Theories beyond the SM that could lead to isolated lepton events were discussed with emphasis on supersymmetric models. The production of single-top quarks through FCNC ($ep \to etX$, $t \to W^+b$), modelled by an effective theory describing the anomalous coupling at the $tq\gamma$- or tqZ^0-vertex, was chosen as a specific signal process. Isolated lepton events with large missing transverse momentum from the decay of the top quark would be characterised by a large value of the hadronic transverse momentum. Cross-section calculations, including published NLO corrections, and simulations of this process were performed considering both the photon and Z^0 exchange for the production and decay of the top quark.

The selection of isolated leptons started from a generic search for events with isolated tracks and large missing transverse momentum. Electrons and muons were identified among those tracks and the resulting preselection was found to be in good agreement with the expectation from simulated SM processes. In the electron channel, 24 events

were observed in the HERA I data from 1994-2000, while $20.6^{+1.7}_{-4.6}$ such events were expected, mainly from badly reconstructed NC DIS events. In the muon channel, where the background expectation is dominated by Bethe-Heitler muon-pair production, 12 events were observed, while $11.9^{+0.6}_{-0.7}$ were expected. A final selection of electron and muon events with large hadronic transverse momentum was applied, which has been optimized to isolate events from the production of single top quarks. No events compatible with single-top quark production were found, while $1.89^{+0.18}_{-0.14}$ events were exptected from Standard Model processes, mainly from the production of W bosons. The results were used, in combination with an independent search for single-top production in the hadronic decay channel of the W boson, to constrain the single-top production cross section and the anomalous coupling constants $k_{tu\gamma}$ and v_{tuZ}. An upper limit on the FCNC coupling $\kappa_{tu\gamma}$ of 0.174 at 95% C.L. was obtained, corresponding to a limit on the cross section of $\sigma(ep \to tX, \sqrt{s} = 318\,\text{GeV}) < 0.225$ pb at 95% C.L.. This limit excludes a substantial region in $\kappa_{tu\gamma}$, which is not ruled out by other experiments.

The search for isolated tau leptons started from the preselection of isolated tracks that were not identified as either electrons or muons. The tau leptons were searched for in the hadronic decay modes with one charged particle in the final state. The resulting pencil-like jets were separated from quark- or gluon-induced jets with an innovative discrimination technique that made use of a range-searching algorithm to exploit six variables characterising the internal structure of the jets. Besides single W-boson production, multi-jet events from CC DIS processes and badly reconstructed NC DIS events contribute as SM background to the tau channel. Very restrictive selection requirements had to be applied to suppress this CC DIS and NC DIS background, which, in conjunction with the reduced efficiency of the tau identification method, lead to a much lower efficiency than in the electron and muon channel. Three tau candidates were found, while $0.40^{+0.12}_{-0.13}$ were expected from Standard Model processes, mainly from charged current deep inelastic scattering and single W-boson production. Following the strategy of the search in the electron and muon channel, a more restrictive selection was applied to isolate tau leptons produced together with a hadronic final state with high transverse momentum, as expected from the decay of a heavy particle. Two candidate events were found, while 0.20 ± 0.05 events were expected from Standard Model processes. The Poisson probability to observe two or more events, when 0.20 ± 0.05 events are expected, is 1.8%. Due to the lower efficiency in the tau channel and the negative search results in the electron and muon channel, the two observed tau events are unlikely to be originating from single-top production or any other process involving the decay of a W boson, which would lead to a much larger excess in the electron and muon channel.

The results of the search in the tau channel were compared with the results in the electron- and muon channel and with similar searches at HERA in the electron- and muon channel performed by the H1 collaboration. Different scenarios for the origin of the excess in both the ZEUS tau channel and the H1 electron- and muon channel were discussed. The combination of all search channels would be most compatible with an anomalous tau production process with small cross section, which could explain the H1 excess in the electron- and muon channel as originating from leptonic tau decays. The

anticipated high-luminosity HERA II data will be needed to clarify the origin of the observed excess in both the H1 electron and muon channel and the ZEUS tau channel.

The sensitivity of the ZEUS searches for isolated lepton events is expected to increase further due to an improved tracking system including a new Silicon Micro Vertex Detector (MVD) for the HERA II data taking period. A radiation monitoring and automatic beam-dump system based on Silicon PIN diodes and Radiation Field Effect Transistors has been designed and installed in the ZEUS experiment to prevent the MVD and its readout electronics from radiation damage during HERA operation. It has been used successfully in the ongoing HERA II commissiong phase to understand the origin and limit the severeness of high background rates that were observed in critical phases of the HERA machine cycle.

Appendix A

Trigger bit definitions

This appendix gives the definitions of the trigger bits used in this analysis.

In the following the indices FLT, SLT and TLT denote that a quantity was reconstructed at the first, second or third trigger level, whereas the indices $FCAL$, $BCAL$ and $RCAL$ indicate the different parts of the calorimeter.

A.1 DST bit 10

The DST bit 10 (B10) is used to select events with reconstructed vertex. B10 is set, if at least one vertex was reconstructed from tracks in the CTD.

A.2 DST bit 34

The DST bit 34 (B34) is used to select CC DIS events from the data. B34 uses information from the SLT and TLT.

The DST B34 is set, if the following requirements are fulfilled:

1. ExoTLT(2) $\vee$ ExoTLT(6) $\vee$ $p_T^{cal}(-1ir) > 6\,\mathrm{GeV}$
2. $p_T^{cal} > 7\,\mathrm{GeV}$
3. Events which satisfy all of the following 8 conditions are vetoed, mainly in order to reject background from beam gas reactions:
   (a) $\neg$ ExoTLT(2)
   (b) $p_T^{cal}(-1ir) < 10$ GeV
   (c) $p_T^{cal} < 25$ GeV
   (d) $p_T^{cal}/E_T < 0.7$ GeV

(e) $E - p_z < 10$ GeV

(f) $p_T^{cal}/p_z^{cal} < 0.8$ GeV

(g) $p_x^{cal} < 0$

(h) $|p_x^{cal}| < 4$ GeV

A.3 SLT

The branch of the SLT, which aims to select CC events is called ExoSLT(4) and has the following logic:

$$(|t_G| < 7 \text{ ns }) \wedge \tag{A.1}$$

$$(((\not{p}_T^{SLT} > 6 \text{ GeV}) \wedge (\mathrm{E_T^{SLT}}(-2\mathrm{ir}) > 6 \text{ GeV}) \wedge (\mathrm{N_{trk}^{good,FLT}} \geq 1) \vee \tag{A.2}$$

$$((\not{p}_T^{SLT} > 9 \text{ GeV}) \wedge (\mathrm{E_T^{SLT}}(-1\mathrm{ir}) > 8 \text{ GeV}) \wedge (\mathrm{E_{FCAL}^{SLT}} > 20 \text{ GeV}))), \tag{A.3}$$

where t_G is the average calorimeter timing, which is first available at the SLT. The time-zero is calibrated to the electron-proton interaction time. The terms '$(-1ir)$' or '$(-2ir)$' indicate that the transverse energy is calculated excluding the innermost or the two innermost rings of FCAL, since the energies deposited in the very forward region are not sufficiently understood. $N_{\mathrm{trk}}^{\mathrm{good,FLT}}$ and $N_{\mathrm{trk}}^{\mathrm{all,FLT}}$ denote the number of good CTD tracks and the number all CTD tracks, respectively. For a good track at the FLT the projection of the CTD hits to the z-direction is required to point to the nominal interaction point.

A.4 TLT

The CC event selection at the TLT is performed by the branches ExoTLT(2) and ExoTLT(6). The logic for ExoTLT(2) can be expressed as follows:

$$(\not{p}_T^{FLT} > 6 \text{ GeV}) \wedge (\mathrm{N_{trk}^{good,TLT}} \geq 1) \wedge \tag{A.4}$$

$$(|z_{vtx}^{TLT}| < 60 \text{ cm}) \wedge (|\mathrm{t_u} - \mathrm{t_d}| < 8 \text{ ns}), \tag{A.5}$$

where z_{vtx}^{TLT} indicates the z-position of the CTD vertex. t_u and t_d are the timings measured in the upper and lower half of the calorimeter. Muons produced in athmospheric shower induced by cosmic radiation leave an earlier timing in the upper half of CAL than in the lower half ('earlyness'). They are removed by the timing cut.
The logic of ExoTLT(6) is:

$$\mathrm{ExoSLT(4)} \wedge (|\mathrm{t_u} - \mathrm{t_d}| < 8 \text{ ns}) \wedge \tag{A.6}$$

$$(\not{p}_T^{TLT} > 6 \text{ GeV}) \wedge ((\mathrm{N_{trk}^{good,FLT}} \geq 1) \vee (\mathrm{E_{FCAL}^{TLT}} > 10 \text{ GeV})) \tag{A.7}$$

Appendix B

Event displays of electron and muon candidate events

This appendix presents the two electron events and five muon events, which were selected in the final single-top selection with a reduced cut on the hadronic transverse momentum of $p_T^{\mathrm{hadr}} > 25\,\mathrm{GeV}$.

The energy deposition in the CAL is proportional to the size and density of shading in the CAL cells. The x-y-view in the lower right corner shows only the energy deposition in the barrel calorimeter. In the upper right corner a lego plot of the energy deposition in the CAL is shown for events with sizeable energy deposition in the BCAL. For events with energy depositions mainly in the FCAL, an $x-y$-view of the FCAL energy depositions is shown instead.

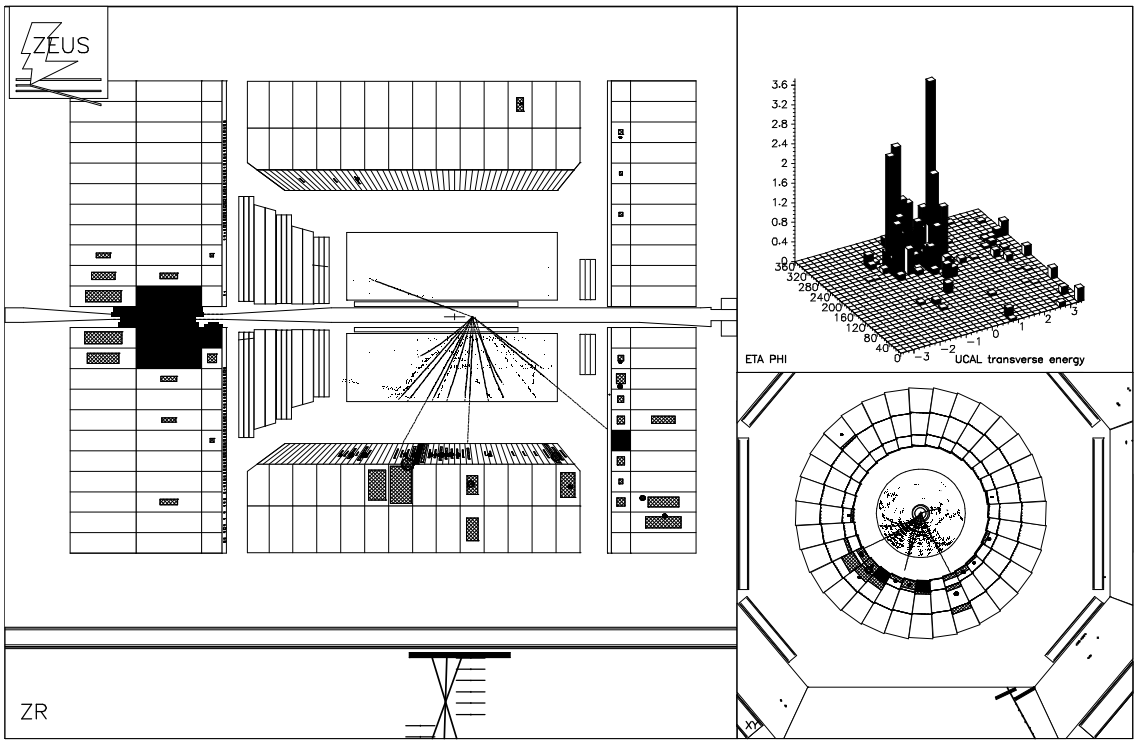

Figure B.1: Muon candidate event (run 31224, event 19966) from an $e^- p$ interaction at $\sqrt{s} = 318\,\text{GeV}$ in the ZEUS detector.
$p_T^{\text{CAL}} = 27\,\text{GeV}$, $p_T^{\text{hadr}} = 27\,\text{GeV}$, $p_T^{\mu} = 6\,\text{GeV}$, $M_T^{l\nu} = 27\,\text{GeV}$.

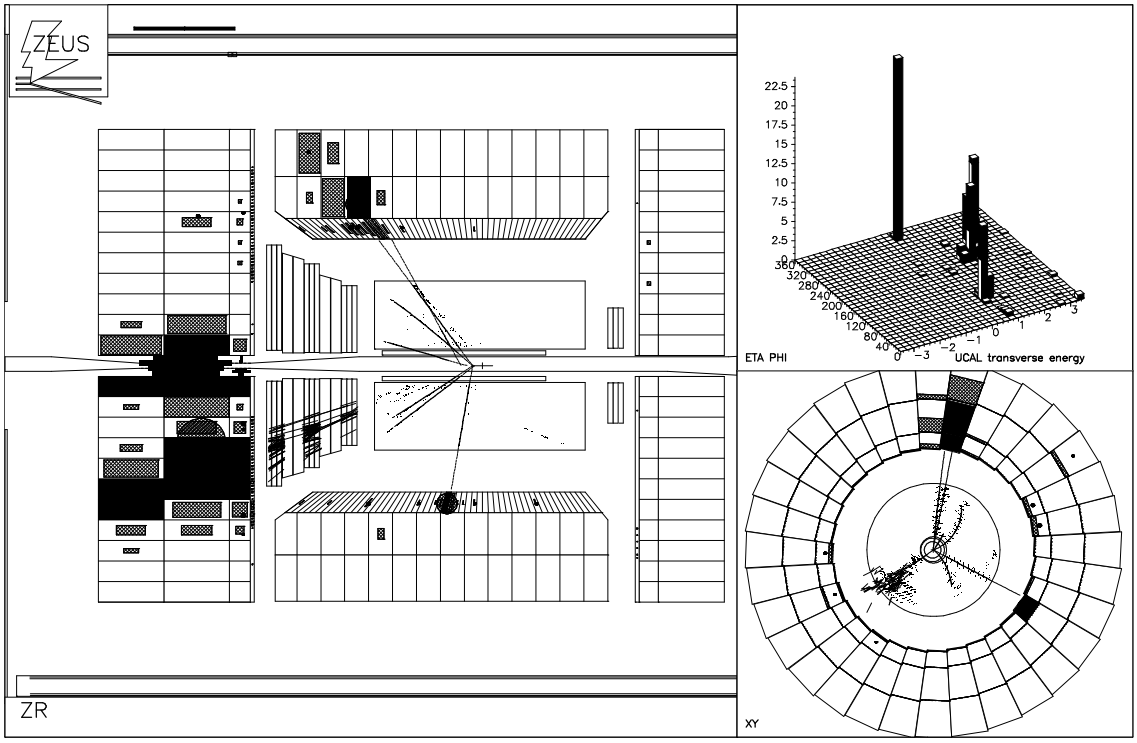

Figure B.2: Electron candidate event (run 32859, event 53874) from an $e^- p$ interaction at $\sqrt{s} = 318\,\text{GeV}$ in the ZEUS detector.
$p_T^{\text{CAL}} = 22\,\text{GeV}$, $p_T^{\text{hadr}} = 33\,\text{GeV}$, $p_T^{el} = 26\,\text{GeV}$, $M_T^{l\nu} = 35\,\text{GeV}$.

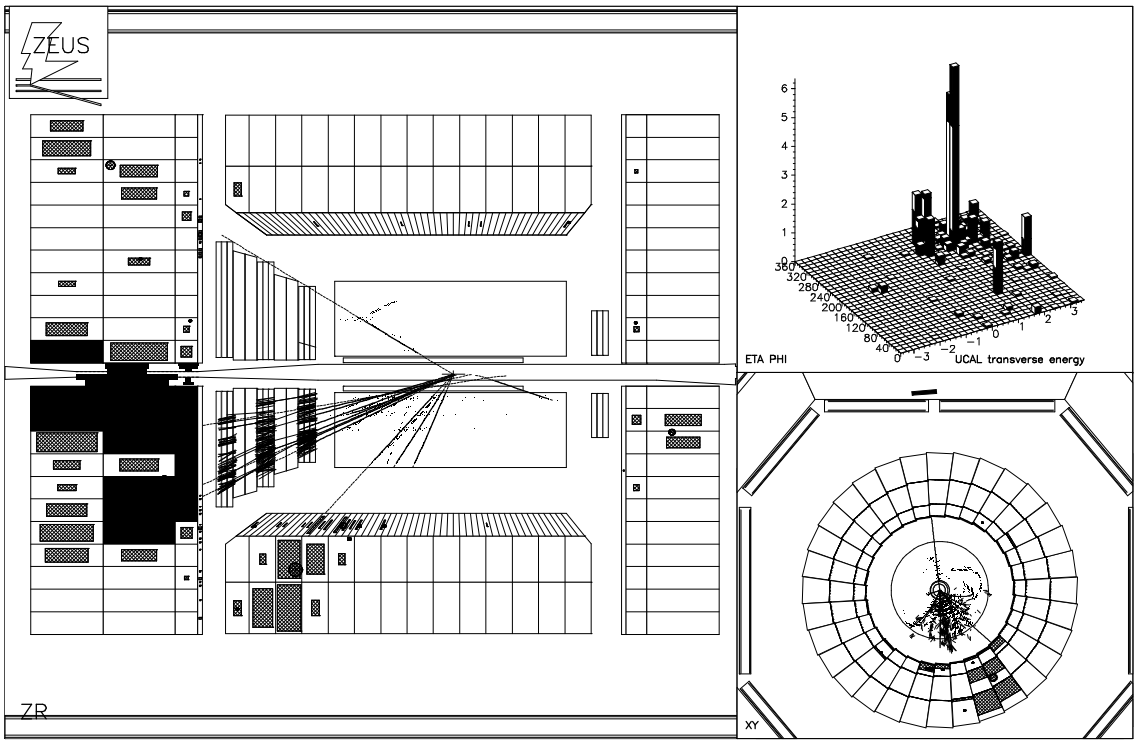

Figure B.3: Muon candidate event (run 33719, event 5856) from an e^+p interaction at $\sqrt{s} = 318\,\text{GeV}$ in the ZEUS detector.
$p_T^{\text{CAL}} = 30\,\text{GeV}$, $p_T^{\text{hadr}} = 30\,\text{GeV}$, $p_T^{\mu} = 781\,\text{GeV}$, $M_T^{l\nu} = 1531\,\text{GeV}$.

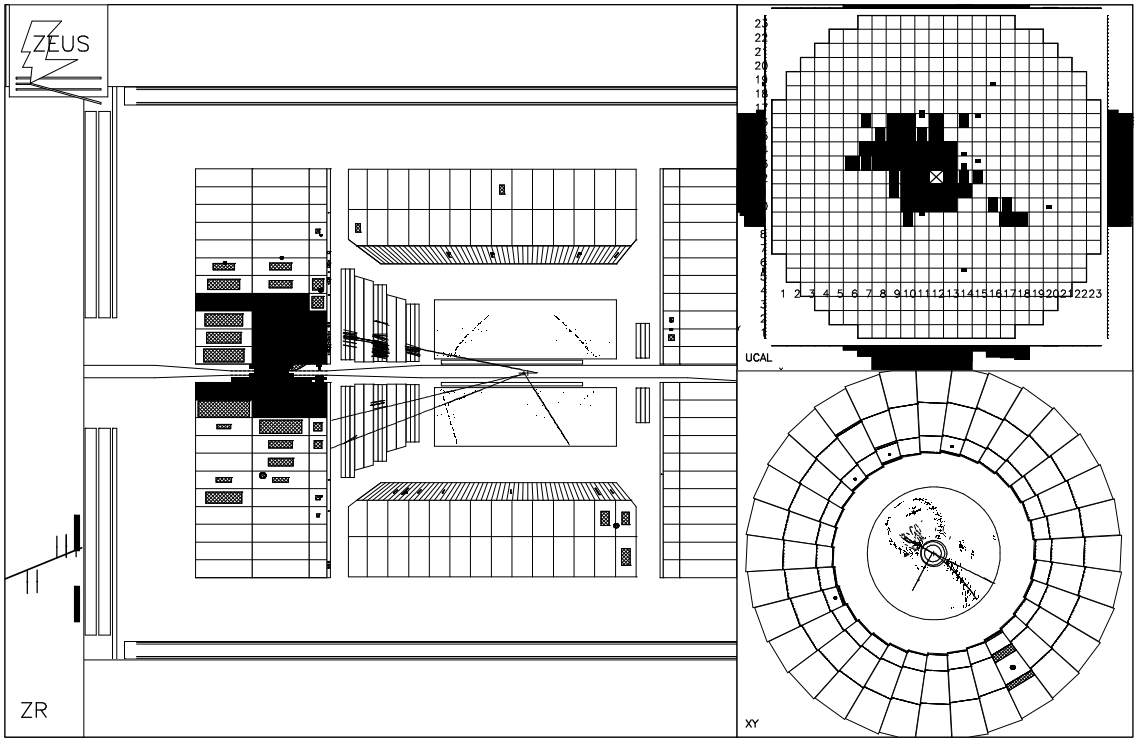

Figure B.4: Muon candidate event (run 34348, event 9897) from an e^+p interaction at $\sqrt{s} = 318\,\text{GeV}$ in the ZEUS detector.
$p_T^{\text{CAL}} = 28\,\text{GeV}$, $p_T^{\text{hadr}} = 28\,\text{GeV}$, $p_T^{\mu} = 13\,\text{GeV}$, $M_T^{l\nu} = 0.2\,\text{GeV}$.

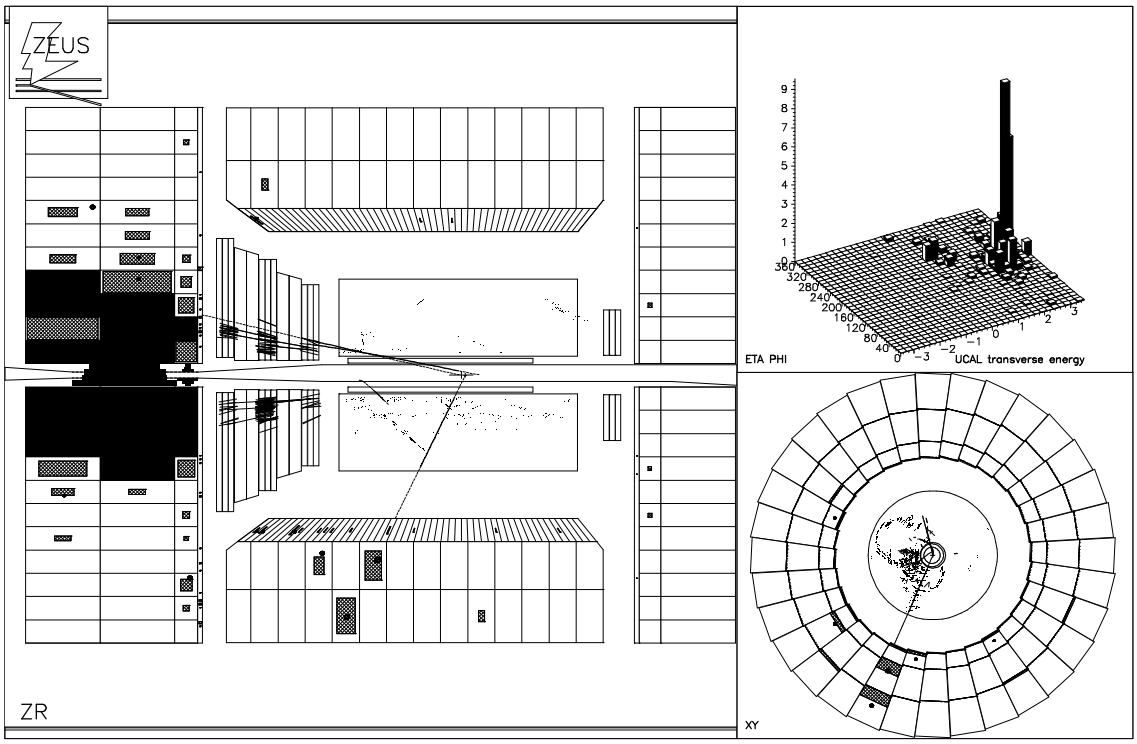

Figure B.5: Muon candidate event (run 35081, event 34896) from an e^+p interaction at $\sqrt{s} = 318\,\text{GeV}$ in the ZEUS detector.
$p_T^{\text{CAL}} = 40\,\text{GeV}$, $p_T^{\text{hadr}} = 40\,\text{GeV}$, $p_T^{\mu} = 38\,\text{GeV}$, $M_T^{l\nu} = 91\,\text{GeV}$.

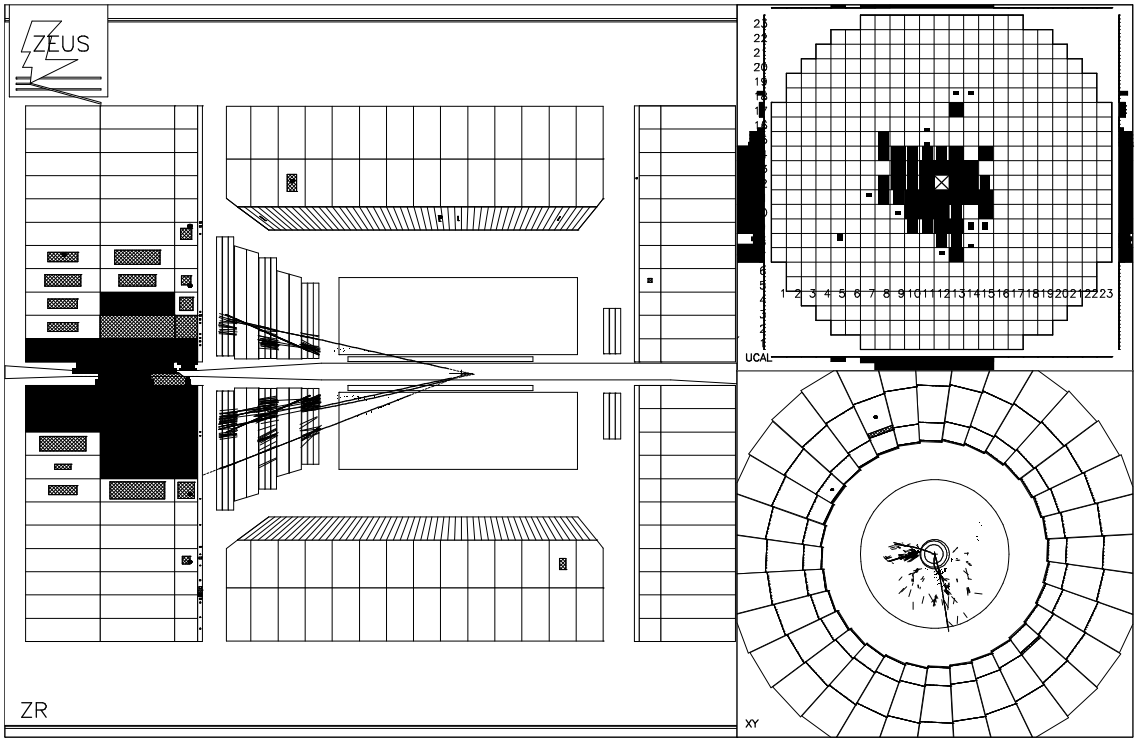

Figure B.6: Muon candidate event (run 35092, event 49609) from an e^+p interaction at $\sqrt{s} = 318\,\text{GeV}$ in the ZEUS detector.
$p_T^{\text{CAL}} = 29\,\text{GeV}$, $p_T^{\text{hadr}} = 29\,\text{GeV}$, $p_T^{\mu} = 8\,\text{GeV}$, $M_T^{l\nu} = 24\,\text{GeV}$.

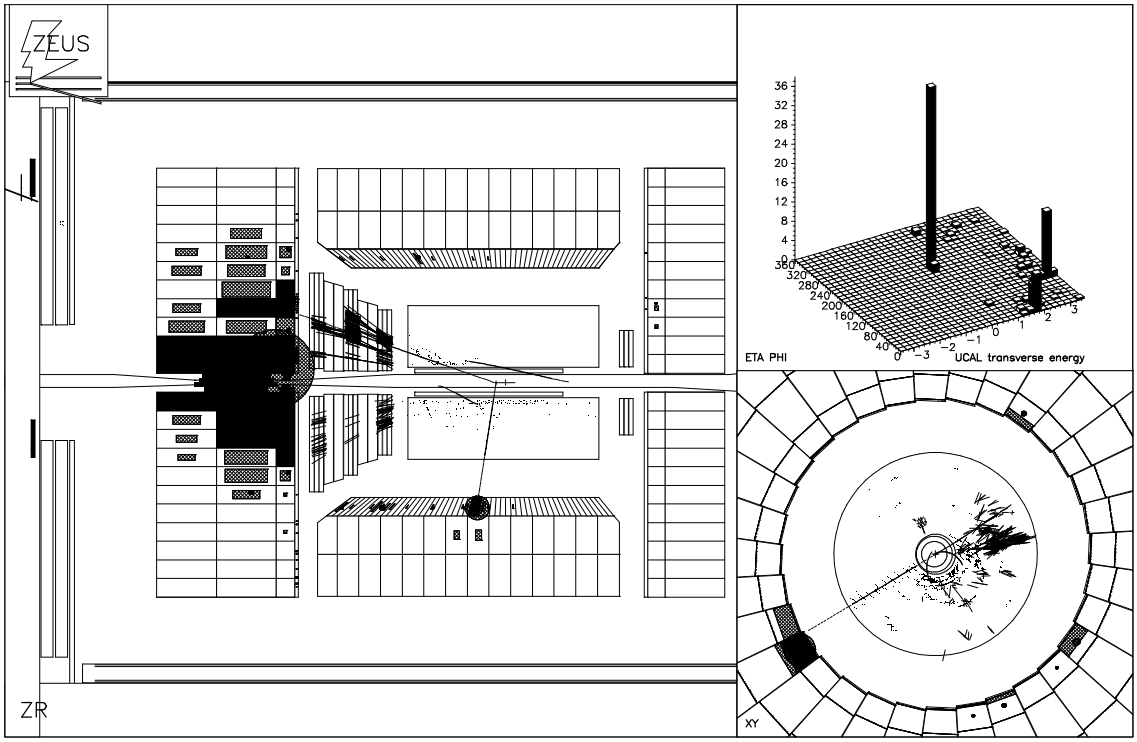

Figure B.7: Electron candidate event (run 36544, event 24240) from an e^+p interaction at $\sqrt{s} = 318\,\text{GeV}$ in the ZEUS detector.
$p_T^{\text{CAL}} = 20\,\text{GeV}$, $p_T^{\text{hadr}} = 30\,\text{GeV}$, $p_T^{el} = 44\,\text{GeV}$, $M_T^{l\nu} = 57\,\text{GeV}$.

Appendix C

Event displays of tau candidate events

This appendix presents the three events selected as tau candidates with a value of the tau discriminant $D > 0.95$. The energy deposition in the CAL is proportional to the size and density of shading in the CAL cells. The x-y-view in the lower right corner shows only the energy deposition in the barrel calorimeter. The arrow in the x-y view indicates the direction of the missing transverse momentum in the calorimeter, $\not{P}_T$.

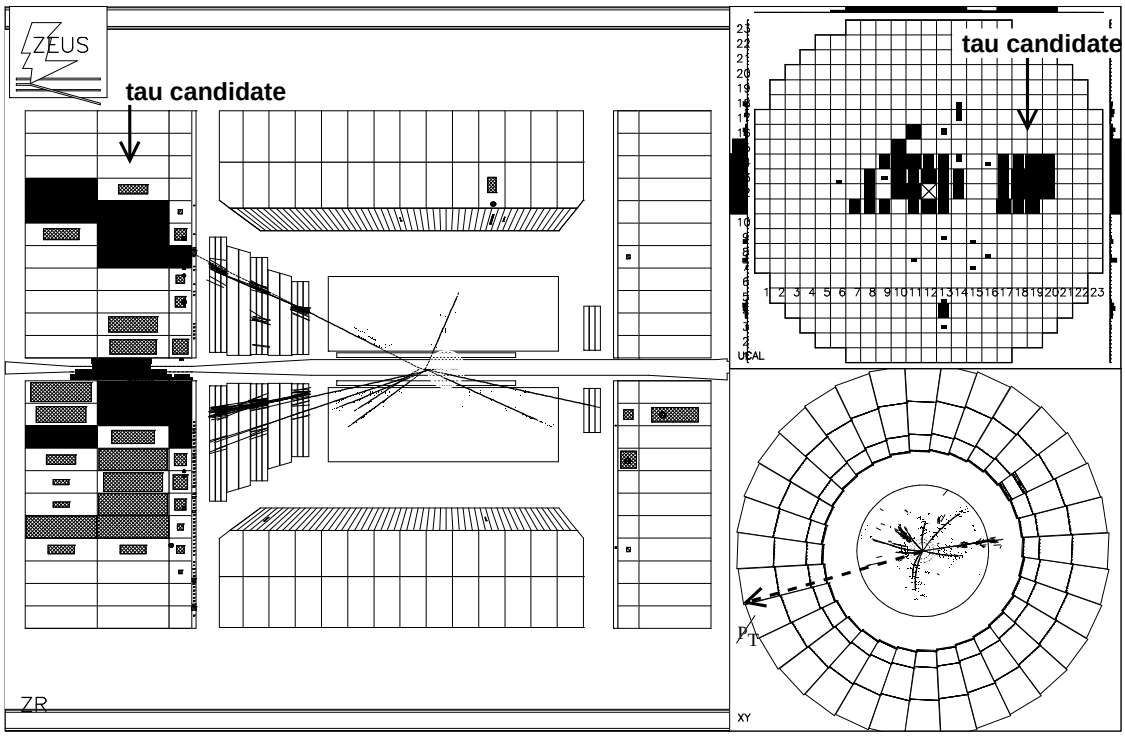

Figure C.1: Tau-candidate 1, with a low value of P_T^{hadr}, from an $e^- p$ interaction at $\sqrt{s} = 318\,\mathrm{GeV}$ in the ZEUS detector. In the upper right corner an $x - y$-view of the FCAL is shown. The tau candidate is visible as a clearly separated cluster of energy depositions in the FCAL. Selected event variables for all tau candidates are given in Tab. 9.2.

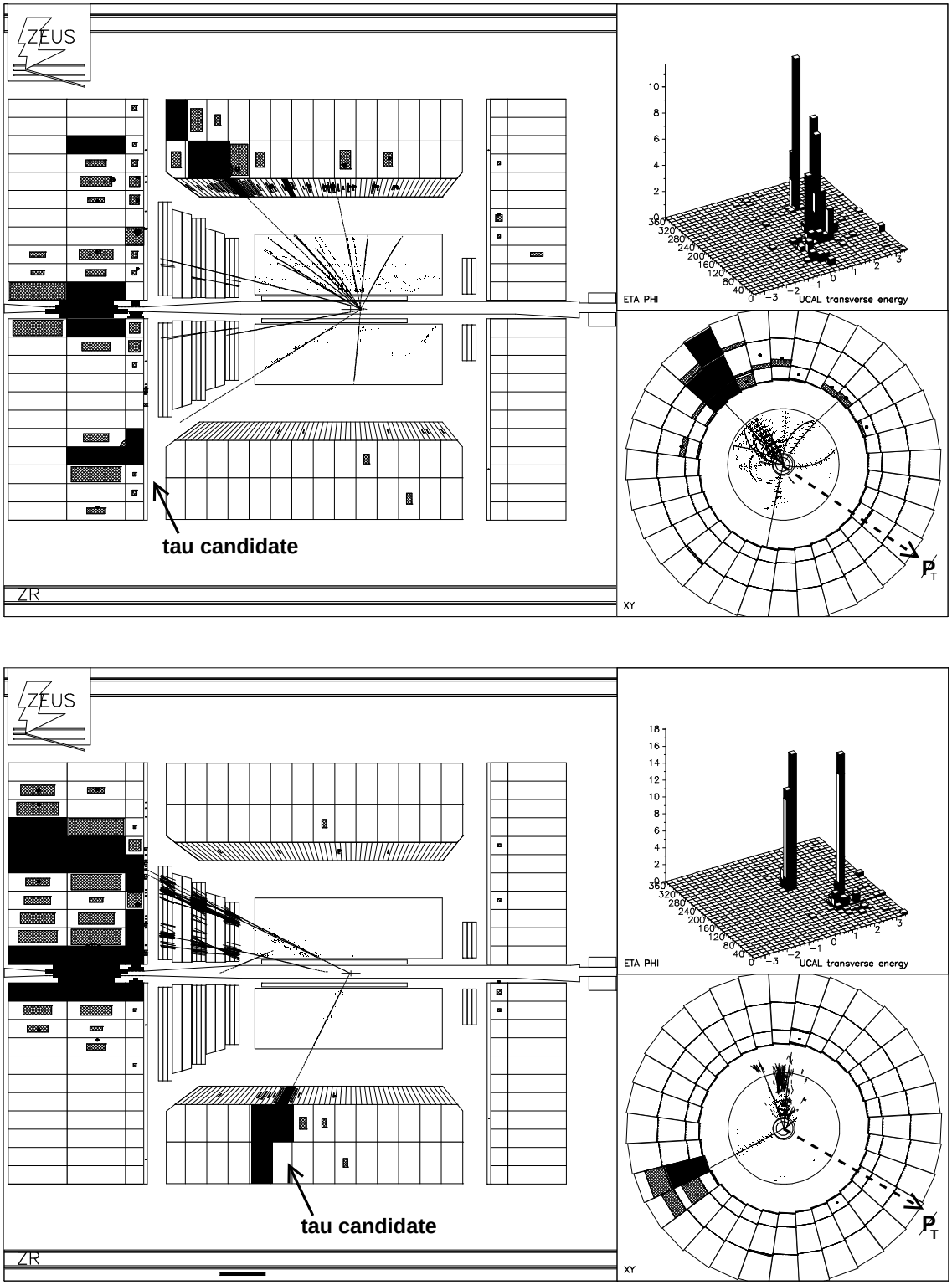

Figure C.2: Tau-candidate 2 (upper picture) and 3 (lower picture), with large values of P_T^{hadr}, from e^+p interactions at $\sqrt{s} = 318\,\mathrm{GeV}$ in the ZEUS detector. In the upper right corner an $\eta - \phi$-view of the transverse energy in the CAL is shown. The tau candidates are visible as clearly separated clusters of energy deposition. Selected event variables for all tau candidates are given in Tab. 9.2.

Appendix D

ZEUS preliminary results for EPS 2001

The results from a previous search for single-top production in the electron and muon channel, as performed by another group inside the ZEUS collaboration, were presented at the EPS 2001 conference [104]. Those results were obtained with a tighter set of selection cuts and without correcting the CAL energy values for detector effects. The CAL energy correction leads, on average, to larger values of the global transverse momenta. Therefore it acts like effectively lowering the selection cuts on p_T^{CAL} and p_T^{hadr}. As a cross check, the event selection from the previous analysis was reproduced by modifying the preselection cuts from section 6.1 according to the main differences in the two analyses.

For the preselection of isolated electron and muon events, the modified selection cuts were:

- Cut on uncorrected $p_T^{\mathrm{CAL,uncorr}} > 20\,\mathrm{GeV}$ instead of corrected $p_T^{\mathrm{CAL}} > 20\,\mathrm{GeV}$.
- General requirement for tracks: $p_T^{\mathrm{trk}} > 200\,\mathrm{MeV}$ (instead of $p_T^{\mathrm{trk}} > 100\,\mathrm{MeV}$).
- Cut on the transverse momentum of the isolated track: $p_T^{\mathrm{trk}} > 10\,\mathrm{GeV}$ (instead of $p_T^{\mathrm{trk}} > 5\,\mathrm{GeV}$).
- Cut on acoplanarity: $\phi_{\mathrm{acopl}}^{\mathrm{event}} > 0.20\,\mathrm{rad}$ (instead of $\phi_{\mathrm{acopl}}^{\mathrm{event}} > 0.14\,\mathrm{rad}$).

To reproduce the final selection of single top-quark candidates, the following cuts were modified:

- Muon channel: Uncorrected $p_T^{CAL,uncorr} > 25$ (40) GeV (instead of corrected $p_T^{\mathrm{hadr}} > 25$ (40) GeV).
- Electron channel: Uncorrected $E - p_Z^{\mathrm{uncorr}} > 45\,\mathrm{GeV}$ (instead of corrected $E - p_Z > 47\,\mathrm{GeV}$).

- Muon channel: $p_T^{\rm miss} > 12\,{\rm GeV}$ (instead of $p_T^{\rm miss} > 10\,{\rm GeV}$).
- Muon channel: Accept only events with not more than one muon (instead of no such constraint).

Table D summarises the obtained event yields at three different stages of the selection. A good agreement between the two analyses was observed, taking into account the remaining differences in the details of the event selection and the considered background MC samples. 10 of the electron events and 6 of the muon events from the preselection, as well as the previously selected electron and muon event at $p_T^{\rm hadr} > 25\,{\rm GeV}$, were in common for the two analyses.

ZEUS EPS 2001 analysis, 1994-2000 data, 130 pb^{-1}						
selection	Electrons			Muons		
stage	obs.	SM exp.	from W	obs.	SM exp.	from W
Preselection	10	11.0 ± 1.6	2.7	7	5.4 ± 0.7	1.3
$p_T^{\rm hadr} > 25\,{\rm GeV}$	1	1.14 ± 0.06	1.10	1	1.29 ± 0.16	0.95
$p_T^{\rm hadr} > 40\,{\rm GeV}$	0	0.46 ± 0.03	0.46	0	0.50 ± 0.08	0.41
Present ZEUS analysis with old selection cuts, 1994-2000 data, 130 pb^{-1}						
selection	Electrons			Muons		
stage	obs.	SM exp.	from W	obs.	SM exp.	from W
Preselection	11	10.0 ± 1.5	2.8	6	5.3 ± 0.3	1.5
$p_T^{\rm hadr} > 25\,{\rm GeV}$	1	1.88 ± 0.27	1.13	2	1.63 ± 0.16	1.03
$p_T^{\rm hadr} > 40\,{\rm GeV}$	0	0.63 ± 0.08	0.46	0	0.86 ± 0.12	0.61

Table D.1: Event yields for different stages of the event selection. The number of observed events in the data, the number of expected background events from all SM processes and the number of expected events from W production are compared for a previous analysis [104] and for the present analysis with modified selection cuts. The quoted errors are the statistical errors on the SM background expectation.

References

[1] H1 Coll., C. Adloff et al., Eur. Phys. J. **C 5**, 575 (1998).

[2] H1 Coll.. Paper 824 submitted to the International Europhysics Conference on High Energy Physics, Budapest, Hungary, July 12-18, 2001.

[3] H1 Coll.. Paper 1022 submitted to the XXXI International Conference on High Energy Physics, Amsterdam, The Netherlands, July 24-31, 2002.

[4] H1 Coll.. Paper 1024 submitted to the XXXI International Conference on High Energy Physics, Amsterdam, The Netherlands, July 24-31, 2002.

[5] H1 Coll., V. Andreev et al., Phys. Lett. **B561**, 241 (2003).

[6] D.H. Saxon, *Proc. HERA Workshop*, R.D. Peccei (ed.), Vol. 2, p. 903. DESY, Hamburg, Germany (1987).

[7] ZEUS Coll., U. Holm (ed.), *The ZEUS Detector*. Status Report (unpublished), DESY (1993), available on `http://www-zeus.desy.de/bluebook/bluebook.html`.

[8] N. Harnew et al., Nucl. Inst. Meth. **A 279**, 290 (1989);
B. Foster et al., Nucl. Phys. Proc. Suppl. **B 32**, 181 (1993);
B. Foster et al., Nucl. Inst. Meth. **A 338**, 254 (1994).

[9] M. Derrick et al., Nucl. Inst. Meth. **A 309**, 77 (1991);
A. Andresen et al., Nucl. Inst. Meth. **A 309**, 101 (1991);
A. Caldwell et al., Nucl. Inst. Meth. **A 321**, 356 (1992);
A. Bernstein et al., Nucl. Inst. Meth. **A 336**, 23 (1993).

[10] H. Bethe and W. Heitler, Proc. Roy. Soc. Lond. **A146**, 83 (1934).

[11] W. H. Smith, K. Tokushuku and L. W. Wiggers. *Proc. Computing in High-Energy Physics (CHEP), Annecy, France, 1992*, C. Verkerk and W. Wojcik (eds.), p.222. CERN, Geneva, Switzerland (1992). Also in preprint DESY-92-150B.

[12] S.M. Fisher and P. Palazzi,
ADAMO Programmers Manual – Version 3.2. CERN ECP and RAL, available on `http://adamo.web.cern.ch/Adamo/programmers_manual/TOC_of_adamo.html`.

[13] C.G. Callan and D.J. Gross, Phys. Rev. Lett. **22**, 156 (1969).

[14] ZEUS Structure Functions and Electroweak Physics working group, *Combined H1 and ZEUS results on NC and CC cross sections* (unpublished), 2000, available on `http://www-zeus.desy.de/physics/sfew/PUBLIC/sfew_results/preliminary/lp99/nc-cc-h1-zeus/index.html`.

[15] V.N. Gribov and L.N. Lipatov, Sov. J. Nucl. Phys. **15**, 438 (1972);
G. Altarelli and G. Parisi, Nucl. Phys. **B 126**, 298 (1977);
Yu.L. Dokshitzer, Sov. Phys. JETP **46**, 641 (1977).

[16] ZEUS Coll., S. Chekanov et al., Preprint DESY-02-105, 2003.

[17] U. Baur and D. Zeppenfeld, Nucl. Phys. **B 325**, 253 (1989).

[18] P. Nason, R. Rückl and M. Spira, J. Phys. **G25**, 1434 (1999).

[19] M. Spira, Preprint DESY-99-060 (hep-ph/9905469), 1999.

[20] K.P. Diener, C. Schwanenberger and M. Spira, Eur. Phys. J. **C25**, 405 (2002).

[21] K. P. Diener, C. Schwanenberger and M. Spira, Preprint hep-ex/0302040, 2003.

[22] W. Porod, D. Restrepo and J.W.F. Valle, Preprint hep-ph/0001033, 2000.

[23] T. Kon and T. Kobayashi, Phys. Lett. **B409**, 265 (1997).

[24] CDF Coll., F. Abe et al., Phys. Rev. Lett. **74**, 2626 (1995).

[25] DØ Coll., S. Abachi et al., Phys. Rev. Lett. **74**, 2632 (1995).

[26] K. Hagiwara et al., Phys. Rev. **D 66**, 010001 (2002).

[27] N. Cabibbo, Phys. Rev. Lett. **10**, 531 (1963).

[28] M. Kobayashi and T. Maskawa, Prog. Theor. Phys. **49**, 652 (1973).

[29] S. Moretti and K. Odagiri, Phys. Rev. **D57**, 3040 (1998).

[30] S. L. Glashow, J. Iliopoulos and L. Maiani, Phys. Rev. **D10**, 1285 (1970).

[31] CLEO Coll., R. Ammar et al., Phys. Rev. Lett. **71**, 674 (1993).

[32] CLEO Coll., S. Chen et al., Phys. Rev. Lett. **87**, 251807 (2001).

[33] J. A. Aguilar-Saavedra and B. M. Nobre, Phys. Lett. **B553**, 251 (2003).

[34] T. Han et al., Nucl. Phys. **B454**, 527 (1995).

[35] V. F. Obraztsov, S. R. Slabospitsky and O. P. Yushchenko, Phys. Lett. **B426**, 393 (1998).

[36] T. Han et al., Phys. Rev. **B426**, 073008 (1998).

[37] T. Han and J. L. Hewett, Phys. Rev. **D60**, 074015 (1999).

[38] H. Fritzsch and D. Holtmannspotter, Phys. Lett. **B457**, 186 (1999).

[39] J. M. Yang, B. L. Young and X. Zhang, Phys. Rev. **D 58**, 055001 (1998).

[40] DELPHI Coll., *Search for single top quark production in the framework of R-parity violation.* Paper 225 submitted to the XXXI International Conference on High Energy Physics, Amsterdam, The Netherlands, July 24-31, 2002.

[41] D. Atwood, L. Reina and A. Soni, Phys. Rev. **D55**, 3156 (1997).

[42] B. Grzadkowski, J. F. Gunion and P. Krawczyk, Phys. Lett. **B268**, 106 (1991).

[43] F. del Aguila, J. A. Aguilar-Saavedra and R. Miquel, Phys. Rev. Lett. **82**, 1628 (1999).

[44] A. Pukhov et al., Preprint INP MSU 98-41/542 (hep-ph/9908288), 1999.

[45] A.D. Martin et al., Eur. Phys. J. **C 4**, 463 (1998).

[46] A.D. Martin et al., Eur. Phys. J. **C 14**, 133 (2000).

[47] Ch. Berger and W. Wagner, Phys. Rep. **146**, 1 (1987).

[48] A. Belyaev and N. Kidonakis, Phys. Rev. **D65**, 037501 (2002).

[49] A. Belyaev and N. Kidonakis, private communication, 2002.

[50] F. Abe et al., Phys. Rev. Lett. **80**, 2525 (1998).

[51] ALEPH Collaboration, R. Barate et al., Phys. Lett. **B494**, 33 (2000).

[52] ALEPH Coll., A. Heister et al., Phys. Lett. **B543**, 173 (2002).

[53] G. Abbiendi et al., Phys. Lett. **B521**, 181 (2001).

[54] L3 Coll., P. Achard et al., Phys. Lett. **B549**, 290 (2002).

[55] ZEUS Coll., S. Chekanov et al., Phys. Lett. **B559**, 153 (2003).

[56] ZEUS Coll.. Paper 495 submitted to the International Europhysics Conference on High Energy Physics, Aachen, Germany, July 17-23, 2003.

[57] G. Gustafson and U. Pettersson, NP **B306**, 746 (1988).

[58] B. Andersson et al., Phys. Rep. **97**, 31 (1983).

[59] B. R. Webber, Nucl. Phys. **B 238**, 492 (1984).

[60] H.J. Kim and S. Kartik, Preprint LSUHE-145-1993, 1993.

[61] K. Hagiwara, S. Komamiya and D. Zeppenfeld, Z. Phys. **C 29**, 115 (1985).

[62] U. Baur, M. Spira and P.M. Zerwas, Phys. Rev. **D 42**, 815 (1990).

[63] F. Boudjema, A. Djouadi and J.L. Kneur, Z. Phys. **C 57**, 425 (1993).

[64] G. Ingelman, A. Edin and J. Rathsman, Comp. Phys. Comm. **101**, 108 (1997).

[65] T. Sjöstrand, Comp. Phys. Comm. **39**, 347 (1986);
T. Sjöstrand and M. Bengtsson, Comp. Phys. Comm. **43**, 367 (1987);
T. Sjöstrand, Comp. Phys. Comm. **82**, 74 (1994).

[66] T. Sjöstrand, Comp. Phys. Comm. **135**, 238 (2001).

[67] G. Marchesini et al., Comp. Phys. Comm. **67**, 465 (1992).

[68] H.L. Lai et al., Phys. Rev. **D 55**, 1280 (1997).

[69] M. Glück, E. Reya and A. Vogt, Phys. Rev. **D 46**, 1973 (1992).

[70] A. Kwiatkowski, H. Spiesberger and H.-J. Möhring, Comp. Phys. Comm. **69**, 155 (1992). Also in *Proc. Workshop Physics at HERA*, 1991, DESY, Hamburg.

[71] G.A. Schuler and H. Spiesberger, *Proc. Workshop on Physics at HERA*, W. Buchmüller and G. Ingelman (eds.), Vol. 3, p. 1419. Hamburg, Germany, DESY (1991).

[72] CTEQ Coll., H.L. Lai et al., Eur. Phys. J. **C 12**, 375 (2000).

[73] L. Lönnblad, Comp. Phys. Comm. **71**, 15 (1992).

[74] M. Kuhlen, *QCD and the hadronic final state in deep inelastic scattering at HERA*. Habilitation Thesis, Universität Hamburg, Report MPI-PhE/97-33, 1997.

[75] N.H. Brook et al., Preprint hep-ex/9912053, 1999.

[76] T. Abe, Comp. Phys. Comm. **136**, 126 (2001).

[77] U. Baur, J.A.M. Vermaseren and D. Zeppenfeld, Nucl. Phys. **B 375**, 3 (1992).

[78] P. Aurenche et al., Z. Phys. **C56**, 589 (1992).

[79] R. Brun et al., GEANT3, Technical Report CERN-DD/EE/84-1, CERN, 1987.

[80] S. Chekanov et al., Phys. Lett. **B539**, 197 (2002).

[81] J. Grosse-Knetter, *Corrections for the Hadronic Final State* (unpublished). ZEUS-98-031, Internal ZEUS-note, 1998.

[82] ZEUS Coll., J. Breitweg et al., Eur. Phys. J. **C 11**, 427 (1999).

[83] G.F. Hartner, *VCTRAK(3.07/04): Offline Output Information* (unpublished). ZEUS-97-064, Internal ZEUS-note, 1997.

[84] G. F. Hartner, *VCTRAK Briefing: Program and Math* (unpublished). Zeus-98-058, Internal ZEUS-note, 1998.

[85] ZEUS Coll., J. Breitweg et al., Z. Phys. **C 74**, 207 (1997).

[86] A. Kappes, *Verwendung Neuronaler Netze zur Identifikation des gestreuten Elektrons in ep-Ereignissen mit hohem Q^2 bei ZEUS.* Diploma Thesis, Universität Bonn, Bonn, Germany, Report BONN-IB-97-28, 1997, available on `http://www-zeus.physik.uni-bonn.de/german/diploma.html`.

[87] S. Catani et al., Nucl. Phys. **B406**, 187 (1993).

[88] S.D. Ellis and D.E. Soper, Phys. Rev. **D 48**, 3160 (1993).

[89] O. Gonzalez, *Precise Determinations of the Strong Coupling Constant at HERA.* PhD Thesis, Univ. Madrid, Madrid (Spain), Report DESY-THESIS-2002-020, 2002.

[90] O. Gonzalez, H. Raach and J. Terron, *Measurements of the inclusive jet cross sections in NC DIS in the Breit Frame* (unpublished). ZEUS-02-007.

[91] T. Matsushita, *Search for events with a high energy isolated lepton and large missing transverse momentum in ep collisions at $\sqrt{s} = 300\,GeV$.* PhD thesis, Tokio Metropolitan University, Tokio (Japan), 1998.

[92] ZEUS Coll., S. Chekanov et al., Preprint DESY-02-105, 2002.

[93] C.N. Nguyen. Diploma Thesis, Universität Hamburg, Hamburg (Germany), Report DESY-THESIS-2002-024, 2002.

[94] L.A.T. Bauerdick et al., Nucl. Inst. Meth. **A501**, 340 (2003).

[95] E. Maddox, *A Kalman filter trackfit for the ZEUS microvertex detector* (unpublished). ZEUS-02-007.

[96] S. Chekanov et al., Phys. Lett. **B539**, 197 (2002).

[97] H1 Coll., C. Adloff et al., Nucl. Phys. **B 545**, 3 (1999).

[98] ZEUS Coll., S. Chekanov et al., Phys. Lett. **B558**, 41 (2002).

[99] J.R. Forshaw and M.H. Seymour, JHEP **09**, 009 (1999).

[100] M. H. Seymour, Nucl. Phys. **B421**, 545 (1994).

[101] T. Carli and B. Koblitz. Adv. Comp. Analysis Techniques in Phys. Research (Batavia, USA, 2000), P. Bath and M. Kasemann, Eds., pp 110, also in hep-ph/0011224, 2000;
T. Carli and B. Koblitz, Nucl. Inst. Meth. **A501**, 576 (2003).

[102] B. Koblitz, *Search for Instanton-Induced Processes with the H1 Detector in Deep-Inelastic-Scattering Electon-Proton Collisions at HERA*. PhD thesis, Universität Hamburg, Hamburg (Germany), Report DESY-THESIS-2002-015, 2002.

[103] D. Lelas, private communication, 2003.

[104] ZEUS Coll., S. Chekanov et al.. Paper 650 submitted to the International Europhysics Conference on High Energy Physics, Budapest, Hungary, July 12-18, 2001.

[105] ZEUS Coll., S. Chekanov et al.. Paper 906 submitted to the XXXI International Conference on High Energy Physics, Amsterdam, The Netherlands, July 24-31, 2002.

[106] H1 Coll., T. Ahmed et al., Preprint DESY-94-248, DESY, 1994.

[107] H1 Coll.. Paper 974 submitted to the International Conference on High-Energy Physics, Osaka, Japan, July 2000, 2000.

[108] V. Blobel and E. Lohrmann, *Statistische und Numerische Methoden der Datenanalyse*, in Teubner-Studienbücher Physik. B.G. Teubner, Stuttgart, Leipzig (Germany), 1998. In German.

[109] U. Schneekloth, *The HERA Luminosity Upgrade*, Technical Report DESY HERA 98-05, DESY, 1998.

[110] M. Feuerstack-Raible, Nucl. Inst. Meth. **A447**, 35 (2000).

[111] V. Chiochia, Nucl. Inst. Meth. **A501**, 60 (2003);
E. Koffeman, Nucl. Inst. Meth. **A473**, 26 (2001);
M. C. Petrucci, Int. J. Mod. Phys. **A16, Suppl. 1C**, 1078 (2001);
U. Kötz, Nucl. Inst. Meth. **A461**, 210 (2001);
E. Koffeman, Nucl. Inst. Meth. **A453**, 59 (2000);
C. Coldewey, for the ZEUS MVD group, Nucl. Inst. Meth. **A 453**, 149 (2000);
C. Coldewey, Nucl. Inst. Meth. **A 447**, 44 (2000);
R. Klanner, *The ZEUS Micro Vertex Detector*. Proceedings of the International Europhysics Conference on High Energy Physics, EPS-HEP 99, Tampere, Finland, 1999;
A. Garfagnini, Nucl. Inst. Meth. **A435**, 34 (1999).

[112] D. Dannheim et al., Nucl. Inst. Meth. **A505**, 663 (2003).

[113] D. Pitzl et al., Nucl. Inst. Meth. **A454**, 334 (2000).

[114] D. Bailey et al., *Study of beam-induced backgrounds in the ZEUS detector from 2002 HERA running* (unpublished), 2002, available on `http://www-zeus.desy.de/~kuze/zeusbg/`.
ZEUS-02-018,ZEUS-02-020,ZEUS-02-027.

[115] D. Dannheim, *The silicon strip detectors of the ZEUS microvertex detector.* Diploma Thesis, Universität Hamburg, Hamburg (Germany), Report DESY-THESIS-1999-027, 1999.

[116] J.J. Velthuis, *Radiation hardness of the ZEUS MVD frontend chip and Strangeness production in ep scattering at HERA.* PhD thesis, University of Amsterdam, Amsterdam (Netherlands), 2003.

[117] SINTEF Electronics and Cybernetics. http://www.ittf.no/ecy.

[118] E. H. Nicollian and J. R. Brews, *MOS physics and technology.* John Wiley & Sons, 1982.

[119] Iseg Spezialelektronik GmbH. http://www.iseg-hv.com.

[120] T. I. Meyer, Int. J. Mod. Phys. **A16S1C**, 1084 (2001).

[121] S.M. Sze, *Physics of semiconductor devices.* John Wiley & Sons, 1981.

[122] NMRC, Ireland. http://www.nmrc.ie/projects/radfets/index.html.

[123] A. Vasilescu and G. Lindstroem, *Displacement damage in silicon, on-line compilation*, 2000, available on `http://sesam.desy.de/members/gunnar/Si-dfuncs.html`.

[124] M. Moll et al., Nucl. Inst. Meth. **B186**, 100 (2002).

[125] S. Dittongo et al., *Studies on radiation damage by 900 MeV electrons on standard and oxygen enriched silicon devices.* Presented at the 9th European symposium on Semiconductor Detectors, Schloss Elmau (Germany), to appear in NIM A, 2002.

[126] M. Moll, *Radiation Damage in Silicon Particle Detectors.* Ph.D. Thesis, University of Hamburg, Report DESY-THESIS-1999-040, 1999.

[127] CERN radiation-test facility. http://irradiation.web.cern.ch/irradiation/.

[128] C. J. Damerell, *Vertex detectors: The State of the art and future prospects.* Proceedings of the 1995 SLAC Summer Institute on Particle Physics: The Top Quark and the Electroweak Interaction, SLAC-R-494, 1995.

[129] B. Holzer, private communication, 2003.

[130] H. Feick, *Analysis of the radiation tolerance of the LHCb silicon vertex detector.* Report LHCb-98-043, 1998.

[131] U. Holm, private communication, 2000.

Acknowledgements

The results of this thesis could not have been achieved without the combined efforts of the members of the ZEUS collaboration and many others. In particular, I would like to thank:

Prof. Robert Klanner for making this thesis possible and for his continous support and trust in my work; Tancredi Carli for being an enthusiastic and unfailing tutor and supervisor of my analysis, also after having moved to Geneva; Prof. Peter Schleper for taking over the supervision in the final phase and for guiding this thesis to an end; Masahiro Kuze for suggesting the isolated lepton search topic in the first place and for many important questions and hints; Lorenzo Bellagamba for the great teamwork in the single-top search and for all his encouraging support concerning the other parts of the analysis; Elisabetta Gallo for coordinating the analysis efforts and creating an especially friendly and productive working atmosphere in the exotics group; Katarzyna Klimek for her support and vivid interest and for reading and correcting the draft; Bruce Straub for valuable criticism and many explanations; Prof. Juan Terron for discussions concerning the single-top phenomenology and the limit setting procedure; Claudia Glasman, Monica Vazquez, James Ferrando and Xiang Liu for help, in particular, with generating Monte Carlo events; Prof. Erich Lohrmann and Prof. Volker Blobel for advice concerning the H1 and ZEUS comparison method; Achim Geiser for stimulating ideas and discussions; Christian Schwanenberger for explanations concerning the W cross-section calculations; Alexander Belyaev and Nikolaos Kidonakis for providing the algorithm for the single-top NLO calculations; Chi-Nhan Nguyen and Damir Lelas for sharing the fun of the tau-search; Birger Koblitz for providing us the necessary range-searching algorithm;

Ulrich Kötz, Ingo Bloch, Benjamin Kahle, Isabell Melzer-Pellman, Margherita Milite, Enrico Borsato, Prof. Roberto Carlin, Flavio Dal Corso, Eckhart Fretwurst and Gregor Kramberger for help and advice concerning the radiation monitor chapter; Michael Moll and Maurice Glaser for performing and analysing the irradiation experiment at the CERN PS with me and for useful discussions and explanations;

Prof. Frank Sciulli and Prof. Allen Caldwell for inviting me to Columbia University and for their supervision and concern for my well being during and after my stay in New York; all the other members and guests of the Columbia Physics department who helped to make this both a very productive and the most exiting phase of my PhD; in particular Tulika Bose, Raphael Galea and Jovan Mitrevski for exploring the city with

me; the German Academic Exchange Service for the funding of my stay at Columbia[1];

Stefan Schlenstedt for sharing his Hamburg office with me; Oliver Gutsche for sharing his computing knowledge and also for continuous encouragement and strategic advice; all those associated with the Uni Hamburg ZEUS group for various help and for the superb atmosphere and working environment, besides those mentioned already, namely Volker Adler, Vincenco Chiochia, Nicola Coppola, Alberto Garfagnini, Sonja Hillert, Harald Labes, Matthias Moritz, Elizabeth Nuncio-Quiroz, Maria-Carmela Petrucci, Amita Raval and Raquel Santamarta.

I would like especially to thank my parents, my sister and my brothers for supporting and encouraging me continously and for their patience.

[1]DAAD Doktorandenstipendium im Rahmen des gemeinsamen Hochschulsonderprogramms III von Bund und Ländern